Microscopic view of hydrogen adsorption in size-variant nano-clay materials

Mohammad Abdelsater

▶ **To cite this version:**

Mohammad Abdelsater. Microscopic view of hydrogen adsorption in size-variant nano-clay materials. Materials Science [cond-mat.mtrl-sci]. Université Paris-Saclay, 2024. English. NNT : 2024UPASP168 . tel-05424732

HAL Id: tel-05424732
https://theses.hal.science/tel-05424732v1

Submitted on 19 Dec 2025

HAL is a multi-disciplinary open access archive for the deposit and dissemination of scientific research documents, whether they are published or not. The documents may come from teaching and research institutions in France or abroad, or from public or private research centers.

L'archive ouverte pluridisciplinaire **HAL**, est destinée au dépôt et à la diffusion de documents scientifiques de niveau recherche, publiés ou non, émanant des établissements d'enseignement et de recherche français ou étrangers, des laboratoires publics ou privés.

THESE DE DOCTORAT

NNT : 2024UPASP168

Microscopic view of hydrogen adsorption in size-variant nano-clay materials

Vue microscopique de l'adsorption d'hydrogène dans des matériaux nano-argileux de taille variable

Thèse de doctorat de l'université Paris-Saclay

École doctorale n° 564, Physique en Île-de-France (PIF)
Spécialité de doctorat : Physique
Graduate School : Physique. Référent : Faculté des sciences d'Orsay

Thèse préparée dans l'unité de recherche **Laboratoire de Physique des Solides** (Université Paris-Saclay, CNRS), sous la direction de **Pascale LAUNOIS**, Directrice de Recherche, la co-direction de **Laurent TRUCHE**, Professeur à l'Université Grenoble Alpes, et le co-encadrement de **Stéphane ROLS**, Chercheur

Thèse soutenue à Paris-Saclay, le 18 Décembre 2024, par

Mohammad ABDEL SATER

Composition du Jury

Membres du jury avec voix délibérative

Vanessa FIERRO Directrice de recherche, Université de Lorraine	Présidente
Benoit COASNE Directeur de recherche, Université Grenoble Alpes	Rapporteur & Examinateur
Marie-Vanessa COULET Directrice de recherche, Aix Marseille Université	Rapporteure & Examinatrice
Laurent MICHOT Directeur de recherche, Sorbonne Université	Examinateur
Jean-Marc ZANOTTI Directeur de recherche, Université Paris-Saclay	Examinateur

université PARIS-SACLAY | ÉCOLE DOCTORALE Physique en Île-de-France (PIF)

Titre : Vue microscopique de l'adsorption d'hydrogène dans des matériaux nano-argileux de taille variable.

Mots clés : stockage de l'hydrogène, nano-argiles, physisorption, isothermes d'adsorption, diffusion des rayons X et des neutrons

Résumé : L'hydrogène est le combustible sans carbone par excellence, car sa combustion n'émet que de l'eau. Actuellement, le principal obstacle à un déploiement massif des technologies utilisant l'hydrogène à des fins énergétiques est son stockage. Les technologies basées sur l'adsorption de H_2 figurent parmi les plus explorées. Mais peu de recherches ont été menées sur les argiles pour le stockage d'hydrogène, alors que la découverte récente de fortes teneurs en hydrogène dans des roches riches en argile montre leur potentiel à cet égard.

L'objectif de la présente étude est d'examiner, au niveau microscopique, les mécanismes d'adsorption de H_2 sur des smectites trioctaédriques synthétiques 2:1 de dimensions nanométriques, spécifiquement la Laponite et son précurseur, la pré-Laponite. À partir des isothermes d'adsorption d'hydrogène, nous avons observé que la pré-Laponite présente une capacité de sorption de H_2 plus élevée que la Laponite à 40K et 77K à 1 bar.

La première partie de la thèse se concentre sur la caractérisation des échantillons synthétisés. L'ICP-AES a montré que la Laponite et la pré-Laponite partagent une formule moléculaire identique, tandis que la diffraction des rayons X a révélé une structure atomique similaire mais que la pré-Laponite présente un ordre à longue portée plus réduit. La spectroscopie IR indique un ordre local identique dans les deux matériaux. La spectroscopie d'absorption des rayons X réalisée aux seuils K du Si et du Mg corrobore cette conclusion. La RMN du silicium à l'état solide apporte des informations supplémentaires, révélant trois environnements distincts pour le silicium dans les deux échantillons, les variations des intensités intégrées des signaux correspondants indiquant avec des rapport bord-volume différents dans les deux matériaux. Les isothermes d'adsorption d'azote ont également mis en évidence des différences dans les propriétés texturales : la pré-Laponite présente à la fois de la microporosité et de la macroporosité, tandis que la Laponite est principalement microporeuse avec des contributions mésoporeuses

La seconde partie de la thèse concerne l'adsorption de H_2. Les isothermes d'adsorption à 40 K ont été fittées avec des contributions de type Langmuir et Freundlich. Des simulations Monte-Carlo en Grand Canonique ont permis de déduire que le modèle de Langmuir, représentant les sites de liaison les plus forts avec saturation en monocouche, décrit l'adsorption au sein de l'interfeuillet, tandis que le modèle de Freundlich prend en compte l'adsorption sur la surface externe. Des expériences de diffusion inélastique des neutrons ont été menées pour sonder la transition rotationnelle para-à-ortho de H_2, dont l'énergie est très dépendante de l'environnement de la molécule. À 40 K, trois sites d'adsorption ont été identifiés dans la pré-Laponite. Le premier pourrait correspondre à un site de dissociation de l'hydrogène et les deux autres sont des sites de physisorption dans l'espace interfeuillet.

La dépendance en pression d'hydrogène de l'intensité du pic *001* dans les diagrammes de diffraction des neutrons de la Laponite et de la pré-Laponite révèle que l'hydrogène intercalé forme une monocouche dense. La diffusion des neutrons à grands angles, combinée à des simulations atomistiques, a été utilisée pour sonder la structuration du D_2 (utilisé à la place de H_2 pour améliorer le rapport signal/bruit) dans l'interfeuillet.

Ce travail de thèse contribue à une plus grande compréhension des mécanismes d'adsorption de H_2 dans des matériaux argileux en feuillets, mettant en lumière la capacité de sorption améliorée de la pré-Laponite, et il montre comment les isothermes d'adsorption et les techniques de diffusion des neutrons se complètent mutuellement.

université PARIS-SACLAY | ÉCOLE DOCTORALE Physique en Île-de-France (PIF)

Title: Microscopic view of hydrogen adsorption in size-variant nano-clay materials.

Keywords: hydrogen storage, nano-clays, physisorption, adsorption isotherms, X-ray and neutron scattering

Abstract: Hydrogen is the carbon-free fuel par excellence because its combustion emits only water. At present, the limiting point to a massive deployment of technologies using hydrogen for energy purposes is its storage. Technologies based on sorption are among the most thoroughly explored. Little research has been done on clays for hydrogen storage, while the recent discovery of high hydrogen contents in clay-rich rocks shows their potential for it.

The aim of the present study is to investigate, at the microscopic level, H_2 adsorption mechanisms on synthetic 2:1 trioctahedral smectites of nanometric dimensions, specifically Laponite, and its precursor, pre-Laponite. Starting with the hydrogen adsorption isotherms, we observed that pre-Laponite exhibits a higher H_2 sorption capacity than Laponite at 40K and 77K at 1bar.

The first part of the thesis focuses on the characterization of synthesized samples. ICP-AES showed that Laponite and pre-Laponite share a similar molecular formula, while X-ray scattering revealed similar structure and that pre-Laponite exhibits reduced long-range order. IR spectroscopy points towards similar local order in both materials. X-ray absorption near-edge spectroscopy performed at the Si and Mg K-edges supports this conclusion.. ^{29}Si solid-state NMR provided additional insights, revealing three distinct silicon environments in both samples, with variations in signal area that correlate with differences in the edge-to-volume ratio between the two materials. Nitrogen adsorption isotherms further highlighted differences in textural properties: pre-Laponite exhibits a composite pore structure with both microporosity and macroporosity, whereas Laponite is primarily microporous with mesoporous contributions.

The second part of the thesis concerns H_2 adsorption. The adsorption isotherms at 40 K were fitted with Langmuir and Freundlich contributions. Grand-Canonical Monte-Carlo simulations allowed one to infer that the Langmuir model, accounting for the strongest binding sites with monolayer saturation, describes adsorption within the interlayer, while the Freundlich model accounts for adsorption at the external surface. Inelastic neutron scattering experiments were undertaken to probe the para-to-ortho rotational transition of H_2, the energy of which is highly sensitive to its environment. At 40K, three adsorption sites were identified in pre-Laponite. The first could correspond to a hydrogen dissociation site, while the other two are physiosorption sites in the interlayer space.

The pressure dependence of the *001*-peak intensity in the neutron diffraction diagrams of Laponite and pre-Laponite reveals that interlayer H_2 forms a dense phase. Wide-angle neutron scattering, combined with atomistic simulations, was used to probe the structuration of D_2 (used in place of H_2 for improved signal-to-noise ratio) within this interlayer region.

This thesis work contributes to a deeper understanding of H_2 adsorption mechanisms in layered clay materials, particularly highlighting the enhanced sorption capacity of pre-Laponite, and demonstrates how adsorption isotherms and neutron scattering techniques complement each other.

Résumé en français

L'hydrogène est un carburant sans carbone, car sa combustion ne produit que de l'eau. Les recherches se sont concentrées sur le stockage de H_2 dans des matériaux légers pour les applications automobiles, excluant les argiles en raison de leur poids. Cependant, le stockage terrestre à grande échelle pour des applications industrielles ne nécessite pas de telles spécifications. Dans ce contexte, les minéraux argileux offrent des avantages tels qu'une grande surface spécifique, un faible coût, une abondance et une sécurité environnementale.

Nous avons étudié l'adsorption de H_2 au niveau microscopique sur des smectites trioctaédriques 2:1 synthétiques de dimensions nanométriques, spécifiquement la Laponite et son précurseur, la pré-Laponite.

Préparation du matériau

La synthèse de la Laponite suit un protocole bien établi décrit dans le brevet de Barbara Neumann. La formule moléculaire nominale, confirmée par spectroscopie d'émission atomique à plasma inductif couplé (ICP-AES), est $[Mg_{4.8}\ Li_{1.2}]^{oct}\ [Si_8]^{tet}\ O_{20}(OH)_4$, où « Oct » et « Tet » désignent les positions des cations dans les feuillets octaédriques et tétraédriques. La couche TOT a une charge nette de -1,2e par maille, compensée par des Na^+ dans l'espace interfeuillet. La synthèse commence par la précipitation des précurseurs dans de l'eau deutérée sous agitation contrôlée pendant au moins 30 minutes, suivie d'un reflux à 100°C pendant 1 heure pour obtenir la suspension de pré-Laponite. Cette suspension subit un traitement hydrothermal à 207°C et 17 bars pendant 5 heures et 30 minutes pour produire la suspension de Laponite. Les suspensions de pré-Laponite et de Laponite sont centrifugées à 8000 rpm pendant 5 minutes, lavées trois fois avec du D_2O, puis lyophilisées pour obtenir des échantillons en poudre.

Analyse structurale

Les propriétés structurales de la Laponite et de la pré-Laponite deutérées ont été caractérisées à l'aide de la spectroscopie de diffusion des rayons X (DRX), mettant en évidence les similarités et les différences entre les deux matériaux. Les diffractogrammes des deux échantillons présentent deux types principaux de réflexions. Les pics de Bragg larges *00l*, qui fournissent des informations sur l'agencement des feuillets perpendiculairement à leur base. Des bandes *hk* (et non des pics de Bragg *hkl*), indicatives d'un désordre turbostratique de feuillet à feuillet. La similarité observée entre les diffractogrammes des deux échantillons suggère qu'ils partagent le même agencement atomique, ce qui est cohérent avec leurs formules moléculaires comparables. L'analyse des largeurs des réflexions de Bragg ou de la montée de la bande hk montre une portée moindre de l'ordre dans la pré-Laponite.

L'analyse de la fonction de distribution de paires (PDF) montre également que la Laponite et la pré-Laponite présentent les mêmes distances inter-atomiques. Cependant, une décroissance plus rapide du signal PDF dans la pré-Laponite avec la distance montre un ordre structural à plus courte portée dans la pré-Laponite, comme le montrait aussi l'analyse des diagrammes de diffraction dans l'espace réciproque.

La pré-Laponite présente une structure poreuse composite avec à la fois une microporosité et une macroporosité, tandis que la Laponite est microporeuse avec des contributions de mésoporosité. L'analyse des boucles d'hystérésis suggère que la Laponite présente des pores plus étroits en forme de fente associés à son espace interfeuillet.

La spectroscopie infrarouge (IR) montre elle-aussi que les environnements locaux dans les deux matériaux sont similaires. De plus, les spectres de résonance magnétique nucléaire du ^{29}Si (RMN) montrent des environnements de silicium

comparables, mais un rapport plus important entre environnement Q^3 et Q^2 dans la Laponite, ce qui indique une réduction de la taille des couches dans la pré-Laponite ou la présence de plus nombreux défauts. Ce résultat est en accord avec les longueurs de cohérence diminuées observées par diffraction des rayons X. La spectroscopie d'absorption des rayons X aux bords Si-K et Mg-K (XANES) montre également des similarités notables entre la Laponite et la pré-Laponite. Cependant, les spectres indiquent une homogénéité moindre parmi les sites de silicium dans la pré-Laponite, potentiellement due à la taille réduite des couches.

Vue microscopique de l'adsorption de H_2 dans le (pré-)Laponite

Pour étudier l'adsorption de H_2 dans la (pré-)Laponite, nous avons utilisé une combinaison de courbes d'isothermes d'adsorption, de simulations de Monte Carlo dans le grand canonique (GCMC), et des techniques de diffusion neutronique élastique et inélastique. Les isothermes d'adsorption de H_2 mesurées à température ambiante – 100 bars et à 77 K sous une pression de 1 bar – montrent que la pré-Laponite adsorbe plus d'hydrogène que la Laponite. À 40 K et jusqu'à 1 bar, les données d'adsorption ont été analysées en utilisant à la fois les modèles de Langmuir et de Freundlich. Les simulations GCMC, utilisant le champ de forces COMPASS, révèlent que l'adsorption de H_2 se produit à la fois sur les sites interfeuillet et sur les sites de surface externe. Les sites interfeuillet suivent le modèle de Langmuir, étant les plus favorables sur le plan énergétique pour l'adsorption à faible pression (Figure 1). Cette observation est soutenue par les mesures de diffusion neutronique à petit angle (SANS), qui sondent l'impact de l'adsorption de H_2/D_2 sur le pic 001 à 40 K.

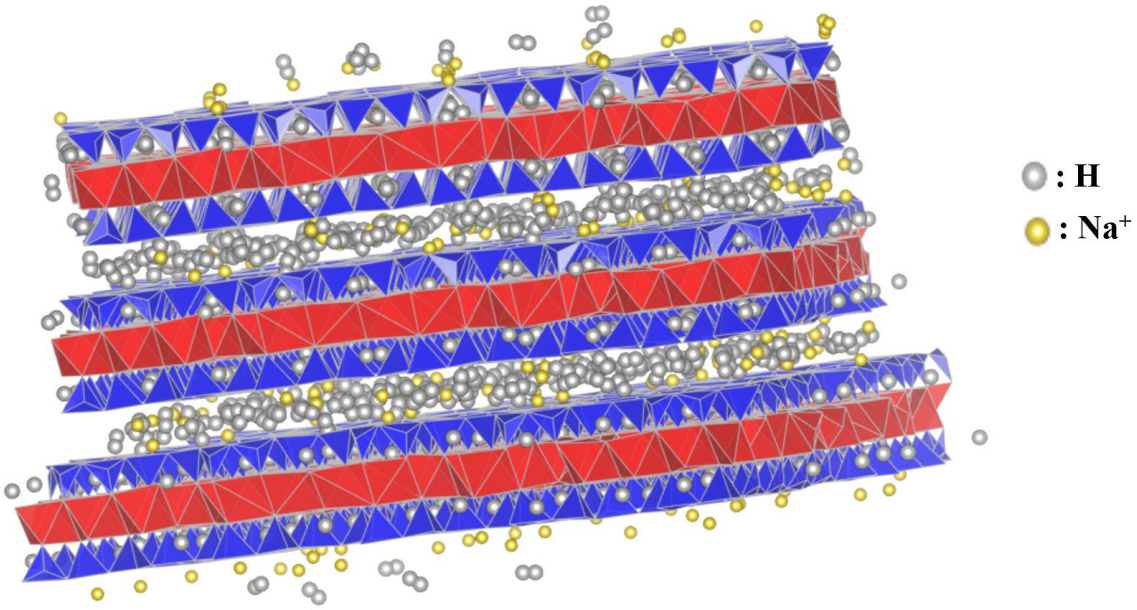

Figure 1: GCMC instantané à 40 K et 2 mbar montrant les molécules de H_2 (sphères grises) et les ions Na^+ (sphères dorées) dans le cadre structurel de la (pré-)Laponite.

Les données expérimentales pour l'adsorption de H_2 dans la pré-Laponite ont été analysées en utilisant un ajustement par loi de puissance avec le vecteur d'one Q en $Q^{-2.7}$ à faible Q, suggérant une morphologie fractale indicative d'agrégats de structures persistants à travers le système. Le pic *001* a été modélisé en utilisant des modèles de disques empilés pour estimer la densité de H_2 adsorbé. Avec un espacement basal (d_{001} = 9.7 Å), la densité de H_2 en fonction de la pression a montré une bonne concordance avec l'isotherme d'adsorption ajusté selon le modèle de Langmuirpour ce qui est de la constante d'affinité.

Les mesures de diffusion neutronique inélastique (INS) in-situ, avec une énergie de neutron incidente de 30 meV, se concentrant sur les caractéristiques inélastiques correspondant à la première transition d'excitation rotationnelle, (J = 0, S = 0) → (J = 1, S = 1) de H_2, qui correspond à une énergie de 14,7 *meV* pour une molécule libre, fournissent des informations précieuses sur l'adsorption de H_2 dans la pré-Laponite et la Laponite à 40 K. En effet, cette transition est extrêmement sensible à l'environnement de l'hydrogène. À très faibles pressions (inférieures à 3 mbar), un site d'adsorption plus prononcé dans la pré-Laponite, appelé "site 0", est observé, où la rotation de H_2 n'est pas observée. Ce site

pourrait être un site de dissociation de l'hydrogène.À mesure que la pression augmente, deux sites supplémentaires, appelés sites 1 et site 2, sont identifiés. Le site 1 correspond au puits de potentiel orientationnel le plus important. Les transitions rotationnelles pour le site 2 sont ajustées en utilisant deux lignes gaussiennes avec un rapport d'intensité de 2:1, ce qui est impliqué que l'axe de la molécule d'hydrogène est préférentiellement aligné parallèlement à la surface d'adsorption. Les barrières de potentiel orientationel associées sont estimées à environ 96 K dans la Laponite et 80 K dans la pré-Laponite. En traçant les intensités intégrées des lignes rotatoires pour les sites 1 et 2, un comportement d'adsorption de type Langmuir est observé pour les deux sites. Cela indique que nous sondons l'hydrogène adsorbé dans la région interfeuillet de la pré-Laponite et de la Laponite, où deux sites d'adorption sont obsevés.

À ce stade de l'étude, la compréhension de la structure de H_2 adsorbé était cruciale. Pour y parvenir, des expériences de diffusion élastique in-situ ont été réalisées, en utilisant du D_2 plutôt que du H_2 en raison de son meilleur rapport signal cohérent-incohérent. Les résultats, interprétés à l'aide de simulations atomistiques basées sur des configurations GCMC, montre que la distance moyenne $D_2 - D_2$ est d'environ 3 Å dans la Laponite et la pré-Laponite, une partie des molécules de D_2 se situant au-dessus des cavités hexagonales de la couche la plus proche. Cette position correspond à l'un des deux sites d'adsorption identifié par diffusion inélastique. L'intensité intégrée du pic de corrélation $D_2 - D_2$, elles suit comme attendu un comportement de type Langmuir. Notamment, la pré-Laponite a montré une prise en charge interfeuillet de D_2 environ trois fois plus élevée que la Laponite.

Grâce à l'analyse approfondie utilisant une combinaison de techniques avancées, cette étude offre une vue microscopique de l'adsorption de H_2 dans les matériaux (pré-)Laponite. Les résultats indiquent que les sites interfeuillet jouent un rôle crucial dans l'adsorption améliorée observée dans la pré-Laponite. Les

conclusions soulignent le potentiel de l'ajustement de l'espacement interfeuillet pour optimiser le stockage de l'hydrogène dans les matériaux argileux. Nous pensons que c’est important non seulement à basse température – basse pression mais également sous pression à température ambiante. Cela ouvre la voie à de futurs développements pour l'utilisation des argiles comme matériaux pour le stockage de l'hydrogène dans des applications industrielles.

"The most complete gift of God is a life based on knowledge"

Ali Ibn Abu Talib

Acknowledgements

This thesis was conducted at the Laboratoire de Physique des Solides (CNRS, Orsay) of Université Paris-Saclay (École Doctorale Physique en Île-de-France) in collaboration with the Institut des Sciences de la Terre (ISTerre) and the Institut Laue-Langevin (ILL). It was funded for three years by the Agence Nationale de la Recherche (ANR).

I would like to begin by thanking the members of the jury – Marie-Vanessa Coulet, Benoit Coasne, Laurent Michot, Vanessa Fierro, and Jean-Marc Zanotti – for evaluating my manuscript and for their stimulating discussions during the defense.

My deepest gratitude goes to my thesis supervisors, Pascale Launois, Stéphane Rols, and Laurent Truche, whose guidance and support have shaped this project into its best possible form.

Pascale, your guidance has been invaluable. Your encouragement, availability, and dedication were always reassuring, and your unwavering support throughout the entire process, right up until the submission of the manuscript, meant a great deal to me. I have learned so much from you. Stéphane, I truly appreciate your optimism and trust. As I mentioned during the defense, you are the most flexible "boss," which allowed me to explore my ideas freely and with confidence. Laurent, I am thankful for our discussions during our meetings.

During my first two years at LPS, I had the privilege of collaborating with the members of the MATRIX group. First and foremost, I extend my thanks to Erwan Panieau for our engaging discussions, especially regarding the materials, and for your exceptional ability to correlate our results with previously published work, particularly during our ANR meetings. A special thanks to Hassan Khoder for the late nights spent during neutron experiments – I especially appreciate your patience and commitment, even when I dozed off, waiting for me to return. I am deeply grateful to the MATRIX group members I interacted with: Stéphane Rouzière, Pierre-Antoine Albouy, Claire Goldmann, and Victor Baledent. A heartfelt thanks to my office mate, Yifan, for our many enriching discussions. I would also like to acknowledge the wonderful group with whom I enjoyed countless games of babyfoot: Yassine, Lucie, Antoine, and Thomas.

During my third year, which I spent primarily at ILL within the CS group, I would like to extend my gratitude to Miguel Gonzalez, Elisa Rebolini, Tobias Weber, and Eric Pellegrini. Additionally, I wish to thank the ILL instrument scientists and technicians for their efforts in preparing the instruments: Viviana Cristiglio, Pascal Mouveau, Olivier Meulien. A special

thanks to Simon Baudoin, engineer at ILL, for preparing the adsorption analyzer for the neutron experiments and adsorption measurements. I would also like to thank Anand for the discussions we had, especially regarding the SANS data.

During my visits to ISTerre, I am deeply grateful to Martine Lanson for introducing me to sample preparation and for our insightful and fruitful discussions. I also had the privilege of collaborating extensively with Valérie Magnin, who provided invaluable assistance during numerous adsorption measurements. I would like to thank Lorella Masci for our discussions, particularly at the beginning of my PhD, which provided motivation and inspiration for the project. Additionally, I extend my thanks to Sabine Sentenac for her efforts in preparing the instrument for ICP-AES measurements.

I would like to thank Cristina Coelho-Diogo for the NMR measurements, Patricia de Rango for room temperature adsorption measurements, Virginie Marry for the MD relaxed structure, Eric Ferrage and Fabien Hubert for the discussions and perspectives shared during our ANR meetings. Additionally, I extend my thanks to Soleil's instrument scientists: Erik Elkaim for the XRS measurements and Delphine Vantelon for the XANES measurements.

I am also grateful to my thesis mentor, Véronique Brouet, and my thesis tutor, Vincent Jacques, for being part of my Comité de Suivi Individuel. Their participation in discussions on my progress and their critical advice were invaluable.

Finally, I would like to express my deepest gratitude to my friends, who have shared in both my challenges and triumphs throughout this journey "Mohammad, Hadi, Ali, Lobnan, Jad, Christelle", especially those who stayed up late to prepare the "pot de thèse." A special thanks to my friend Shadi for being by my side through it all. Your friendship has been a cornerstone of this journey.

Most importantly, I want to extend my heartfelt appreciation to my family for their unwavering support, encouragement, and patience over the past three years.

Table of Contents

Glossary of abbreviation

BET	Brunauer–Emmett–Teller theory
CNTs	Carbon nanotubes
CEC	Cation exchange capacity
CHSMs	Classical hydrogen storage materials
T_c, P_c	Critical temperature, pressure
CP	Cross polarization
DTG	Derivative thermogravimetric
FT	Fourier transform
GCMC	Grand Canonical Monte Carlo
HS	Harkins and Jura
ICP-AES	Inductively coupled plasma atomic emission spectroscopy
IR	Infrared
INS	Inelastic neutron scattering
IEA	International Energy Agency
Q_{st}	Isosteric heat of adsorption
LJ	Lennard-Jones potential
MAS	Magic angle spinning
MD	Molecular dynamic
MOFs	Metal organic frameworks
MWCNTs	Multi-walled carbon nanotubes
***o*-H_2**	Ortho-hydrogen molecule
PDF	Pair distribution function
***p*-H_2**	Para-hydrogen molecule
SBUs	Secondary building units
SWCNTs	Single-walled carbon nanotubes
DSS	Sodium 4,4-dimethyl-4-silapentane-1-sulfonate
RH	Relative humidity
ssNMR	Solid-state nuclear magnetic resonance

SSA	Specific surface area
SANS	Small Angle Neutron Scattering
SLD	Scattering length density
TOT	Tetrahedral-octahedral-tetrahedral
TMS	tetramethyl silane
TGA	Thermogravimetric analysis
TOF	Time-Of-Flight
T_T, P_T	Triple temperature, pressure
vdWs	van der Waals
WANS	Wide Angle Neutron Scattering
XANES	X-ray absorption near edge spectroscopy
XRS	X-ray scattering

List of figures

List of tables

Chapter I. Introduction

In this chapter, we present an overview of hydrogen as a promising energy source, providing a comparative analysis with other alternative energy technologies. We delve into the quantum states of molecular hydrogen, specifically discussing the ortho and para states. The chapter addresses a significant challenge within the hydrogen energy network; low volumetric energy density. Various hydrogen storage methods are examined, including mechanical, chemical, and physical approaches. We place special emphasis on solid-state storage materials, particularly focusing on clay materials due to their abundance and large specific surface areas. The chapter then narrows its focus to 2:1 trioctahedral Laponite, which have been identified as our materials of interest for further investigation.

1. General introduction

Global energy demand has been increasing in parallel with population growth and economic development, as energy consumption permeates every aspect of human activity, including residential, commercial, industrial, and transportation sectors. According to the International Energy Agency (IEA) 2019 report, fossil fuels—i.e., natural gas, coal, and oil—have dominated for primary energy production, comprising 81% of global energy production in 2016. However, these resources are both physically and economically limited, making them finite and non-renewable resources. In addition, fuel combustion produces large amount of CO_2, which poses serious environmental problems such as the greenhouse effect. In the recent years, global CO_2 emissions have increase from 22 Gt/year in 1995 to 33 Gt/year in 2018, with an average rate of 1.7% [1]. Consequently, the Earth's global average temperature has risen by approximately 1 K since 1981, and it is projected to increase by another 1.5K between 2030 and 2052 if the global energy dependence on fossil fuels persists. This temperature rise could lead to the degradation of ecosystems and poses significant risks to human society, including the emergence of infectious diseases driven by warmer and wetter conditions. Various targets have been established to reduce both energy consumption and carbon emissions where studies are focusing on the development of renewable energy technologies alternative to fossil fuels.

Consequently, more countries are implementing policies to support investment in hydrogen technologies, and given hydrogen's primary industrial use, the European Union is prioritizing the shift to green hydrogen production to achieve its net-zero carbon emission goals.

2. Fundamental of hydrogen

2.1. Hydrogen as an energy carrier

Employing pure hydrogen as a primary energy source not only offers a viable pathway for reducing atmospheric carbon, but also represents one of the most promising fuels for energy [2] [3] [4], industry, transport [5] [6], and for the entire economy in general. Hydrogen, the most abundant element in the universe, constituting approximately 75% of its mass [7], possesses unique attributes that make it an ideal candidate for energy source, or more exactly as an energy vector as hydrogen is still not produced as a primary energy source even if recent discoveries tend to indicate that natural hydrogen accumulations may exist on Earth [8].

Hydrogen is the lightest element of the periodic table. It is also non-poisonous, colorless, odorless, and tasteless.

Utilizing renewable energy sources for production, hydrogen boasts minimal environmental impact, as its only combustion byproduct is water. Hydrogen can be utilized either in a combustion engine or, more efficiently, in a fuel cell to generate electric energy [9]. With an energy per mass content equal to 143 $MJ.kg^{-1}$, a value which is up to three time larger than for liquid hydrocarbon based fuels (47 $MJ.kg^{-1}$) [10], hydrogen stands as a very attractive source for storing and releasing energy.

Table I.1: Comparison of various energy storage systems [11].

Technology	**Cost** ($. kWh^{-1})	**Gravimetric energy density**[1] (Wh. kg^{-1})	**Energy Efficiency** (%)
Li-ion battery	600-2500	200-500	85-90
Super-capacitor	100-400	2.5-1	95-98
Hydrogen	2-20	400-1000	-
Flywheel	1000-2000	20-80	90
Pressurized air	2-50	30-60	40-80

Table I.1 shows that hydrogen has a low cost and the highest gravimetric density when compared to other energy storage systems. Furthermore, employing polymer electrolyte membrane fuel cells (PEMFC) for energy conversion can achieve efficiencies[2] of up to 90% in combined heat and power (CHP) mode [12], rendering hydrogen a favorable candidate for energy storage [13].

2.2. Hydrogen basic properties

The hydrogen atom is the simplest atomic species. Under normal conditions, it exists as molecular hydrogen (H_2), the simplest of all molecular species and molecules are in gaseous state. H_2 possesses two planes of symmetry: one axis passing through the two protons (the minor axis) and the perpendicular plane located between the protons (the major plane). The separation distance between the protons is 0.76 Å. At distances corresponding to nearest neighbor separation, in the gaseous state, the charge density is approximately 3×10^{-4} of that at the nuclei,

[1] *Gravimetric energy density: the available energy per unit mass of substance.*
[2] *Energy efficiency: how effectively the system can store and retrieve energy.*

while the ratio of the minor to major axis of the charge density distribution is approximately 0.94 [14]. Thus, at low densities – such as in the gaseous state at low pressures—the molecule should be visualized as nearly spherical rather than dumbbell-shaped. Furthermore, the symmetry of H_2 results in a weak electric quadrupole moment of 0.13eÅ^2, where e is the charge of the electron [15]. Moreover, H_2 is polarizable in the presence of an external potential, with an isotropically averaged polarizability volume of 0.76 Å^3 [16].

The phase diagram of H_2 is shown in Figure I.1**.**

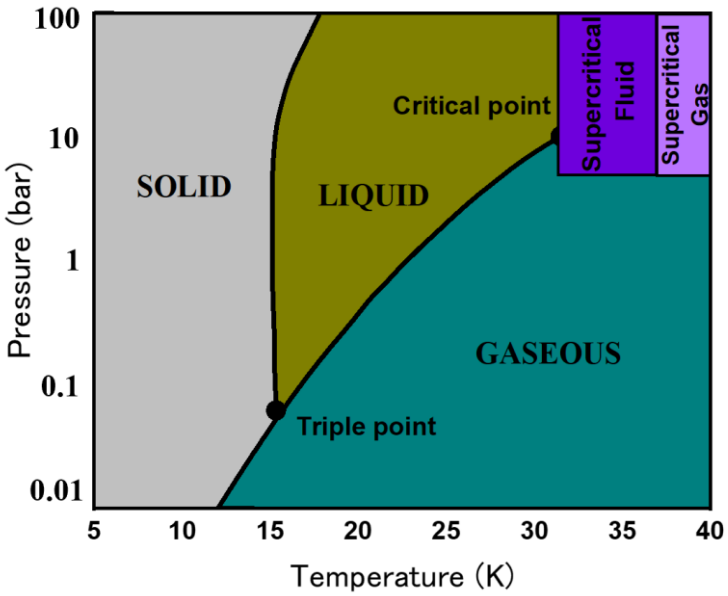

Figure I.1: The phase diagram of H_2 showing transitions points, adapted from [17].

2.3. Ortho- and para hydrogen: spectroscopic characterization

It is widely acknowledged in particle physics that protons possess a magnetic quantum number or spin ½. Fundamental particles with half-integer spin, names fermions, are indistinguishable from one another. The total molecular wavefunction involving the nuclear coordinates, (ψ_{tot}), antisymmetric for proton permutation [18]. Let consider that the total wavefunction can be expressed as the product of the vibrational, rotational, and spin components:

$$|\boldsymbol{\psi_{tot}}\rangle = |\boldsymbol{\psi_{vib}}\rangle|\boldsymbol{\psi_{rot}}\rangle\big|\boldsymbol{\psi_{spin}}\big\rangle \qquad \textbf{(I.1)}$$

The vibrational contribution is always symmetric due to the linear-diatomic nature of the H_2 molecule [19].

Considering that the vibrational wavefunction is symmetric, only two cases are possible which comply with the requirement that the total wavefunction is antisymmetric on proton exchange, as illustrated in Figure I.2.

The achievement of an antisymmetric ψ_{spin} function occurs when the two protons (each with ½ spin) are in an antiparallel configuration, resulting in a total nuclear spin equal zero ($I_N = 0$). Conversely, parallel spins of the protons with $I_N = 1$ lead to symmetric ψ_{spin}. Regarding ψ_{rot}, only the symmetric rotational component corresponds to even energy levels [20], based on Dennison's research. Thus, two spin isomers of H_2 exist; orthohydrogen (o-H_2) and parahydrogen (p-H_2):

- p-H_2 exhibits a symmetric ψ_{rot} corresponding to even rotational quantum number J ($J = 0, 2, 4, \ldots$), and an antisymmetric ψ_{spin} ($I_N = 0$). Since $I_N = 0$, it possesses only one available spin sub-state, leading to its classification as a singlet.
- o-H_2 features an antisymmetric ψ_{rot} corresponding to odd J ($J = 1, 3, 5, \ldots$), and symmetric ψ_{spin} ($I_N = 1$). This configuration allows for three possible spin sub-states, hence earing its classification as a triplet.

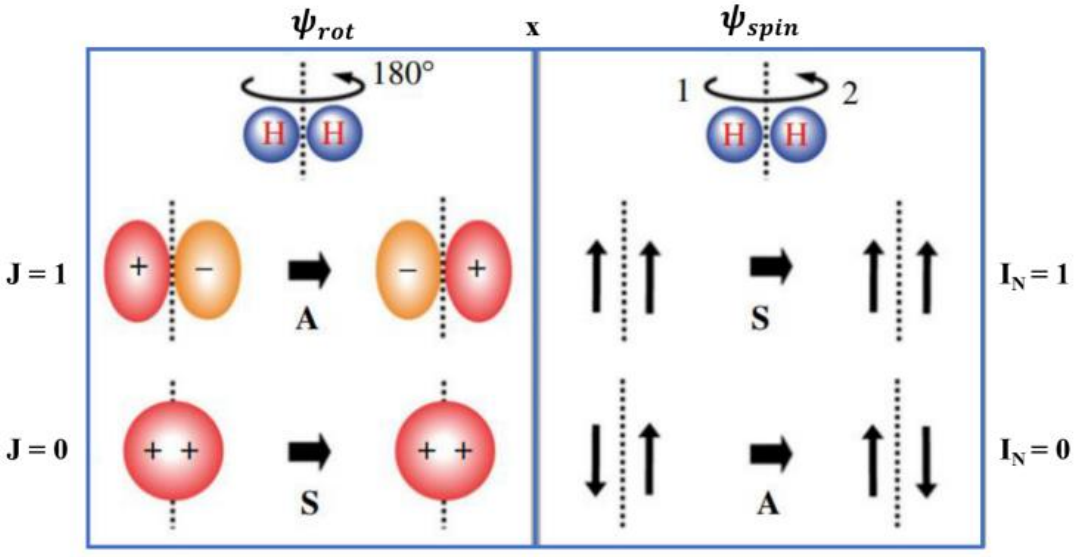

Figure I.2: Illustrating the differences between ortho and para states in terms of rotational and spin wavefunctions, denoted as S (symmetric) and A (antisymmetric), adapted from [21].

Figure I.3, which presents the percentage of p-H_2 versus temperature, shows that at 19 K and at atmospheric pressure, the population of p-H_2 reaches 99.75%, as the available thermal energy is insufficient to significantly populate the higher energy o-H_2 state. As the sample temperature increases to around 78 K, an equilibrium concentration is achieved between p-H_2 and o-H_2.

At room temperatures, H_2 gas is a mixture of 25% *p*-H_2 and 75% *o*-H_2, a proportion equal to their degeneracies. This 1:3 distribution ratio is commonly defined as normal hydrogen. Above room temperature, the percentage of para to ortho-dihydrogen reaches asymptote. In the absence of special catalyst or distillation techniques, *o*-H_2 cannot naturally exist in a pure form.

The rotational properties of H_2 in the gaseous, liquid and low-pressure solid state can be described by the free-rotor model (3D rotor). The wave function of the 3D rotor are the spherical harmonics $Y_{Jm}(\theta, \emptyset)$ where θ (angle between H-H bond and the normal to x-y plane, z) and $\emptyset$ (between the x-axis, defined in the x-y plane, and the projection of the H-H bond onto the x-y plane) are the polar coordinates of a nucleus (refer to Figure I.4).

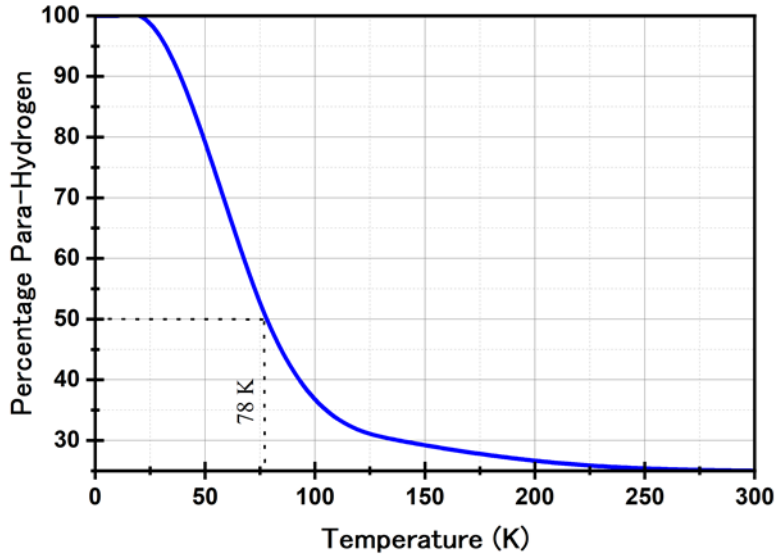

Figure I.3: Percentage of para-hydrogen as a function of temperature at atmospheric pressure. At 78 K, there is equilibrium between ortho and para H_2. Below 19 K, para H_2 dominates with 99.75% purity, while at room temperature, the mixture consists of 25% para and 75% ortho H_2, adapted from [22].

The rotational energy of the molecule in free space is given by E_{rot} in equation (I.2), where J = 0,1,2 … is the rotational quantum number and B is the rotational constant. It can be expressed as a function of I_m, the moment of inertia, which itself depends on the reduced mass μ, and on the intermolecular distance R_v, v being the vibrational quantum number. The rotational degeneracy is denoted by d_r, and the corresponding sublevels are characterized by the magnetic quantum number m_J.

$$\boldsymbol{E_{rot} = B \cdot J(J+1)}$$
$$\boldsymbol{B = \hbar^2/2I_m \; ; \; I_m = \mu R_v^2 \; ; \; \mu = \frac{(m_1 m_2)}{(m_1+m_2)}} \qquad \textbf{(I.2)}$$
$$\boldsymbol{d_r = 2J+1 \; ; \; m_J = 0, \pm 1, \pm 2 \ldots \pm J}$$

H_2, in both its solid and liquid states, exhibits several unique features that distinguish it from other molecular solids and liquids. One particularly notable difference is that in solid state, the free rotor states, which describe the rotational motion of an isolated molecule, are scarcely affected by interactions with neighboring molecules. This behavior classifies solid H_2 as a 'quantum crystal,' where molecules, with their centers of mass fixed at lattice positions, can rotate freely even at the lowest temperatures. This is due to the weak intermolecular interactions (with nearest neighbor distances of approximately 3.8 Å) and the small moment of inertia of the H_2 molecule.

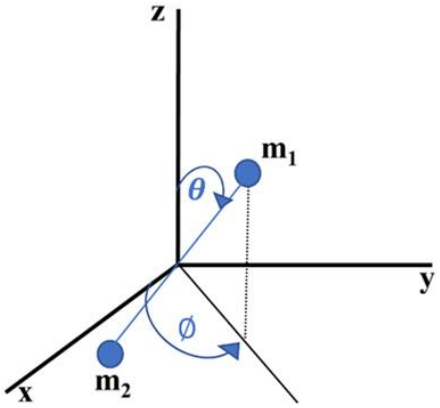

Figure I.4: Spherical coordinates showing the polar angle (θ) and the azimuthal angle ($\emptyset$), adapted from [23]**.**

The angular probability density function, $P(\theta, \emptyset)$, provides the foundation for a visual representation of the rotational states of H_2. This function forms a surface in polar coordinates, where any point on the surface can be connected to the origin by a line. The $(\theta, \emptyset)$ coordinates of the line correspond to the orientation of the H_2 molecular axis, and the probability of any specific orientation occurring is indicated by the length of the line, $P(\theta, \emptyset)$. This method offers a clear pictorial description of the rotational states (Figure I.5**)** and their corresponding probabilities, enhancing the understanding of dihydrogen's unique rotational behavior [23].

In the ground state, $J=0$, $P(\theta, \emptyset)$ is spherical and all molecular orientations are equally probable. However, the first rotational state, $J=1$, has a more complex shape imposed by the sub-states m_J. The distribution can be described in terms of two component shapes. The toroidal shape represents the $m_J = \pm 1$ state, with maximum probability in the x-y plane. An H_2 molecule in an $m_J = \pm 1$ state is most likely (> 85% probability) to be found with its molecular axis within the range $45° < \theta < 135°$. The direction of its horizontal component is equally probable in $\emptyset$ [23].

The "dumbell" shape represents the $m_J = 0$ state, with its maximum probability along the z-axis. As H_2 molecule in this state is most likely (> 64% probability) to be found within the ranges $\theta < 45°$ or $\theta > 135°$. The direction of its horizontal component is equally probable in $\emptyset$. This complex distribution of the first rotational state highlights the intricate spatial orientations of the molecule, related to by its m_J values [23].

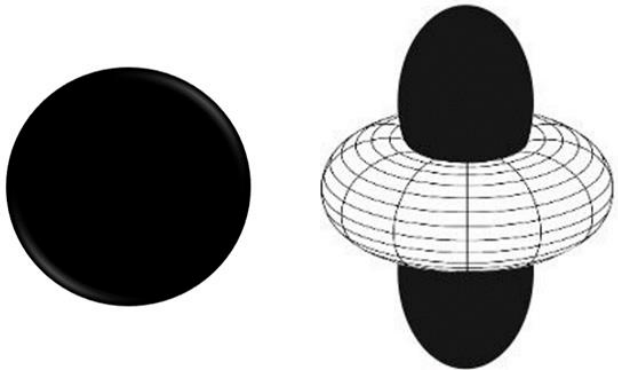

Figure I.5: Diagrammatic representation of the probability distribution function for ortho- and para-H_2, adapted from [23].

In bulk solid H_2, the energy splitting between the singlet ground state (p-H_2) and the three-fold degenerate state (o-H_2) is $\Delta E = 2B$, where $B = 7.37\ meV$ (calculated from equation (I.2)). This energy difference is characterized by a sharp, well-resolved peak observed via inelastic neutron scattering (INS), as shown in Figure I.6**,** while most of the other transitions are observed as broad bands due to simultaneous rotational and translational modes (recoil), which will be further discussed in **Chapter V**.

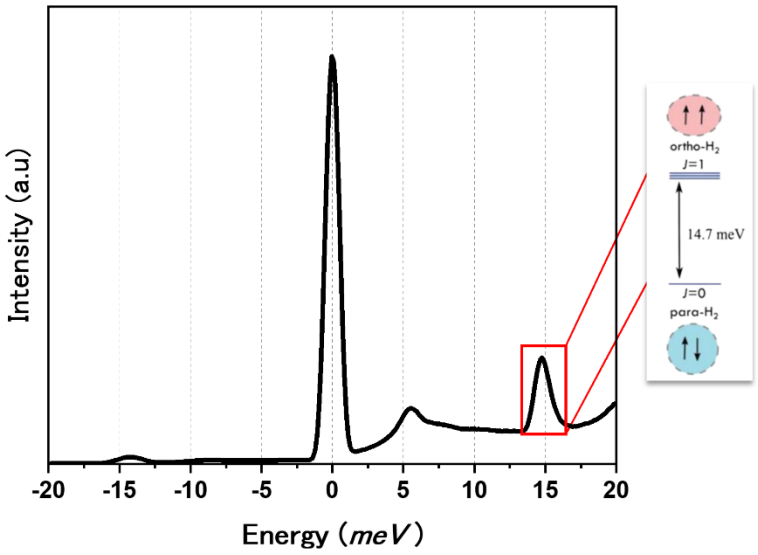

Figure I.6: Experimental INS spectrum of bulk-solid H_2 measured at temperature 2K using [3]PANTHER beamline at ILL.

[3]*PANTHER: Time-OF-Flight spectrometer that replaced IN4C at Institut Laue-Langevin.*

In the adsorbed state (Figure I.7), H_2 molecules are in presence of an anisotropic external potential where the main anisotropy occurs between the xy plane, parallel to the surface of the adsorbant, and the z axis perpendicular to it. It induces perturbations in the H_2 rotational states [24].

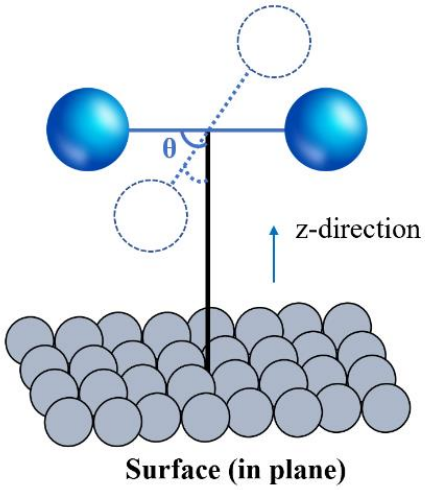

Figure I.7: Diagrammatic representation of H_2 physisorbed on the surface, illustrating the angle θ between the molecule's axis and the z-axis.

Therefore, to determine the energy levels of an adsorbed H_2 molecule, equation (I.2) is no longer applicable. Instead, the simplest model to be considered is the one-dimensional hindered rotor model. In this context, the Hamiltonian for an H_2 molecule in the potential is given by:

$$\hat{H} = \frac{\hat{L}^2}{2I_m} + \frac{V}{2}(1 - \cos 2\theta) \qquad \textbf{(I.3)}$$

where, $\hat{L}$ is the angular momentum operator, and V represents the orientational energy barrier height. The one-dimensional Schrödinger equation is solved by diagonalizing the Hamiltonian matrix. By expanding the rotational potential using a spherical harmonics basis set [25], $Y_{Jm}(\theta, \emptyset)$, the Hamiltonian matrix elements are expressed as follows:

$$H_{J',mJ',J,mJ} = J(J+1) \cdot B_{rot} \cdot \delta_{(J,\ J')} \cdot \delta_{(mJ,\ mJ')} + \left\langle Y_{J',mJ'} \middle| \frac{V}{2}(1 - \cos 2\theta) \middle| Y_{J,mJ} \right\rangle \qquad \textbf{(I.4)}$$

The sign of V provides information into how the H_2 molecule is adsorbed on the surface. If V is positive, the H_2 molecule aligns perpendicular to the surface (1D case). Conversely, if V is negative, the molecule prefers to align parallel to the surface (2D case). Figure I.8, clearly

shows the sign and value of the potential barrier with respect to the type and transition energy of adsorbed H2.

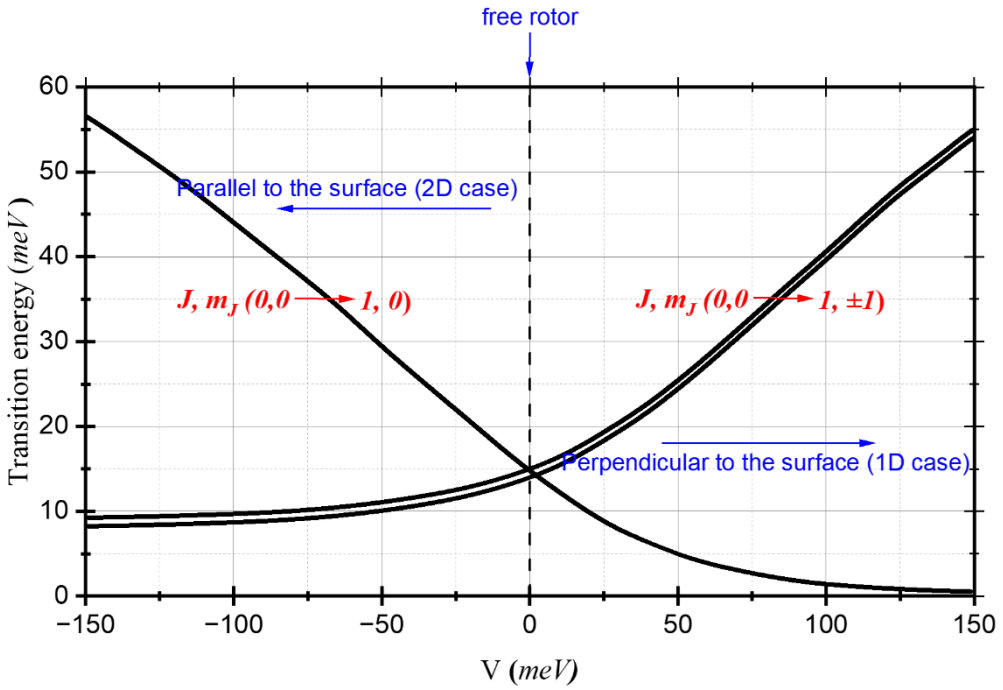

Figure I.8: One-dimensional hindered rotor model: rotational energy level transitions for an H_2 molecule from ground state ($J=0$, $m_J = 0$) to the first two excited states, plotted as a function of the barrier height parameter V_2. The degenerate $m_J = \pm 1$ states are offset just for clarity.

The free rotor transition at 14.74 *meV*, which represents the transition from the $J=0$, $m_J = 0$ ground state to the degenerate state $J=0$, $m_J = 0, \pm 1$, splits into two transition lines under the anisotropic potential exerted by the surface. One line corresponds to the transition from ($J = 0$, $m_J = 0$) to ($J = 1$, $m_J = 0$) and the other corresponds to the transition from ($J = 0$, $m_J = 0$) to ($J = 1$, $m_J = \pm 1$), as illustrated in Figure I.9.

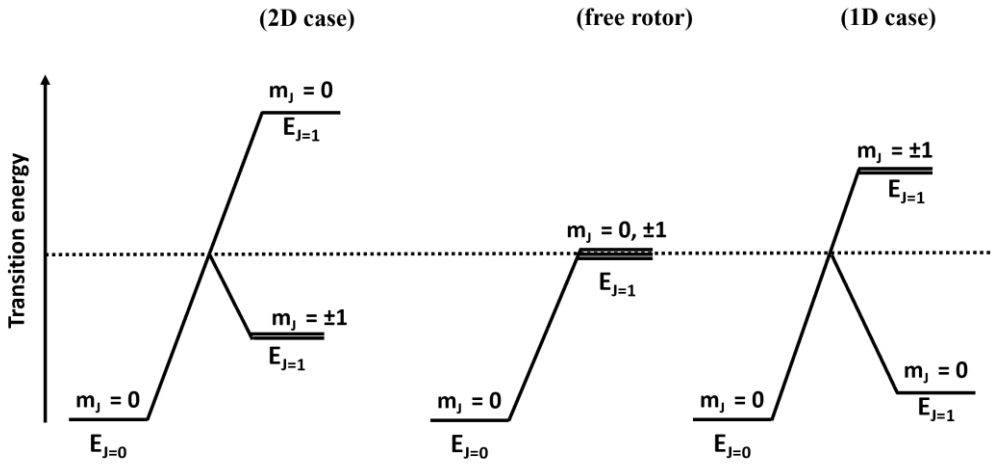

Figure I.9: Quantum rotational transitions between the ground ($J = 0$) and first excited ($J = 1$) states for: H_2 unhindered (free rotor), H_2 hindered in one-dimension (2D case), and H_2 hindered in two dimensions (1D case). The m_J states are offset for clarity.

2.4. Hydrogen molecular isotope

Deuterium (^{2}H or D) is the stable isotope of hydrogen. The nucleus of deuterium contains one proton and one neutron, making it approximately twice as heavy as a hydrogen atom. Despite this difference in mass, D_2 and H_2 molecules share the same intermolecular distance of 0.74 Å in the ground state [26].

Table I.2: Symmetry properties of the nuclei of hydrogen and deuterium. *"I"* denotes the nuclear spin, *"J"* represents the molecular rotational quantum number, "S" and "AS" stand for symmetric and antisymmetric wavefunctions, respectively.

Isotope	I_{Mol} (Symmetry)	J (Symmetry)	Degeneracy	Species
Hydrogen	0 (AS)	0,2,4…(S)	1	Para
(fermion I_N = ½)	1 (S)	1,3,5,7…(AS)	3	Ortho
Deuterium	0, 2 (S)	0,2,4…(S)	6	Ortho
(boson I_N = 1)	1 (AS)	1,3,5,7…(AS)	3	Para

3. Hydrogen storage: state-of-the-art

The storage of hydrogen emerges as a central challenge within the hydrogen network, widely acknowledged as the principal technological obstacle in the hydrogen economy. This issue predominantly arises from the extremely low volumetric density of H_2.

Evaluating the suitability of storage media requires careful consideration of two key parameters: gravimetric density, which measures the weight percentage of hydrogen stored relative to the

total weight of the system, and volumetric density, which assesses the mass of hydrogen stored per unit volume. It is essential to distinguish between these two parameters because their importance varies depending on the intended application. For mobile applications, such as in vehicles, minimizing additional mass is crucial, necessitating a high gravimetric density to optimize fuel efficiency and range. In contrast, for stationary applications like hydrogen storage facilities, weight is less of a constraint, and maximizing volumetric density becomes more critical to store larger amounts of hydrogen in limited space.

One possible solution, known as "compression," involves pressurizing hydrogen and storing it in high-pressure tanks at room temperature. While this method has undergone successful testing in the market, it still faces drawbacks such as relatively low hydrogen density (volumetric density of H_2 at 70 MPa is 5 $MJ.l^{-1}$) [27] and the necessity for very high gas pressures within the systems, which are significant limitations (safety concerns and cost effectiveness). Another alternative is the use of liquid hydrogen (liquefaction at temperature below hydrogen's critical point of 33.23K at 1bar), which increases the mass-to-volume ratio. However, liquefying hydrogen requires a considerable amount of energy—approximately 10–15 kWh per Kg_{H2} of due to the energy demands of cooling to cryogenic temperatures—and evaporation from storage containers is unavoidable, adding to storage challenges [28].

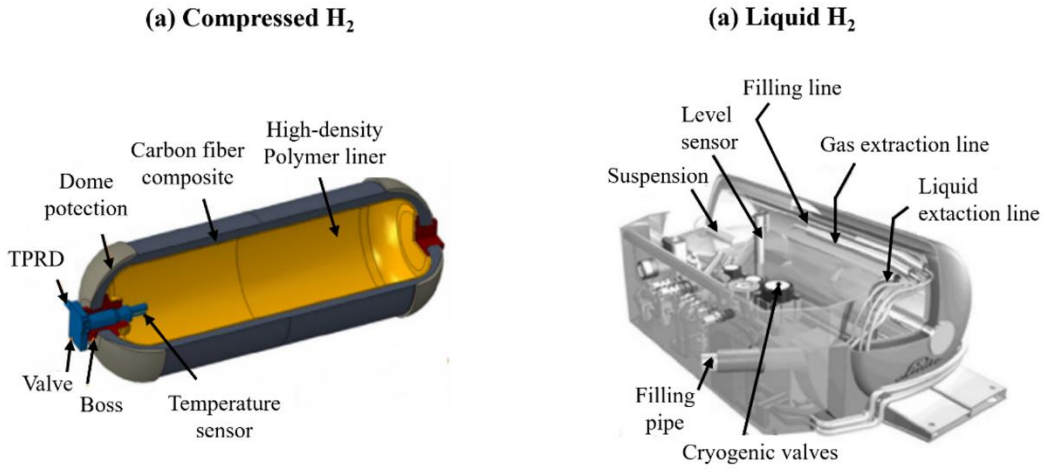

Figure I.10: Mechanical-based storage system where (a) high-pressure gaseous hydrogen (compressed hydrogen), (b) liquid hydrogen is stored in a specially designed physical container, adapted from [29].

Another possibility is to use solid material capable of adsorbing and storing hydrogen with high volumetric densities. Hydrogen storage materials can be categorized into two classes based on the energy involved in adsorption process: chemisorption and physisorption. As described in Figure I.11, in chemisorption, H_2 molecules undergo dissociation into atomic hydrogen, which

then becomes adsorbed into the bulk material, forming strong covalent bonds inside the material. In contrast, in physisorption -which will be considered throughout this thesis- is the process for which H_2 adsorption results from weak van der Waals interactions (~5 -10 kJ.mol^{-1}) with the surface which can be described by one-dimensional Lennard-Jones potential (Figure I.11 (c)) [30].

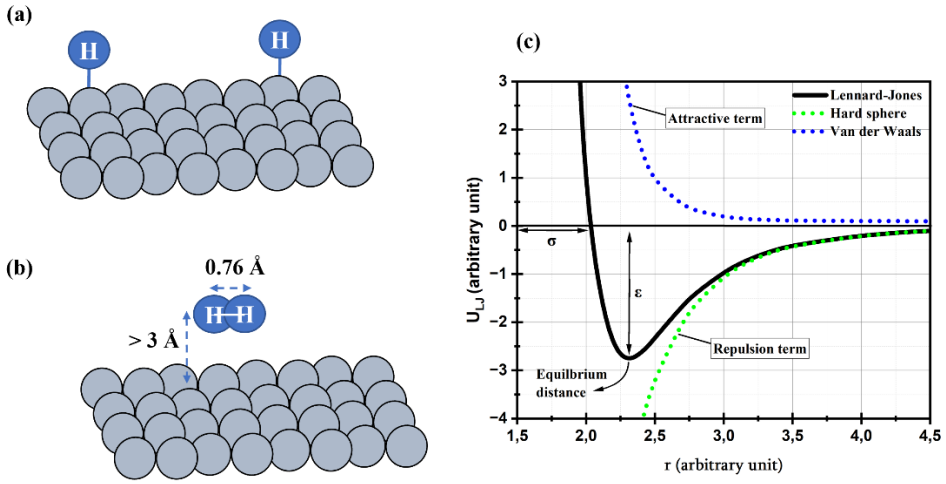

Figure I.11: Adsorption of hydrogen on substrate via (a) chemisorption, (b) physisorption and (c) schematic representation of Lennard-Jones potential, where r is the distance to the substrate. The hard spheres and van der Waals potentials are also shown for clarity.

The potential experienced by the H_2 molecules is the Lennard-Jones potential (Figure I.11), which is the sum of van der Waals and hard sphere interactions. It is usually written as follow:

$$U_{LJ} = 4\varepsilon\left[\left(\frac{\sigma}{r}\right)^{12} - \left(\frac{\sigma}{r}\right)^{6}\right] \qquad \textbf{(I.5)}$$

where U_{LJ} is the intermolecular potential between the two particles (atoms or molecules) resulting from the two terms (van der Waals and Hard Sphere) in the equation, ε is the well depth (measure how strongly the two particles attract each other), σ is the distance at which the intermolecular potential is zero (U_{LJ}) and r is the distance separating the two particles.

Physiosorbed hydrogen has a very small binding energy, normally in the order of 116-1160 K (or ~1-10 kJ/mol), while chemisorbed hydrogen involves stronger covalent bonding, with binding energy of more than 1-2 eV (or ~97-194kJ/mol).

In the upcoming sections, we will delve deeper into the advantages and drawbacks of both chemisorption and physisorption process, as well as into the factors influencing hydrogen storage in each case. The goal is to provide a comprehensive understanding of the complexities involved in hydrogen storage materials.

3.1. Hydrogen storage via chemisorption

Chemisorption occurs when hydrogen molecule comes in contact with the solid surface, dissociates into two hydrogen atoms which diffuse in the solid and form a chemical bound with the solid material.

3.1.1. Metal hydride

Most common materials considered for hydrogen storage *via* chemisorption are metal hydrides (elemental or complex hydrides) where metals react with hydrogen according to the following reaction:

$$M + H_2 \overset{reversible}{\Longleftrightarrow} MH_x + Q$$

where M represents a metal and Q is the heat of hydride formation. Hydrides of metals such as Li, Be, Na, Mg, B and Al are especially attractive due to their high gravimetric and volumetric densities, rendering them components of high-capacity hydrogen storage materials.

One of the best-known examples of metal hydride is magnesium hydride (MgH_2), which has the highest energy density (9 $MJ.kg^{-1}$) among all reversible hydrides suitable for hydrogen storage. With a gravimetric H_2 capacity of 7.7 wt.%, MgH_2 offers the advantage of low cost coupled [31]. However, MgH_2, like most other metal hydrides, suffers from notable drawbacks including high temperature requirements for hydrogen discharge (~300°C) [32], slow desorption kinetics, and a high reactivity towards air and oxygen.

3.1.2. Complex hydride

Complex hydrides stand out among the most interesting materials for hydrogen storage. Elements such as Li, Na, and B, which are lighter than magnesium, show the capability to store hydrogen at high contents, reaching approximately 18 wt.% for $LiBH_4$. However, as for MgH_2, their drawbacks lie in slow kinetics, high temperatures required for hydrogen release. Moreover, one should mention, the formation of undesirable compounds during de-hydrogenation and re-hydrogenation.

In summary, while metal hydrides offer the greatest storage capacity among all materials even at ambient conditions, their main drawbacks are slow desorption kinetics and the high temperatures required to desorb hydrogen.

3.2. Hydrogen storage via physisorption

The volumetric density of H_2 can be increased through attractive interactions between H_2 molecules and adsorbent surfaces. However, to date, achieving high storage capacity via physisorption has been primarily limited to very low temperatures, owing to the weak interactions between H_2 and adsorbents. These adsorbed H_2 can be desorbed reversibly by lowering the sorptive gas pressure or increasing the temperature.

In order to reach high-volumetric density hydrogen storage via physisorption, high surface areas are necessary. Different porous materials, including carbon-based, zeolites, and Metal Organic Frameworks (MOFs) materials, have been extensively investigated for hydrogen storage purposes.

3.2.1. Carbon-based materials

Carbon-based materials have gained significant attention in the field of hydrogen storage due to their abundance, chemical and thermal stability, and the ability to modify their textural properties (i.e., pore size, surface area etc…) [33], and graphitic structure, which enhance hydrogen adsorption capabilities [34].

The term 'activated carbon' refers to a highly porous material with widely distributed pore sizes, as illustrated in Figure I.12. This material is produced from a carbon-rich precursor through activation, which involves a process that increases the material's surface area and porosity. Non-carbon elements (such as hydrogen and oxygen) are removed through heating and carbon is further activated, either physically, for instance by using oxidizing gases at high temperature (~1000°C) or chemically, by using chemical agents at lower temperatures ; both procedures favorize pore's development [35].

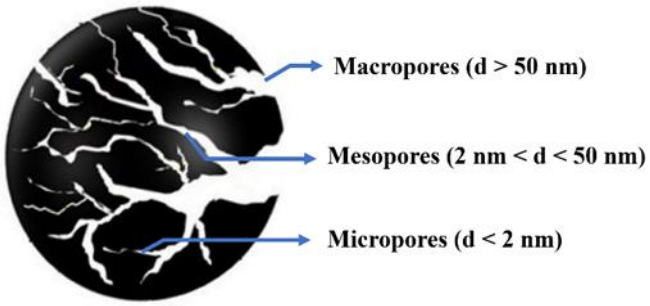

Figure I.12: Illustration of pore structure in activated carbon, depicting macropores (d > 50 nm), mesopores (2 nm < d < 50 nm), and micropores (d < 2 nm), adapted from [36].

Activated carbons: have a long history as hydrogen adsorbents, first studies back to 1967, for which the large capacity is attributed to their large surface area (SSA > 1000 $m^2.g^{-1}$) and

significant pore volume (> 0.5 $cm^3.g^{-1}$) [34]. At ambient temperature and 60 bars, the adsorption capacity for activated carbons (ACs) reaches approximately 0.5 wt.%. However, under cryogenic conditions, this capacity can increase to around 5 wt.% at 60 bars [37].

3.2.2. Zeolites

One of the proposed solutions for solid-state storage materials is zeolite, characterized by its micro-porosity, large surface area (approximately 1000 $m^2. g^{-1}$), low cost, and high stability. These materials consist of aluminosilicate structures based on assemblies of SiO_4 and AlO_4 tetrahedra. In addition, zeolites are commonly classified into different classes such as type-CHA, type-FAU, type-A, type-X (LTA), and type-Y [38] based on their crystalline structure and Si:Al ratio. For clarity regarding the structure of zeolites, Figure I.13 illustrates the structures of LTA, FAU and CHA types.

Zeolites are characterized by the presence of exchangeable cations. This exchangeability enables zeolites to be tailored for different applications. In terms of hydrogen adsorption, the most promising results have been achieved with CaX, with a reported hydrogen capacity of 2.19 wt.% at 77K and 15 bars [39]. However, classical atomistic simulations suggest a theoretical limit of hydrogen uptake capacity ranging 2.86 – 2.65 wt.% [40], indicating that zeolites may not be qualified candidates for hydrogen storage applications.

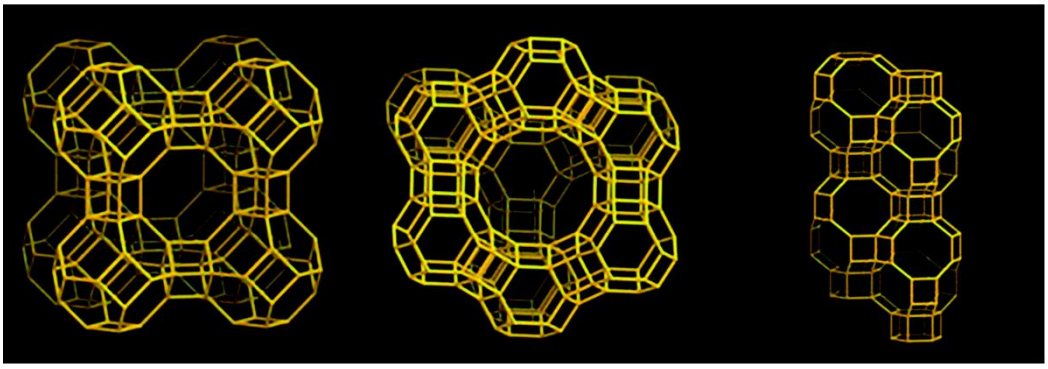

Figure I.13: Zeolites framework structure: (a) zeolite A and (b) zeolite X and Y, adapted from [41].

3.2.3. Metal Organic Frameworks

A study on activated carbon and zeolite proposed that materials with a larger volume of micropores with suitable diameters may achieve higher gas adsorption [42]. This concept aligns particularly in MOFs. Over the past decade, hydrogen storage in MOFs has received a worldwide attention. As a class of crystalline porous materials, MOFs reveals a unique structure

characterized by the absence of dead volume, thereby enabling the enhancement of volumetric hydrogen storage. Additionally, MOFs materials have the potential to be cost-effective and lightweight which aids in achieving high gravimetric storage capacity [43]. Similar to zeolite, MOFs reveals a cage-like structure, as illustrated in Figure I.14, formed by secondary building units (SBUs) and organic linkers. These SBUs and linkers combine to form different MOFs. An organic ligand can be combined to form different MOFs with various SBUs.

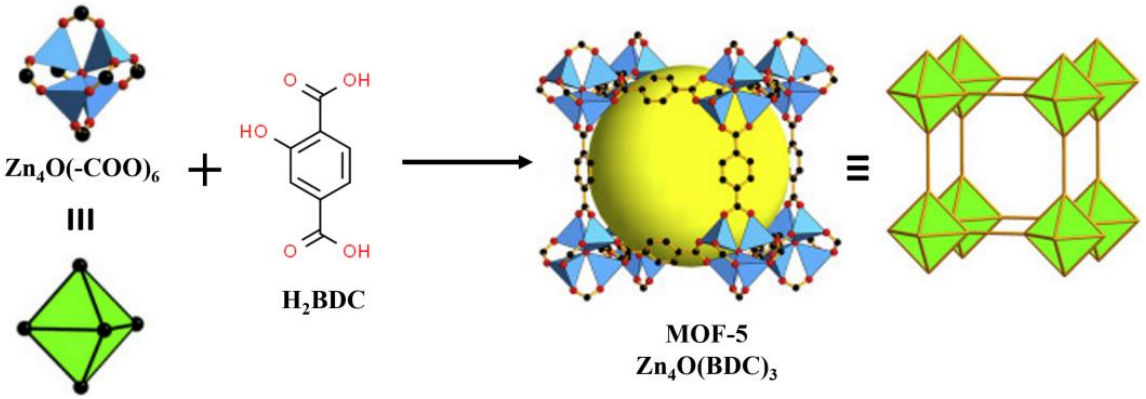

Figure I.14: Schematic representation of MOF-5 formation. The blue polyhedra represent the SBUs composed of Zn_4O clusters, while the green tetrahedra represent the organic linker, benzene-1,4-dicarboxylate (H_2BDC). The black spheres represent carbon, and the red spheres represent oxygen. The large yellow spheres represent the largest guest molecule that could fit into the pores without touching the van der Waals surfaces of the framework, adapted from [44].

MOFs possess extremely high SSA, with the highest BET SSA recorded for MOF-210, 6240 $m^2.g^{-1}$, which is composed of $Zn_4O(\text{-}COO)_6$ units and 4,4',4''-(benzene-1,3,5-triyl-tris-ethyene-2,1-diyl)tribenzoate (BTE) and biphenyl-4,4'-dicarboxylate (BPDC) linkers [45]. However, many MOFs have pore sizes that are too large to effectively confine hydrogen molecules. In terms of hydrogen storage, MOF-5 for example, shows a hydrogen uptake of 4.5 wt% at 78K and 1 bar [46]. In comparison, MOF-210 demonstrates the highest hydrogen uptake of 8 wt% at 77 K and 50 bars [47].

Significant research efforts have been directed towards enhancing hydrogen storage in MOFs, necessitating a thorough understanding of the key factors influencing the adsorption mechanism.

Hydrogen bonding strength: is one of the most crucial factors impacting storage. The bonding strength of H_2 molecules to the adsorbent surface, which is proportional to the isosteric heat of adsorption, plays a key role. For MOFs, the isosteric heat of adsorption typically ranges between 4-7 $kJ.mol^{-1}$ [48].

However, according to calculations by *Garrone, E. et al.* [50], the isosteric heat of adsorption should be in the range of 22-25 $kJ.mol^{-1}$ to store approximately 7 wt% of hydrogen at 298 K and 30 bar. This indicates that the adsorption capacity of MOFs needs to be enhanced by 3-4 times.

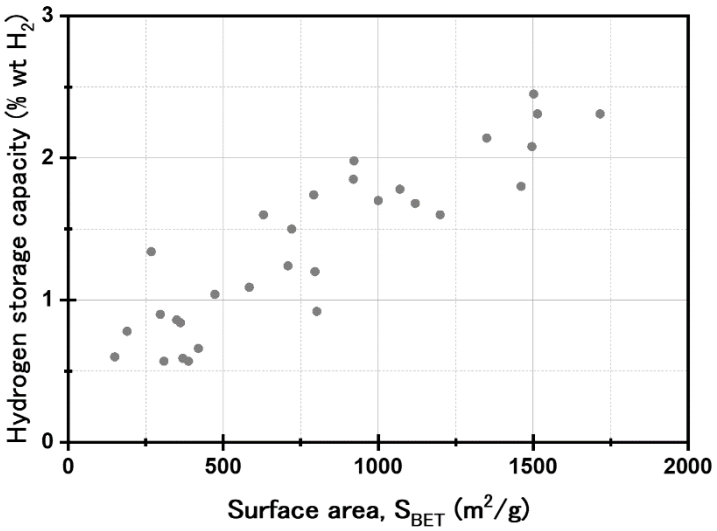

Figure I.15: Gravimetric hydrogen capacity in MOFs at 77 K-1bar plotted versus BET surface area, adapted from [49].

Specific surface area: Specific surface area is an important factor influencing hydrogen adsorption in porous materials. As shown in the Figure I.15, there is a strong correlation between the S_{BET} and the gravimetric hydrogen capacity at 77 K and 1 bar [49]. However, it's important to note that different molecules are considered in these measurements.

Pore volume: is another crucial factor affecting hydrogen storage in the physisorption category. Calculations by *Frost, H. et al.* [51], for different families of MOFs with the same framework topology and surface chemistry but varying pore volumes, demonstrate three distinct adsorption regions at 77 K: at low pressure, hydrogen uptake correlates with the heat of adsorption; at intermediate pressure, uptake correlates with surface area; and at high pressure, uptake correlates with pore volume as shown in Figure I.16.

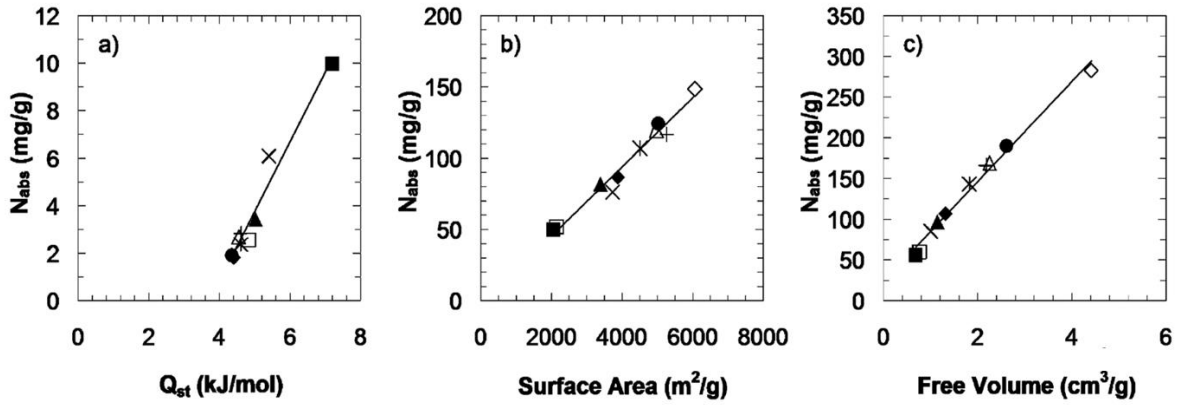

Figure I.16: (a) Absorbed amount at 0.1 bar vs. isosteric heat of absorption, (b) absorbed amount at 30 bars vs. accessible surface area, and (c) absorbed amount at 120 bars vs. free volume [51].

Classical hydrogen storage materials such as activated carbons, zeolites, and MOFs have made significant contributions to the development of hydrogen storage technologies. Activated carbons are favored for their simplicity of production, high surface area, and tunable pore structures, but their hydrogen adsorption capacity remains limited, especially under ambient conditions. Zeolites, on the other hand, offer high stability and micro-porosity, but their adsorption capabilities fall short of the theoretical maximum, limiting their overall potential in large-scale hydrogen storage. MOFs, with their exceptionally high specific surface area and tunable frameworks, exhibit promising hydrogen uptake capacities. However, many MOFs suffer from oversized pores and weak interactions with hydrogen, requiring further enhancement to meet practical storage demands.

While each of these materials has its own merits, their limitations in terms of production cost, complex manufacturing processes, and, in some cases, insufficient stability or adsorption performance suggest that alternative materials should be explored. In this context, clay materials, with their natural abundance, non-toxic, and stability, emerge as a promising candidate for next-generation hydrogen storage solutions.

4. Clay minerals

Clay minerals, are ubiquitous in Earth. They encompass a diverse range of ions, including iron, magnesium, alkali metals, alkaline earth metals, and other cations. These minerals are considered as constituents of soil, primarily formed through the erosion of rocks [52]. Sedimentary environments are known to host clay minerals, and factors such as temperature, weathering, and organic materials influence the variety of clay minerals present.

Clay minerals form a distinct realm in which these small, flat minerals interfere extensively with their environment, possessing the ability to absorb, retain, release, and incorporate a wide variety of ions or molecules into their lattice structure, making them versatile materials for various applications. They play a significant role in everyday life, from their use in white-coated paper to the containment of hazardous waste storage, cosmetics, pneumatics, paints, and building materials [53], [54].

4.1. Structure and composition of clay minerals

Clay minerals, identified as phyllosilicate minerals, consist of sheet-like two-dimensional crystal structures that may vary in composition and dimension [55].

Clay minerals are primarily known as complex silicates composed of various ions such as silicon, magnesium, aluminum etc... These ions can be arranged into two types, as shown in Figure I.17**:**

- 4-fold coordination: consists of silicon surrounded by four oxygen atoms to form a silica sheet.
- 6-fold coordination: described by aluminum or magnesium, this arrangement consists of the metal surrounded by six hydroxyl groups, combining to form a gibbsite-like sheet (if aluminum is the dominant atom) or a brucite-like sheet (if magnesium is the dominant atom).

The main atom in the tetrahedral sheet is the Si^{4+} cation, where three basal oxygens, link all the tetrahedra in one plane in such a way to form a hexagonal – shaped network [56] as shown in Figure I.18. The fourth oxygen atom, known as the apical oxygen, remains free and bonds with other elements in different polyhedral. Apical oxygens, located in a separate plane, connect the tetrahedral sheet to the octahedral sheet. Since each tetrahedron has only one apical oxygen, it shares a corner with an octahedron in the octahedral sheet.

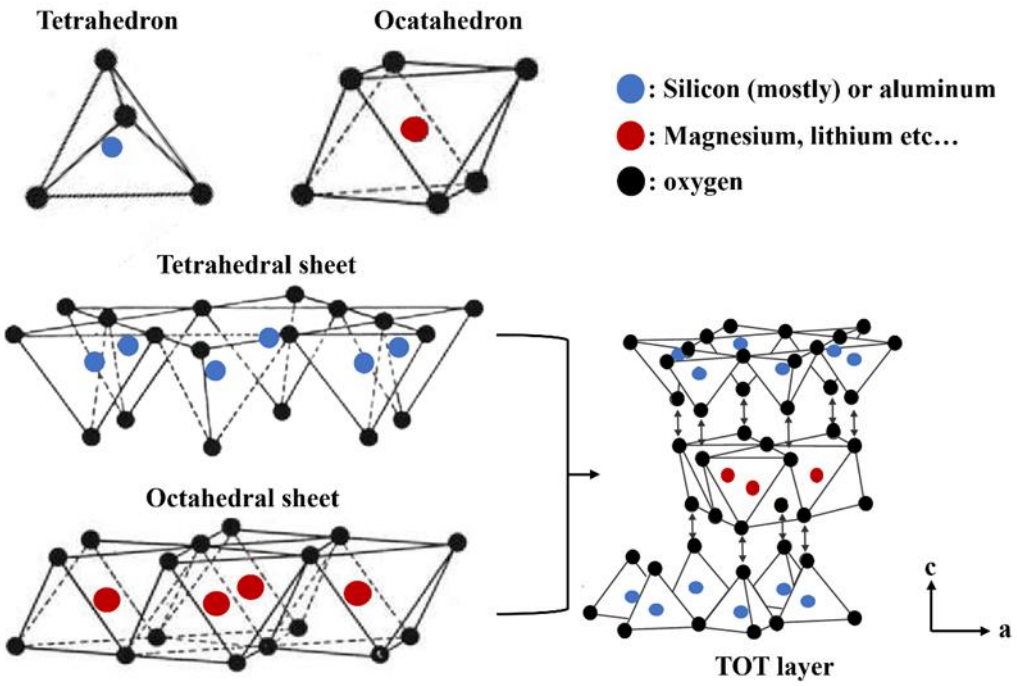

Figure I.17: Illustration of the formation of a TOT sheet of clay. The figure shows the progression from individual tetrahedron and octahedron units to the formation of tetrahedral and octahedral sheets, leading to complete TOT sheet "side-view".

The octahedral polyhedron contains a cation coordinated by six oxygen atoms or hydroxyl groups, forming eight faces building block known as an octahedron. The linkage of tetrahedrally and octahedrally coordinated cations is the fundamental characteristic of phyllosilicates.

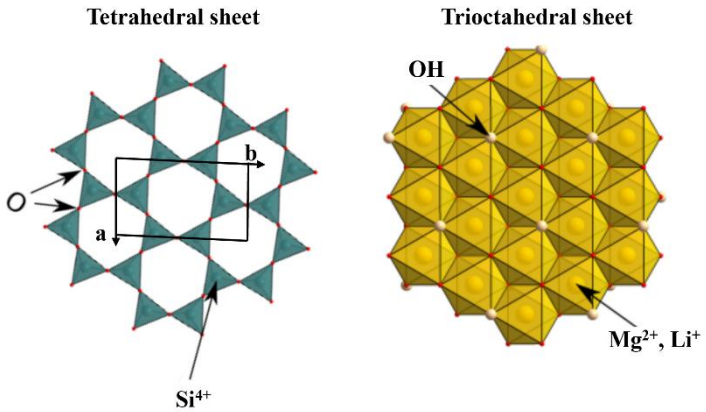

Figure I.18: Illustration of the tetrahedral and trioctahedral sheets of clay minerals, clearly showing the hexagonal-shaped network "top-view", atoms are shown as example just for clarity, adapted from [57].

Phyllosilicates can be classified according to their structural and molecular arrangement, elemental composition, and swelling properties. Based on Figure I.19, the main structural models are the 1:1 structure (kaolinite and serpentine subgroup), which consists of one tetrahedral sheet and one octahedral sheet bonded together, the 2:1 structure (talc-pyrophyllite, vermiculite, smectite, and micas groups), and the 2:1:1 structure (chlorite group). Structural

changes in clay minerals occur due to equivalent or non-stoichiometric substitutions of cations in either the octahedral or tetrahedral sites. These substitutions modify the layer charge and influence the mineral's physical properties, including swelling behavior and interlayer interactions. Focusing on the octahedral sites, the negative charge is equivalent to six charges, leading to two occupancy types of octahedral coordinated sites: dioctahedral sheets, where two-thirds of the octahedral sites are present. On other hand, trioctahedral sheets have all the octahedral sites fully occupied.

The general molecular formula for fully dehydrated 2:1 dioctahedral phyllosilicates is presented in equation (I.6):

$$\underset{octahedral}{[\boldsymbol{M^{3+}}_{4-x}\,\boldsymbol{M^{2+}}_{x}]}\quad\underset{tetrahedral}{[Si^{4+}{}_{8-y}\,Al^{3+}{}_{y}]}\quad O_{20}(OH)_4\quad\underset{interlayer}{E^{c+}{}_{(x+y)/c}} \tag{I.6}$$

For fully dehydrated 2:1 trioctahedral phyllosilicates, the formula is presented in equation (I.7):

$$\underset{octahedral}{[\boldsymbol{M^{2+}}_{6-x}\,\boldsymbol{M^{3+}}_{x}]}\quad\underset{tetrahedral}{[Si^{4+}{}_{8-y}\,Al^{3+}{}_{y}]}\quad O_{20}(OH)_4\quad\underset{interlayer}{E^{c+}{}_{(x+y)/c}} \tag{I.7}$$

where M represents the cations in the octahedral sites, x and y indicate the degree of cation substitution in the octahedral and tetrahedral sheets, respectively. E denotes the interlayer cations that balance the overall charge of the mineral, while c represents the charge of these interlayer cations.

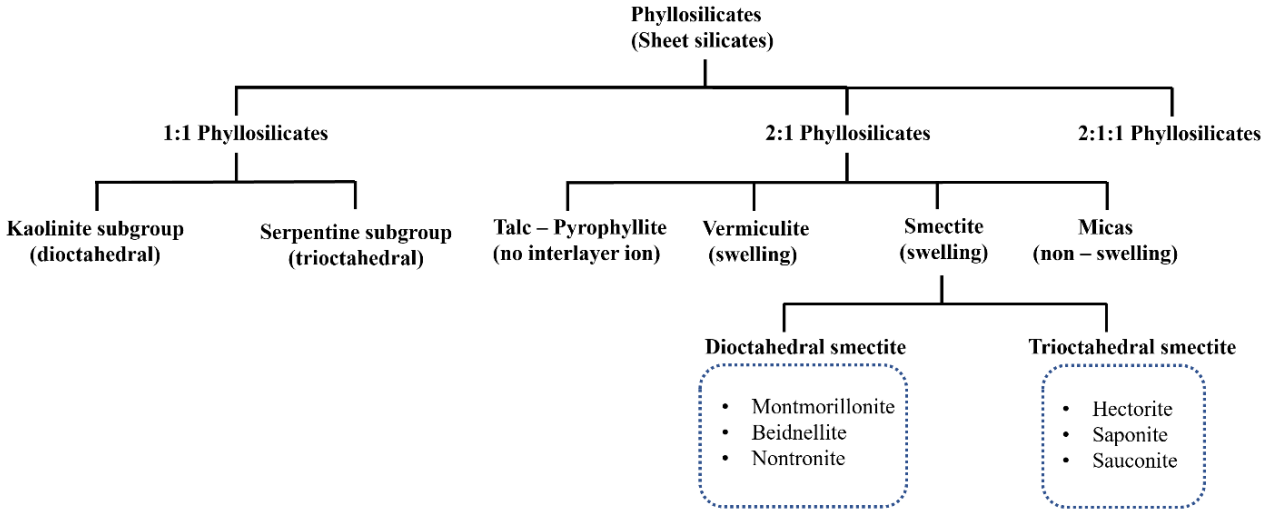

Figure I.19: Classification of sheet silicates materials into three main categories: 1:1 phyllosilicates, 2:1 phyllosilicates, and 2:1:1 phyllosilicates.

Another pathway to describe phyllosilicates is based on elemental substitutions. For example, tetrahedral Si^{4+} can be substituted by Al^{3+}, and Mg^{2+} in the octahedral site can be substituted by Fe^{3+} to balance the charge [56]. Additionally, it is possible to achieve electrostatic balance through interlayer substitution, meaning adding another ion to the surface of the tetrahedral-octahedral network. This ion typically has a charge of +1 or +2. The compositional variation results in different cell dimensions and atomic arrangements due to the charge relationships of the polyhedra. Lastly, phyllosilicates can also be classified based on their swelling capacity to adsorb water.

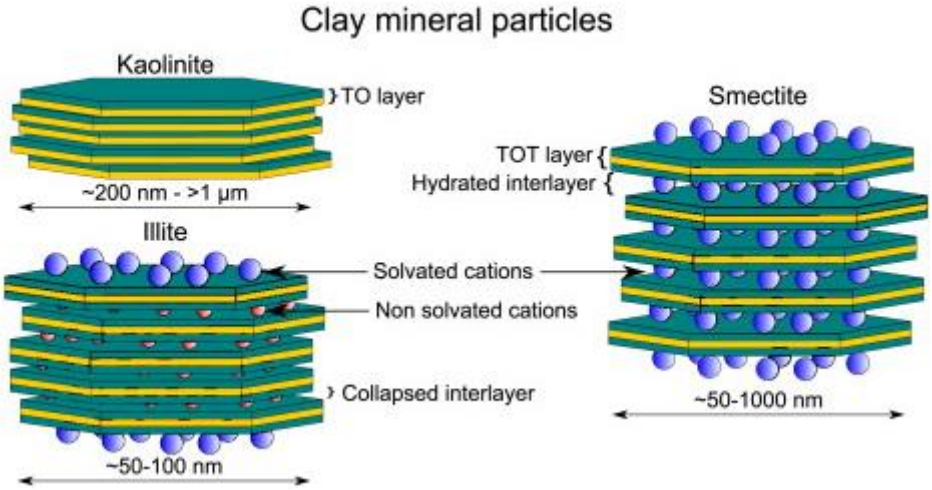

Figure I.20: Schematic illustration of layered structure of three types of phyllosilicate, adapted from [58].

Each group has a unique interlayer distance determined by its surface charge characteristics [59]. For instance, neutral-charge kaolinite and high-charge illite do not swell. On the other hand, smectite with low surface charges, do exhibit swelling. Figure I.20 depicts the general structure of these three types.

4.2. Smectite clay mineral

Smectites are based on either trioctahedral 2:1 or dioctahedral 2:1 structure. In smectites, interactions between sheets are rather weak. The interlayer space, occupied by exchangeable cations, can also accommodate water molecules, resulting in layer distances typically ranging from 9.6 Å to 22 Å depending on the relative humidity [60].

The layer charge density (number of electrons per $O_{10}(OH)_2$ half unit formula) for smectite ranges from 0.2 to 0.6 [61], which is sufficient to create a binding potential between layers, through the interlayer cations, but not strong enough to prevent the hydration of interlayer cations, hence their swelling capacity. The cation exchange capacity (CEC), the quantity of

cations required to balance the charge deficiency caused by these substitutions, is crucial for determining many important properties of smectites and their intercalation compounds [62] [63].

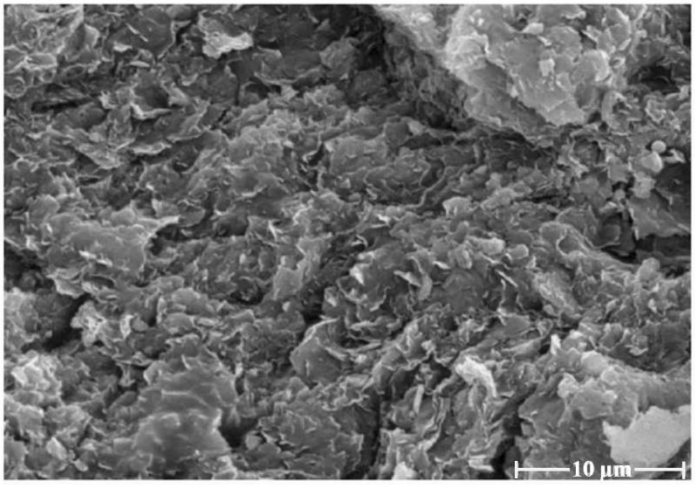

Figure I.21: SEM micrograph shows smectite leaf-like structure [64].

Smectites typically appear as very thin plates with irregular outlines [65] and, in some soils, they form leaf-like structures (Figure I.21). These materials exhibit notable characteristics such as a large chemically active surface area, high CEC values, and significant swelling and shrinkage capacities [66]. The two most important members of trioctahedral smectites are saponite, and hectorite. As the most of this thesis work was focused on the study of synthetic hectorite, some general structural details are given regarding to hectorite.

- **Hectorite**

Hectorite belongs to the 2:1 trioctahedral smectite group, and its molecular formula is provided in equation (I.7). In the octahedral site, it is represented as $[{Mg^{2+}}_{6-x}\ {Li^{+}}_{x}]$, while the tetrahedral sites are fully occupied by Si^{4+}.

Octahedral	*Tetrahedral*		*Interlayer*	
$[\boldsymbol{{Mg^{2+}}_{6-x}\ {Li^{+}}_{x}}]$	$[{Si^{4+}}_{8}]$	$O_{20}(OH)_4$	${Na^{+}}_{x}$	**(I.8)**

The cation exchange capacity (CEC) of hectorite is 0.53 meq/g clay, the smallest among smectites. Despite its natural occurrence, pure hectorite is rarely found due to the diverse geological environments and conditions in which it forms. Moreover, hectorite deposits exhibit varying degrees of crystallinity and may contain impurities, which limits their practical use [67]. To address this scarcity, synthetic methods have been developed to produce synthetic hectorite-like compound, known as laponite.

- **Laponite**

Laponite, a synthetic hectorite clay first synthesized by Neumann [68], exhibits high adsorption capacity and a significant ability for cation exchange, with a slightly higher CEC of 0.75 meq/g clay compared to its natural counterpart [69]. The primary particles of Laponite are uniform and disk-shaped, with a thickness of 1 nm and a diameter of ~30 nm [70], as shown in Figure I.22. These particles possess negative charges on their surfaces due to isomorphic substitution of Mg^{2+} ions with Li^{+} in the octahedral sheets. Consequently, in dry state the resulting net negative charge on the surface of the Laponite particles is counterbalanced by sodium cations (Na^{+}) in the interlayer space. Upon dispersion in aqueous media, water penetrates the inter-disk space, causing swelling and the dissociation of Na^{+} ions [71] [72] rendering a permanent negative charges to the faces of the Laponite particles.

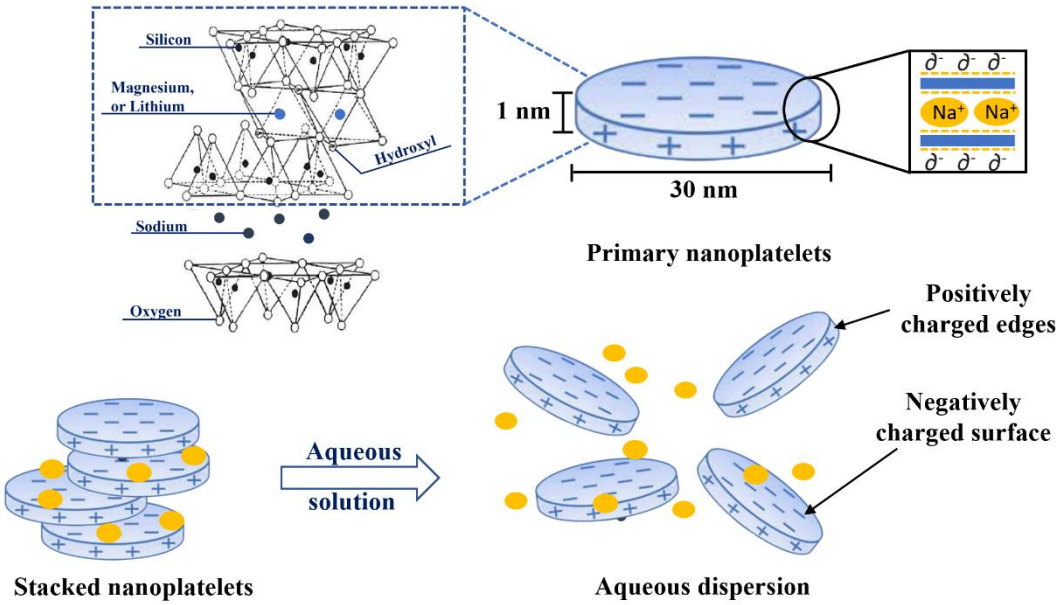

Figure I.22: Schematic representation of single Laponite nanoplatelets and nanoplatelets dispersed in an aqueous medium.

The edges of the Laponite particles predominantly contain MgOH groups, derived from the octahedral magnesia sheets. The point of zero charge (PZC) for magnesium oxides and hydroxides is above a pH of 10 [73]. Therefore, below the PZC, the edges of the particles are positively charged. Laponite has been extensively employed as an adsorbent and catalyst for eliminating cationic dyes [74] and metal ions [75].

5. General motivation of the thesis

Smectites, with their adjustable interlayer sizes, are promising materials for hydrogen storage applications. The interlayer space can be tailored based on the cationic size and hydrated state, making it large enough to allow H_2 penetration while maintaining proximity between the layers to enhance binding strength. However, the H_2 adsorption capacity of smectites has been little studied so far, Al-pillared montmorillonite [76] has demonstrated a maximum gravimetric sorption capacity of approximately 0.2 wt% H_2 at 77 K and around 1 bar of H_2. *Ziemiański and Derkowski et al.* [77] investigated H_2 adsorption on montmorillonite at temperatures ranging from 25°C to 70°C and pressures up to 145 bars. Under these conditions, the maximum H_2 uptake did not exceed 0.04 wt%, except for montmorillonite exchanged with tetramethylammonium cation (a large organic cation), which displayed an uptake of 0.1 wt% at 25°C and 145 bars. Additionally, *L. Masci et al.* [78] studied saponite materials modified with nickel and observed a maximum uptake of 0.19 wt% at 77K and 1 bar, and up to 0.12 wt% at 298 K and 120 bars for the "gel" (nano-crystallized) precursor used in saponite synthesis.

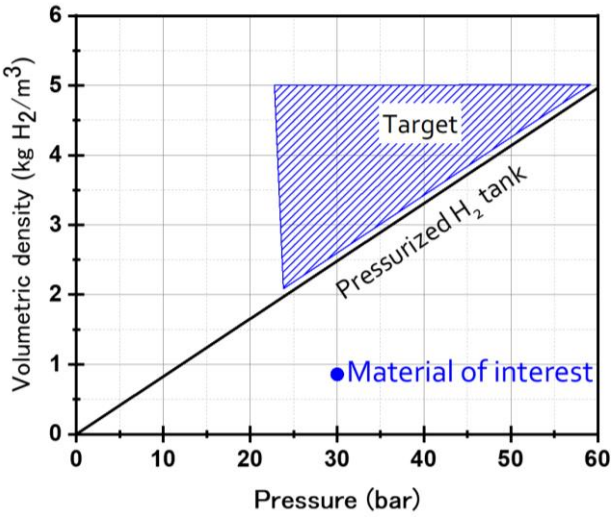

Figure I.23: Volumetric density of hydrogen storage in the studied clay material at room temperature compared to the target volumetric density required to surpass pressurized hydrogen tanks.

The hydrogen volumetric density in clay materials remains significantly below the target needed to exceed the performance of pressurized hydrogen tanks, as illustrated in Figure I.23. Enhancing hydrogen storage capacity in these materials is a complex challenge. Therefore, this thesis aims to provide a deeper understanding of the adsorption mechanisms in Laponite and its pre-Laponite precursor in the synthesis, which have been identified as materials of interest as it will be shown in **Chapter V**.

The research is divided into two main parts:

1. **Structural and textural characterization**: The first part focuses on synthesizing and characterizing the materials to understand their structural, textural, and chemical differences. Various techniques are employed for this purpose, including X-ray scattering with pair distribution function analysis, nitrogen adsorption measurements, and other relevant characterization methods.
2. **In-Situ Neutron Scattering**: The second part is dedicated to in-situ neutron scattering experiments, which provides insights into the most relevant adsorption sites with their rotational potential barriers, as well as on the localization and quantification of H_2 within the materials. The neutron scattering data are complemented by Monte Carlo simulations to gain a comprehensive understanding of the H_2 adsorption mechanism.

This page was intentionally left blank

Chapter II. Experimental methods and formalism

In this chapter, we outline the materials and methods used in this project. We started by describing the experimental procedures, including the preparation of clay samples and their chemical analysis using inductively coupled plasma atomic emission spectroscopy. Next, we discuss various methods for material characterization, such as thermogravimetric analyses, nuclear magnetic resonance and infra-red spectroscopy. We then explore adsorption isotherms in detail, examining the forces behind physisorption, the classification of isotherms, and the analysis of nitrogen isotherms to determine the textural properties of the materials. The chapter concludes with an overview of scattering techniques formalism, including both X-ray and neutron scattering, to provide detailed insights into the structure of the materials at the atomic levels.

1. Experimental methods

1.1. Clay preparation

The synthesis of Laponite follows a well-established protocol outlined in Barbara Neumann's patent [68]. The nominal formula of such laponite is $[Mg_{4.8}\ Li_{1.2}]^{Oct}\ [Si_8]^{Tet}\ O_{20}(OH)_4$, where Oct and Tet indicate the appurtenance of the cations inside a layer to tetra- and octahedral sheets. The TOT layer has a net negative charge of 1.2e *per* unit cell, which is compensated by Na^+ cations in the interlayer space. The synthesis proceeds in two stages: first, the preparation of a pre-laponite sample, followed by hydrothermal treatment to obtain the laponite sample. It was realized at at Institut des Sciences de la Terre (Grenoble, France), either by me or by Martine Lanson, who trained me. Syntheses were performed either with H_2O or with D_2O. In the latter case, the objective is to obtain deuterated sample (D-samples) for neutron scattering studies.

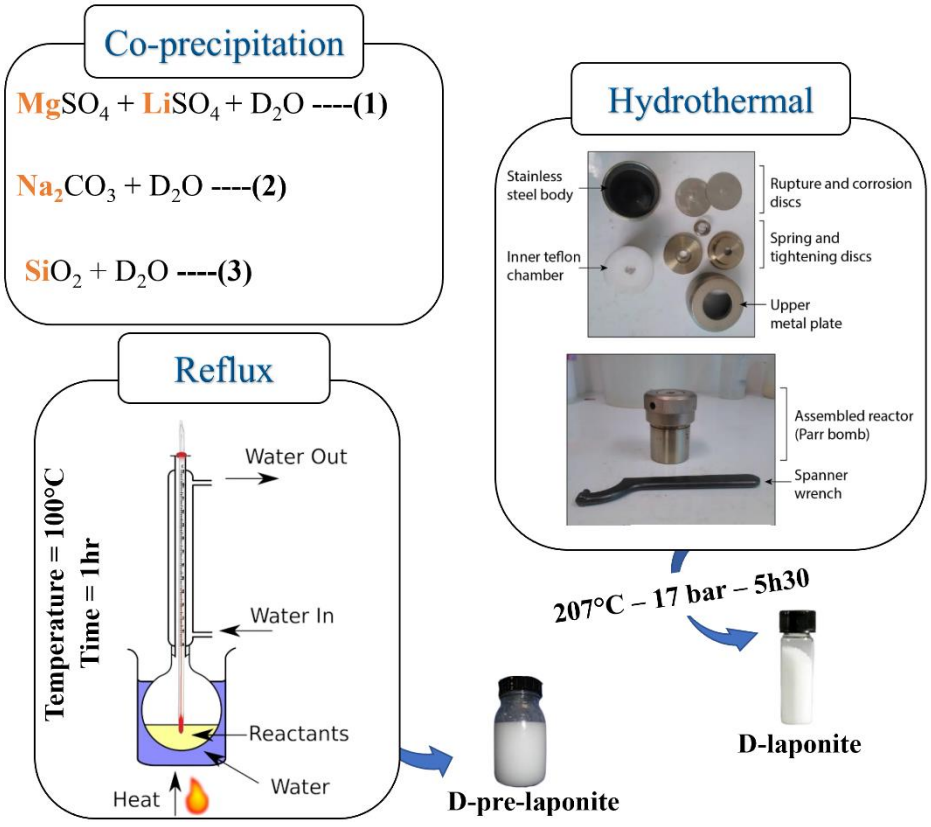

Figure II.1: Schematic illustration of the synthesis process for D-pre-Laponite and D-Laponite samples. The synthesis was conducted under a nitrogen flow environment to ensure an inert atmosphere to minimize H-D exchange. The 'D' in the sample names referred to deuterated samples.

The synthesis protocol summarized in (Figure II.1**)** consists of: precipitating 0.72 mol of $MgSO_4 \cdot 7H_2O$ and 0.09 mol of $Li_2SO_4 \cdot H_2O$ in 85 mL of D_2O (solution 1). Then, solution 1 is

added[4] to 0.07 mol of Na_2CO_3 in 60 mL D_2O (solution 2) to precipitate $MgCO_3$. Following this, introducing[4] 0.121 mol of Si (from a solution of 29% SiO_2 and 8.8% Na_2O) in 25 mL of D_2O (solution 3) to the mixture (solution 1+2) to precipitate Si. Each addition is carried out under gentle agitation (100 rpm) for at least 30 minutes under a nitrogen atmosphere to minimize H-D exchange. The mixture is then boiled with a reflux condenser at atmospheric pressure for 1 hour. Subsequently, the sample is cooled in an ice bath, followed by centrifugation at 8000 rpm for 5 minutes, washed three times with D_2O, and subjected to freeze-drying to produce the powdered pre-Laponite sample.

The hydrothermal treatment is performed on the pre-Laponite suspension (before freeze-drying) at 207°C and 17bars for 5 hours and 30 minutes. Following the hydrothermal treatment, the same separation, washing, and drying techniques is used (as for pre-Laponite) to obtain the powdered Laponite.

The choice to employ deuterated water (D_2O) instead of protonated water (H_2O) in our experimental protocol is motivated by the necessity to minimize incoherent scattering originating from hydrogen atoms. This decision is particularly crucial, given that the selected samples are destined for neutron experiments, will be discussed further in **Chapter V**.

Throughout this manuscript, references to pre-Laponite and Laponite samples indicate that the samples are deuterated, otherwise defined.

1.2. Inductively coupled plasma atomic emission spectroscopy

Inductively coupled plasma atomic emission spectroscopy (ICP-AES) used to determine precisely the elemental composition/concentration in the targeted sample. ICP-AES uses high-energy plasma from an inert gas (like argon) to burn analytes very rapidly. The wavelength (color) of the electromagnetic radiation is characteristic of the elements present, and the intensity of the spectral signal gives the concentration of the elements that is present. A schematic view of a typical experimental-setup is shown in Figure II.2.

- **How does it work?**

ICP-AES operates by detecting photons emitted from analytes that have been excited to high energy states by high-energy plasma. This plasma is generated by passing argon gas through an alternating electric field produced by an inductively coupled coil. When the analytes are

[4] *The Solution should be added at a controlled rate, at least for 30min.*

excited, their electrons release the absorbed energy as they return to a lower energy ground state, emitting light in the process. The specific wavelength of the emitted light corresponds to the energy difference between the excited state and the ground state, which is characteristic of each element based on its electron configuration. By analyzing the intensities of emitted light at these wavelengths, the concentration of different elements in the sample can be calculated.

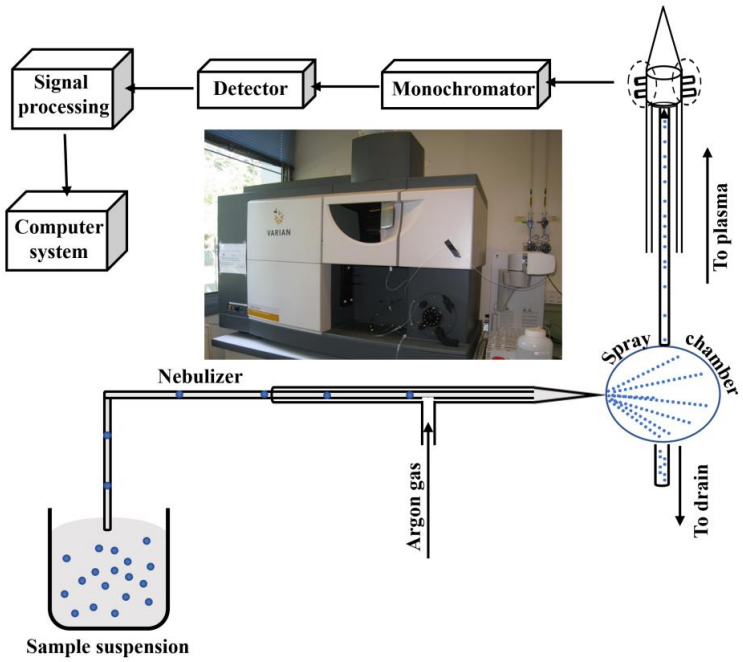

Figure II.2: Schematic representation of the Inductively Coupled Plasma - Atomic Emission Spectroscopy (ICP-AES) setup. The sample suspension is introduced into the nebulizer, where a high-velocity stream of argon gas transforms it into a fine aerosol. The fine droplets are then transported to the spray chamber, where larger droplets are removed. The remaining aerosol is directed into the plasma, where the sample undergoes atomization and excitation. The emitted light from the excited atoms and ions is then directed into the monochromator, which isolates specific wavelengths corresponding to different elements. The detector measures the intensity of these wavelengths, and the signal is processed and interpreted by the computer system, providing detailed elemental analysis.

- **Preparation of clay suspension**

To prepare the clay suspension, 50 mg of powdered pre-Laponite (or Laponite) dispersed in 45 g of milli-Q water. The mixture was then sonicated at ambient temperature (22°C). Subsequently, due to the high concentration of elements such as Si and Mg, the resulting supernatant was diluted by factors of 2, 5, 10, 20, and in some cases up to 100 and 1000. It is important to note that sonication duration has a significant impact on the element's concentration, particularly in the case of pre-Laponite, as will be detailed in **Chapter IV, §1**.

The diluted supernatant samples were then analyzed using ICP-AES Varian 720ES at Institut des Sciences de la Terre. Each sample analysis last for a duration ranging from 15 to 90 seconds, followed by a washing period for a 30 to 90 seconds to ensure measurement precision and

accuracy. For each element, at least two distinct wavelengths were used: 279.5, 280.3, and 285 nm for Mg; 568.8 and 589 nm for Na; 185, 212.4, 250.7, 251.4, 252.8, and 288.2 nm for Si. Finally, the measured intensities were compared to a previously constructed calibration curve (Figure II.3), which was generated from a series of known standard solutions containing the respective metal atoms/ions of interest.

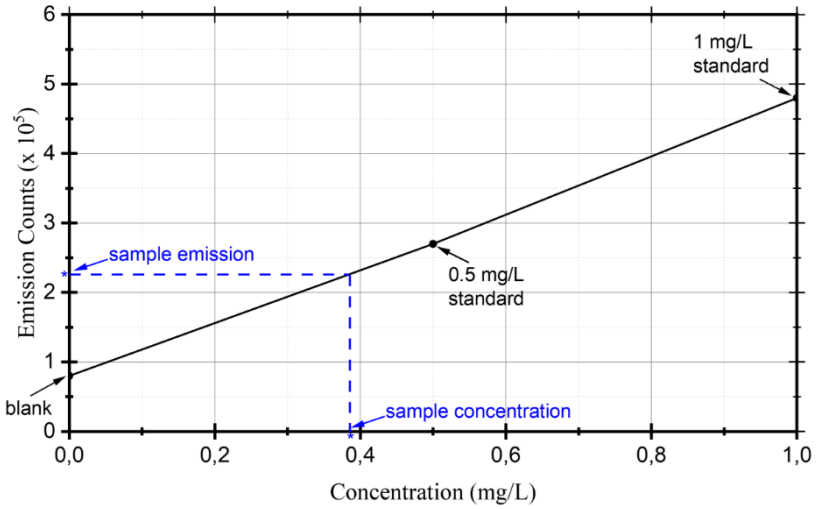

Figure II.3: Example of the calibration curve, illustrates the relationship between emission intensity and concentration for elements of interest, using standard solutions of known concentrations. A blank sample is included to account for background signals and interferences.

2. Material characterization

2.1. Infrared spectroscopy

Infrared (IR) spectroscopy is based on the absorption of electromagnetic radiation by the sample. When the frequency of the radiation matches the vibrational modes of molecular groups within the sample, such as stretching or bending modes, energy is absorbed. Adsorption frequencies are specific to the atoms involved and the strengths of their bonds, making IR spectroscopy a powerful tool for investigating local structure.

To obtain an IR spectrum, the intensity of the transmitted beam passing through the sample is measured using a detector, generating an interferogram. Fourier transformation of the interferogram yields the IR absorption spectrum. For that, 1 mg of pre-Laponite (or Laponite), was blended with 99 mg of KBr[5], and pressed at 6 tons into a transparent disk. IR spectra were acquired using a Nicolet iS100FTIR spectrometer in transmission mode at room temperature,

[5] *KBr acts as host matrix and it is transparent to infrared light.*

averaging 64 scans with a resolution of 4 cm^{-1} over the spectral range of 4000 – 400 cm^{-1}, at Laboratoire de Physique des Solides (Orsay, France).

2.2. Thermogravimetric analysis

Thermogravimetric analysis (TGA) is used to measure mass changes in materials as they are heated at a constant rate or held at a constant temperature. This method provides valuable insights into the composition and thermal stability of samples. In our study, TGA enables the identification of characteristic temperatures associated with mass loss and facilitates the quantification of water content in both Laponite and pre-Laponite.

The TGA measurements were carried out using TGA/DSC3+ instrument sourced from Mettler Toledo® at Institut des Sciences de la Terre. Approximately 50 mg of sample were dispensed into a 150 µL alumina crucible. The experimental conditions encompassed a controlled N_2 atmosphere with a flow rate of 20 mL/min. Temperature was increased from room temperature to 900 °C, employing a heating ramp of 5 °C/min.

2.3. ^{29}Si solid-state nuclear magnetic resonance

Silicon-29[6] solid-state nuclear magnetic resonance spectroscopy (^{29}Si ssNMR) is a powerful technique for examining the local environment of silicon atoms in solid-state materials. Among the three main isotopes of Si present in nature (^{28}Si, ^{29}Si and ^{30}Si), it is the only one with non-zero spin (its spin is equal to ½) so it is the only one which can be observed by NMR. When placed in a strong magnetic field and exposed to radio-frequency pulses, the ^{29}Si nucleus resonates at frequencies that reveal detailed information about its chemical environment, helping to identify the different silicon-containing phases and structural features. However, it is a rather difficult nucleus to study because of its low natural abundance (~4.7 %) and low NMR sensitivity at constant field (7.84 x 10^{-3}) compared to ^{1}H.

One of the main techniques used in ssNMR to improve resolution is Magic Angle Spinning (MAS). MAS involves rotating the sample at a specified angle (54.74°) relative to the magnetic field. This rotation averages out anisotropic interactions (such as dipole couplings and chemical shift anisotropy) which can serve to broaden NMR signals [79].

Another important technique in ssNMR is cross polarization (CP). CP enhances the sensitivity of NMR experiments by transferring polarization from abundant nuclei, such as ^{1}H, to less

[6] *Silicon (Si-29) has a spin quantum number ½, making it NMR active.*

abundant nuclei, such as ^{29}Si. This transfer is achieved by applying radio-frequency fields simultaneously to both types of nuclei, under the “Hartmann-Hahn matching condition [80]. CP is particularly useful for studying nuclei with low natural abundance or low sensitivity, as ^{29}Si is.

Another important technique in ssNMR is cross polarization (CP). CP enhances the sensitivity of NMR experiments by transferring polarization from abundant nuclei, such as ^{1}H, to less abundant nuclei, such as ^{29}Si. This transfer is achieved by applying radio-frequency fields simultaneously to both types of nuclei, under the Hartmann-Hahn matching condition. CP is particularly useful for studying nuclei with low natural abundance or low sensitivity.

Solid-state NMR experiments were performed by Cristina Coelho at the NMR platform of the Fédération de Chimie et Matériaux de Paris Centre, Sorbonne Université, using a Bruker AV700 spectrometer with ^{29}Si MAS/CP-MAS setup operating at a spinning speed of 10 kHz. The relaxation delay was set to 60 seconds for MAS and 3 seconds for CP-MAS, with 1024 scans for MAS and 2048 for CP-MAS. The contact time in the CP-MAS experiment was 1 millisecond. DSS (sodium 4,4-dimethyl-4-silapentane-1-sulfonate) was used for power calibration and as a reference, with a chemical shift of 1.67 ppm relative to TMS (tetramethylsilane).

3. Adsorption isotherm

Adsorption phenomena are widely recognized and applied across various fields, such as gas purification [81], hydrogen-powered vehicles [82] and gas storage. Adsorption refers to the accumulation of molecules in the interfacial layer between two phases, typically a solid and gas. The solid material on which adsorption occurs is termed the "adsorbent," while the substance in the adsorbed state is known as the "adsorbate." When discussing the substance in the bulk prior to adsorption, it is referred to as the "adsorptive" (for clarity see Figure II.4) The opposite of adsorption is "desorption," where adsorbed molecules (ad-molecules) are released from the adsorbent surface. Additionally, in highly porous solids there may be internal diffusion process of the ad-molecules.

The relationship, at constant temperature, between the equilibrium of the adsorbate in the gaseous phase and the equilibrium adsorption amount in the solid phase is known as the adsorption isotherm. Modeling adsorption data using isotherms provides critical insights into adsorption capacity and surface interactions.

As described previously in **Chapter I, §3**, there are two categories of adsorption, but in the subsequent sections will focus exclusively on physisorption phenomena. In physisorption systems, ad-molecules are weakly bound to the adsorbent, primarily through vdWs- and/or dispersion forces resulting from induced dipole-dipole interactions.

Physisorbates, can exhibit many different features that reflect the underlying molecular mechanism. The most interesting types present in this manuscript are described as follows:

- **Monolayer adsorbates:** The adsorbent surface consists of numerous adsorption sites that are energetically uniform or nearly identical. In this process, the adsorbate forms a single molecular layer, with each molecule directly attached to the adsorbent. The system operates under low pressure conditions, where the gas pressure of the adsorbate remains well below its saturation point, preventing the formation of additional layers.
- **Multilayer adsorbates:** The adsorbent surface contains a variety of adsorption sites, which can vary in energy or be energetically uniform. At higher gas pressures, approaching the saturation pressure of the adsorbate, multiple layers of molecules are adsorbed. In this case, only the first layer is in direct contact with the adsorbent, while subsequent layers build up through interactions between adsorbed molecules.
- **Capillary condensation:** Capillary condensation occurs when gas condenses into a liquid-like phase within pores at pressures below the saturation pressure. This phenomenon is due to the enhanced attractive forces within the confined space of the pores, which lowers the energy barrier for condensation. This process is particularly pronounced in mesoporous materials.
- **Quantum sorbates:** adsorbent contains very narrow sub-micropores (<1 nm) through which light molecules such as hydrogen (H_2) and deuterium (D_2) can permeate. At low temperatures, when the pore diameter approaches the de Broglie wavelength[7] of these molecules, quantum sieving effects may occur. This phenomenon allows for the separation of isotopes based on their different diffusion velocities. Detailed discussions on this topic will be provided in **Chapter IV**.

[7] *The de Broglie wavelength of H_2 at 1 atm and at T = 20K is about 0.5 nm; it is 0.1 nm at 300 K* [83].

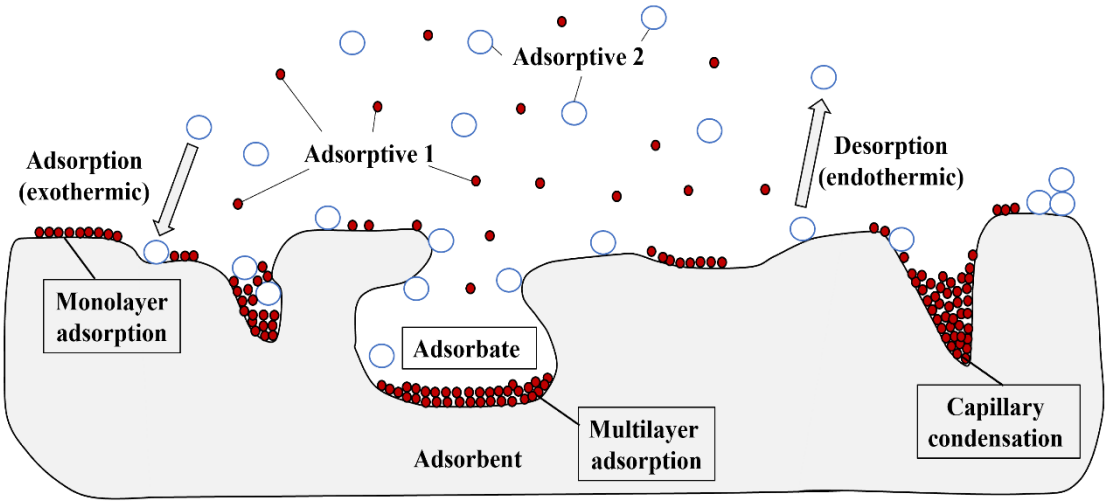

Figure II.4: Schematic representation of a two-component sorptive gas (Adsorptive 1, Adsorptive 2), a sorbed phase or adsorbate including also the two-component with different concentrations than in the gas phase due to their different interactions with the sorbent atom, and a solid sorbent phase (adsorbent). Initially, a single layer of molecules builds up over the surface of the solid (monolayer adsorption). As the fluid concentration increases, more layers are formed (multilayer adsorption), and the number of layers formed may be limited by the size of the pore. Finally, capillary condensation may occur, in which the capillary becomes filled with condensed adsorbate, adapted from [84].

3.1. Classification of adsorption isotherm

The ability of porous materials to perform the desired function in a particular application is directly related to the size, shape, and volume of their pores. Pores are classified into three main categories in layered clay material, based on their size: micropores, mesopores and macropores as illustrated in Figure II.5 [85].

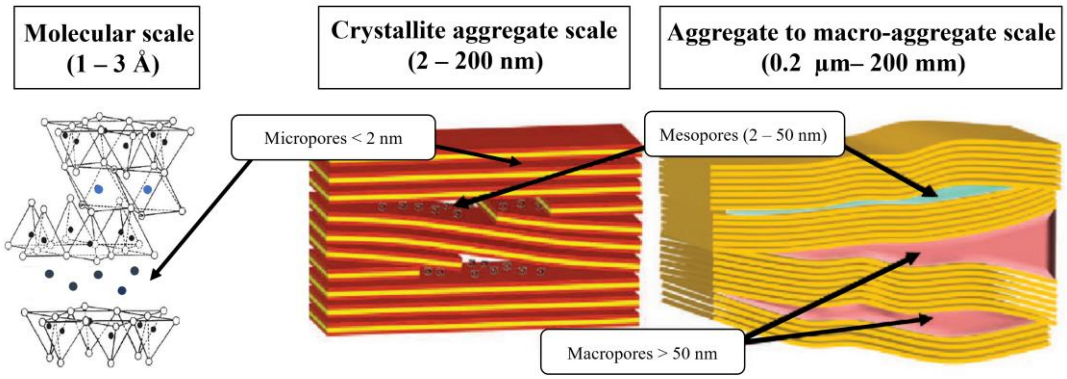

Figure II.5: Overview of pore size classifications according to IUPAC terminology at different scales for layered clay material, adapted from [86].

These pores exhibit different adsorption behaviors as illustrated by the various adsorption isotherm types classified by IUPAC (Table II.1). These isotherms are characteristic of

adsorbents that are microporous (type I), nonporous and macroporous (types II, III, and VI) materials, and mesoporous (types IV and V) materials. Micropores can be considered as spaces where molecules fill into a nano-space, experiencing a deep potential field due to the overlapping of wall potentials [87]. This results in adsorption isotherms characterized by a steep rise at very low relative pressures and a plateau after saturation. In contrast, adsorption in mesopores is dominated by capillary condensation rather than molecule-solid interactions [88], leading to a sharp adsorption rise around the mid relative-pressure region. . Adsorption in macropores and on nonporous surfaces shows no essential difference between them.

The differences between types II and III and between types IV and V isotherms are attributed to the relative strength of adsorbate-adsorbent and adsorbate-adsorbate attractive interactions. A stronger adsorbate-adsorbent attractive interaction compared to adsorbate-adsorbate interactions results in types II and IV isotherms, while the opposite scenario leads to types III and V behaviors. Type VI isotherms represent adsorption on nonporous or macroporous solid surfaces where stepwise multilayer adsorption occurs.

Table II.1: Overview of adsorption isotherm types: characteristics, graphs, and examples.

Isotherm type	Description	Sample graph	Examples / references
Type I isotherms (convex upward)	Characterized by rapid rise in adsorbed quantity with increasing pressure up to saturation, i.e., a plateau that is nearly or quite horizontal.	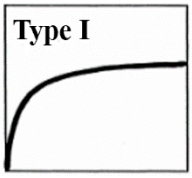	Hydrogen adsorption at 77K and 87K on MOFs [89].
Type II isotherms	Describes adsorption on macroporous material, monolayer at low pressure and multilayer near saturation pressure, with only one inflection point.	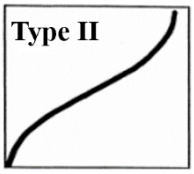	Nitrogen adsorption at 77K on silica gel, water vapor adsorption on natural fibers [90].
Type III isotherms (concave upward)	This type occurs when adsorbate-adsorbate interaction is stronger than adsorbate-sorbent.	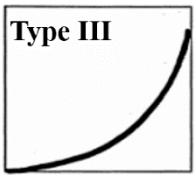	Iodine adsorption at 348K on MOF (Cu-BTC) [91].
Type IV isotherms	Characterized by two inflection points and a hysteresis loop which is attributed to the filling/vacating of mesopores by capillary condensation. Uptake fairly increases with pressure within the low-pressure region and then it undergoes monolayer-multilayer adsorption.	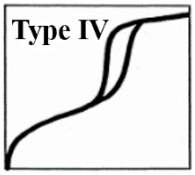	Water vapor adsorption on various porous charcoals and carbon black [92].
Type V isotherms	This type indicates the presence of mesopores where pore condensation may occur during phase change and is characterized by one inflection point.	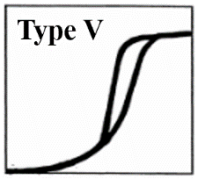	Water vapor adsorption on activated carbon [93].
Type VI isotherms	Characterized by multilayer adsorption, particularly by spherically symmetrical, non-polar adsorptive. It shows several inflection points.	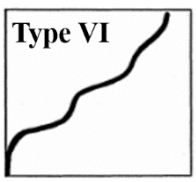	Argon [94] and krypton [95] adsorption on graphitized carbon at liquid nitrogen temperature.

3.2. Adsorption hysteresis

Hysteresis appearing in physisorption isotherms is usually associated with capillary condensation in mesopore structures. The classification adopted by IUPAC in 1984 [96] is shown in Figure II.6. Although the effect of various factors on adsorption hysteresis is not fully understood yet. However, the shapes of hysteresis loops are often related to specific pore geometries.

Type H1 hysteresis loops are often associated with porous materials known, from other evidence, to consist of agglomerates[8] or compacts of approximately uniform spheres in a fairly regular array, resulting in narrow distributions of pore size. The H2 loop was previously attributed to differences in the condensation and evaporation mechanisms occurring in pores with narrow necks and wide bodies (commonly referred to as "ink bottle" pores). However, it is now recognized that network effects must also be considered. The H3 loop is observed with aggregates[9] of plate-like particles, which give rise to slit-shaped pore. Similarly, the Type H4 loop is often associated with narrow slit-like pores.

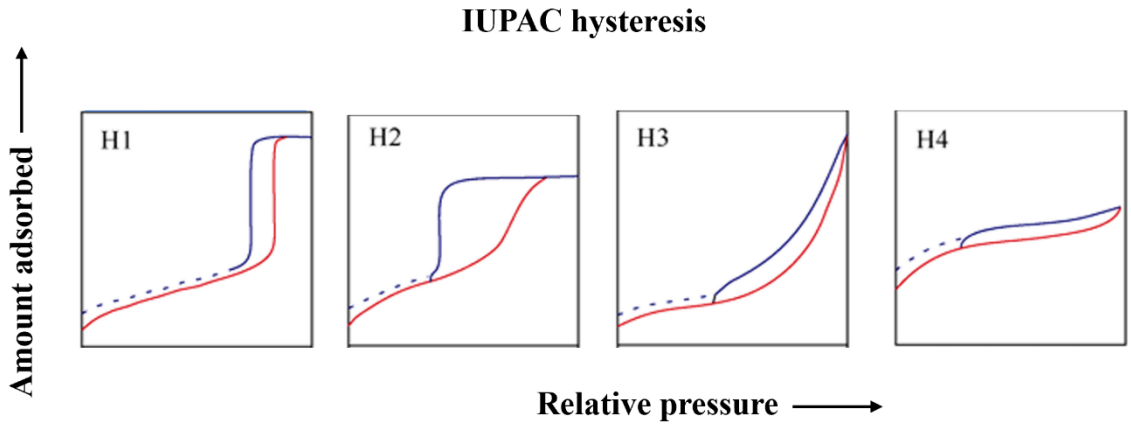

Figure II.6: The IUPAC classification of adsorption isotherm hysteresis loops. The red line represents adsorption, the blue line denotes desorption, and the dashed line indicates the trendline for desorption, adapted from [97].

For all experimental adsorption measurements, the materials were initially outgassed at 150°C for 6 hours under secondary vacuum conditions. This process was performed to ensure the complete removal of residual water prior to the adsorption measurements.

[8] *An agglomerate is defined as an assemblage of particles rigidly joined together.*
[9] *An aggregate is an assemblage of particles which are loosely coherent.*

3.3. Pores and surface characterization

Nitrogen (N_2) sorption analysis is a powerful tool for investigating material porosity. The basic principle of this technique involves measuring the amount of N_2 adsorbed by the material under specific conditions and applying theoretical models to convert this data into textural material properties, such as surface area, micropore volume etc…

The amount *n* of N_2 adsorbed by the material depends on temperature *T*, equilibrium pressure *p*, and on the nature of the N_2-adsorbent system:

$$\boldsymbol{n = f(p, T, system)} \quad \textbf{(II.1)}$$

If a specific N_2-adsorbent system is maintained at a constant temperature *T*, which is below the nitrogen critical temperature (T ~ 126 k), the nitrogen adsorption isotherm for this specific system is:

$$\boldsymbol{n = f\left(\frac{p}{p_0}\right)_T} \quad \textbf{(II.2)}$$

Where p_0 is the N_2 saturation pressure at temperature *T*. N_2 isotherm describes the relation between adsorbed N_2 amount and relative pressure p/p_0.

N_2 adsorption/desorption isotherms (~ 200 mg / sample) were measured with the help of Valérie Magnin at 77 K using liquid N_2 as cryogen in the relative pressure range of 10^{-6} – 0.995 in 50 steps for adsorption and 40 steps for desorption using the ASAP 2020 PLUS volumetric gas sorption instrument from Micromeritics Instruments® at Institut des Sciences de la Terre (Grenoble, France), (Figure II.7). The dead volume of the sample cell was reduced by inserting non-porous glass filler rod, which were assessed using Helium gas (purity 99.99%) before each run.

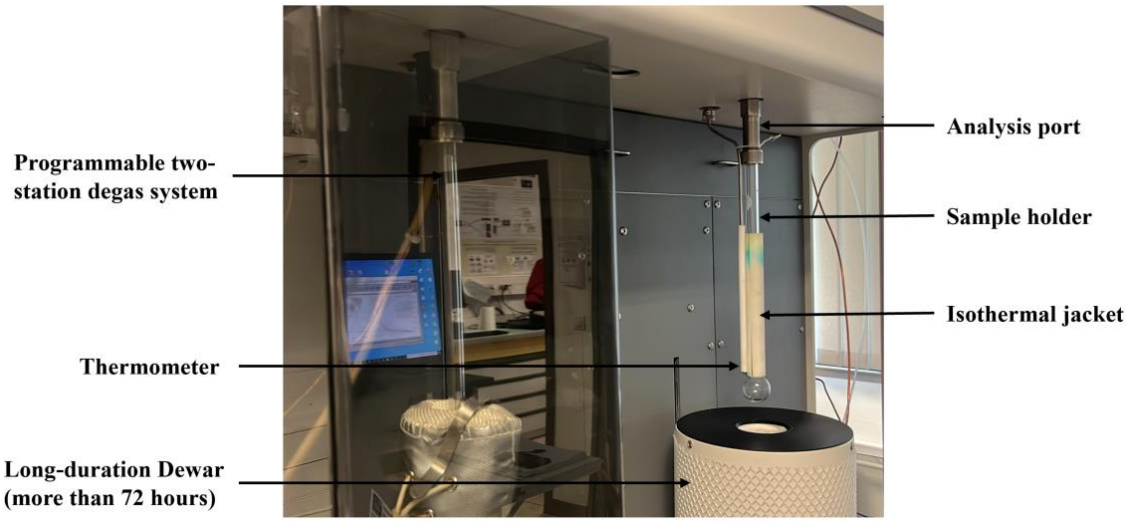

Figure II.7: The ASAP 2020 Instrument from Micromeritics Instruments® at ISTerre, Grenoble.

Various models are used to analyze nitrogen adsorption isotherm data. The Brunauer-Emmett-Teller (BET) model is the most convenient and widely used for estimating the surface area of materials. For microporous materials, the choice of sorbate significantly impacts the results especially when using swelling clays [98], as smaller molecules can penetrate smaller pores[10]. Nevertheless, the BET method is based on the following equation:

$$\frac{\mathbf{1}}{\boldsymbol{n_a}\left(\frac{\boldsymbol{p}}{\boldsymbol{p_0}}-\mathbf{1}\right)}=\frac{\mathbf{1}}{\boldsymbol{n_m C}}+\frac{\boldsymbol{C}-\mathbf{1}}{\boldsymbol{n_m C}}\frac{\boldsymbol{p}}{\boldsymbol{p_0}} \qquad \textbf{(II.3)}$$

where n_a is the amount of nitrogen adsorbed at pressure p, n_m is the amount of nitrogen forming the surface coverage, and C is constant which is related to the adsorption energy in the first adsorbed monolayer.

By plotting $1/n_a\left(\frac{p}{p_0}-1\right)$ versus p/p_0 yields a linear plot. Computing the intercept and the slope, enables to determine the monomolecular capacity n_m which is related to the surface area using the following equation:

$$\boldsymbol{S}=\frac{\boldsymbol{n_m}}{\boldsymbol{M_r}}\boldsymbol{N_A}\boldsymbol{\sigma} \qquad \textbf{(II.4)}$$

where M_r is a molecular weight of N_2, N_A is the Avogadro constant, and σ is the N_2 cross-sectional area (0.162 nm^2 at 77K) [99]. However, extreme caution is needed for the application

[10]*Since N_2 has a diameter of approximately 3.64 Å, which is larger than that of H_2, it tends to underestimate the surface area available for H_2.*

of BET method, especially with the presence of micropores and main criteria of its application are given [100]:

- The fitted linear trend should have positive intercept, otherwise (negative *C* quantity) indicates an inappropriate pressure range.
- $\frac{1}{n_a\left(\frac{p}{p_0}-1\right)}$ increase as function of $^{p}/_{p_0}$.
- The relative pressure where monolayer completion is formed should be included in the calculation.

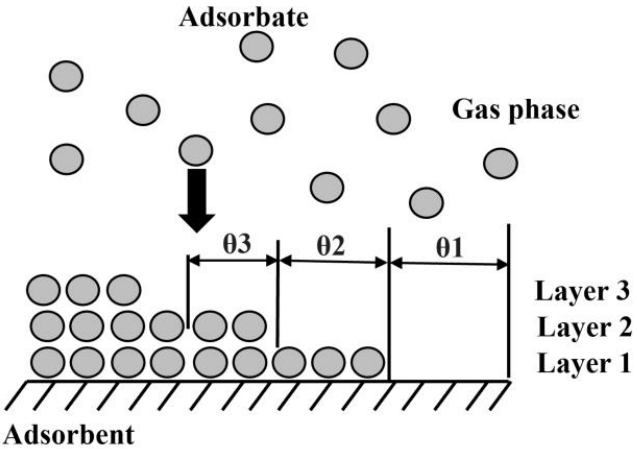

Figure II.8: The BET model adsorption mechanism, adapted from [101]**.**

Note that the BET constant *C* provides insight into the adsorbent – adsorbate interaction, since it is related to the heat of adsorption using the following equation:

$$\boldsymbol{C = exp\left(\frac{q_1 - q_L}{RT}\right)} \qquad \textbf{(II.5)}$$

where q_1 is the heat of adsorption of first layer and q_L is the heat of liquification of the adsorbate. However, to differentiate between micropores and external surface area, we applied the t-plot method. So we employed the *Harkins* and *Jura* [102] relation as the standard reference t-curve for this analysis. This approach allowed us to calculate the external surface area (S_{ext}) and the micropore volume (V_m) from the slope and the intercept of the linear fit, respectively. The t-curve represents the average thickness of the adsorbed layer as a function of relative pressure, based on the following equation:

$$\boldsymbol{t = \sqrt{\frac{A_{HJ}}{B_{HJ} - log\left(^{p}/_{p_0}\right)}}} \qquad \textbf{(II.6)}$$

with A_{HJ} = 13.99 Å^2 and B_{HJ} = 0.034, and thickness *t*, is expressed in Å.

3.4. Hydrogen isotherm

Hydrogen adsorption measurements constitute a critical aspect of this thesis manuscript. These measurements were conducted under various conditions (temperature – pressure), necessitating the use of different instruments, each tailored to specific experimental parameters. Consequently, three distinct instruments were employed: one for hydrogen adsorption at 40K and up to 1 bar, another at 77K, 87K and up to 1 bar, and a third for measurements at 298K and up to 120 bars. The skeletal or dead volume (i.e. taken up by the material itself, excluding the volume of any internal pores) are measured using inert gas helium (measurement known as pycnometry) prior to adsorption experiments.

- Sorption at 40K – 1bar

H_2 and D_2 adsorption isotherms (~ 700 mg / sample filled in aluminum cylindrical cell) were measured at 40K using an Orange cryostat (operating range: 1.5K - 500K) with a temperature regulation accuracy of ± 0.03K.

A Hiden Isochema IMI Sievert apparatus, equipped with a low-pressure sensor ranging from 0 to 1 bar with an accuracy of 0.2% of the maximum pressure, was used to dose H_2 and D_2 (purity 99.99%) into the system. These measurements were conducted using the setup (Figure II.9) designed by Simon Baudoin at Institut Laue-Langevin (Grenoble, France).

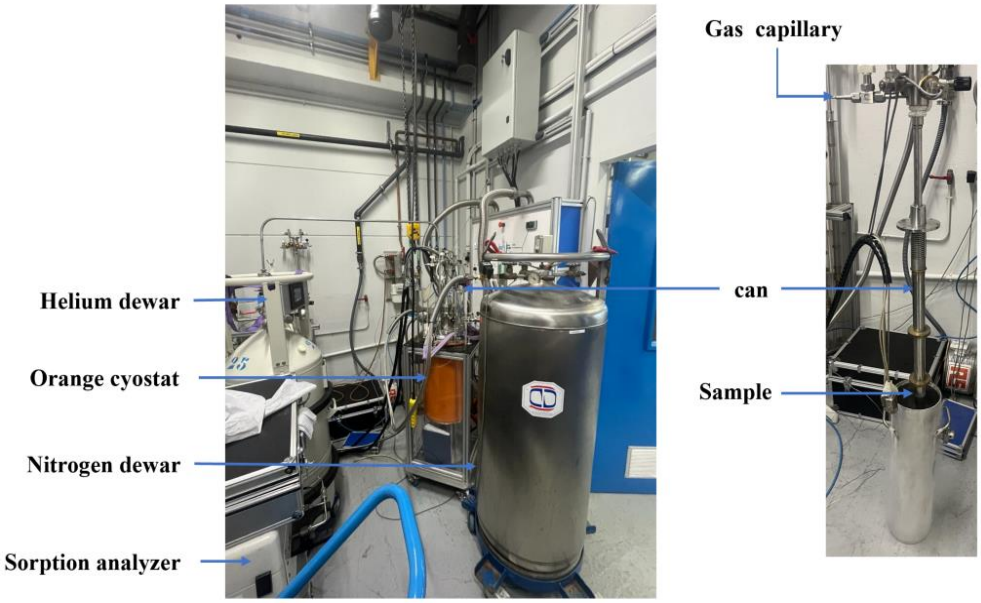

Figure II.9: Adsorption setup for H_2 and D_2 at 40K and 1 bar. This setup includes an orange cryostat for precise temperature control and a Hiden Isochema IMI Sievert apparatus for low-pressure dosing of gases.

- Sorption at 77K – 1bar

H_2 adsorption/desorption isotherms (approximately 200 mg/sample) were measured with the help of Valérie Magnin using the same ASAP 2020 PLUS volumetric gas sorption instrument from Micromeritics Instruments® at Institut des Sciences de la Terre (Grenoble, France) for N_2 isotherm (Figure II.7). The measurements were conducted at 77 K using liquid N_2 as the cryogen. The relative pressure range for the measurements was from 10^{-6} to 0.01 bar in 6 steps, and from 0.01 to 1 bar in 19 steps for adsorption and 10 steps for desorption. To reduce the dead volume of the sample cell, non-porous glass filler rods were inserted and assessed using He (purity 99.99%) gas before each run.

- Sorption at 298K – 100bar

High-pressure hydrogen experiments were performed by Patricia de Rango at 298 K and 100 bars using a PCT Hiden® IMI system apparatus at Institut Néel – CNRS (Grenoble, France). Approximately 400 mg of powdered samples were placed in a steel sample holder with an internal volume of about 200 mm^3, which included a small amount of glass wool to prevent powder loss during vacuuming. Adsorption and desorption isotherms were obtained with an equilibration time of 15 to 30 minutes for routine analysis.

The hydrogen uptake measured in an adsorption isotherm is plotted as a function of the equilibrium pressure and analyzed by fitting them using an appropriate model. For that used models in this manuscript are described below:

Low coverage adsorption

Low coverage adsorption is considered when the system is characterized by extremely low concentrations of adsorptive gas molecules. Under these conditions:

- There are no significant interactions between the adsorbed molecules.
- The adsorption behavior can be described by an equation similar to the ideal gas law.
- The initial region of the adsorption isotherm is linear, indicating that the amount of gas adsorbed is directly proportional to the pressure.

This relationship can be expressed using Henry's law, which is given by the equation:

$$\boldsymbol{n_a = K_H(T) \cdot p} \qquad \textbf{(II.7)}$$

where n_a represent the uptake, $K_H(T)$ is the Herny's constant (i.e. energetic constant that depends only on temperature).

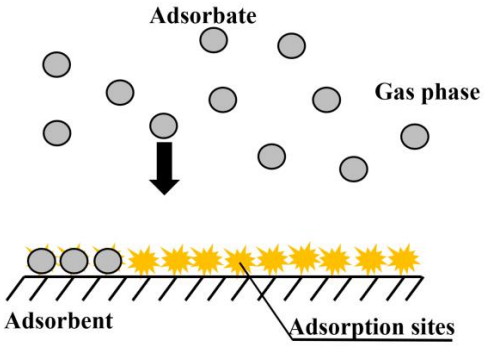

Figure II.10: The adsorption mechanism revealed by the linear model, adapted from [101].

Langmuir model

The simplest and most-widely used model to represent the gas-solid adsorption being the Langmuir model (*Langmuir, 1918*), describing a monolayer coverage occurring at homogenous sites on the surface of solid adsorbent material. In this model there is several assumptions:

- All adsorption sites are energetically equivalent.
- Each adsorption site present on the surface can be occupied by one entry.
- Heat of adsorption is constant and independent of the degree of surface coverage.
- There is no interaction between adsorbate molecules occupying at different sites.

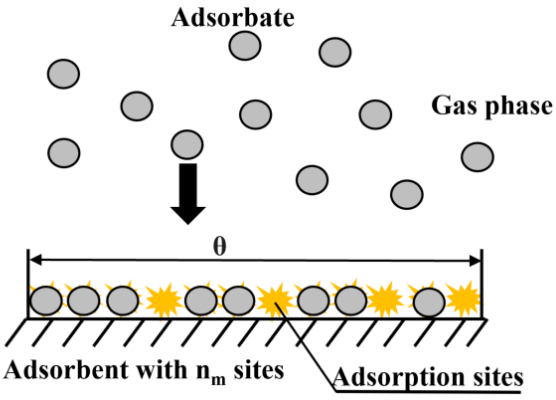

Figure II.11: The adsorption mechanism revealed by Langmuir isotherm model, adapted from [101].

The function of fractionally occupied sites θ can be expressed as:

$$\boldsymbol{\theta = \frac{n_a}{n_m} = \frac{bp}{1 + bp}} \qquad \textbf{(II.8)}$$

where n_m is the total number of sites which can be occupied in the monolayer (i.e., uptake at saturation) and coefficient b (bar^{-1}) represent the affinity constant of Langmuir isotherm which

reflects the strength of adsorptive substrate binding and its turn as temperature dependent, which can be expressed as:

$$b = b_{\infty}\left(\frac{-\Delta H_{ads}}{RT}\right) \qquad \textbf{(II.9)}$$

where b_{∞} represent the maximum affinity constant and ΔH_{ads} being the binding enthalpy.

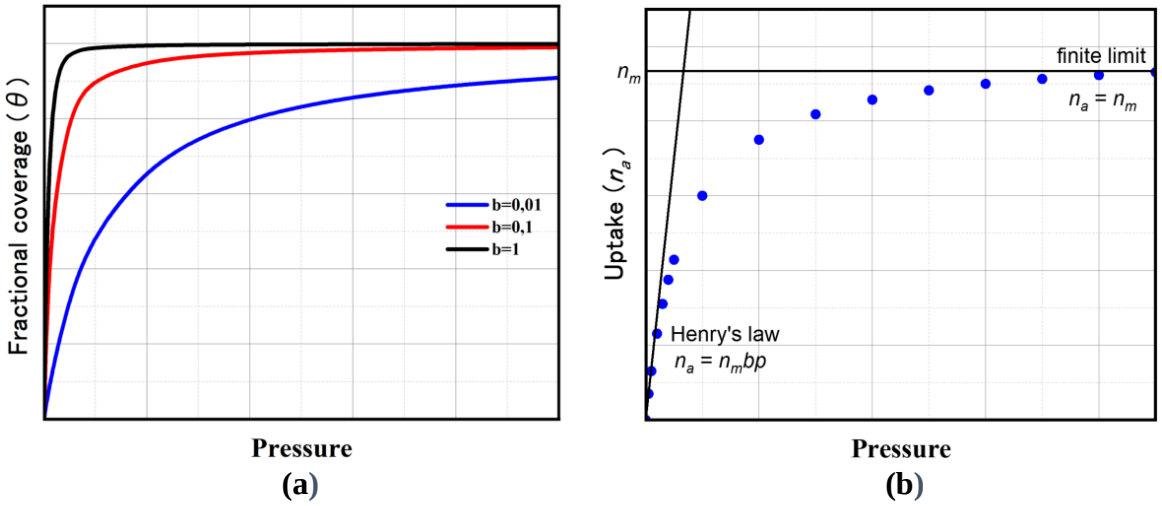

Figure II.12: (a) Schematic illustration of the Langmuir model for three different affinity constants. Fractional coverage (θ) versus pressure: the black curve represents b=1, indicating a higher adsorption affinity; the red curve represents b=0.1, indicating intermediate adsorption affinity; and the blue curve represents b=0.01, indicating lower adsorption affinity. (b) Uptake (n_a) versus pressure: For b=0.01, the plot highlights two distinct regions—Henry's law ($n_a = n_m bp$) and the finite limit ($n_a = n_m$).

Figure II.12(a), represent the fractional coverage versus pressure**,** clearly shows how the curvature of the isotherm is affected by the affinity constant, taking the example of low (b=0.01), intermediate (b=0.1), and high (b=1). It is noteworthy that at very low pressure ($bp \ll 1$), the Langmuir model conforms to Henry's law. However, at sufficiently high pressure ($bp \gg 1$), the model predicts a finite limit for the amount adsorbed as shown in Figure II.12(b).

Freundlich model

Another widely used model for adsorption is the Freundlich model, which is commonly applied to adsorption in zeolites [103] and the adsorption of pesticides in clay minerals [104]. The Freundlich model is reliable for interpreting adsorption beyond one layer considering both the heterogeneity of adsorption sites and the tendency for the ΔH_{ads} to decrease exponentially with coverage. Its non-linear form can be expressed as:

$$n_a = K_F p^{1/n} \qquad \textbf{(II.10)}$$

where K_F is the Freundlich constant, and n is an empirical constant related to the heterogeneity of the adsorbent surface, where $n \approx 1$ indicates homogenous adsorbent surface, while n > 1 indicates a heterogenous surface. This model does not exhibit saturation at high pressure and does not obey Henry's law at low pressure, unlike the Langmuir model.

The values of n and K_F can be obtained by plotting the linear form of Equation (II.10):

$$\boldsymbol{log\, n_a = log\, K_F + \frac{1}{n} log\, p} \qquad \textbf{(II.11)}$$

By plotting $log\, n_a$ versus $log\, p$, $^1/_n$ represent the slope while K_F represents the y-intercept.

The choice of model for fitting the experimental data is crucial for understanding the underlying adsorption mechanisms and for quantitatively comparing the adsorption quantities of different gases (H_2 and D_2) on various adsorbents (pre-Laponite and Laponite). However, when calculating the isosteric enthalpy of adsorption, the primary concern is how accurately the model can extrapolate data between the measured points, particularly at low pressure range.

4. X-ray scattering

X-ray scattering is a powerful technique for probing the atomic and molecular structure of materials. X-rays are a form of transverse electromagnetic radiation with wavelengths typically ranging from 1 to 0.01 Å, comparable to the inter-atomic distance. This wavelength allows X-rays to interact with the atomic structure of a material, creating interference patterns that reveal detailed structural information.

When X-rays are directed at a material, they can be scattered in two primary ways: elastic (Thomson) scattering and inelastic (Compton) scattering. In elastic Thomson scattering, the photons remain coherent, which provides crucial structural information about the material. In contrast, inelastic Compton scattering involves a change of the state of the atoms which with the photon, they are in excited state and photons which give part of their energy to the atoms are no more coherent. The theory behind elastic X-ray scattering, which is essential for understanding structural properties and differences of pre-Laponite and Laponite, will be briefly discussed below. This subsection will cover the key concepts, but for readers interested in more in-depth information, reference [105] is recommended.

5.1. Scattering theory

In elastic scattering, scattered photons interfere with each other, and the relationship between their wave-vectors is crucial to understand the scattering process. The scattering vector $\vec{Q}$ is defined as the difference between the wave-vectors of the scattered $\vec{k'}$ and incident $\vec{k}$ X-rays:

$$\vec{Q} = \vec{k'} - \vec{k}, \qquad \|\vec{k}\| = \|\vec{k'}\| \tag{II.12}$$

This vector relationship is illustrated in Figure II.13(a), which shows the construction of the Ewald sphere.

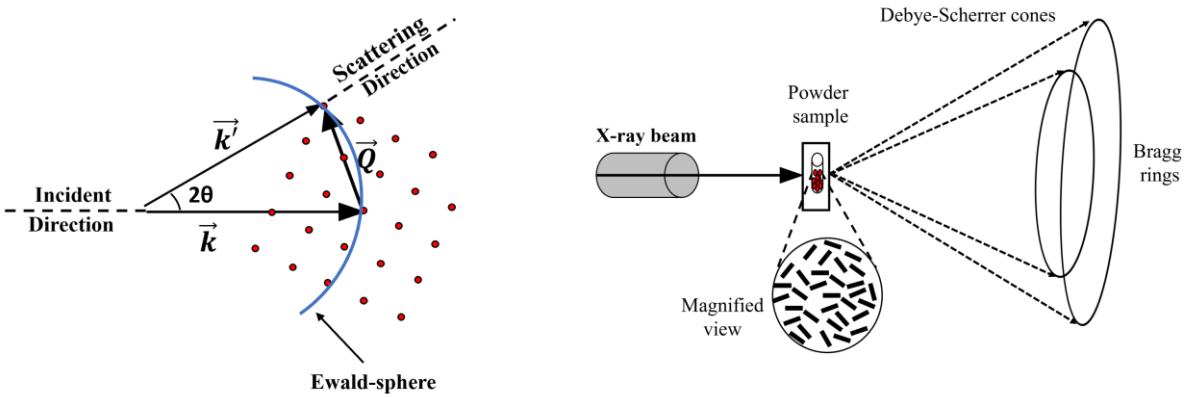

(a) **(b)**

Figure II.13: (a) The Ewald sphere is a sphere of radius k, the origin which is the sample; the origin of the reciprocal space is the intersection of the Ewald sphere with the incident X-ray beam. In the figure, the vector $\vec{k}$ represents the incident direction of the X-ray, while $\vec{k'}$ represents the scattered direction, and $\vec{Q}$ is the scattering vector. We take here the example of single-crystalline sample. Observable Bragg peaks are those which intersect the Ewald sphere. (b) Example of what is observed in powder diffraction: angularly averaged lattice points give rise to concentric circles around the origin of reciprocal space. Their intersection with the Ewald sphere leads to scattering cones, giving rise to rings on a two-dimensional detector.

The magnitude of the scattering vector $\vec{Q}$ can be related to the scattering angle θ using Bragg's law:

$$Q = \frac{4\pi}{\lambda} \sin\theta \tag{II.13}$$

where, λ is the incident (scattered) wavelength.

Experimentally the X-ray scattering pattern is represented by the scattered intensity $I(\vec{Q})$, which is proportional to the square of the amplitude of the scattered wave:

$$I(\vec{Q}) \propto \left|A(\vec{Q})\right|^2 \tag{II.14}$$

The amplitude $A(\vec{Q})$ of the scattered wave can be described as the sum of contributions from all atoms in the scattering object:

$$\boldsymbol{A(\vec{Q}) = \sum_{i=0}^{N} f_i\,(Q) e^{-i\vec{Q}\cdot\vec{r_i}}} \qquad \textbf{(II.15)}$$

Here, $f_i(Q)$ is the atomic form factor, which is the Fourier transform of the electronic density of the atom. The atomic form factor decreases with the increasing scattering vector $\vec{Q}$.

5.2. X-ray – matter interaction

Understanding X-ray scattering related to the crystal structure, which is defined by its unit cell. The elementary unit cell is the smallest repeating unit in a crystal lattice and is described by three vectors, $\vec{a}$, $\vec{b}$ and $\vec{c}$ which provides the cell's shape, size and orientation in space. The atomic positions within the unit cell are defined relative to these basis vectors, and their periodic repetition forms the entire crystal structure. The periodic nature of the crystal lattice implies that any atomic position in the lattice can be represented as a linear combination of the unit cell vectors, such as:

$$\boldsymbol{\vec{R}_{n_1,n_2,n_3} = n_1\vec{a} + n_2\vec{b} + n_3\vec{c}} \qquad \textbf{(II.16)}$$

where n_1, n_2 and n_3 are integers. In addition to the direct lattice we may defined the reciprocal lattice, described by the dual basis of the direct lattice vectors $\vec{a^*}$, $\vec{b^*}$ and $\vec{c^*}$. They are defined as follows:

$$\boldsymbol{a^* = \frac{b \times c}{a \cdot (b \times c)}, \qquad b^* = \frac{c \times a}{a \cdot (b \times c)}, \qquad c^* = \frac{a \times b}{a \cdot (b \times c)}} \qquad \textbf{(II.17)}$$

The Bragg peak positions are given by:

$$\boldsymbol{\vec{Q}_{h,k,l} = h\vec{a^*} + k\vec{b^*} + l\vec{c^*}} \qquad \textbf{(II.18)}$$

with h, k and l integers. A crystal can be viewed as the convolution products between the lattice defined by its unit cell and the atomic positions within a unit cell. Thus, the amplitude is the product of the form factor (Fourier transform of the unit cell) and the Fourier transform of direct lattice positions, and the intensity writes:

$$\boldsymbol{I(\vec{Q}) = \left|F(\vec{Q})\right|^2 \cdot S(\vec{Q})} \qquad \textbf{(II.19)}$$

For a crystal with infinite dimension, the structure factor represents a sum of delta functions located at the Bragg peaks, then its amplitude is given by:

$$I(\vec{Q}) = \left|\sum_{i=0}^{N} f_i(Q) e^{-i\vec{Q}\cdot\vec{r_i}}\right|^2 \cdot \sum_{hkl} \delta(\vec{Q} - \vec{Q}_{hkl}) \qquad \textbf{(II.20)}$$

Finally, in the case of powder samples, where the material is composed of randomly oriented crystallites, the scattering pattern on a two-dimensional detector placed after the sample consists of concentric rings, (Figure II.13(b)) rather than discrete Bragg peaks, as the reciprocal lattice points are angularly averaged.

5.2.1. Experiments on MORPHEUS platform at LPS

To conduct X-ray scattering measurements in the laboratory, MarCu (Figure II.14(a)) instrument was used on the MORPHEUS platform (https://equipes2.lps.u-psud.fr/matrix/morpheus/) at the Laboratoire de Physique des Solides (Orsay-France). The X-ray are generated by a copper (Cu) rotating anode (Micromax007, Rigaku Corp., Japan).

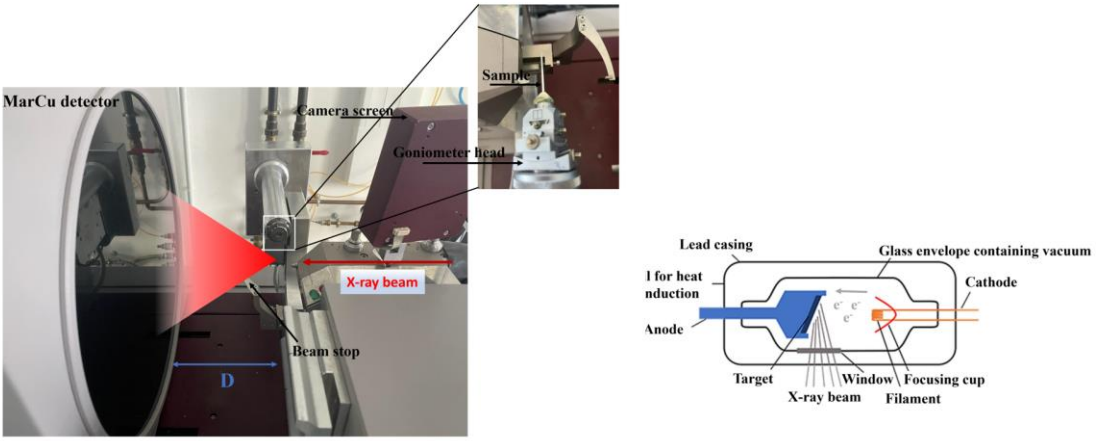

(a) **(b)**

Figure II.14: (a) Image of the MarCu diffractometer located at MORPHEUS platform – LPS, (b) An X-ray tube consists of a cathode (filament where the electrons are coming from), an anode (where the electrons are stopped) and a high voltage in between to accelerate the electrons under a vacuum, adapted from [106].

Since the first X-ray tube was developed by Coolide in 1913 [107], the basic operating of X-ray sources has remained relatively unchanged. X-rays are generated using a sealed-tube source, under vacuum, where electrons driven by a potential difference, collide with a metal anode (Figure II.14(b) for clear visualization).

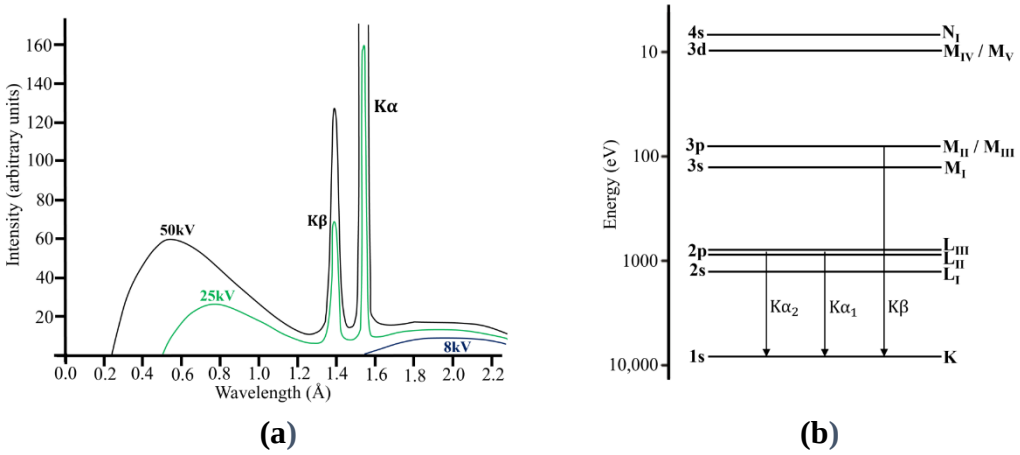

Figure II.15: (a) Typical spectrum emitted from a Cu anode and (b) energy level diagram for a copper atom, adapted from [108].

This collision triggers a series of electronic transitions for the atoms of the target material, releasing electromagnetic radiation as they return to their ground state. However, to manage the heat produced, anodes have been designed as cylinders rotating on their axis (rotating anode). The anode material needs to be an efficient conductor of electricity and heat, with a sufficiently high melting point. Copper is one of the most commonly used target elements. This type of X-ray sources operates at typical voltages of 40-50 kV and electric current of 40-150 mA. The typical spectrum emitted by a Cu anode is shown in Figure II.15**.**

The discrete peaks, known as the "characteristic radiation" of the material, occur due to the ejection of an electron from one of the inner electron's shells of the metal atom: an electron of an outer shell falls into the inner shell, emitting a quantized photon characteristic of the metal use for the target**.** During the experiment, the monochromaticity of the X-ray beam in this setup is ensured by a W/Si multilayer optic (Osmic), which produces a convergent X-ray beam. The slits integrated into the Mar diffractometer provide a beam with a cross-section of approximately 0.4 mm^2. This instrument enables users to easily modify several parameters, such as the exposure time and sample-to-detector distance D. It is worthy to note that the resolution presented in Table II.2 was calculated using a Gaussian fit of the Bragg peaks of a quartz sample placed in a 1 mm glass capillary at distance D=100 mm, the sample-to-detector distance used for the experiments. The resolution is represented by the full width at half maximum (FWHM) of the Gaussian peak fit.

Table II.2: Key parameters of the MarCu diffractometers, where λ is the wavelength of the X-rays used. P_x is the pixel size of the circular detector with radius R. D is the sample-to-detector distance. Q_{min} and Q_{max} provide an estimate of the achievable wavevector range.

Properties	**Value**	
λ [Å^{-1}]	1.5418	
P_x [mm]	0.15	
R [mm]	172.5	
	D_{min}	D_{max}
D [mm]	50	350
Q_{min} [Å^{-1}]	0.4	0.05
Q_{max} [Å^{-1}]	4.9	1.8

Scattering images were collected from powder samples filled in 1 mm glass capillaries, which were preheated at 150°C for 6 hours under primary vacuum to remove absorbed water, then sealed. These measurements were carried out with sample-to-detector distance of 100 mm, a beam stop positioned 15 mm from the sample, and an exposure time of 30 minutes. The resulting image was isotropic, consisting of concentric circles at constant Q. The image was then radially integrated to produce a one-dimensional diffraction pattern using a house-made software "IMAGE", after beam centering using another house-made script (Figure II.16 (a)).

$$\boldsymbol{Q = \frac{4\pi}{\lambda}\sin\left(\frac{1}{2}\tan^{-1}\left(\frac{r \cdot pix}{D}\right)\right)} \qquad \textbf{(II.21)}$$

where λ is the wavelength of the incident beam, r is the radial distance on the detector in pixels, and *pix* is the pixel size of the detector.

After obtaining the one-dimensional pattern, background corrections were applied:

$$\boldsymbol{I(\vec{Q})_s = \frac{I(\vec{Q})_m + I(\vec{Q})_{Sn}(T_s - 1)}{T_s T_H} - \frac{I_H}{T_H}} \qquad \textbf{(II.22)}$$

Where $I(\vec{Q})_s$ is the intensity scattered by the sample, $I(\vec{Q})_m$ is the measured intensity (sample + capillary) normalized to the flux, $I(\vec{Q})_{Sn}$ is intensity measured from a 1 mm diameter tin wire used as an absorber to detect bypass-sample X-ray, I_H is the intensity from the empty capillary (1 mm), T_s and T_H are the transmissions of the sample and the empty capillary, respectively, measured by placing a photodiode in front of the detector.

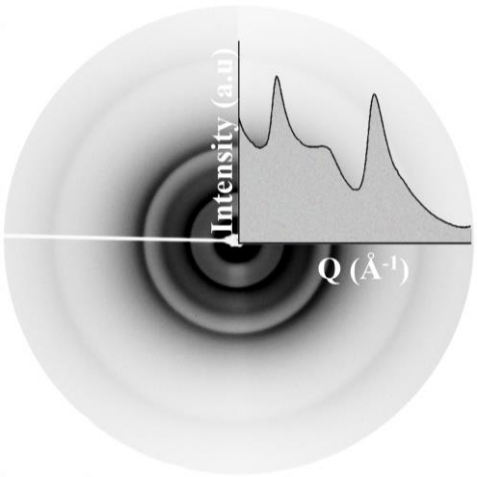

Figure II.16: Example of a two-dimensional X-ray scattering pattern obtained by Image Plate MAR detector, along with a corresponding one-dimensional scattering profile (shown in gray), obtained through radial integration of the two-dimensional data.

After background correction, three other corrections are applied:

- Geometric correction: the intensity is divided by $\cos^3(2\theta)$ as we use a planar detector, which cause intensity distortion.
- Polarization correction: the intensity is divided by $\frac{1+\cos^2(2\theta)}{2}$**.** This correction accounts for the unpolarized character of the X-rays emitted by the anode. It's simple from results from the low diffraction angle on the multilayer optics.
- Absorption correction: this correction accounts for the absorption of X-rays in the air behind the sample. The intensity is divided by $A = e^{-\mu * D(-1+\frac{1}{\cos(2\theta)})}$, where μ is the linear attenuation coefficient, which for CuK_α radiation is 0.012 cm^{-1} [109].

Directly comparable to the intensity calculated from the fundamental formula (II.14) and (II.15) or equivalent ones such as the Debye formula for powders (see **Chapter III**) convoluted to the experimental resolution.

5.2.2. Experiment on CRISTAL at SOLEIL

X-ray scattering experiments were conducted on Laponite (and pre-Laponite) samples on CRISTAL beamline at SOLEIL, specifically to access a wider Q-range for PDF analysis, which will be discussed in next subsection.

A synchrotron is a particle accelerator designed with a storage ring that houses multiple experimental stations, known as beamlines. In this setup, electrons are initially accelerated to an energy of 100 MeV in a 16-meter-long linear accelerator known as the LINAC. They are then directed to secondary circular accelerator, the Booster, where their energy is increased to

2.75 GeV. At this step, the electrons are injected to 354-meter storage ring, where magnetic fields from bending magnets regularly alter their paths. As the electrons move between these magnets they traverse through devices called undulators and wigglers, which are linear arrays of dipole magnets arranged in an alternating polarity pattern. The magnetic fields produced by these devices cause the electrons to follow a wavy, sinusoidal path, leading to the emission of X-rays [110]. Therefore, the resulting beam has more favorable characteristics than that produced by a rotating anode:

- Brilliance: defined as the flux of photons per solid angle per area of the source and per bandwidth in energy, which is 10^{12} times higher for a synchrotron undulator or wiggler than for a rotating anode.
- Source pulsed: emits isolated pulses of radiation as the electrons circulate in packets within storage ring, enabling time-resolved measurements.
- Wide spectral range: ranging from infrared (a few hundred μeV) to hard X-rays (100 keV). Therefore, "white source" experiment can be performed.
- Polarized: controlled and can be set to linear, circular or elliptical.

CRISTAL beamline uses a U-20 undulator as the source and features a Si(111) double-crystal monochromator to adjust the X-ray beam energy between 4 and 30 KeV, with an energy resolution of approximately, $\Delta E/E \sim 10^{-4}$. The system includes three different diffractometers – six-circle, four-circle, and two-circle – designed for studying both monocrystals and polycrystalline materials. Powder diffraction was carried out using the two-circle diffractometer, where the detection unit comprises a 21-crystal (Si(111)) analyzer followed by a fast YAP(Ce) scintillation detector (Scionix), all mounted on a motorized rotation stage for precise measurement of scattered intensity as a function of the 2θ angle (Figure II.17).

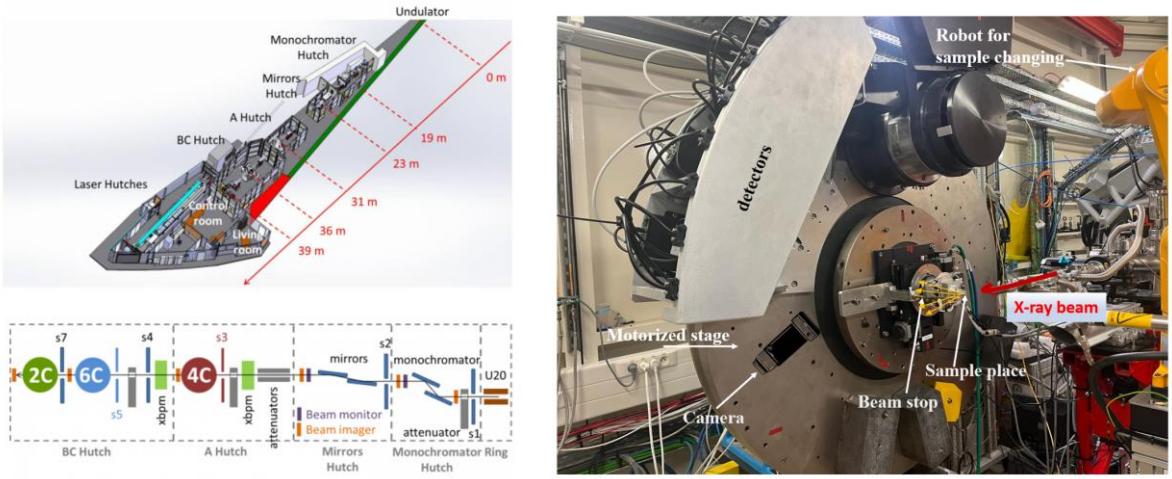

(a) **(b)**

Figure II.17: (a) schematic 3D view of the CRISTAL beamline setup at SOLEIL synchrotron [111]. (b) image of the experimental setup.

Data on Laponite (and pre-Laponite) samples were collected with the help from Erik Elkaim. The samples were prepared in 1 mm glass capillaries and after drying at 150°C for 6 hours. A wavelength of 0.51344 Å was used, determined by reference sample, LaB6 (Lanthanum hexaboride), with a well-known lattice parameter. Transmission were recorded, within 3 steps at 0.001s per step, and diffraction patterns were measured over 20 minutes per sample while the capillaries were rotating on themselves. The obtained data were only corrected from background using Equation (II.22), with no geometric or absorption corrections are needed as the detector moves in a circle, and no polarization correction is required since the polarization lies in the scattering plane

5.3. Pair distribution function

Analyzing the structural differences between Laponite and pre-Laponite present a significant challenge, as deviation from the average structure – such as disorder, defects, and nanostructures – often give rise to unique properties. Understanding these structural features is crucial for explaining the relationship between structure and adsorption properties. However, this is difficult to achieve using traditional crystallography, which only offers an average crystal structure over the entire sample (i.e., global structure). This limitation has led to increase interest in the pair distribution function (PDF), as it is sensitive to structural information across short-, medium-, and long-range (include the one giving rise to diffuse scattering and not to Bragg peaks), and this explains why, PDF is particularly valuable in studying amorphous materials, where diffuse scattering plays a greater role compared to well-ordered single crystals, where it is minimal. The PDF reflect the ratio between the number of atoms at a distance r from

any atom $p(r)$ and the average number density of atoms in the system p_0. The PDF can be expressed mathematically as follow [112]**:**

$$\boldsymbol{g(r) = \frac{p(r)}{p_0} = \frac{1}{4\pi r^2 N \rho_0} \sum_i \sum_{j \neq i} \delta(r - r_{ij})} \quad \textbf{(II.23)}$$

Here, $4\pi r^2$ accounts for the shell volume, r_{ij} is the distance between the *i*th and *j*th atoms, *N* is the total number of atoms, and δ is a Dirac delta function representing the position of atoms as a function of r.

While $g(r)$ is the fundamental term to understand local structure. However, the experimentally obtained quantity is the reduced PDF**,** $G(r)$, which is defined as:

$$\boldsymbol{G(r) = 4\pi r \rho_0 [g(r) - 1]} \quad \textbf{(II.24)}$$

$G(r)$ contains a wealth of structural information, where peak position reflects atomic distances, or 'bond length', in real space, peak areas represent the abundance of relevant atomic pairs weight by their scattering power and peak widths are related to the disorder of relevant atomic pairs. The maximum atomic distance at which peaks are observable gives insight into the size of the coherent domain in the material, which indicates the average particle size.

$G(r)$ can be obtained experimentally through the Fourier transform of the structure factor[11] $S(Q)$ which is defined as:

$$\boldsymbol{S(Q) = 1 + \frac{I(Q) - \sum c_i |f_i(Q)^2|}{|\sum c_i f_i(Q)|^2}} \quad \textbf{(II.25)}$$

$$\boldsymbol{G(r) = \frac{2}{\pi} \int_{Qmin}^{Qmax} Q\,[S(Q) - 1] \sin(Qr) dQ} \quad \textbf{(II.26)}$$

However, to achieve a good resolution for $G(r)$, $S(Q)$ must be measured over a wide range of Q, with a $Qmax$ as large as possible, as the resolution determined by the equation $\Delta r = {2\pi}/{Qmax}$ [113]. Figure II.18 displays the PDF as function of *r*, highlighting the first coordination shell (nearest neighbor). As r increases, $p(r)$ oscillates and gradually approaches the average number density, p_0.

[11] *The structure factor used here differ from that defined in equation(II.19), as the structure factor can be found to be used in different ways.*

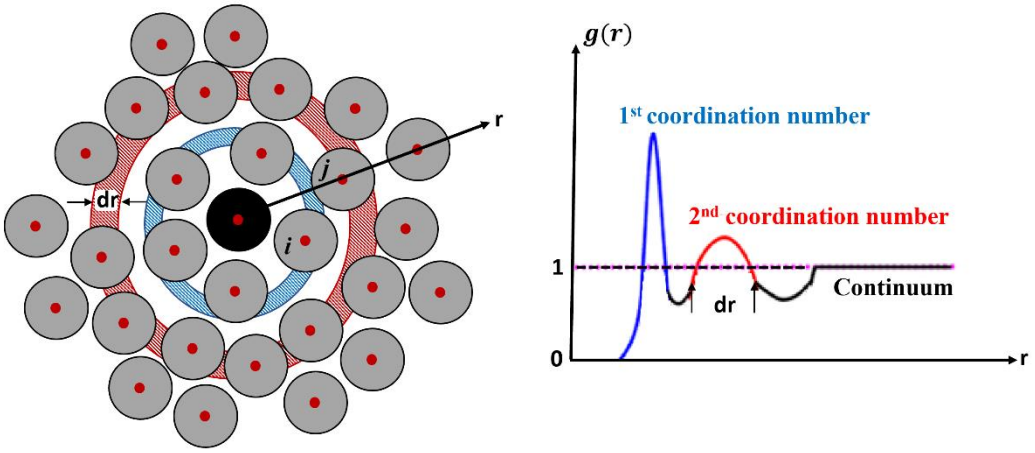

Figure II.18: Schematic representation of the pair distribution function, $g(r)$, illustrating its dependence on the distance r from a reference particle. The figure shows the first and second coordination shells and the transition to the continuum, highlighting how $g(r)$ varies with increasing distance, adapted from [114].

6. X-ray Absorption Near Edge Spectroscopy

When X-rays hit the sample, they interact with the electrons in the material, providing insights into its electronic properties. According to the Beer-Lambert law, the percentage of the transmitted beam is given by:

$$\frac{I}{I_0} = e^{-\mu(E)\cdot l} \qquad \textbf{(II.27)}$$

where I_0 and I are the intensities of the incident and the transmitted beam, respectively, l is the sample thickness and $\mu(E)$ is the energy – dependent linear absorption coefficient of the sample

X-ray Absorption Near Edge (XANES) measures the absorption coefficient, $\mu(E)$, as a function of energy near an absorption edge of a type of atom in a material. The energy range for XANES spectra typically extends up to 50 eV after the edge. In contrast, Extended X-ray Absorption Fine Structure (EXAFS) covers the energy range from approximately 50 to 2000 eV after the edge.

The principle behind XANES is that by tuning the incident beam's energy through the absorption edge one gets to excite a core electron to an empty electronic state. This process is both chemically specific, as each atomic species has well defined core level binding energies, it is sensitive to the orbital characteristics of the electron. Therefore, XANES is sensitive to the local symmetries and electronic structure around the absorbing atom.

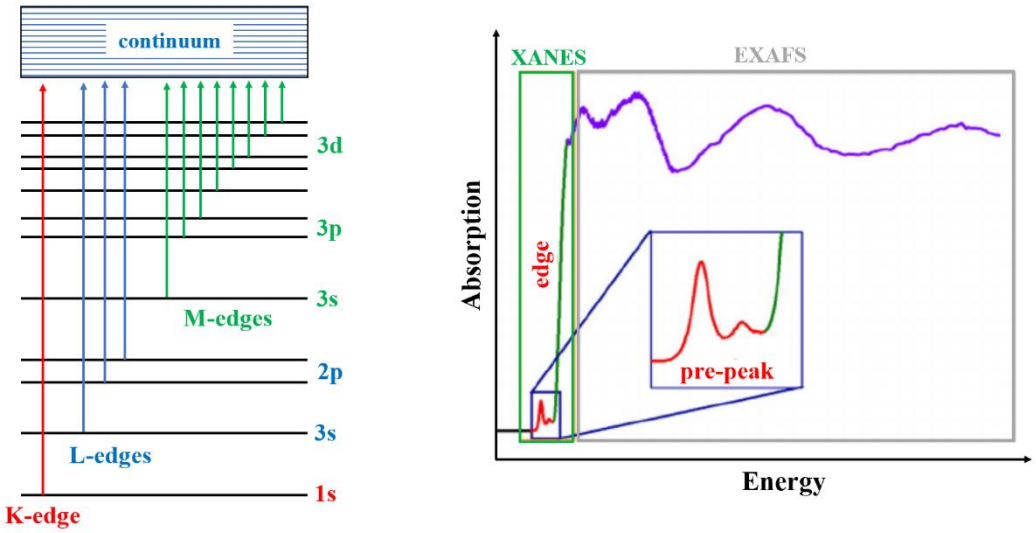

Figure II.19: (a) schematic representation of the transition resulting from the excitation of a core electron and corresponding XAS edges. (b) X-ray absorption spectrum showing the XANES including the pre-edge feature and EXAFS region, adapted from [115].

The nomenclature of XANES reflects the core level from which the electron originates. For example: K-edge corresponds to the transition from a 1s core orbital, L-edges correspond to 2s and 2p levels, and M-edges to 3s, 3p and 3d levels as shown in Figure II.19(a). The XANES region as shown by Figure II.19(b), shows two characterized features: sharp increase in absorption, which result from the ejection of a core electron and the pre-edge peak, which originates from the transitions to empty molecular orbitals localized on the photo absorber. In this study, only XANES was used to analyze the samples using LUCIA beamline at SOLEIL synchrotron, focusing on the fine details of the structural environment near the absorbing edge.

6.1. Experiment on LUCIA

The LUCIA (Line for Ultimate Characterization by Imaging and Absorption) beamline at the SOLEIL synchrotron, facilitating X-ray microabsorption and microfluorescence experiments within the "tender" X-ray energy range (0.8 – 8 keV). This energy range enables the investigation of K-edges of elements from sodium to iron, L-edges from nickel to gadolinium, and M-edges of rare earth elements and actinides.

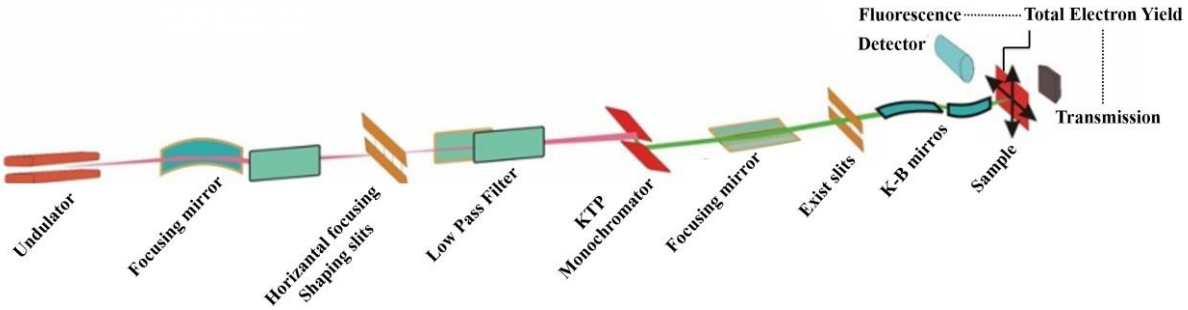

Figure II.20: Schematic representation of the operating principle of the LUCIA beamline at synchrotron SOLEIL.

LUCIA working principle can be understood by following the schematic provided in Figure II.20. The process begins with the generation of X-rays by an undulator, which produces the X-ray beam from the synchrotron storage ring, then the emitted X-ray beam is firstly focused by a spherical mirror and further shaped by horizontal focusing slits. However, to ensure the required monochromaticity of the beam, a low-pass filter and a KTP monochromator crystal are used to filter the X-ray wavelengths to the desired energy range.

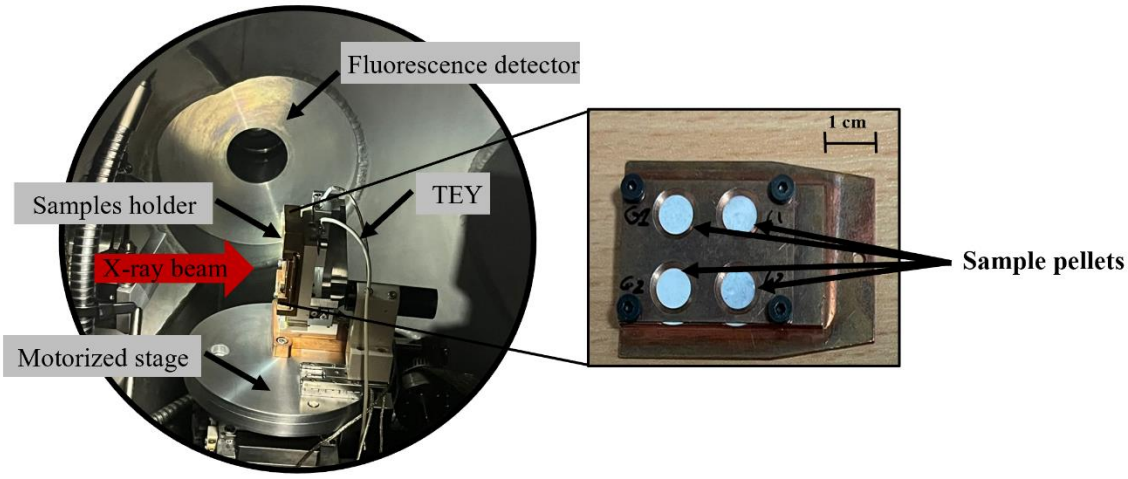

Figure II.21: Experimental setup on the LUCIA beamline. The image on the left shows the sample holder mounted on the motorized stage with incident X-rays directed at the sample (red arrow). The fluorescence detector is positioned to capture emitted X-rays. The image on the right displays the 1 cm sample pellets affixed to the sample holder.

Subsequently, the monochromated X-ray beam undergoes a final stage of focusing using a combination of focusing mirrors, slits, and a Kirkpatrick-Baez (K-B) mirror system, thereby achieving a beam with a cross-section of approximately 3 µm × 3 µm. This finely focused beam is then directed onto the sample. Detectors positioned around the sample capture the transmitted X-ray beam, fluorescence signals, and total electron yield (TEY) generated by the Auger effect (it is the phenomena in which the filling of an inner-shell vacancy of an atom is accompanied by the emission of an electron from the same atom).

In this manuscript, clay samples (~40 mg) were mixed with 4 mg of cellulose powder and pressed under 2 tons to form 1 cm diameter pellets, which were held between two molybdenum plates (see Figure II.21) for the measurements at magnesium and silicon K-edges.

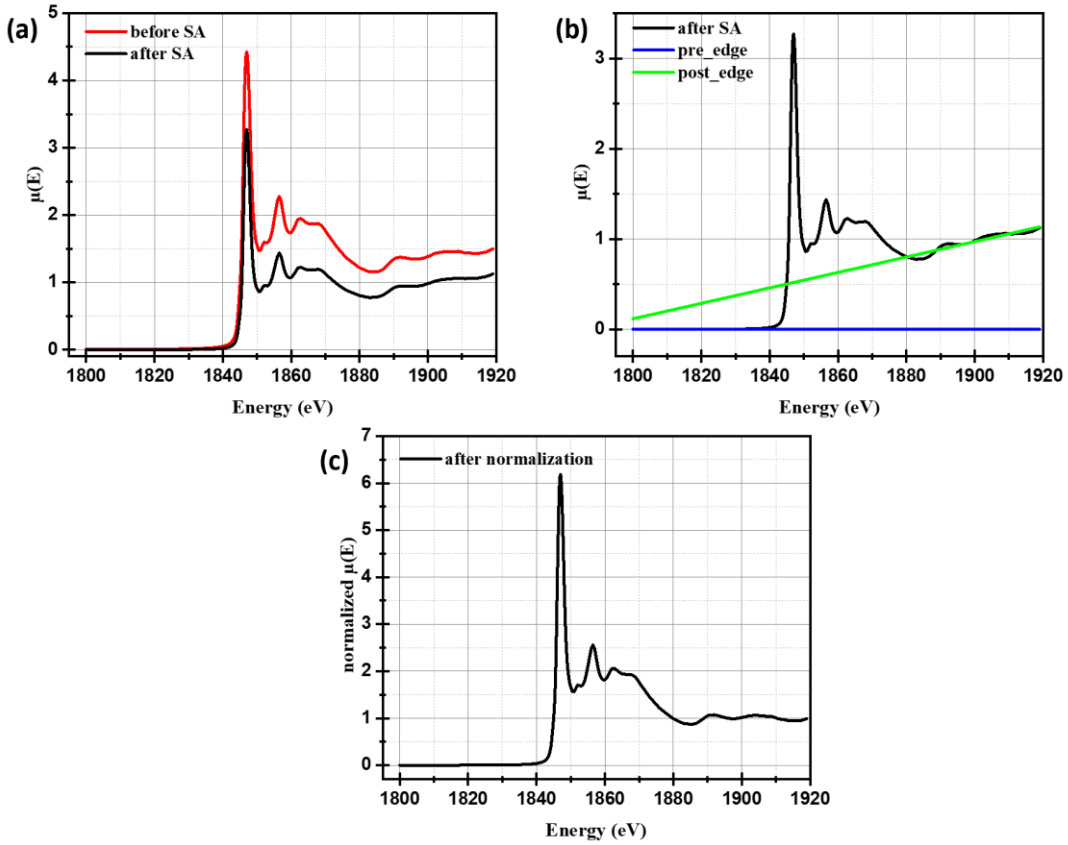

Figure II.22: (a) Si k-edge absorption coefficient determined from fluorescence measurements before (red curve) and after (black curve) self-absorption correction, illustrating the impact of the correction process. (b) Pre-edge (blue line) and post-edge (green line) baselines applied for background correction. (c) Normalized spectrum after background correction.

The XANES spectra were recorded under secondary vacuum over an energy range of 1280–1400 eV for the Mg K-edge and 1800–1920 eV for the Si K-edge. The data shown in Figure II.22 were processed after data summation, self-absorption correction, and background normalization following the guidelines provided in the Athena software documentation.

7. Neutron scattering

Neutron spectroscopy is an ideal technique for examining the quantum effects, discussed in **Chapter I**, **§2.3**, of dihydrogen physisorbed onto a solid surface, providing insights into the potential energy surface (interaction and symmetry) around the adsorption sites. Neutrons beams are made available to the scientific community at different facilities around the world

(see the list in Figure II.24). Producing neutron can be achieved through either spallation or fission as shown in Figure II.23 .

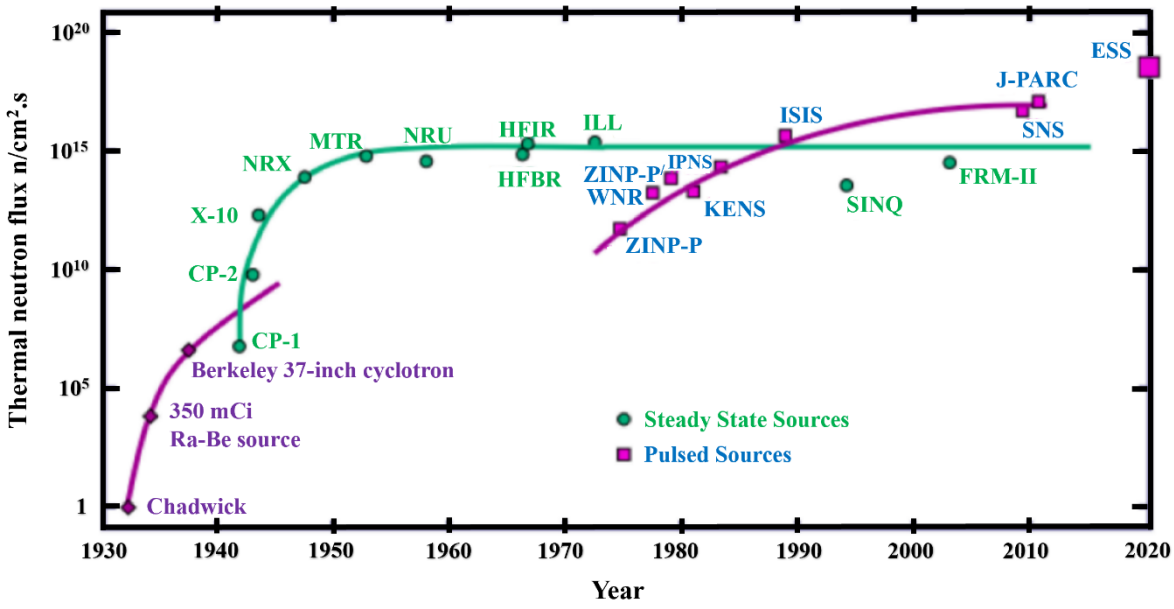

Figure II.23: Thermal neutron flux by pulsed and steady sources, since the discovery of neutron in 1932 by James Chadwick, adapted from [116] .

- **Fission:** A continuous flux of neutrons is produced when a thermal neutron is absorbed by a meta-stable nucleus, such as ^{235}U (used at ILL), which then decays and emits, on average, three neutrons. One of these emitted neutrons sustains the chain reaction, generating more neutrons, while the others contribute to beam production across different beamlines.
- **Spallation:** Neutron pulses are produced when a high-energy proton, generated by an accelerator, hit a target of heavy atoms such as *U*, tungsten (W), or mercury (Hg). Upon collision with the nucleus, the proton generates several dozens of neutrons with energies of a few MeV. By thermalizing these neutrons, a wide range of neutron energies can be produced, suitable for different types of experiments. Facilities like ISIS in the United Kingdom and the upcoming European Spallation Source (ESS) in Sweden use this method for neutron production.

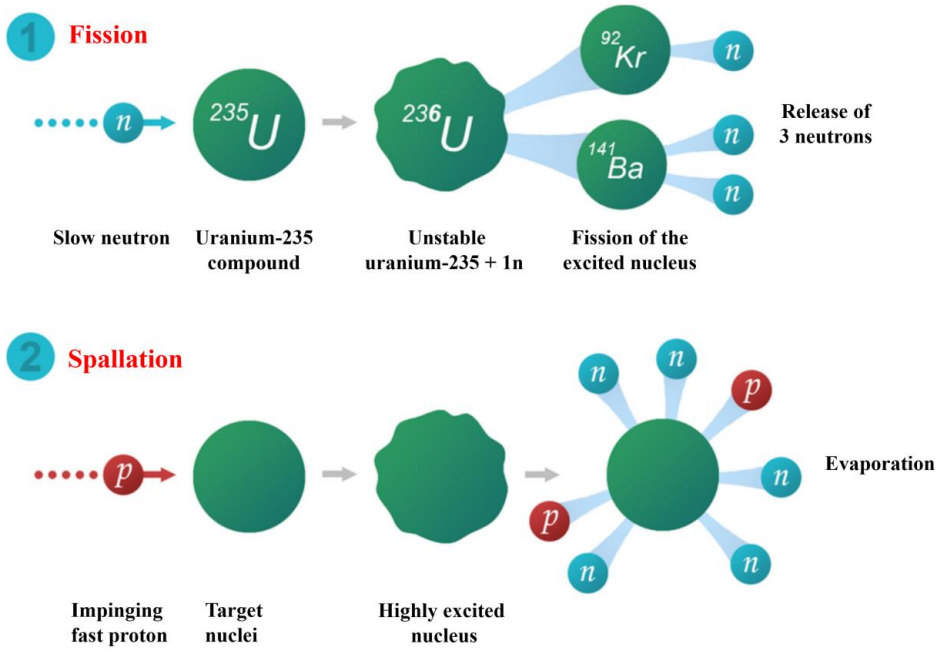

Figure II.24: Schematic representation of the two most commonly used neutron sources for experimental measurements, fission and spallation, adapted from [117].

Finally, to be able to use the neutron they need to be moderated by a medium that reduces their energy through collisions. Table II.3 present the three types of neutron with their properties.

Table II.3: Approximate values for three types of neutron sources in a reactor, with the moderators used at ILL.

Properties / Types	Moderator (at ILL)	Temperature (T / K)	Energy (E / *meV*)	Wavelength (λ / Å)
Cold neutrons	D_2	25	0.1 – 10	30 – 4
Thermal neutrons	D_2O	300	5 – 100	4 – 1
Hot neutrons	graphite	2000	100 – 500	1 – 0.4

Upon the classification and properties of neutrons present in Table II.3, it's important to consider the unique characteristic of neutron (Table II.4):

* The de Broglie wavelength of the thermal neutrons being of the order of inter-atomic distances, interference effects between the incident and scattered beam occur allowing one to derive structural information at the atomic/molecular scale (i.e., elastic scattering)
* The energy of thermal neutrons corresponds to the energy scale of different genuine excitations in condensed matter (photons, magnons etc…). When neutrons undergo inelastic scattering, the change in their energy provide precise information about the nature of these excitations.

* Neutrons have a small magnetic moment, thus interaction with spin and orbital magnetic moments present in the sample is possible.

Table II.4: Basic properties of thermal neutron, where μ_N is the nuclear magneton.

Mass (kg)	$\mathbf{1.675 \cdot 10^{-27}}$
Charge	0
Spin	$^1/_2$
Magnetic dipole moment, μ_n	$-1.913\ \mu_N$
Life time	$t_{1/2} = 820\ s$

* Neutron scattering cross-sections, σ, vary depending on the atomic number and isotopic species of the atoms. This enables the use of isotopic substitution to adjust the contrast, a crucial aspect of this project.

Neutron – matter interaction can lead to two different processes:

- **Neutron Absorption:** This phenomenon more pronounced at lower neutron energies is when the nuclei absorb the incident neutron and reaches an excited state. This phenomenon is at the basis of neutron detector technologies. ^{3}He, Cd, and ^{10}B are strong absorbers.
- **Neutron Scattering:** Refers to the process that the incident neutron is not absorbed by released with a change in its directions and/or in its wavelength/speed/energy. In this category, we will distinguish between different types of scattering: elastic / inelastic, coherent/incoherent. Momentum always changes during scattering, but if energy is conserved (i.e., no change in the incident neutron's energy), the scattering is classified as elastic. If there is an energy change, it is considered inelastic. When the neutron loses kinetic energy during the interaction, the scattering is referred to as the "**Stokes**" regime. Conversely, if the neutron gains energy, it is known as the "**anti-Stokes**" regime (Figure II.25). However, a particular case of INS is quasi-elastic scattering (QENS), where energy transfer is in the range of ± 1 *meV* causing a broadening in the elastic peak, providing information about diffusive motion of the nuclei in the sample.

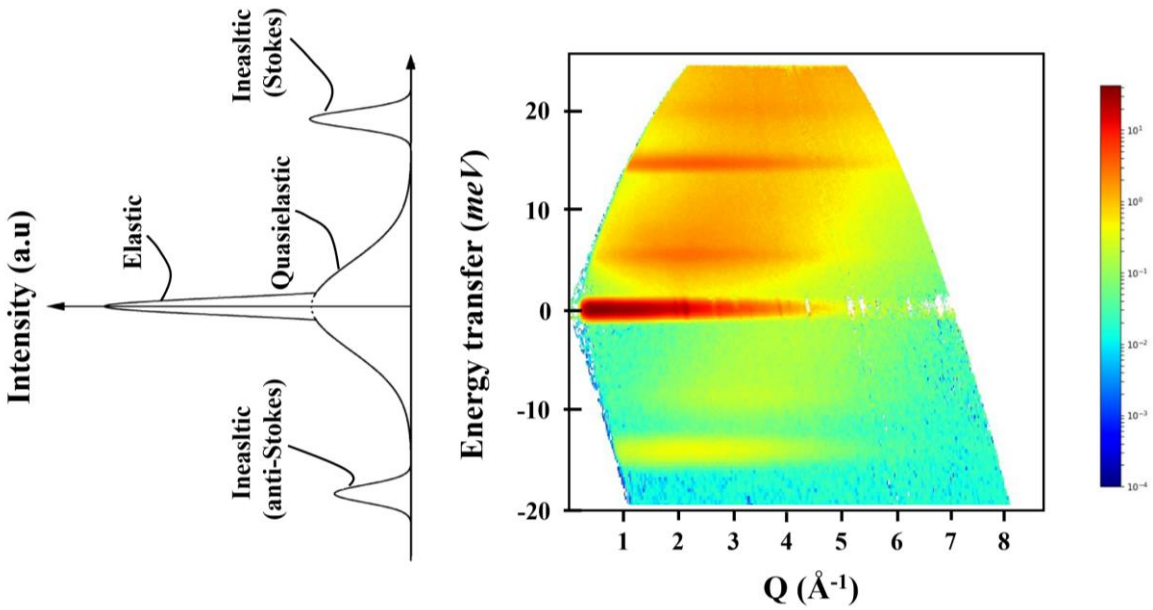

Figure II.25: Experimental data of the dynamical structure factor (will be discussed later) on bulk H_2. The figure illustrates different scattering process: (a) elastic, quasi-elastic, and inelastic scattering (Stokes and anti-Stokes regime). The color scale on the right represents the intensity of the scattering.

In the following subsection, the key quantities necessary for understanding the experimental results will be defined and discussed. For a more comprehensive formalism, reference [118] is recommended.

7.1. Neutron – matter interaction

In a neutron scattering experiments, the measured quantity is represented by the double differential cross section (DDXS), $\frac{d^2\sigma}{d\Omega dE}$,which describes the number of neutrons scattered, N_s, with a wave vector $\vec{k}$' and an energy $E + dE$, through a solid angle $\Omega + d\Omega$. The DDXS can be separated into two components, coherent and incoherent scattering, arising from the interaction of neutron and nucleus of various elements.

$$\frac{\boldsymbol{d^2\sigma_{\vec{k}\to\vec{k'}}}}{\boldsymbol{d\Omega dE}} = \left(\frac{\boldsymbol{d^2\sigma_{\vec{k}\to\vec{k'}}}}{\boldsymbol{d\Omega dE}}\right)_{\boldsymbol{coh}} + \left(\frac{\boldsymbol{d^2\sigma_{\vec{k}\to\vec{k'}}}}{\boldsymbol{d\Omega dE}}\right)_{\boldsymbol{inc}} = \frac{\boldsymbol{N_s(d\Omega, dE)}}{\boldsymbol{\Phi d\Omega dE}} \qquad \textbf{(II.28)}$$

where Φ denotes the incident flux. Similar to how the interaction of X-ray is characterized by the atomic form factor, in neutron scattering, this interaction is described by the scattering length b.

To better understand the scattering event, it is advantageous to use polar spherical coordinates (r, θ, ϕ), as the scattered flux, at a sufficiently large distance from the sample will be radial, see Figure II.26.

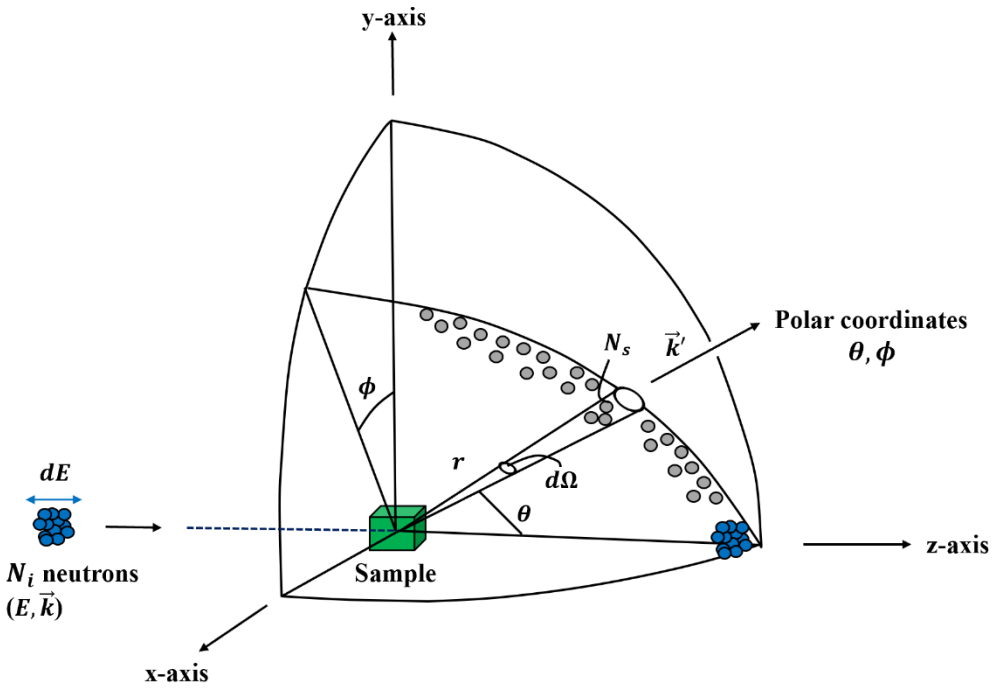

Figure II.26: Illustration of the scattering experiment geometry.

7.1.1. Coherent and incoherent scattering length

For a given element *i*, two terms are associated with the scattering length: the coherent and incoherent scattering lengths. The coherent scattering length, $b_i^{coh} = \overline{b_\iota}$, is defined as the statistical average of the scattering lengths across all spin states and all isotopes. The incoherent scattering length, $b_i^{inc} = \sqrt{\overline{b_\iota^2} - \overline{b_\iota}^2}$, represents the root mean square deviation. Therefore, the coherent scattering length reflects the behavior of the system if all atoms of the same species had identical scattering lengths. In contrast, incoherent scattering arises from variation around this average length.

Table II.5: Coherent and incoherent scattering length, scattering cross sections, and absorption cross sections for the elements interested in this thesis work, extracted from the NIST website [119].

Isotope or element	**Spin**	b_{coh} (fm)	b_{inc} (fm)	σ_{coh} (barn)	σ_{inc} (barn)	σ_{abs} (barn)
^{1}H	1/2	-3.7406	25.274	1.7583	80.27	0.3326
^{2}H or D	1	6.671	4.04	5.592	2.05	0.000519
^{16}O	0	5.803	0	4.232	0	0.0001
^{28}Si	0	4.107	0	2.12	0	0.177
^{24}Mg	0	5.66	0	4.03	0	0.05

^{6}Li	1	2.00-0.261*i*	-1.89+0.26*i*	0.51	0.46	940
Na	3/2	3.63	3.59	1.66	1.62	0.53
Al	5/2	3.449	0.256	1.495	0.0082	0.231
^{51}V	7/2	-0.402	6.35	0.0203	5.07	4.9
Cd	----	4.87-0.70*i*	----	3.04	3.46	2520

Table II.5 present the coherent and incoherent scattering lengths, as well as scattering cross sections, which represent the probability of a neutron interacting with a nucleus, expressed in barns (1 b = 10^{-24} cm^2). For an isolated atom, the cross section is related to the scattering length by the following relation:

$$\boldsymbol{\sigma = 4\pi b^2} \qquad \textbf{(II.29)}$$

In the case of H_2, it is important to note why certain states shows no incoherent scattering length. This phenomenon can be understood by considering a scattering process involving a neutron having a spin ½ and a nucleus with a spin of *I*. The scattering event temporarily forms a "compound nucleus", which can exist in two possible spin state: J^+ with spin I + ½ and J^- with spin I – ½ for the parallel and antiparallel cases, respectively. These states correspond to probabilities $p_+ = \frac{I+1}{2I+1}$ and $p_- = \frac{I}{2I+1}$.

The coherent scattering length is then defined as:

$$\boldsymbol{b_{coh} = \frac{I+1}{2I+1} b_+ + \frac{I}{2I+1} b_-} \qquad \textbf{(II.30)}$$

where b_+ and b_- corresponds to the scattering lengths associated with the parallel and antiparallel spin orientations respectively.

The incoherent scattering length is further defined as below:

$$\boldsymbol{b_{inc} = \frac{(|b_+| - |b_-|)\sqrt{I(I+1)}}{2I+1}} \qquad \textbf{(II.31)}$$

This equation explains why isotopes with total nuclear spin I = 0 are purely coherent scatterers. We note here that para-H_2 has a total nuclear molecular spin (I = 0) and is therefore also a purely coherent scatterer.

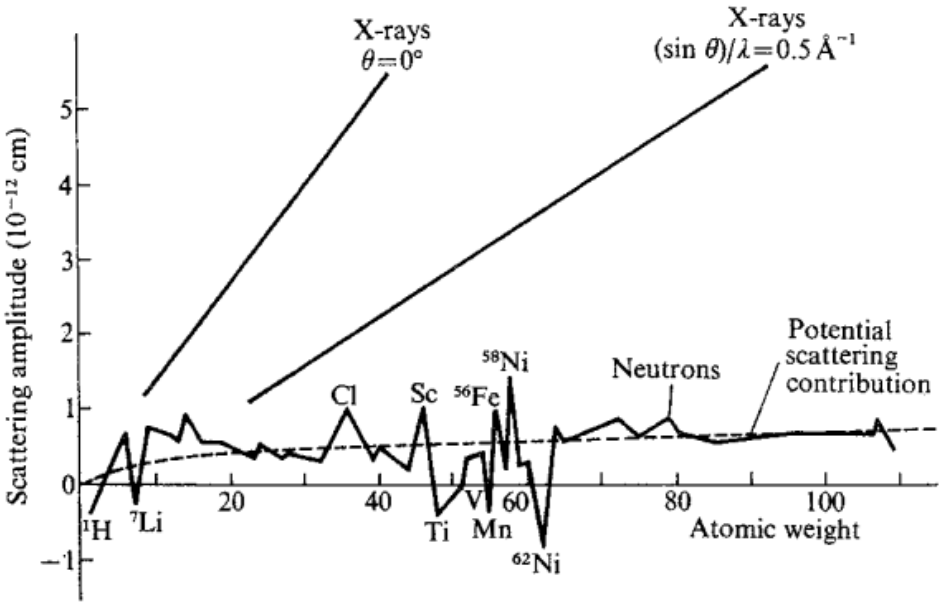

Figure II.27: Coherent scattering length for both neutron and X-ray as a function of the atomic number. Figure adapted from [120].

Figure II.27 illustrates the coherent scattering lengths for both X-ray and neutrons for different elements. The X-ray scattering amplitude is directly related to the atomic number of the elements, whereas the neutron scattering length does not exhibit any correlation with the atomic number.

Below are several comments on specific elements listed in Table II.5:

— Aluminum absorbs few neutrons and has low incoherent scattering, making it commonly used for sample holders, sample environments (cryostats, sample cell, etc.…).

— Vanadium is a purely incoherent scatterer and is used for detector calibration.

— Cadmium strongly absorbs neutrons and is used to mask certain parts of the sample holder, to eliminate parasitic reflections, and it is used to manufacture slits.

7.1.2. Inelastic scattering: dynamical structure factor

Returning to the primary definition of the measured quantity provided in Equation (II.28), we use the Born approximation to relate the double differential cross section to the dynamical structure factor:

$$\frac{d^2\sigma}{d\Omega dE} = \frac{\|\vec{k'}\|}{\|\vec{k}\|} S(\vec{Q}, \omega) \qquad \textbf{(II.32)}$$

During a scattering event, the interaction between the neutron and the sample can be described as quantum mechanical perturbation, where the system transition from an initial state to a final state is characterized by distinct wave vectors and energies. Under certain approximation and utilizing Fermi's golden rule [121], the scattering function can be expressed in terms of the scattering lengths and atomic positions:

$$\boldsymbol{S(\vec{Q},\omega) = \frac{1}{2\pi\hbar}\sum_{i,j}^{N} b_i b_j \int_{-\infty}^{+\infty} \langle e^{i\vec{Q}\cdot\left(\vec{r_i}(t)-\vec{r_j}(0)\right)} \rangle\, e^{itE/\hbar}\, dt} \qquad \textbf{(II.33)}$$

where $\vec{r_i}(t)$ represents the position of atom *i* at time t, and $\langle\cdot\rangle$ denotes that a thermodynamic average over all possible sample configuration has to be taken. The term in the angular brackets, is commonly referred to as intermediate scattering function, $I(\vec{Q},t)$. In Table II.5, the scattering lengths are presented with both real and imaginary components, where the imaginary part accounts for absorption by the element; however, only the real part should be considered in the scattering equations.

The dynamical structure factor can be decomposed into a coherent and an incoherent component:

$$\boldsymbol{S(\vec{Q},\omega) = S(\vec{Q},\omega)_{coh} + S(\vec{Q},\omega)_{inc}} \qquad \textbf{(II.34)}$$

In the case of a single type of atom. The coherent dynamical structure factor is defined as:

$$\boldsymbol{S(\vec{Q},\omega)_{coh} = \frac{\sigma_{coh}}{8\pi^2\hbar}\sum_{i,j}^{N} \int_{-\infty}^{+\infty} \langle e^{i\vec{Q}\cdot\left(\vec{r_i}(t)-\vec{r_j}(0)\right)} \rangle\, e^{itE/\hbar}\, dt} \qquad \textbf{(II.35)}$$

and incoherent dynamical structure factor given by:

$$\boldsymbol{S(\vec{Q},\omega)_{inc} = \frac{\sigma_{inc}}{8\pi^2\hbar}\sum_{i}^{N} \int_{-\infty}^{+\infty} \langle e^{i\vec{Q}\cdot\left(\vec{r_i}(t)-\vec{r_i}(0)\right)} \rangle\, e^{itE/\hbar}\, dt} \qquad \textbf{(II.36)}$$

where σ_{coh} and σ_{inc} are the coherent and incoherent scattering cross section, which are characteristic of this atomic species ($\sigma_{coh} = 4\pi b_{coh}^2$, $\sigma_{inc} = 4\pi b_{inc}^2$).

To further clarify the physical significance of the coherent and incoherent components, we can describe them as follows:

- **Coherent scattering function:** depends on both, the correlation between the positions of the particles at different times. It accounts for interference effects and it describe collective properties like the atomic structure.
- **Incoherent scattering function:** represents the correlation between the positions of the same particle at different times. It appears because of the variation of the scattering lengths of the atoms in a sample caused by non-zero nuclear spins or different isotopes. Intensities scattered from individual nuclei add up independently.

When a system involves a strongly dominating incoherent scatterer as H, $S(\vec{Q},\omega)$ is dominated by the incoherent dynamical structure factor.

7.1.3. Elastic scattering

Elastic neutron scattering, a process where neutrons scatter from a target material without any change in kinetic energy, is fundamentally described by the following differential cross-section (DCS):

$$\frac{d\sigma}{d\Omega} = \frac{N_s(d\Omega)}{\Phi d\Omega} \propto S(\vec{Q}) \qquad \textbf{(II.37)}$$

where $N_s(d\Omega)$ represents the number of scattered particles detected within a solid angle element, $d\Omega$. It can be decomposed into coherent and incoherent contributions. The coherent elastic DCS, which accounts for the interference effects between all scattering centers, is given by:

$$\frac{d\sigma}{d\Omega_{coh}} = \frac{\sigma_{coh}}{4\pi}\sum_{i,j}^{N}\langle e^{i\vec{Q}(\vec{R_i}-\vec{R_j})}\rangle \qquad \textbf{(II.38)}$$

On the other hand, the incoherent DCS, which arises from random variations in scattering lengths, is expressed as:

$$\frac{d\sigma}{d\Omega_{inc}} = \frac{\sigma_{inc}}{4\pi}\sum_{i,i}^{N}\langle e^{i\vec{Q}(\vec{R_i}-\vec{R_i})}\rangle = \frac{\sigma_{inc}}{4\pi}N \qquad \textbf{(II.39)}$$

Figure II.28 presents the coherent and incoherent scattering, illustrating how the coherent scattering intensity varies with Q due to interference effects, while the incoherent scattering intensity remains independent of Q (after accounting for the Debye-Waller factor).

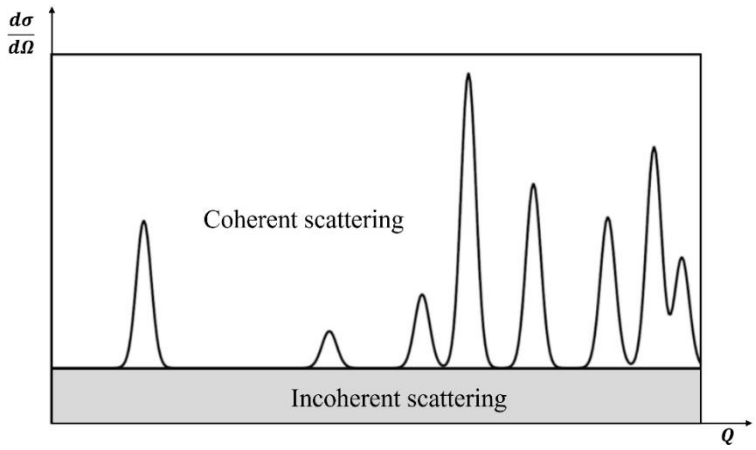

Figure II.28: Schematic figure showing the coherent and incoherent scattering parts of the differential cross section [122].

7.1.4. Small Angle Neutron Scattering

Small Angle Neutron Scattering (SANS) is a powerful technique used to measure the shape of large objects and/or correlations at large distances. As such this technique has been used intensively for understanding the structure of porous media. In the peculiar case of layered materials like Laponite and pre-Laponite, for which the interlayer d-spacing is significantly larger than interatomic distances, the low Q region of the diffractograms, associated to "small angle scattering", is characterized by the presence of a peak known as the (*001*) peak and generally represents the largest periodic spacing in the sample. In this manuscript, SANS was employed to determine the interlayer distance and to investigate the pore density as a function of pressure of H_2 and D_2 within the interlayers of the two different materials. This analysis was performed using the "Stacked disks" model available in the SASview software, which will be discussed in detail in **Chapter V**.

7.2. Neutron sources: Institut Laue-Langevin

Neutrons can be produced through either fission or spallation, with the goal of releasing as many neutrons as possible to achieve high luminosity. Since 1972, one of the most powerful continuous neutron sources, based on a nuclear reactor RHF for "Réacteur à Haut Flux", has been the Institut Laue-Langevin (ILL). ILL generates an extremely high neutron flux (2×10^{15} n. $cm^{-2}.s^{-1}$) [123], which supplies ~40 scientific instruments located in the main reactor hall and two neutron guide halls, as depicted in Figure II.29.

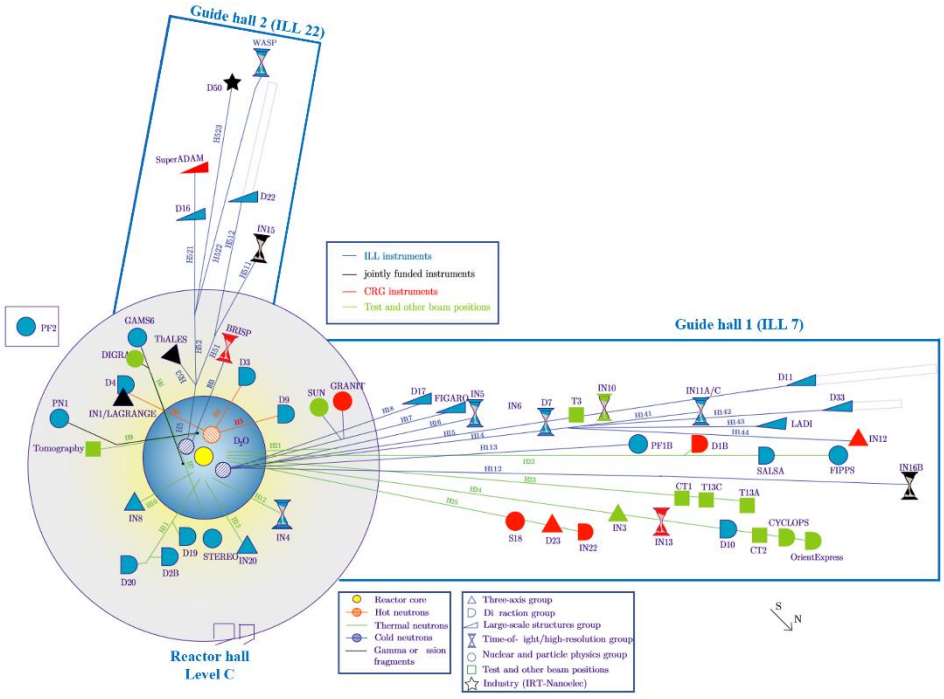

Figure II.29: Instruments layout of the Institut Laue-Langevin.

In this work, two types of neutron instruments were used: time-of-flight spectrometers and a diffractometer, both of which are introduced below. Data reduction and analysis were carried out using the Mantid software [124], with custom data reduction scripts written in python. The data fitting was performed using the fitting interface implemented in Mantid.

7.2.1. Thermal neutron time-of-flight spectrometer: PANTHER

The PANTHER beamline at the Institut Laue-Langevin (ILL) is a state-of-the-art thermal neutron time-of-flight (TOF) spectrometer, designed for advanced studies of excitations in condensed matter. The spectrometer is equipped with double-focusing monochromators made of either graphite or copper, a Fermi chopper, and position-sensitive helium-3 (^{3}He) detectors that cover a solid angle of 2 steradians (Figure II.30). To minimize thermal neutron background, the instrument incorporates a radial oscillating collimator, a beam dump, and an intricate system of cadmium (Cd) shielding within the evacuated detector tank.

PANTHER is a direct TOF spectrometer meaning that an incident neutron energy E_i is selected from the thermal white beam, and that the scattered neutron energy E_f is analyzed by the TOF technique. E_i is adjustable between 7.5 and 150 meV. The instrument delivers a high pulsed neutron flux in the 15-76 meV range, with an energy resolution varying from ~ 3% to 6% of the incoming energy when using the highly oriented pyrolytic graphite (HOPG) monochromator face, depending on the take-off angle [125].

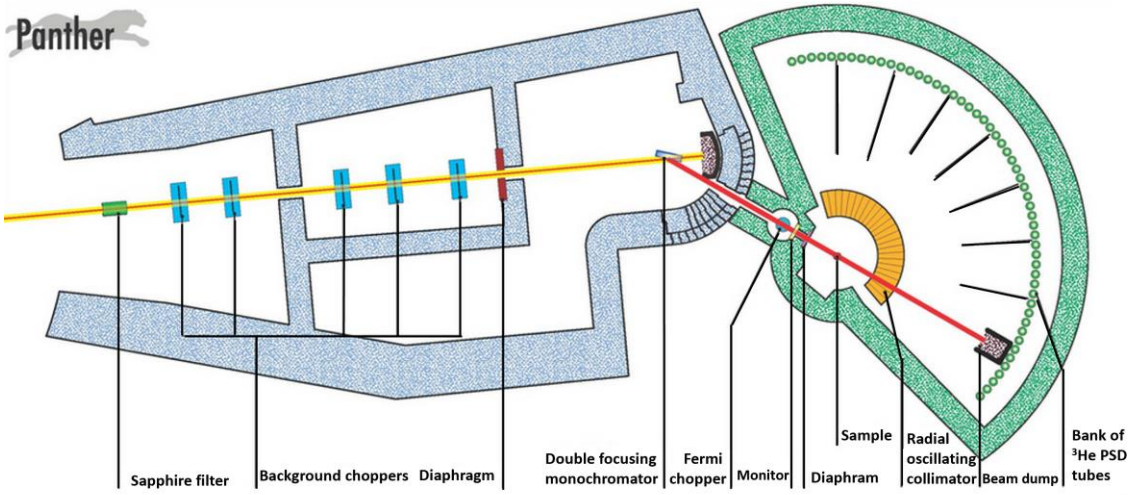

Figure II.30: Geometry of the time-of-flight beamline, PANTHER, at Institut Laue-Langevin.

TOF instruments are based on the neutron properties, mass m_n and speed v with kinetic energy given by:

$$E_{kinetic} = \frac{1}{2} m_n v^2 \qquad \textbf{(II.40)}$$

A TOF spectrometer measures the velocity of scattered neutron to determine the energy exchange with the sample. However, in practical, not all the energy and momentum transfer values are experimentally accessible with TOF instruments. For a given initial and final wavevector ($\vec{k}$ and $\vec{k'}$), only a specific region in reciprocal space, known as the "kinematically allowed region", can be accessed experimentally (Figure II.31). This region is defined by the constrains of energy and momentum during scattering process:

$$\vec{Q} = \vec{k} - \vec{k'} \qquad \textbf{(II.41)}$$

$$\hbar\omega = E_i - E_f = \frac{\hbar^2}{2m_n}(k^2 - k'^2) \qquad \textbf{(II.42)}$$

Here one separates direct geometry, for which initial energy is defined by the instrument configuration while the final energy is analyzed. The $(\vec{Q}, \omega)$ domain accessible is given by:

$$\frac{\hbar Q^2}{2m_n} = 2E_i - \hbar\omega - 2\sqrt{E_i(E_i - \hbar\omega)}\cos(\theta) \qquad \textbf{(II.43)}$$

In the inverse geometry, the final energy is fixed and the initial energy is varied with the accessible $(\vec{Q}, \omega)$ region given by:

$$\frac{\hbar Q^2}{2m_n} = 2E_f + \hbar\omega - 2\sqrt{E_f(E_f + \hbar\omega)}\cos(\theta) \quad \textbf{(II.44)}$$

PANTHER employs a direct geometry measurement approach. In this configuration, the spectrum on the positive side (Stokes region) is limited by the incident neutron energy, and the resolution at the elastic peak worsens with increasing the incident energy. Therefore, to optimize the resolution around the H_2 para-ortho transition, and to access sufficiently high energies to observe other rotational lines, we used two incident energies: 30 *meV* and 60 *meV*.

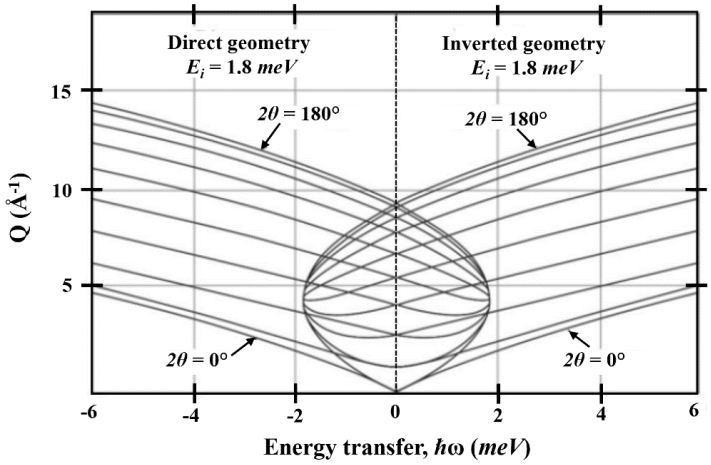

Figure II.31: TOF kinematically allowed region for both direct and inverted geometry.

This approach balances the need for high resolution with the ability to probe the necessary energy range. Notably, for a given incident energy, the resolution is more or less constant in the Stokes side. For samples preparation, approximately 600 mg of the samples were initially outgassed at 150°C for 6 hours under secondary vacuum. Following this procedure, the material was wrapped in aluminum foil (to minimize the dead volume) before being inserted into an aluminum cylindrical cell. The latter is realized under controlled vacuum inside a glove box[12].

Table II.6: PANTHER experimental features: timescale and *Q*-range probed at two incident energies.

Incident energy (*meV*)	**Energy resolution** *(meV)*	**Timescale** (ps)	***Q*-range** ($Å^{-1}$)
30	~ 1.5	~ 0.8	[0, 7]
60	~ 3	~ 0.4	[0, 10]

[12]*The material is handled inside the glove box to avoid hydration, which would significantly affect interlayer spacing and, in turn, alter adsorption properties, while also minimizing H-D exchange.*

Several approaches were undertaken to properly investigate the local symmetry associated to the adsorption sites and the energy barriers to overcome for molecular rotations. Initially, temperatures-dependent experiments were conducted on bulk hydrogen using a 30 *meV* incident energy. Subsequently, both 30 *meV* and 60 *meV* incident energies were used to investigate the pressure dependence on D-pre-Laponite and D-Laponite at 40K.

7.2.2. Diffractometer: D16

D16 (Figure II.32) is a cold-neutron diffractometer situated on the cold H521 neutron guide. The instrument utilizes a focusing monochromator made of nine highly oriented pyrolytic graphite (HOPG) crystals to reflect the primary white beam. This monochromator housing includes two beam holes, offering take-off angles of 85° and 115°, which correspond to incoming wavelengths of 4.5 Å and 5.6 Å, respectively. The setup also features a collimating slit system, comprising newly installed precision slits both in the casemate and at the sample position. When paired with the large, vertically focusing HOPG monochromator, it ensures a high neutron flux at the sample position and provides high resolution in the horizontal plane. The diffracted neutrons are detected by a large curved position-sensitive 2D detector based on the new trench technology developed at the ILL. The detector, mounted on a rotation table, allows for a θ range of [–5°, 120°], corresponding to a Q range of [0.02, 2.5] $Å^{-1}$.

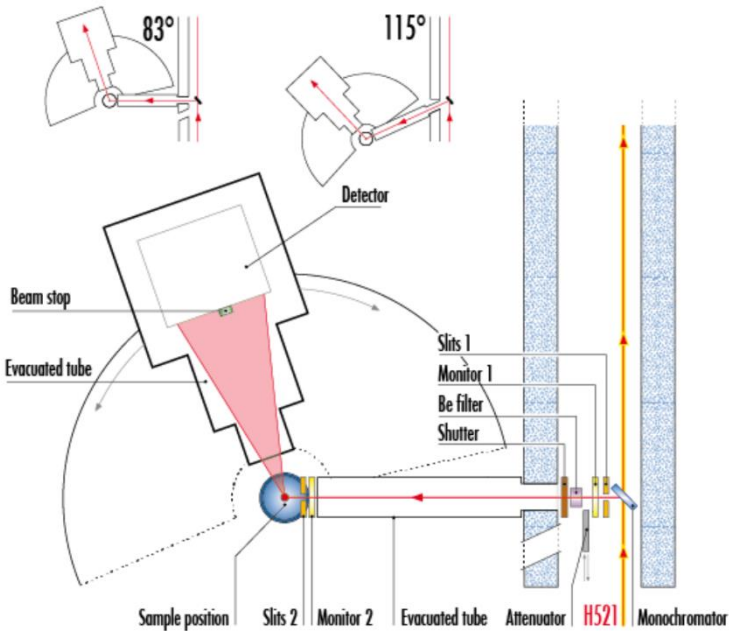

Figure II.32: Geometry of the diffractometer, D16, at Institut Laue-Langevin.

Three instrument configurations corresponding to three detector positions were done: 40°, 45°, and 90°. The 40° position, with a beam attenuator put on the incident neutron path, was

dedicated to transmission measurements and beam center determination, while the 90° and 45° positions were employed for the recording of the wide-angle and small-angle patterns, respectively, with incident wavelength 4.503 Å. The measurements were conducted for a fixed temperature by varying the gas pressure, similarly to what was done for inelastic neutron scattering investigation. Prior to the experiment, the samples were outgassed at 150°C for 6 hours, then wrapped in aluminum foil within a glove box, and subsequently placed in an aluminum cylindrical cell (Figure II.33).

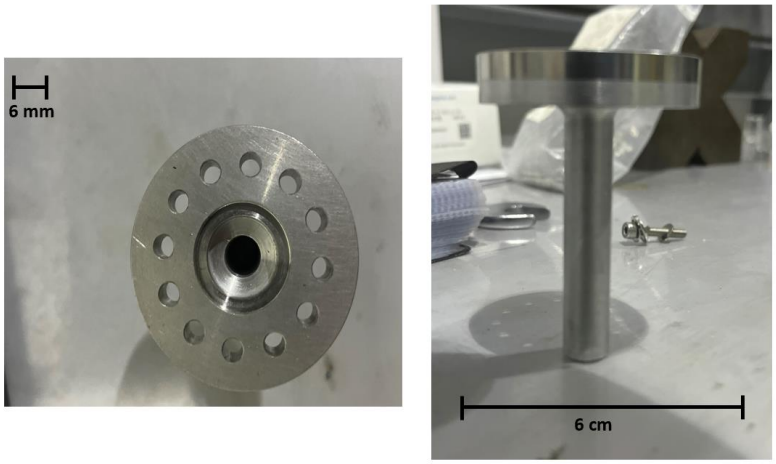

Figure II.33: Aluminum cylindrical cell used for neutron experiments.

The raw data were normalized to the incident flux and corrected for the background and cell scattering which were accounted for by measuring the scattering of an empty cell and of a strong absorber sample (Cd inside the cell). The reduced 2D scattered intensities were further radially integrated to produce one-dimensional diffraction patterns. The latter were further normalized to the neutron-irradiated mass of the dried host matrix within the cell.

This page was intentionally left blank.

Chapter III. Computational modeling

This chapter focuses on the application of Monte Carlo and atomistic simulation to study the structural characteristics of the nano-clays and H_2 adsorption in a host matrix.

1. Introduction

Computational modeling is a technique that uses computer-based models and algorithms to replicate and study real or theoretical systems. In the study of adsorption mechanisms in porous materials, experimental methods are crucial, but interpreting the results at a detailed structural level can be difficult. By combining experimental data to computational techniques, it becomes possible to enrich the analysis and gain a deeper understanding of the system at the molecular level. As shown in Figure III.1, different computational methods operate across various length and time scales.

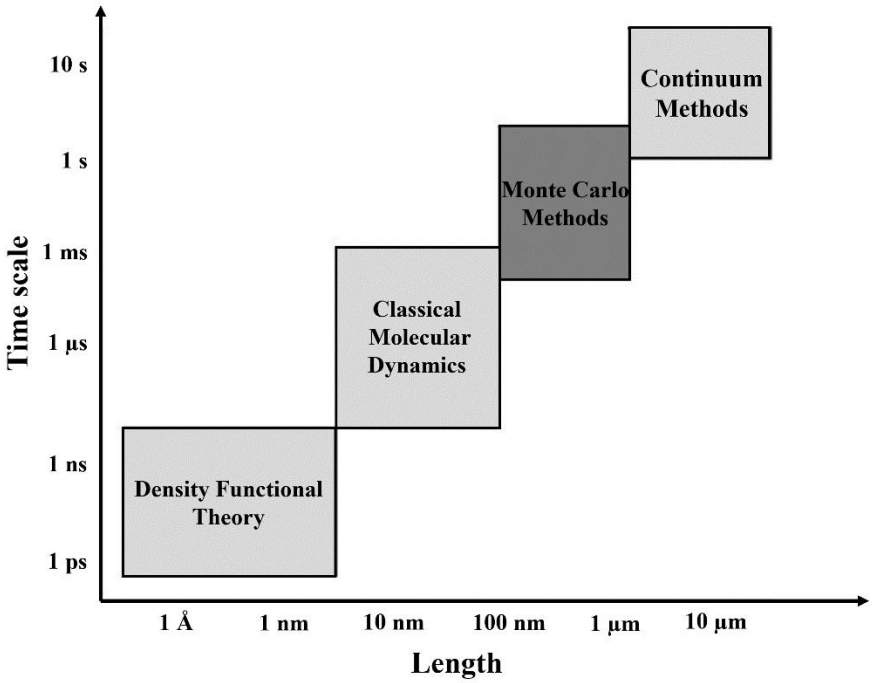

Figure III.1: Overview of computational methods across different length and time scales adapted from [126]**.**

As layered materials consist of various adsorption sites, it is crucial to decompose the contributions of these sites to the overall adsorption isotherms and diffraction patterns. To achieve this, Monte Carlo simulations were employed to evaluate the adsorption isotherms for H_2 adsorbed in the relaxed Laponite structure. The pressure-dependent configurations generated from these simulations were subsequently used to calculate the diffraction pattern, focusing on the large Q region, using atomistic calculations.

2. Monte Carlo simulations

Monte Carlo (MC) methods are based on random sampling of the configurational space. These methods enable the determination of structural and thermodynamic information [127] by

generating samples according to a probability distribution, typically the Boltzmann distribution, which accounts for the energy distribution of the system. The averages over these sampled configurations are used to estimate the expectation value of properties. Since these simulations are conducted within the framework of equilibrium statistical mechanics, certain state variables, such as temperature or volume, remain constant depending on the ensemble used.

One of the significant advantages of Monte Carlo (MC) simulations is their flexibility to simulate systems using various ensembles, including isothermal-isobaric, canonical, grand canonical, microcanonical, isothermal-isotension, and Gibbs ensembles. In this manuscript, we used the grand canonical ensemble to change the number of molecules in the simulation process to perform MC calculations.

The grand canonical ensemble, first introduced by Norman and Filinov [128], is characterized by a constant chemical potential, volume, and temperature (constant - μVT). In this ensemble, the number of particles is allowed to fluctuate. When considering two subsystems, the volume of subsystem 1 remains fixed, but it can exchange both energy and particles with the reservoir (subsystem 2).

In grand canonical ensemble, the partition function is given by [129]:

$$\boldsymbol{Z(\mu,V,T)=\sum_{N=0}^{\infty}\frac{V^N e^{\beta\mu N}}{\Lambda^{3N}N!}\int e^{-\beta U(s^N;h)}d^N s} \qquad \textbf{(III.1)}$$

where N is the number of particles, Λ the thermal de Broglie wavelength normalization factor, $\beta=\frac{1}{K_B T}$ the inverse temperature with K_B being the Botlzman constant, and $U(s^N;h)$ is the potential energy of the system as a function of particle positions and external parameters, h. For a particular configuration, the probability is given by:

$$\boldsymbol{P(s^N,V)\propto\frac{V^N e^{\beta\mu N}}{\Lambda^{3N}N!}e^{-\beta U(s^N;h)}} \qquad \textbf{(III.2)}$$

The pressure p in the reservoir is related to the chemical potential by:

$$\boldsymbol{\beta\mu=\mu^0{}_{IG}+ln(\beta f)} \qquad \textbf{(III.3)}$$

where $f=\phi p$ is the fugacity, and $\mu^0{}_{IG}$ the chemical potential of the ideal gas, given by:

$$\boldsymbol{\mu^0{}_{IG}\equiv\frac{ln(\Lambda^3)}{\beta}} \qquad \textbf{(III.4)}$$

Notably, fugacity is not exactly the same as pressure, but it represents the effective pressure or "activity" of gas, and it has the same units as pressure. The fugacity coefficient ϕ is defined as the exponential difference between the Gibbs free energy of the real gas and the ideal gas divided by *RT*. In a GCMC simulation, each step involves one of three possible actions: random displacement (move), insertion and deletion, randomly chosen. The acceptable probabilities of:

Displacement

$$\boldsymbol{acc(move) = min\left(1, e^{-\beta[U(new)-U(old)]}\right)} \quad \textbf{(III.5)}$$

Insertion

$$\boldsymbol{acc(N \rightarrow N+1) = min\left(1, \frac{\beta V \phi p}{N+1} e^{-\beta[U_n(s^{N+1};h)-U_o(s^N;h)]}\right)} \quad \textbf{(III.6)}$$

Deletion

$$\boldsymbol{acc(N \rightarrow N-1) = min\left(1, \frac{N}{\beta V \phi p} e^{-\beta[U_n(s^{N-1};h)-U_o(s^N;h)]}\right)} \quad \textbf{(III.7)}$$

2.1. Building block of Laponite

The structure optimization of Laponite was performed by Virginie Marry (laboratory PHENIX, Paris) for an isolated Laponite layer with nominal structure $Si_8Mg_{4.8}Li_{1.2}\ Na_{1.2}O_{20}(OH)_4$, putting one half of the Na^+ ions above the layer and the rest below the layer, the layer being made of 50 rectangular centered unit cells with a=5.26 Å and b=a$\sqrt{3}$. The layer shape was 10a and 5b.

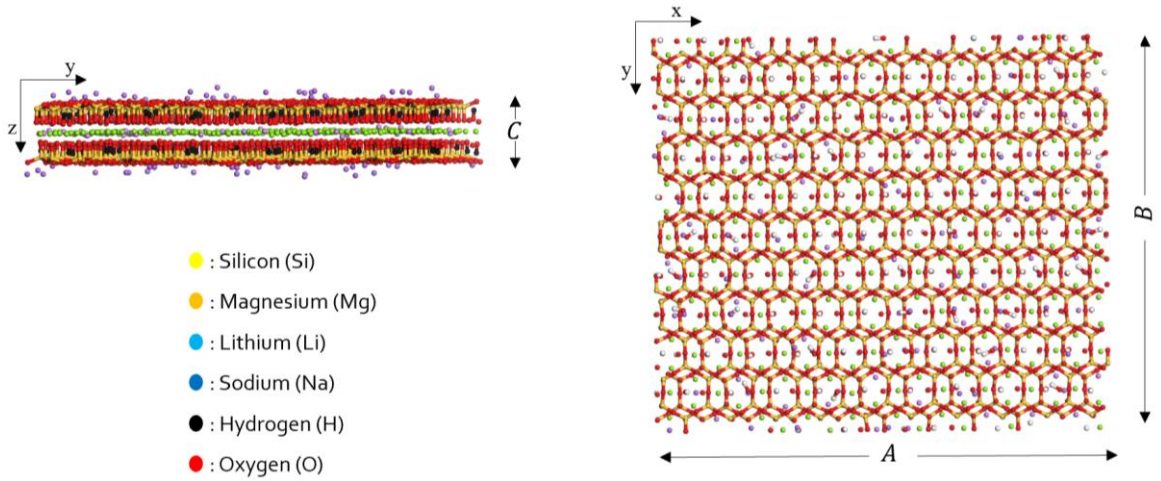

Figure III.2: Atomic structure of a single TOT (2:1) layer in a Laponite model. The left image shows the side view along the z-axis, highlighting the layer spacing. The right image shows the top view, illustrating the hexagonal arrangement of atoms within the ab-plane. The color scheme represents different atoms: Silicon (Si) in

yellow, Magnesium (Mg) in orange, Lithium (Li) in light blue, Sodium (Na) in dark blue, Hydrogen (H) in black, and Oxygen (O) in red.

Optimization steps were performed using the LAMMPS molecular dynamics software, beginning with an NVT ensemble at 1000 K to facilitate cation mobility and system equilibration. An anisotropic NPT ensemble was then applied at 1 bar in the x and y directions to achieve structural relaxation and stabilization. After optimization, the resulting structure had dimensions of $A = 52.608$ Å, $B = 45.606$ Å.

2.2. Force field selection

In this work, we have used the COMPASS force field available in the Forcite module of the Material Studio package to model both $H_2 – H_2$ and H_2 – Laponite interactions, with the Laponite atoms kept immobile. The total potential energy of the system (U) is given by the sum of intramolecular and intermolecular contributions:

$$\boldsymbol{U = E_{stretching} + E_{bending} + E_{vdWs} + E_{electrostatic}} \quad \textbf{(III.8)}$$

Intramolecular interactions, including bond stretching and angle bending, are represented by harmonic potentials:

$$\boldsymbol{E_{bending} = \frac{1}{2} k(\theta - \theta_0)^2} \quad \textbf{(III.9)}$$

where k is the force constant, r the bond length, and θ the bond angle. For intermolecular interactions (unbound), van der Waals forces are described using the Lennard-Jones (LJ) potential, while electrostatic interactions are modeled using Coulomb's law:

$$\boldsymbol{U_{unbound} = 4\varepsilon_{ij}\left[\left(\frac{\sigma_{ij}}{r_{ij}}\right)^{12} - \left(\frac{\sigma_{ij}}{r_{ij}}\right)^{6}\right] + \frac{q_i q_j}{4\pi\epsilon_0 r_{ij}}} \quad \textbf{(III.10)}$$

In equation (III.10), $\varepsilon_{ij} = \sqrt{\varepsilon_i \varepsilon_j}$ is the LJ well depth, $\sigma_{ij} = \frac{\sigma_i + \sigma_j}{2}$ is the LJ size, r_{ij} is the distance between atoms i and j, ϵ_0 is the dielectric constant, q_i and q_j are the charges of atoms i and j, respectively. Figure III.3 presents a schematic representation of the four different types of interactions.

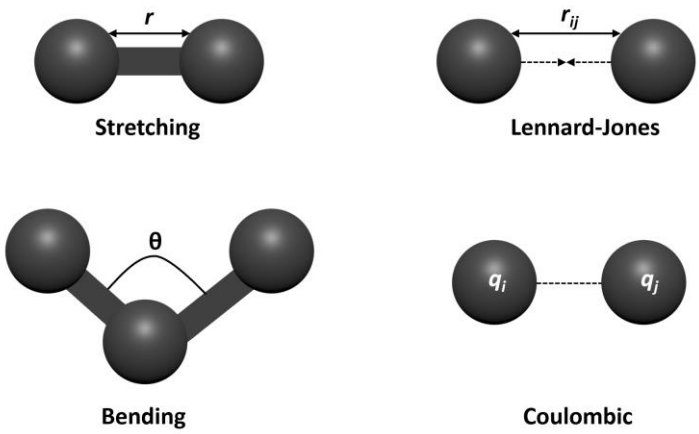

Figure III.3: Schematic representation for both intramolecular and intermolecular interactions.

2.3. Computational details

GCMC were employed to model the isotherm adsorptions. For that, the simulation box used had dimensions of $75 \times 75 \times 50\ \text{Å}^3$ and is composed of three TOT layers, which were saturated with hydrogen at their borders, stacked in turbostatic mode, characterized by random translations and rotations from one sheet relative to another, with a varied interlayer spacing of $d_{interlayer}$ (Figure III.4). This turbostratic stacking discussed further in **Chapter IV**. The simulation box volume is fixed and maintained in equilibrium with the adsorbate reservoir (H_2) at a constant temperature and chemical potential. During the simulations, in order to compute the long-range coulombic interactions, a cutoff distance cannot be used because it decreases very slowly as $\propto r^{-1}$. Therefore, long-range electrostatic interactions were calculated using the Ewald & Group summation method, while van der Waals (vdWs) interactions were handled using the atom-based summation method. The host structure was kept fixed, and periodic boundary conditions were applied in all three dimensions. Each state point involved 1 million equilibration steps followed by 100,000 production steps. The fugacity was varied from 2 to 1000 mbar across 20 fugacity steps.

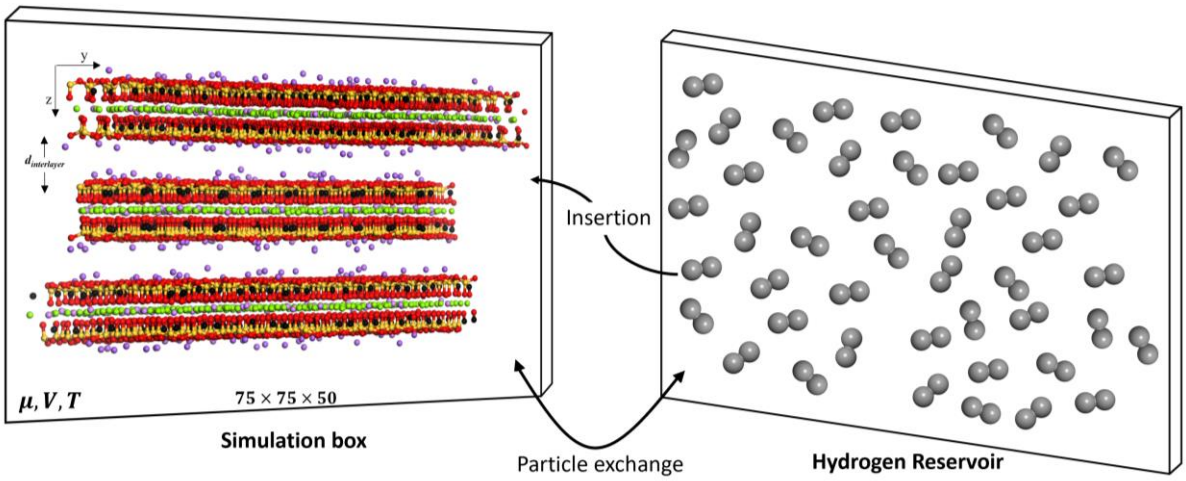

Figure III.4: Schematic representation of the GCMC simulation setup. The simulation box contains three turbostratically stacked TOT layers, with an interlayer spacing of $\boldsymbol{d_{interlayer} = 3}$ Å. The box dimensions are $\boldsymbol{75 \times 75 \times 50}$ Å$^{\boldsymbol{3}}$. The system is in equilibrium with a hydrogen reservoir, allowing particle exchange via insertion and deletion processes, while maintaining constant chemical potential (μ), volume (V), and temperature (T).

It is important to note that the adsorption amount obtained from the simulations is the absolute adsorbed amount (N_{ab}), while the experimentally measured data represent the excess adsorbed amount (N_{ex}). The relationship between these two quantities is given by [130]:

$$\boldsymbol{N_{ab} = N_{ex} + \rho V_{free}} \quad \textbf{(III.11)}$$

where ρ is the adsorbate gas density and V_{free} is the free volume of the adsorbent. However, in this manuscript, only a qualitative comparison with experimental results was conducted. Therefore, simulation results are presented as absolute adsorption amounts. However, at sub-atmospheric pressure, absolute and excess adsorption do not differ significantly, but these differences become relevant at pressure close to and exceeding 100 bar

3. Atomistic calculations

In order to compute the X-ray or neutron scattering patterns starting from the atomic positions of the models, one can use the Debye formula. This formula calculates the intensity $I(Q)$ scattered by a powder from the interatomic distances present in the material.

$$\boldsymbol{I(Q) \propto \sum_{i,j} f_i(Q) f_j(Q) \frac{sin(Q r_{ij})}{Q r_{ij}}} \quad \textbf{(III.12)}$$

where $f_i(Q)$ and $f_j(Q)$ are the atomic form factors of atoms i and j respectively (for neutron scattering these should be replace by the coherent scattering lengths b_i and b_j), and r_{ij} is the

distance between these atoms. For dry (pre-)Laponite the calculation of $I(Q)$ was performed using the atomic positions from the relaxed Laponite layer. It was reported with periods A and B, or cut, depending on the size of the layer one wants to consider. The number of layers as well as the interlayer distance were also chosen in the program. To accurately reflect the random stacking of the layers, the intensity was calculated for "N = 100" particles with different (x,y) relative positions of a layer with respect to another.

For adsorbed H_2/D_2, we used either the positions of H(D) atoms obtained from Monte Carlo Simulations or we generated H_2 (D_2) positions in a random way. Intensity calculations have been speed up using highly parallel calculation on GPUs [131]. Calculated intensities were finally convoluted with experimental resolution to allow for a direct comparison with experimental diagrams. For MarCu experimental data, a Gaussian convolution was applied to model the experimental resolution (FWHM = 0.0281 $Å^{-1}$). In contrast, for CRISTAL data, no convolution was necessary, as resolution effects were negligible.

This page was intentionally left blank.

Chapter IV. Structural and textural characterization

This chapter explores the comparative analysis of Laponite and pre-Laponite, laying the groundwork for the comparative study of H_2 adsorption in these two compounds which is detailed in chapter V. It begins with a chemical analysis demonstrating that both materials share similar chemical compositions. One then studies the thermal behavior of the two compounds with TGA, showing that dehydroxylation occurs at lower temperature for pre-Laponite. Detailed XRS analysis by atomistic simulations based on MD structural minimization, coupled to PDF, shows that the two materials have the same TOT trioctahedral structure, with smaller in-plane correlation lengths and reduced layer packing for pre-Laponite. Finally, N_2 isotherms highlights differences in textural properties.

In this chapter, we use the deuterated Laponite and pre-Laponite samples that will also be employed in the subsequent neutron studies.

1. Elemental characterization of dried materials

Laponite is a synthetic hectorite [Neumann patent]. It is a trioctahedral smectite of nominal formula [Si8] [$Mg_{6-x}Li_x$] Na_x $O_{20}(OH)_4$. Based on the relative amounts of the synthesis precursors given in **§1.1,Chapter II,** one finds x=1.2. The chemical composition of deuterated pre-Laponite and Laponite was analyzed through ICP-AES analysis, as described in **Chapter II**.

Table IV.1: Chemical composition of pre-Laponite and Laponite calculated from ICP-AES measurements.

Element / Sample	Ratio		
	Si:Mg	Si:Na	Mg:Na
Pre-Laponite†	7.4 ± 1	0.55 ± 0.01	0.07 ± 0.01
Pre-Laponite††	1.57 ± 0.03	5.48 ± 0.4	3.49 ± 0.45
Laponite†	1.8	7.76 ± 0.45	4.32 ± 0.3
Theoretical†††	1.67	6.67	4

†Measurements were taken after 1 minute of sonication, with the powder added immediately prior to the sonication.
††Measurements were taken after 1 hour of sonication with sample-solution 1-day contact.
†††Values calculated based on the starting precursors.

2. Thermogravimetric analysis

TGA experiments were performed on deuterated Laponite and pre-Laponite samples under N_2 atmosphere, with a heating ramp of 5 °C/min. Figure IV.1 shows the weight loss as a function of temperature**.** In order to identify the different mass loss steps, the TGA first derivative, DTG (rate of mass loss) is also reported.

A first mass loss occurs below 200°C, as is the case with smectites [133]. It corresponds to dehydration of physiosorbed water. The overall amount of water released depends on the initial hydration state, which is influenced by the relative humidity (RH) at room temperature prior to the measurements.

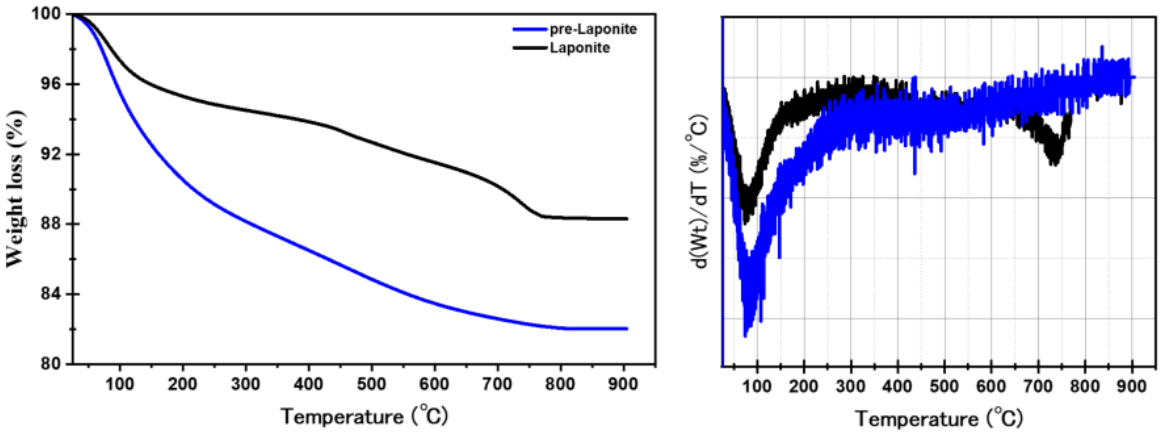

(a) **(b)**

Figure IV.1: (a) TGA and (b) DTG profiles of pre-Laponite (blue) and Laponite (black) powders in 150 µL alumina crucible.

Another major weight loss in Laponite is observed around 730°C. For trioctahedral smectites [132], [133] this feature corresponds to dehydroxylation i.e. to the loss of structural OH groups. For two adjacent OH groups, dehydroxylation leads to the formation of a water molecule and a residual oxygen. In the case of trioctahedral phyllosilicates, there is no octahedral vacancy where the residual oxygen could reside, so that OH groups cannot be removed without a reconstruction of the octahedral sheet. Dehydroxylation is therefore accompanied by recrystallization and occurs at temperatures higher than 700°C [133], as is the case for Laponite. In pre-Laponite, dehydroxylations occurs on a broader and lower temperature range. To explain this phenomenon, if we assume that the Laponite and pre-Laponite compounds have the same trioctahedral structure, which will be confirmed in **§3**, one may consider two hypotheses: (i) an incomplete layer formation i.e. the presence of defects that would make it easier to release the remaining oxygen, (ii) a reduced size of the layers, with a sufficiently large edge effect to allow the release of oxygen.

3. Structural analysis

3.1. X-ray scattering: experimental and calculated diagrams

The structural characteristics of both deuterated Laponite and pre-Laponite were examined using XRS on the MarCu diffractometer described in **Chapter II**, **§5.2.1**. Figure IV.2 presents the corrected XRS diffraction patterns of these samples. Geometric and polarization corrections together with correction for air adsorption between the sample and the detector were applied to the data. Very weak intensity peaks, marked by asterisks, are attributed to minor parasitic

phases formed during synthesis of Laponite. However, these parasitic phases are present in trace amounts, with negligible impact on the properties of Laponite.

A first important conclusion can be drawn from the comparison of the diffraction diagrams of Laponite and pre-Laponite in Figure IV.2. They appear very similar, although diffraction features are larger for pre-Laponite. This similarity, together with our previous finding that Laponite and pre-Laponite share the same chemical formula, shows that Laponite and pre-Laponite present the same atomic structures.

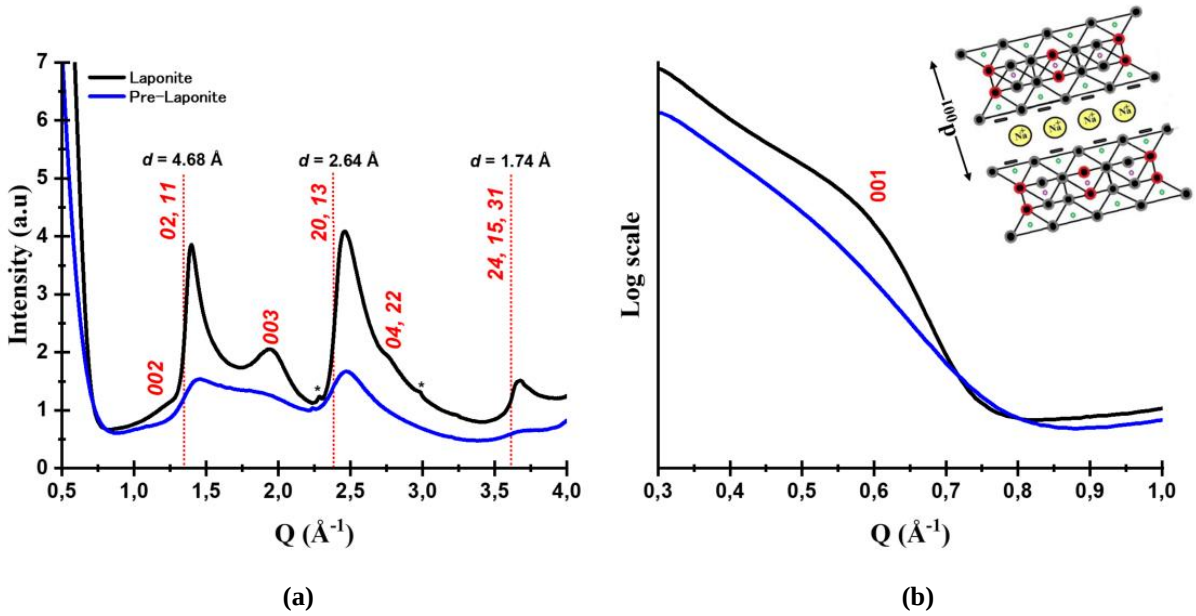

Figure IV.2: XRS patterns of Laponite (black) and pre-Laponite (blue) samples. (a) shows the intensity of diffraction peaks as a function of scattering vector Q, with key peaks labelled by their corresponding Miller indices in red and their associated interplanar spacing, *d*. Peaks marked with asterisks (*) are due to parasitic crystalline phases in extremely small amount. (b) Low-Q region on a logarithmic scale, highlighting the *001* peak.

The *00l* reflections in both samples reveal the stacking of the layer $d_{001} \approx 9.7$ Å. This distance includes both the 2:1 clay layer and interlayer space, see inset Figure IV.2. The *003* appears more well defined that the *001* peak, which is rather surprising. One may suppose that the *001* peak is partially masked by small-angle scattering due to porosity of the nanomaterials. In any case, a basal spacing of 9.7 Å is consistent with the fully dehydrated state [134]. Moreover, when comparing Laponite to pre-Laponite, the FWHM of the *00l* peaks in pre-Laponite is broader, indicating weaker stacking order, that is a smaller number of stacked layer and/or larger distribution of interlayer distances. In the following, we'll consider only a variable number of stacked layers. Additionally, the patterns show *hk* bands rather than *hkl* peaks in both cases, which indicates turbostratic disorder, resulting from the lack of in-plane correlation between stacked sheets – a common stacking mode observed in smectite materials [135]. *hk*

indices refer to the two-dimensional unit cell within the layer. It is a centered rectangular unit cell so that *h,k* indices verify *h+k* even. Unit cell parameters are $a = 5.26$ Å and $b = a\sqrt{3}$. The in-plane coherence length can be determined from the slope of the band's rising edge [136]. Detailed demonstration can be found in [137] for uncorrelated atomic lines and similar results can be obtained for uncorrelated atomic planes, as is illustrated in Figure IV.3. Although the band positions are the same in both samples, pre-Laponite shows a smoother rising edge. This shows that, despite a similar global structure, pre-Laponite exhibits reduced long-range order. The reduced long-range order means either a smaller average lateral dimension of the TOT sheets or a large amount of in-plane structural defects in pre-Laponite. This observation is in agreement with the interpretation we proposed for the early dehydroxylation in pre-Laponite compared to Laponite.

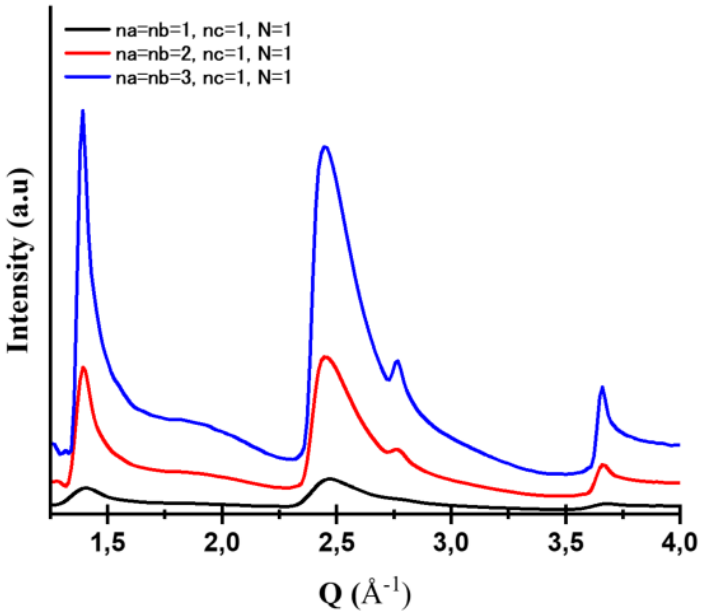

Figure IV.3: Calculated XRS pattern with varying in-plane sizes. Simulations are performed with fixed parameter $\boldsymbol{n_c}$ =1, while varying in-plane dimensions: $\boldsymbol{n_a} = \boldsymbol{n_b} = 1$ (black), $\boldsymbol{n_a} = \boldsymbol{n_b} = \mathbf{2}$ (red), and $\boldsymbol{n_a} = \boldsymbol{n_b} = \mathbf{3}$ (blue).

To determine the lateral dimension of the sheets, we used the atomic model for a Laponite layer determined by Molecular Dynamics simulations (**Chapter III, §2.1**). The layer size in the model is A = 52.6 Å and B = 45.6 Å. We calculated the scattering diagram of n_c randomly stacked layers distant from d_{001}, the layer dimensions being given by $n_a \cdot A$ and $n_b \cdot B$ and we convoluted it to the experimental resolution using a homemade python program (see **§3** in **Chapter III**). When dimensions were smaller than the ones of the initial layer, we kept only a part of the layer with the right size and when they were larger, we took advantage of the in-plane periodicity of the layer. Comparison between calculated and experimental intensities were made with $n_a = n_b$, to simplify our approach.

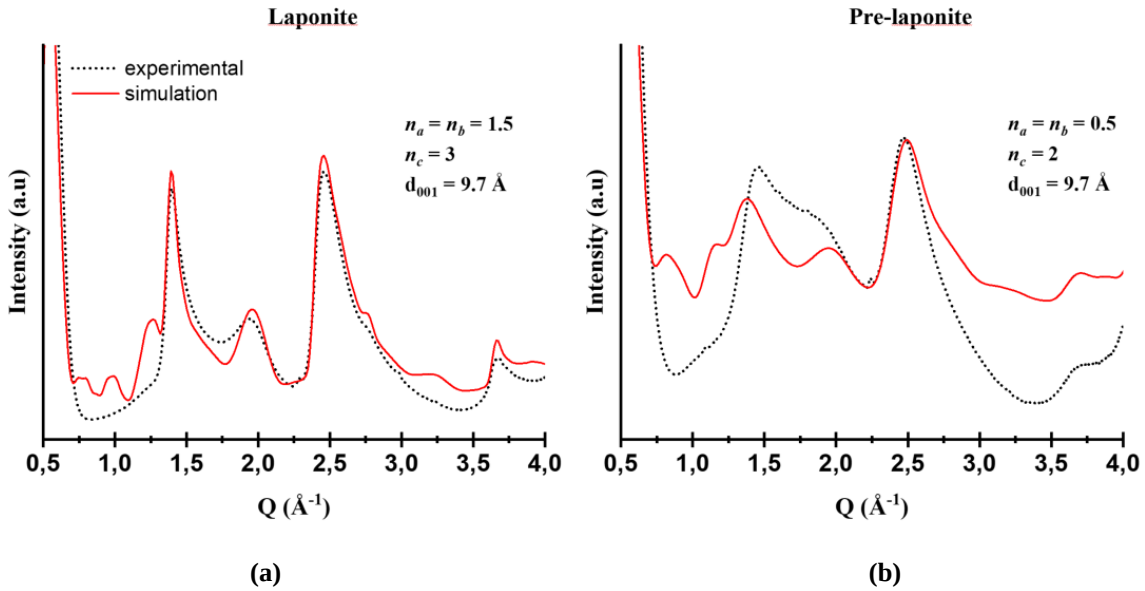

Figure IV.4: Experimental and calculated patterns for (a) Laponite and (b) pre-Laponite.

Figure IV.4 presents the calculated and experimental XRS diagrams for Laponite and pre-Laponite, with the best agreement obtained for $n_a = n_b = 1.5$, $n_c = 3$ for Laponite and $n_a = n_b = 0.5$, $n_c = 2$ for pre-Laponite. The global agreement between calculated and experimental diagrams shows that the structural model we used for Laponite is correct, which is important with respect to the numerical simulations that we'll present in the following concerning the uptake of hydrogen and its structuration. Moreover, we have quantified the difference between Laponite and pre-Laponite in terms of the extent of the order: the in-plane coherence lengths differ by a factor 3 (which means a factor 9 for the coherence surfaces) and Laponite particles consist in $n_c = 3$ stacked layers in average while $n_c = 2$ in pre-Laponite. These results are summarized in Table IV.2.

Furthermore, the position of the *003* reflection is in good agreement between the experimental and calculated patterns for Laponite. However, for pre-Laponite, the reflection is shifted towards a smaller Q-value in the experimental pattern. This shift shows that the basal spacing of pre-Laponite is slightly larger than 9.7 Å, indicating that the interlayer spacing in pre-Laponite is slightly higher compared to Laponite.

Table IV.2: Lateral dimensions of Laponite and pre-Laponite sheets along crystallographic axes *a* and *b*, along with the average number of stacked sheets along *c* axis, determined by comparing experimental XRS patterns to simulated patterns.

Samples	$n_a = n_b$	n_c	Lateral dimensions (nm)	
			along *a*	along *b*
Laponite	1.5	3	~7.9	~6.8
Pre-laponite	0.5	2	~2.6	~2.3

1.2. Pair Distribution Function analysis

To examine the atomic structure within Laponite and pre-Laponite using PDF analysis, a powerful method allowing one to treat all scattering feature and to account for both order and disorder in direct space, presented in **§5.3 in Chapter II**, it is essential to access a wider Q-range. Figure IV.5(a) presents the background-corrected diffraction pattern obtained at the CRISTAL beamline.

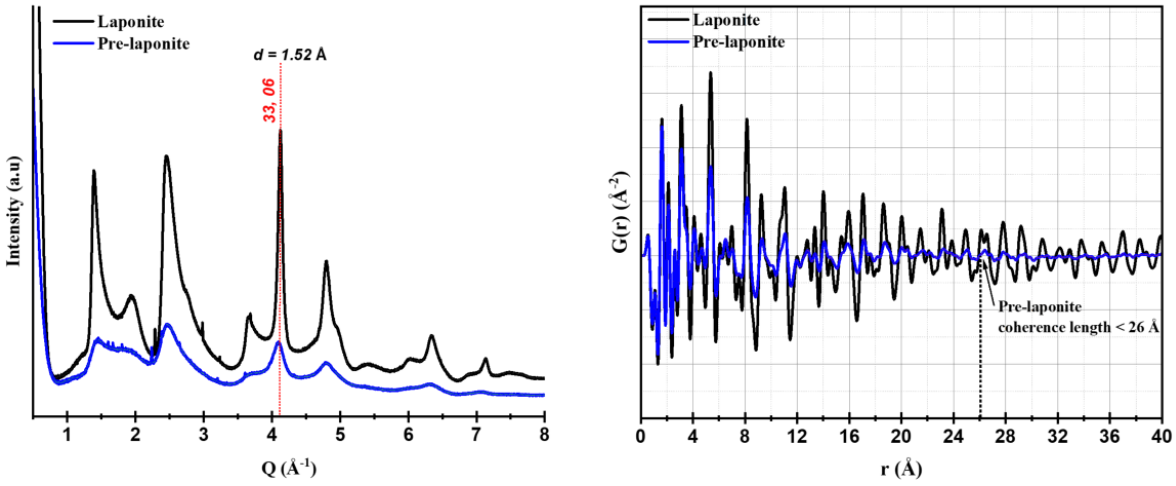

(a) **(b)**

Figure IV.5: (a) XRS patterns of Laponite (black) and pre-Laponite (blue) powdered samples, (b) PDF patterns was obtained using a Q_{min} of 0.3 Å^{-1} and Q_{max} of 14.8 Å^{-1}, with a real-space resolution of Δr = 0.42 Å.

A brief aside before considering the PDF. The position of the *06* reflection varies with the composition of the octahedral sheet. Trioctahedral smectites show *06* reflections at 1.52 – 1.54 Å, while values between 1.49 and 1.51 Å indicate dioctahedral smectites [138]. The studied Laponite and pre-Laponite display a reflection at ~1.52 Å, confirming their characterization as trioctahedral smectites, as expected.

The PDF patterns shown in Figure IV.5(b) exhibit similar pair correlation distances over a large range in interatomic distances in Laponite and pre-Laponite. Together with the previous calculations of scattering diagrams, it shows that their atomic arrangements are comparable. However, the decay of the PDF intensity for pre-Laponite, from low- to high-r regions, points towards a smaller coherent domains size in pre-Laponite. The coherence length deduced from XRS diagrams calculations is indicated in Figure IV.5(b), in fairly good agreement with this decay.

4. Complementary characterization

4.1. FTIR, ^{29}Si NMR, and XANES spectroscopy

IR spectra of Laponite and pre-Laponite KBr pellets are displayed in Figure IV.6. The trioctahedral nature of this smectite, already deduced from XRS diagrams and their analysis, is also evidenced here with the low-intensity band at 3648 cm^{-1}, corresponding to the stretching vibrations of Mg_3OH groups [139] (inset Figure IV.6). Additionally, a shoulder at 3713 cm^{-1} (inset Figure IV.6) is attributed to the stretching vibrations of Mg_2LiOH. A broad band from 3700 to 3000 cm^{-1} is attributed to the OH stretching vibrations of H_2O molecules adsorbed on both, clay samples and KBr used for the IR measurements. A small peak observed at 2715 cm^{-1} is assigned to OD stretching vibrations [140], as the samples were synthesized using deuterated water.

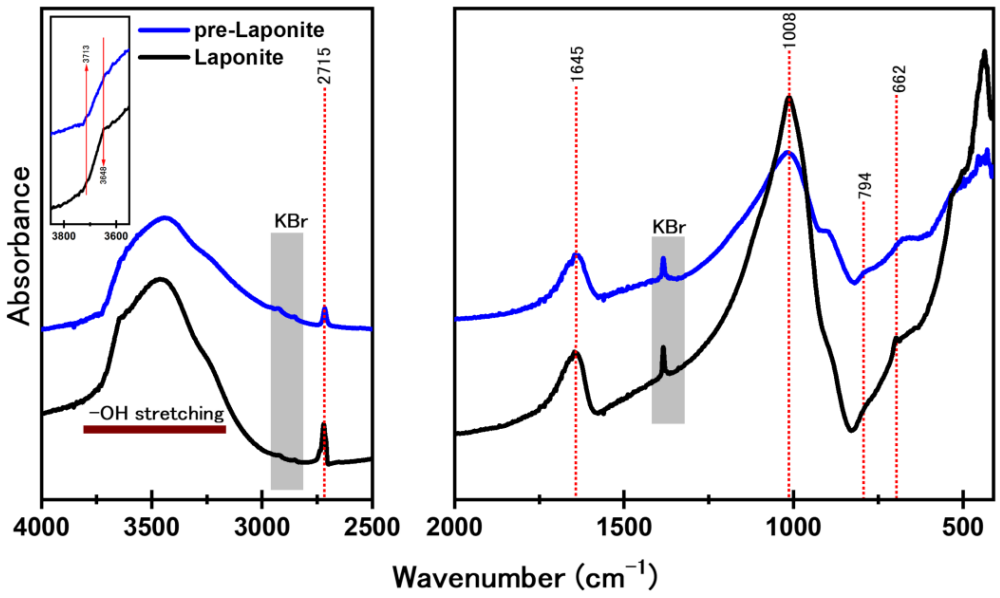

Figure IV.6: Infrared spectrum of Laponite (black) and pre-Laponite (blue) pellets.

The peak observed around 1645 cm^{-1} corresponds to the bending vibrations of adsorbed H_2O molecules [141]. The intense band at 1008 cm^{-1} is attributed to Si–O stretching vibrations within the tetrahedral sheets. Additionally, a shoulder near 794 cm^{-1} corresponds to Ox_b–Si–Ox_a bending vibrations, where 'Ox_b' represents the basal oxygen atoms, and 'Ox_a' refers to the apical non-bridging oxygen atoms (Figure IV.7). The OH bending vibration of Mg_3OH is observed at 662 cm^{-1}. In addition, the region below 500 cm^{-1} consists of complex bands attributed to overlapping of Si–O–Mg and Si–O –Si bending modes [142].

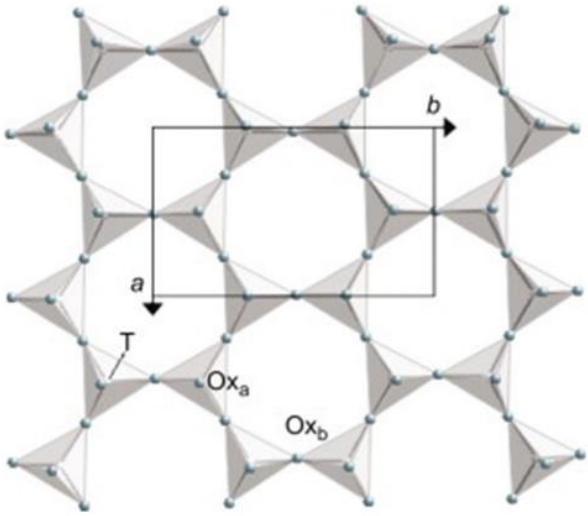

Figure IV.7: Overhead diagram of the tetrahedral sheet. Ox_a = apical pxygen atoms; Ox_b = basal oxygen atoms; T = tetrahedral cations (Si^{4+}); a and b refer to the unit cell parameters, adapted from [143].

To conclude, the indexation of the modes is in line with the structure proposed to analyze XRS diagrams and the identical IR spectra of Laponite and pre-Laponite confirm that their chemical compositions and bonding environments are the same. However, ^{29}Si NMR offers more detailed information regarding the local tetrahedral silicon environments. Direct excitation spectra for both Laponite (a) and pre-Laponite (b) are shown in Figure IV.8, with the data fitted using three Gaussian functions, interpreted and summarized in Table IV.3, based on the number of SiO_4 tetrahedron connected via bridging oxygen atoms. The Q^3 environment denotes an SiO_4 group with one terminal oxygen and three common oxygen vertices with three other SiO_4 tetrahedra, $Si(OMg)(OSi)_3$ and $Si(OLi)(OSi)_3$. The spectra of both materials are dominated by an intense peak (in blue), resonating at -93.3 ppm for Laponite and -91.8 ppm for pre-Laponite, which was straightforwardly assigned to the Q^3. Moreover, additional signal of lower intensity is observed at -83.3 ppm. Based on the literature, this signal is attributed to Q^2 environments, where a silicon tetrahedron is only linked to two other octahedra by a common oxygen atom. They are mostly present as $Si(OMg)(OSi)_2OH$ silanols, at the clay broken edge [145][146][147][148]. Additionally, a shoulder observed at -77.8 ppm can be attributed to the $Q^{2'}$ site environment, to

$Si(OLi)(OSi)_2OH$. This assignment aligns with the substitution of Mg^{2+} by Li^+ at octahedral sites, which leads to slightly more covalent Li–O bonds compared to Mg–O bonds. This effect can be attributed to the difference in electronegativity between lithium (1.2) and magnesium (1.0), which induces de-shielding of the silicon atoms in the tetrahedral layer. The observed bump in the spectra, indicated by asterisks, corresponds to the spinning sideband [148].

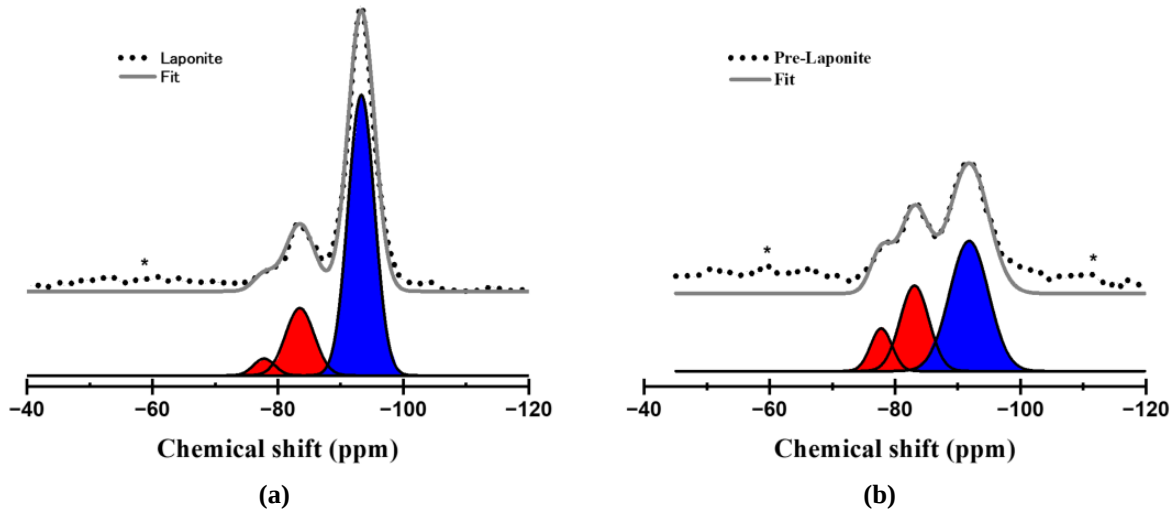

Figure IV.8: ^{29}Si MAS NMR spectra of (a) Laponite and (b) pre-Laponite. The experimental data are shown as black dotted points, with the gray line representing the sum of the three fitted gaussian components (in red and blue). Spinning sidebands are marked with an asterisk.

In brief, ^{29}Si NMR spectra are composed of three main peaks corresponding for the most intense one to Q^3 sites and for the two other ones, to Q^2 sites at the layer edges. It shows that Laponite and pre-Laponite have very similar Si environments.

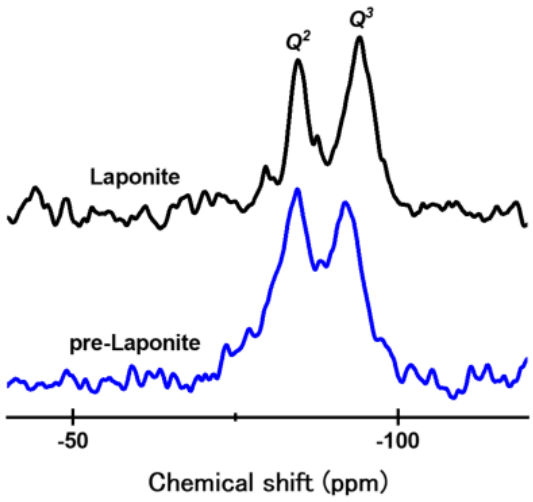

Figure IV.9: CPMAS NMR spectra of Laponite (black) and pre-Laponite (blue).

The main difference between the two samples arises from the $Q^3/totQ^2$ area ratio ($totQ^2$ referring to Q^2+ $Q^{2'}$). Pre-Laponite ($Q^3/totQ^2$ = 1.5) shows a notably lower ratio compared to

Laponite ($Q^3/totQ^2$ = 3.2). This lower ratio is compatible with a reduced layer size of pre-Laponite, which decreases the surface-to-edge ratio and, consequently, the proportion of Q^3 sites. The peaks assignments and peak intensity-layer size relation are further supported by the enhanced Q^2 signal through H-to-Si cross-polarization (Figure IV.9). This enhancement indicates that Q^2 sites are primarily located at the particle broken edge.

Table IV.3: Summarized fitting parameters from ^{29}Si MAS NMR, including chemical shifts (δ), peak maximum intensities (*I*), and standard deviation (σ) of the Gaussian functions, for three distinct Q^n environments in Laponite and pre-Laponite samples.

	Q^3 ; Si(OMg)(OSi)$_3$			**Q^2 ; Si(OMg)(OSi)$_2$OH**			**$Q^{2'}$; Si(OLi)(OSi)$_2$OH**		
	δ (ppm)	***I***	**σ (ppm)**	**δ (ppm)**	***I***	**σ (ppm)**	**δ (ppm)**	***I***	**σ (ppm)**
Laponite	-93.3	100	2.1	-83.5	24	2.3	-77.8	6	1.7
pre-Laponite	-91.8	33.5	3.1	-83.1	22	2.3	-77.8	11	1.7

Figure IV.10 (a) presents the Mg K-edge XANES spectra for Laponite and pre-Laponite samples. These spectra reveal a triplet structure with bands located at 1310, 1314, and 1318 eV, along with a broad peak around 1330.7 eV and a distinct feature at 1324 eV. Additionally, a shoulder at 1315 eV is observed. The bands are labeled A, B, C, D, and E. They are consistent with those found in 2:1 trioctahedral smectites (see Figure IV.10 (b)). Furthermore, the observed features are assigned based on literature [149], where band B is primarily related to the first oxygen shell, while the other peaks are mainly attributed to multiple scattering effects and scattering paths at longer distances. The XANES spectra for the Mg K-edge of Laponite and pre-Laponite exhibit similar absorption features, confirming that both samples consist in a trioctahedral layer and not in a dioctahedral one.

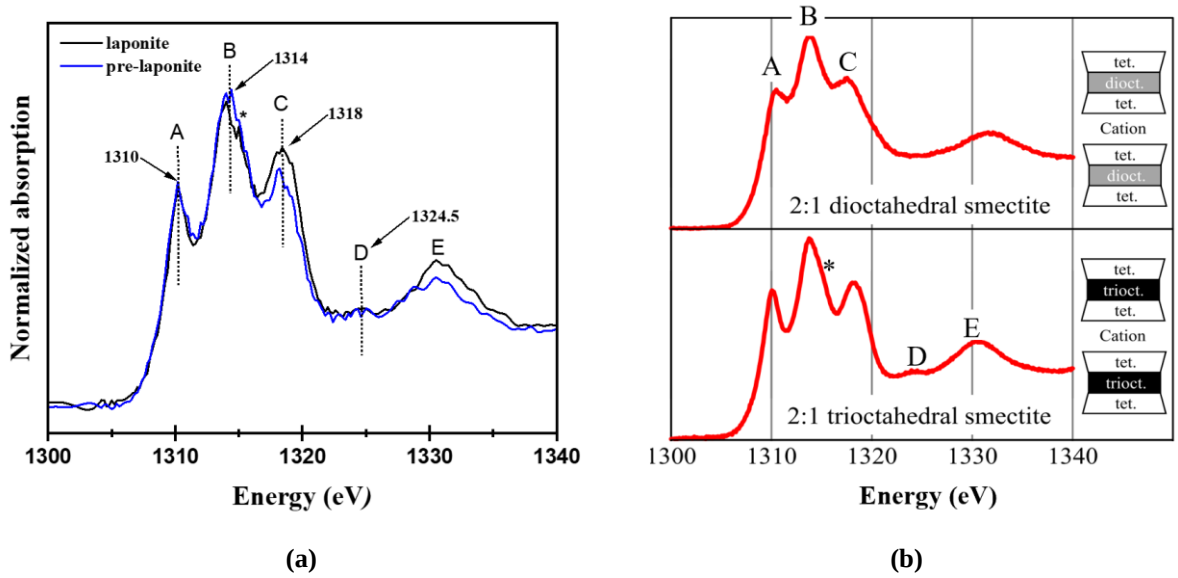

Figure IV.10: XANES spectra at the Mg k-edge of (a) Laponite (black) and pre-Laponite (blue) pellets, (b) 2:1 di- and trioctahedral smectite, adapted from [150].

Measurements performed at the Si_4^{4-} K-edge spectra for Laponite and pre-Laponite are shown in Figure IV.11(a). The white band A' in the figure corresponds to the transition of Si 1s electrons to the 3p states. Both Laponite and pre-Laponite exhibit similar spectra at the silicon k-edge, corroborating that they share a comparable Si environment at the atomic level. However, the more defined post-edge features (C', D', and E') in Laponite suggest a higher degree of homogeneity among the Si environment, compared to pre-Laponite. It can be attributed to the reduced size of layer sheets and the eventual presence of defects in pre-Laponite: there is a larger deviation from the average environment experienced by Si atoms in pre-Laponite than in Laponite, due to either a larger edge/bulk ratio or local stress effect

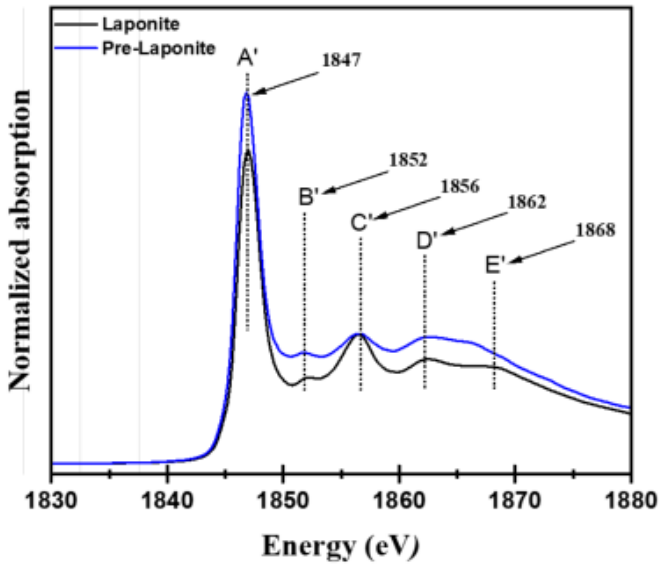

Figure IV.11: XANES spectra at the Si K-edge for (a) Laponite (black) and pre-Laponite (blue) pellets.

5. Textural properties

The nitrogen adsorption-desorption isotherms of Laponite (black) and pre-Laponite (blue) are shown in Figure IV.12(a). Prior to analysis, the samples were treated at 150°C under secondary vacuum to remove adsorbed water. The distinct shapes of the isotherms, combined with the t-plot and BET analysis data, reveal a detailed picture of the materials' porosity and surface area, highlighting key differences between the two materials.

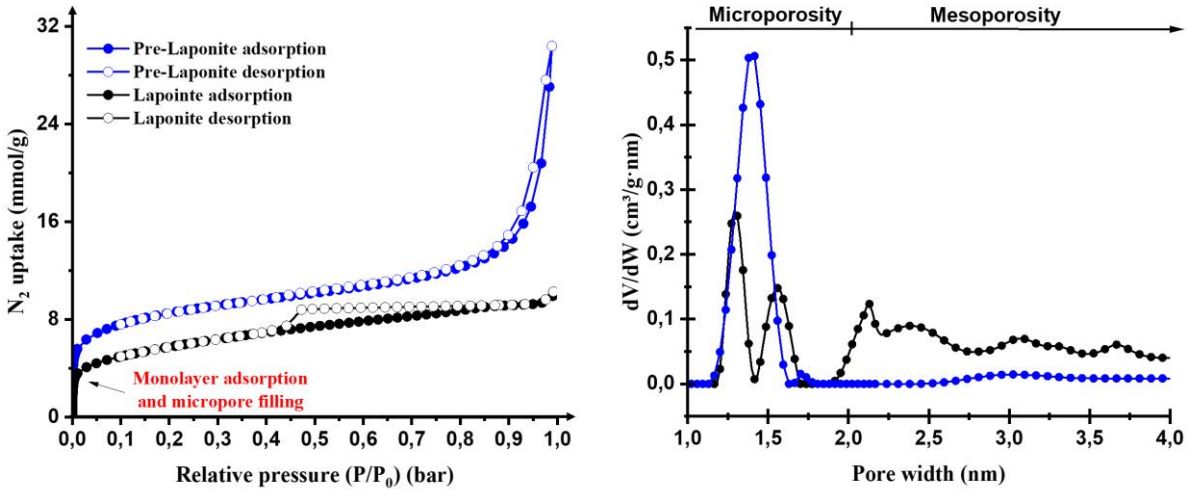

(a) **(b)**

Figure IV.12: (a) Nitrogen adsorption-desorption isotherm of Laponite (black) and pre-Laponite (blue), (b) pore-size distribution by DFT using cylindrical pore geometry, where $\boldsymbol{dV/dW}$ represents the differential pore volume (in cm^3/g) as a function of pore width (in nm).

5.1. Analysis of isotherm shapes and pore size

The adsorption-desorption isotherm for pre-Laponite exhibits a nearly reversible Type II profile, typical of macroporous materials (pore size > 50 nm). The gradual increase in nitrogen uptake with increasing relative pressure (at high pressure) suggests an accessible macroporous network. At the same time, the isotherm shows a significant uptake at low relative pressures ($P/P_0 < 0.01$), characteristic of microporosity (pore size < 2 nm). This combination of Type I and Type II characteristics implies a composite pore structure in pre-Laponite, featuring both micropores and macropores.

Laponite primarily exhibits Type I isotherm with the steep uptake at low pressures (microporosity), but the slight rise in uptake at higher pressures indicates some mesoporous (2 nm < pore size < 50 nm) contributions, leading to a Type I/IV composite isotherm.

5.2. Hysteresis and pore geometry

The hysteresis loops observed in both pre-Laponite and Laponite adsorption isotherms provides further insights into their pore geometries. Pre-Laponite shows an H3-type hysteresis loop, which is often associated with slit-shaped pores within aggregated plate-like particles, commonly observed in clay materials [151]. Laponite, on the other hand, displays an H4-type hysteresis loop, which is indicative of narrower slit-like pores. Let us consider that these slit-like pores correspond mainly to the interlayer space, which is a rather natural interpretation. Narrower interlayer space may be related to the larger in-plane coherence length and to better stacking in Laponite than in pre-Laponite. Similarly, decrease of the interlayer distance between graphene sheets is observed during carbonisation of PAN fibres, when the in-plane coherence length and the number of sheets increase [152]. The H4 hysteresis in Laponite could suggests a denser packing of particles, while the H3 hysteresis in pre-Laponite implies more open, accessible pores.

5.3. Surface area and microporosity

The BET model applied within the relative pressure range of 0.05 to 0.3 for Laponite and 0.05 to 0.1 for pre-Laponite allowed for determination of the total surface area (S_{BET}) for both samples. Pre-Laponite (S_{BET} = 472 m^2/g) exhibits a slightly higher surface area compared to Laponite (S_{BET} = 445 m^2/g).

Figure IV.12(b) presents the pore-size distribution of Laponite and pre-Laponite, obtained through standard Density Functional Theory (DFT) analysis of N_2 isotherm. The DFT model assumes a silica adsorbent surface and applies NLDFT equilibrium corrections tailored for cylindrical pores. Although the interlayer structure in Laponite and pre-Laponite is slit-like, this geometry was not available within the software options (ASAP 2020 Plus). The resulting data indicates that pre-Laponite is predominantly microporous, with a micropore volume, based on peak area, approximately twice higher than that in Laponite.

A detailed interpretation of the N_2 adsorption isotherm is still in progress.

Take home messages

- **ICP-AES analysis** reveals that the chemical composition of Laponite and pre-Laponite closely matches the nominal formula $[Si_8]$ $[Mg_{4.8}Li_{1.2}]$ $Na_{1.2}$ $O_{20}(OH)_4$.

- **TGA/DTG analysis** shows that dehydroxylation occurs at lower temperature in pre-Laponite compared to Laponite; it could be related to a reduced size of the layers or the presence of defects in pre-Laponite.

- **XRS and PDF analyses reveals** that Laponite and pre-Laponite share the same trioctahedral TOT structure, which is well captured by MD simulations. Comparison between experimental and calculated diagrams show that pre-Laponite exhibits reduced long-range order within the layers (coherent surfaces are 9 times smaller than in Laponite) and a lower degree of stacking. In-plane coherence lengths are corroborated by PDF analysis.

- **The local order** of Laponite and pre-Laponite shows largely similar bonding environments, as evidenced by their IR spectra, thus corroborating XRS analysis. The ^{29}Si NMR spectra reveal comparable silicon environments in both materials and point towards a reduced layer size in pre-Laponite, consistent with reduced coherent lengths found by XRS (although reduced coherence length may correspond to reduced size and/or to the existence of defects). Additionally, XANES spectra at the Si K-edge and Mg K-edge are rather similar in Laponite and pre-Lapointe, with however less homogeneity of the Si sites, in agreement again with reduced layer size and/or the presence of defects in pre-Laponite.

- **N_2 isotherms** reveal significant differences in the pore structure and surface area of Laponite and pre-Laponite. Pre-Laponite exhibits a composite pore structure with both microporosity and macroporosity, whereas Laponite is primarily microporous with mesoporous contributions. Hysteresis analysis suggests that Laponite has narrower slit-like pores, corresponding to the interlayer space.

This page was intentionally left blank.

Chapter V. Hydrogen adsorption and neutron insights

In the following chapter, the hydrogen adsorption mechanism is investigated on dried Laponite and pre-Laponite, combining isotherm studies, INS, and neutron diffraction. Starting with adsorption isotherms, supported by GCMC simulations, two adsorption regions are identified at 40K: the interlayer, where adsorption is described by Langmuir model, dominating at low pressure with monolayer saturation below 1 bar, and the outer surface, with non-saturated Freundlich behavior. INS then evidence three adsorption sites in both Laponite and pre-Laponite. Sites 0 and 1 are found to be more numerous in pre-Laponite compared to Laponite. Rotation is hindered in site 0 while the rotational energy barrier in site 1-clearly higher than that in site 2. Site 2 is attributed to H_2 axis aligns parallel to the adsorption surface with an orientational potential well of -96K in Laponite and -80K in pre-Laponite. Site 0 could be a hydrogen dissociation site, whereas sites 1 and 2 are attributed to interlayer-adsorbed H_2. One also investigates the structuring of adsorbed H_2/D_2 using WANS, the analysis being supported by atomistic calculations based on GCMC simulations. The results indicate a mean D_2-D_2 separation of ~3 Å, where part of D_2 molecules align within the hexagonal cavities of the closest layer. Furthermore, SANS shows the impact of D_2/H_2 adsorption on the *001* peak, corroborating the filling of the interlayer by these molecules. Finally, the chapter highlights the quantum effect observed between H_2 and D_2 in the pre-Laponite interlayer at 40K.

1. Literature review on H_2 adsorption in clays

H_2 adsorption on clay materials remains relatively underexplored. In the following, the emphasis is on studies carried out on smectites, since Laponite and pre-Laponite are smectites.

L. Masci et al. [78] investigated H_2 adsorption at 77K – 1bar and 298K – 120 bar on Ni-functionalized smectite; specifically saponite.

Ni-functionalized saponite outgassed at 150°C shows a modest uptake of approximately 0.02 $wt\%$ H_2 at 77K – 1bar and below 0.05 $wt\%$ H_2 at 298K – 120bar. It is concluded that Ni-functionalization has no impact on H_2 adsorption. For Ni-pillared sample ($Ni(OH)_2$ pillars in the interlayer), outgassed at 70°C, hydrogen uptake at 77K – 1 bar (0.11 $wt\%H_2$) is higher compared to outgassing at 150°C (Figure V.1). It is assumed that the dehydration of the interlayer at 150°C leads to its collapse despite the presence of the pillars.

It should be noted that the adsorption of hydrogen by the synthesis precursor has also been studied in ref. [78]. It is the equivalent of pre-Laponite for Laponite. H_2 uptake is found higher for this precursor: up to 0.19 $wt\%$ at 77K and 1 bar and up to 0.12 $wt\%$ at 298K and 120 bar. However, the reasons why adsorption is better in pre-saponite than in saponite are unknown.

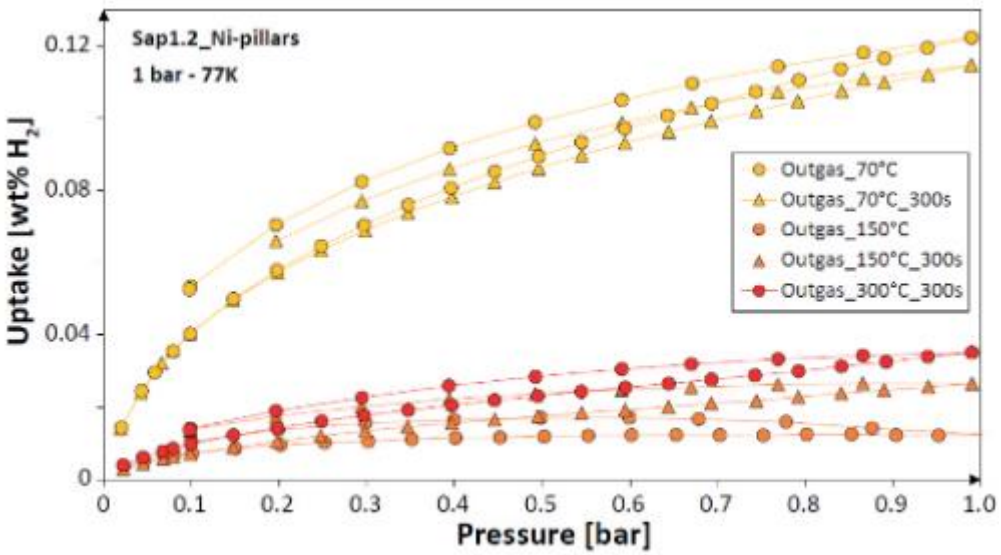

Figure V.1: Hydrogen adsorption-desorption isotherm at 77K – 1 bar on Sap1.2_Ni_pillars at different outgassing temperatures [78]. Sap 1.2 refers to the saponite nominal composition: $Si_{8-x}Al_xMg_6O_{20}(OH)_4Na_x$ with x=1.2.

Another study by *J. Edge* [16] investigated H_2 adsorption on various Laponite samples, reporting that partially hydrated Na-laponite and Ca-laponite (RD) rapidly physisorb up to 0.6 $wt\%$ H_2 at 77 K and 80 bar. For Ca-laponite and Mg-laponite (EL), adsorption reaches up to

0.7 $wt\%$ under the same conditions. Remarkably, Mg-laponite (B) exhibits an uptake of 0.6 $wt\%$ H_2 at 77 K at only 1 bar. At room temperature, the saturation uptake for all samples is below 0.1 $wt\%$, above 100 bars. RD refers to the research grade of the molecular formula $Si_8Mg_{6-x}Li_xM^{c+}_{x/c}O_{20}(OH)_4$, with x between 0.3 and 0.4, while EL refers to the high-cationic density grade with x = 0.95. For the fluorosilicate grade "B," the $(OH)_4$ group is replaced by $[(OH)_{2.5}F_{1.5}]$. Furthermore, neutron diffraction [153] on partially hydrated Ca-laponite with 1.0 – 1.5 water content per calcium allow J. Edge *et al.* to determine the period (basal spacing) perpendicularly to the layers. It is equal to about 12.3 Å. Based on quasi-elastic neutron scattering measurements [153], the authors asserted that part of the molecules in the interlayer is located close to the partially hydrated cations, the rest of them performing jump diffusion. At 40K, under 0.49 bar, the H_2 diffusion coefficient is equal to $2.3 \pm 0.5\ 10^{-5}$ cm^2s^{-1}, an order of magnitude smaller that the value extrapolated for bulk H_2.

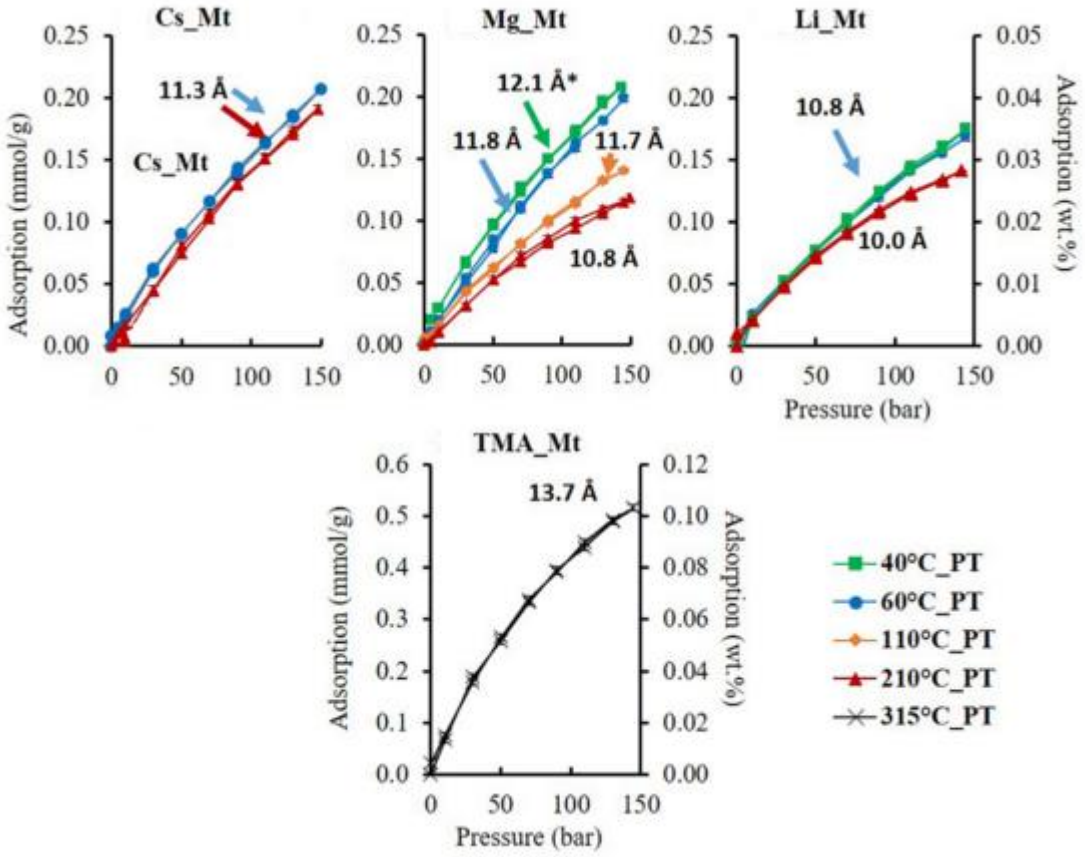

Figure V.2: Hydrogen adsorption isotherms at 25°C on montmorillonite, up to 150 bar [78]. The values given in Å represent the basal spacing, and 'PT' refers to the temperature of the drying step in °C.

Ziemiański and Derkowski [77], investigated H_2 adsorption on montmorillonite (Mt) at temperatures ranging from 25°C to 70°C and pressures up to 150 bars. The samples were pre-

dried at temperatures between 40°C and 315°C to reduce water content, resulting in varying basal spacings. The results show that H_2 intercalates into the montmorillonite interlayers with a basal spacing larger than 10.8 Å. It is reported that more than 50% of adsorbed H_2 is located in the interlayers. Moreover, the adsorption of H_2 consistently decreases as the temperature increases from 25°C to 70°C. Focusing on Mg_Mt at 145 bars, as shown in Figure V.2B), one sees that the decrease in interlayer height due to sample drying at progressively higher temperatures is accompanied by a decrease in H_2 adsorption. Interestingly, TMA-Mt, with a high basal spacing of 13.7 Å, with tetramethylammonium (TMA) acting as pillars, shows an enhanced uptake above 0.1 $wt\%$ at 25°C and 150 bar.

C. Mondelli et al. [155] studied hydrogen adsorption and its diffusion using quasi-elastic neutron scattering in Na-montmorillonite with varying Fe(III) ratios: their nominal composition is $Na_{0.33}[(Al_{1.67-x}Fe_xMg_{0.33})Si_4O_{10}(OH,F)_2].nH2O$ with x=0, 0.017 and 0.67. Experiments were performed on samples dried at 120°C under vacuum, with a basal spacing of about 13Å. The authors conclude that structural Fe (III) does not affect the sorption, in agreement with previous experiments reported by *M. Didier et al.* [154]. It does not affect either the diffusion properties. H_2 adsorption at 90°C exhibited saturation around 50 bars, with an average uptake of 0.2= $wt\%$. The H_2 diffusion coefficients at 40 bars in the temperature range 25-300K fall in the interval 0.1-1 10^{-7} m^2s^{-1}.

Based on studies of H_2 adsorption on swelling smectites, it appears that adsorption in the interlayer increases with the interlayer height [77, 78] and that there is a minimum interlayer height for the adsorption of H2 in the interlayer. In montmorillonite, it corresponds to a basal spacing of 10.8 Å [77]. Interlayer height can be tailored through the degree of hydration or interlayer cationic species [16, 153], or by using other sorts of pillars than the hydrated cations, for instance $Ni(OH)_2$ pillars in ref. [78]. Our study, presented below, focuses on hydrogen adsorption in dehydrated Laponite and pre-Laponite, with an interlayer spacing of about 9.7 Å. We will show that, contrary to what is reported for montmorillonite with an interlayer spacing below 10.8 Å for high temperature and high pressure, a significant amount of the hydrogen adsorbed in (pre-)Laponite is in the interlayer at low temperature and low pressure. At low pressure, we did not observe quasi-elastic scattering, so we will not discuss the quasi-elastic results in refs. [153, 155], obtained in different conditions, in particular for larger basal spacings.

2. Hydrogen adsorption in Laponite and pre-Laponite

Prior to the H_2 adsorption isotherm measurements, Laponite and pre-Laponite were outgassed at 150°C for 6 hours under secondary vacuum, to remove water from the samples.

2.1. Measurements at 298K – 100 bars and 77K – 1 bar

In this study, H_2 (or D_2) uptake is expressed either in mmol of H_2 (or D_2) per gram of (pre-)Laponite or in weight percent ($wt\%$) using the following formula:

$$\boldsymbol{wt\%\ H_2(D_2) = uptake\ in\ mol/g\ \times M_{H_2}} \qquad \textbf{(V.1)}$$

where $M_{H_2(D_2)}$ is the molar mass of H_2 (D_2).

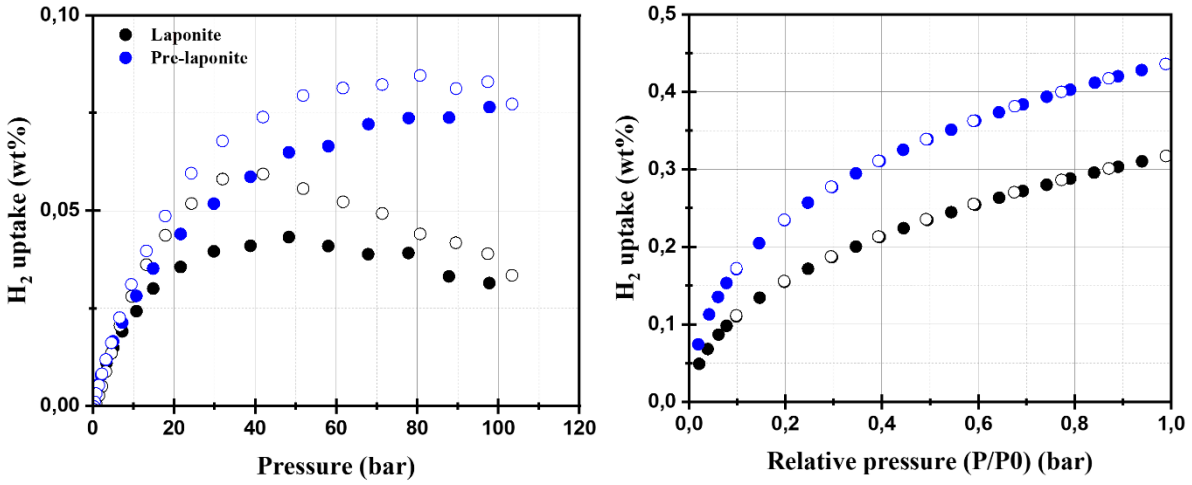

(a) **(b)**

Figure V.3: Hydrogen adsorption (filled circles)-desorption (empty circles) isotherms for Laponite (black) and pre-Laponite (blue) measured at (a) 298 K and 120 bars, and (b) 77 K and 1 bar.

H_2 sorption isotherm measurements at room temperature under high pressures for Laponite and pre-Laponite present significant challenges due to (1) potential gas leakage caused by the high diffusivity of H_2 and (2) a low accuracy resulting from relatively low H_2 uptake capacities. Despite these limitations, the data in Figure V.3(a) indicate that H_2 uptake in Laponite is lower than in pre-Laponite, although the anomalous curve shape above 40kbar is not well understood. In the precursor pre-Laponite H_2 uptake reaches approximately 0.08 $wt\%$ at 298 K and 100 bars. Additionally, H_2 isotherm measurements at 77 K and 1 bar shown in Figure V.3(b), demonstrates a 1.5-fold increase in H_2 uptake in pre-Laponite compared to Laponite. These measurements are reliable to within ±0.01 $wt\%$ H_2 at 1 bar, as confirmed by reproducibility tests on commercial Laponite (LapRD).

This observed difference in H_2 uptake between Laponite and pre-Laponite can potentially be linked to variations in specific surface area, a factor known to correlate with H_2 adsorption at 1 bar and 77K across a variety of porous materials as previously mentioned [156], [157], [158]. Figure V.4 presents a comparison of S_{BET} values and H_2 uptake among various clay samples (measurements done by Valérie Magnin) and the current samples of interest. Generally, the correlation line between S_{BET} and H_2 uptake holds across these materials. However, pre-Laponite exhibits a deviation to this linear behavior.

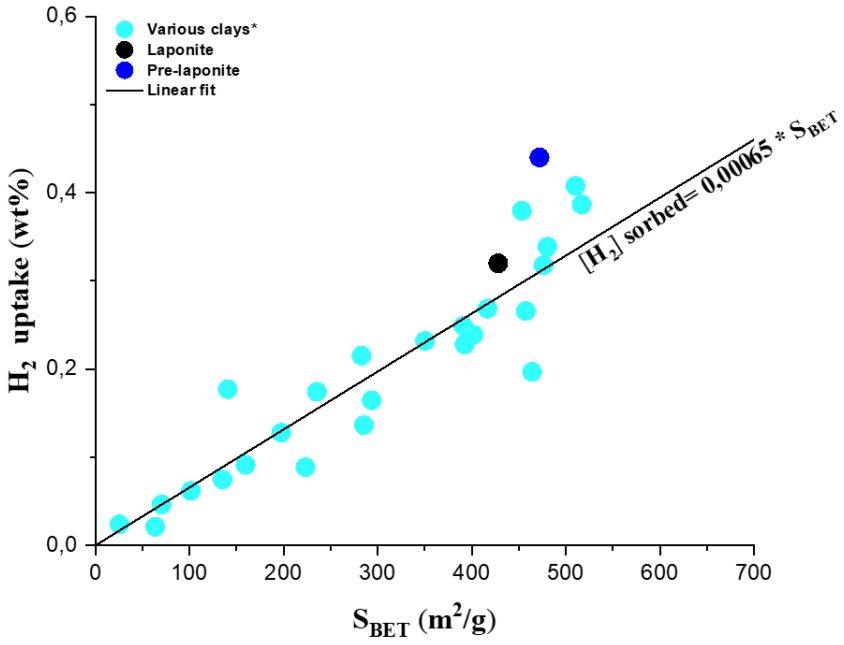

Figure V.4: Correlation between S_{BET} and H_2 uptake at 1 bar and 77K across various clay samples, with Laponite (black) and pre-Laponite (blue) highlighted.

It's important to remind that the S_{BET} is calculated based on N_2 adsorption isotherms, with N_2 molecules having a kinetic diameter of 3.64 Å—larger than the kinetic diameter of H_2 (2.84 Å). This size difference implies that certain sites may be accessible to H_2 but not to N_2, potentially leading to enhanced H_2 uptake that is not fully predicted by N_2-based measurements. This effect becomes particularly relevant in materials with microporosity, where smaller molecules can preferentially adsorb. Furthermore, in Laponite and pre-Laponite, the situation becomes more complex to understand the reason behind the enhanced adsorption, because several adsorption sites (Figure V.5) with possible varying affinities for H_2 should be considered. Such adsorption sites are of course also present in other smectites but most smectites have much larger layer size and stacking, so that the dominant site is the interlayer, if it height suits for the adsorbed molecules of interest. At 77K, it can be challenging to differentiate between adsorption sites because the thermal energy may mask subtle differences in adsorption behavior. To better

resolve the distinct adsorption sites within these materials, we aimed to conduct hydrogen isotherm measurements at a lower temperature, 40K, where reduced thermal energy allows a clearer differentiation between adsorption sites.

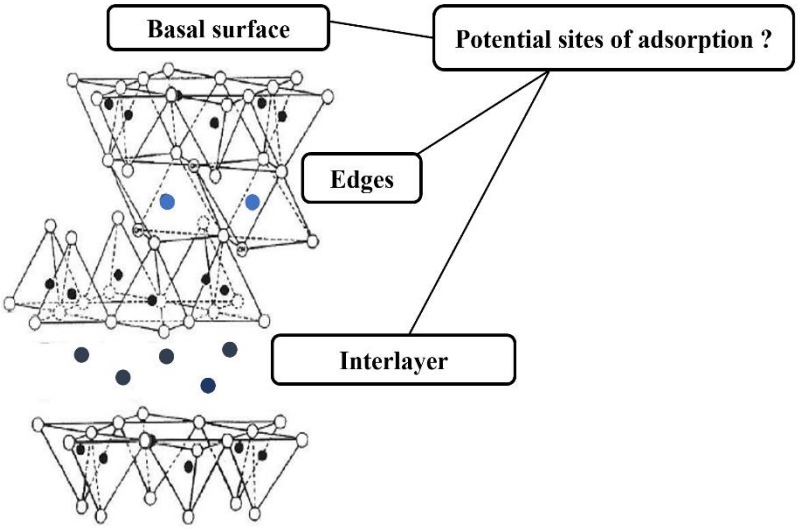

Figure V.5: Schematic representation of potential adsorption sites in layered material, highlighting the basal surface, edges, and interlayer regions.

2.2. Measurements at 40K – 1bar

Figure V.6. presents the H_2 adsorption isotherms for pre-Laponite at 40K up to 1bar. It is important to note that the Laponite sample used here is representative but not identical to the one analyzed in **Chapter IV** (correlation lengths may vary between two syntheses) and in the upcoming neutron investigation.

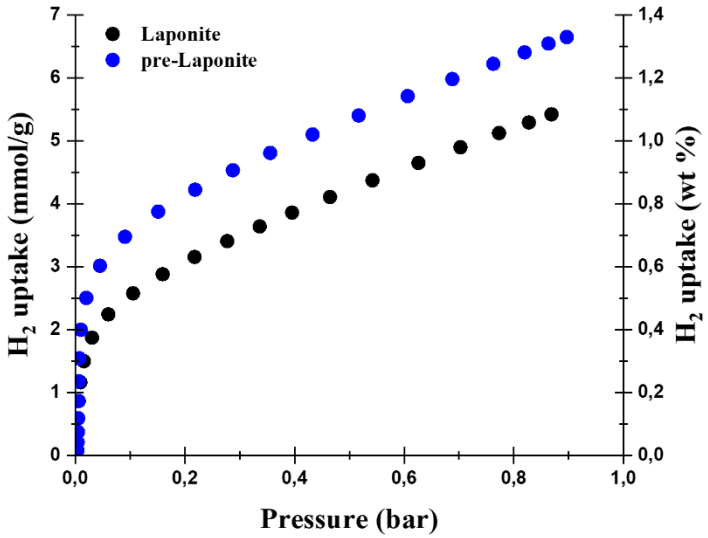

Figure V.6: H_2 adsorption isotherm for pre-Laponite at 40K and ~1 bar.

This Laponite sample was found to have a lateral dimension ($n_a = n_b = 1$) closer to pre-Laponite than to Laponite, with a stacking order intermediate between Laponite and pre-Laponite. Therefore, a detailed analysis of this specific Laponite sample will not be provided. The isotherm shows that pre-Laponite exhibits higher H_2 uptake than Laponite, with the difference being particularly pronounced at lower pressures.

For instance, at 0.2 bar, pre-Laponite achieves an uptake of 0.84 $wt\%$, approximately 1.3 times greater than that of Laponite (0.63 $wt\%$). This increase in uptake at lower pressures underscores the importance of identifying and characterizing the specific adsorption sites that contribute to the isotherm, especially at low pressure.

2.2.1. GCMC simulation

To analyze the contribution of different adsorption sites in (pre-)Laponite, two configurations with $n_a = n_b = 1$, were created for GCMC simulation. In the first configuration, one took d_{001} = 9.7Å, as was found experimentally, where d_{001} is the period of the layers projected along their perpendicular direction z. In the second configuration, d_{001} is take equal to 12Å, corresponding to a larger interlayer space. We calculated adsorption isotherms at T = 40K thanks to GCMC simulations, fixing the positions of Laponite atoms and of the Na^+ cations to the values determined by Molecular Dynamics (**Chapter III, §2.1**) and using the COMPASS force field available in the Forcite module of the Material Studio package to model both H_2 – H_2 and H_2 – Laponite interactions. They are shown in Figure V.7, together with the corresponding snapshots of Laponite and H_2 molecules for high fugacity values. The snapshot for a smaller pressure value, in configuration 2, is also shown in Figure V.8.

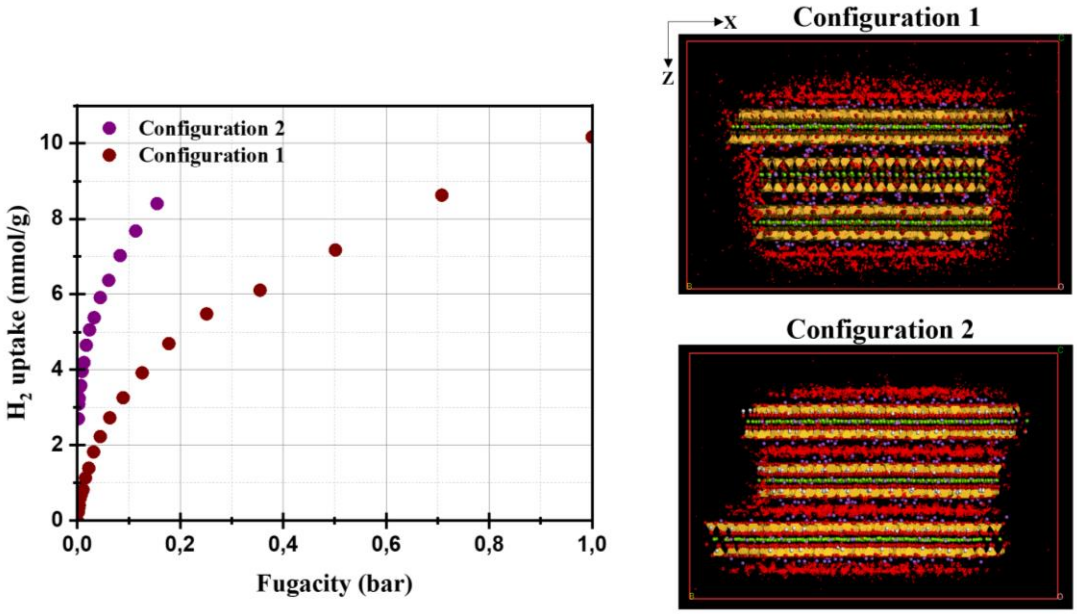

Figure V.7: Calculated H_2 adsorption isotherms at 40K (left) and H_2 density map for two configurations at the last isotherm point (right): with and without interlayer site.

Comparison of the calculated isotherms shows significantly enhanced H_2 uptake at low pressures in configuration 2 compared to configuration 1. The snapshots in Figure V.7 show that in configuration 2, for an absolute hydrogen uptake close to 8 mmol/g (1.6 $wt\%$), hydrogen molecules are located in the interlayer and on the external surfaces of the layers. In configuration 1, for an absolute hydrogen uptake close to 10 mmol/g (2.6 $wt\%$), they are located above and below the clay particle but also on its sides. The steeper step at low fugacity in configuration 2 compared to configuration 1 thus shows that the most energetic site is the interlayer, where interlayer spacing is sufficiently large. It is confirmed in Figure V.8(a) where the configuration 2 snapshot at low pressure shows that the interlayer is filled first. In configuration 1, there is no hydrogen in the interlayer for the force field used. Comparison of the two snapshots in Figure V.7 also shows that the external layer surfaces adsorb hydrogen molecules before the sides of the particle. Furthermore, no attraction is observed between the D_2 molecules and Na cations in the interlayer (Figure V.8(b)), using COMPASS forcefield

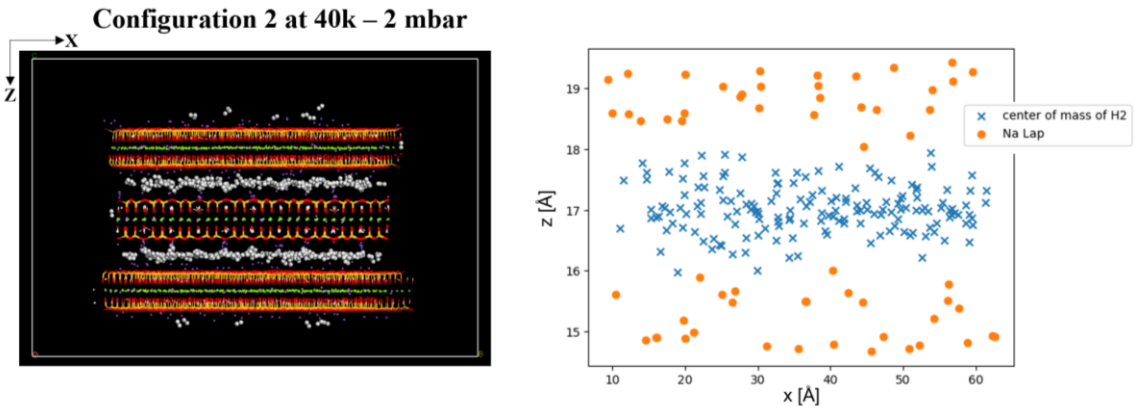

(a) **(b)**

Figure V.8: Snapshot of configuration 2 at 40K and 2 mbar. (a) Most H_2 molecules (shown in white) are intercalated within the interlayer. (b) Lack of attraction between Na and H_2 in the interlayer; blue crosses mark the centers of H_2 molecules, while orange points indicate the positions of Na cations.

In summary, GMCM simulations showed that adsorption can occur in the interlayer -providing the interlayer distance is large enough-, on the external layer surfaces and on the edges of the particles, the most attractive adsorption sites being inside the interlayer when d_{001} is taken equal to 12Å. It is important to underline that site is not accessible to H_2 molecules for d_{001} = 9.7Å (the experimentally derived value of the interlayer spacing) adsorption curve rather smooth at low pressure values. This last observation is in contradiction with the steep increase in hydrogen adsorption at low pressure values in the experimental Figure V.6, and reveals that the simulations failed at reproducing the observations. Many reasons could be evoked to explain this inconsistency, the first one being the justification of the choice of the COMPASS force field which has not been developed in order to reproduce the data of clay materials. One could imagine that by a fine tuning of the parameters of the force field (or changing to use the CLAYFF force field for example). One could reproduce the experimental data better. One should also claim that quantum effects should be included in the simulations if one wants to be very precise on the relation between temperature/pressure and the probability of one light H_2 molecule going through a tiny aperture. Such effects are known to be important for light atoms/molecules and at low temperatures, but are not accounted for in classical GCMC simulations. However, as will be shown below, GMCM simulations give us interesting guides to interpret neutron data. Moreover, at this stage, based on GMCM calculations, the steep increase of adsorption observed experimentally at low pressure may be attributed to an interlayer filling, as it is rather similar to the one observed at low pressure for configuration 2.

2.2.2. Isotherm modeling

At this stage, it is crucial to initiate a quantitative analysis of the experimental isotherms. The Sips model [159], often used in adsorption studies for porous materials like MOFs [160], [161], combines aspects of both the Langmuir and Freundlich models. However, it does not obey Henry's law at low coverage. Alternatively, the Toth model satisfies Henry's law at low pressures, improving the fit over a broader pressure range, though it has a known limitation of overestimating adsorption capacity at saturation. To this aim, the isotherm data were modeled using two shapes: i) a Langmuir line shape to account for microporous adsorption inside the interlayer, and (ii) Freundlich line shape to account for the progressive adsorption in the other less defined sites.

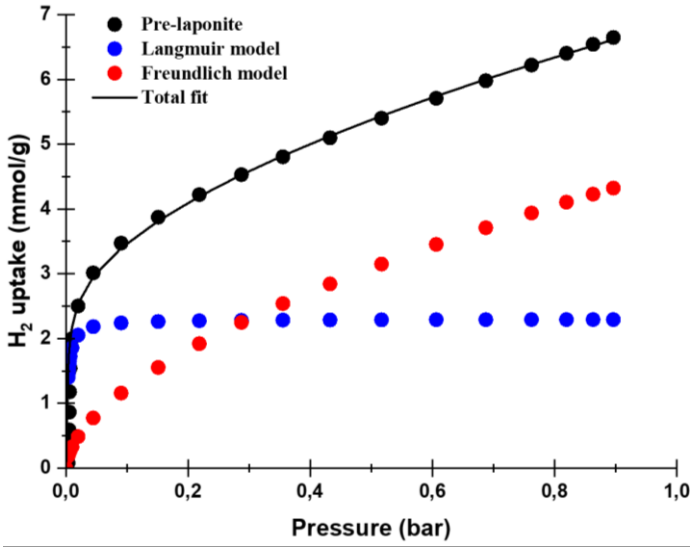

Figure V.9: Hydrogen adsorption isotherm at 40K for pre-Laponite (black), with the total fit (solid black line) composed of the Langmuir model (blue) and the Freundlich model (red).

The Langmuir model, represented in Figure V.9, captures the adsorption at very low pressure, in what we attribute as being the interlayer region. This good match suggests that a monolayer of H_2 molecules is formed in this site, the monolayer being saturated at pressures below 0.1bar. In contrast, the Freundlich model describes adsorption on the outer-particles sites, where the uptake progressively increases without reaching a saturation point. The fitted parameters for both models are summarized in Table V.1. The meaning of each parameter is discussed in detail in **§3.4**, **Chapter II**.

Table V.1: Fitted parameters of the Langmuir and Freundlich models for H_2 adsorption in pre-Laponite at 40K and 1 bar.

Sample	Langmuir model		Freundlich model	
	n_m	b	K_f	1/n
	mmol/g	1/mbar	mmol/g	1/mbar
Pre-Laponite	2.3 ± 0.007	0.42 ± 0.01	4.6 ± 0.006	0.574 ± 0.01

3. H_2 quantum rotor: INS insights

This section is organized into two parts. The first part describes the INS characteristics of bulk H_2 across different phases (gas, liquid, and solid), highlighting the distinct features observed in each state. The second part focuses on the H_2 para-to-ortho transition in Laponite and pre-Laponite samples at 40K as a function of pressure, offering insights into the different adsorption sites. The data presented here were measured on the PANTHER beamline, as detailed previously in **Chapter II.** All experiments used room temperature "normal H_2" (n-H_2) gas, comprising a 1:3 equilibrium mixture of the two nuclear spin isomers of hydrogen, *para*–H_2 and *ortho*–H_2, respectively.

3.1. Bulk H_2: temperature dependence

For bulk H_2 spectra, the experiment was performed by injecting 1 bar of n-H_2 at 80K into an empty cell, followed by cooling down to 2K. The pathway followed in the (P,T) phase diagram with decreasing temperature is shown in Figure V.10 in green. This curve was calculated assuming that hydrogen is a perfect gas. INS spectra were recorded at different temperatures and corrected from empty cell. Figure V.11 shows the dynamical structure factor, $S(Q,\omega)$, of bulk H_2 at three temperatures, 2K, 16K and 80K representing its solid, liquid and gaseous phase respectively according to its known phase diagram (see **§2.2, Chapter I)** .

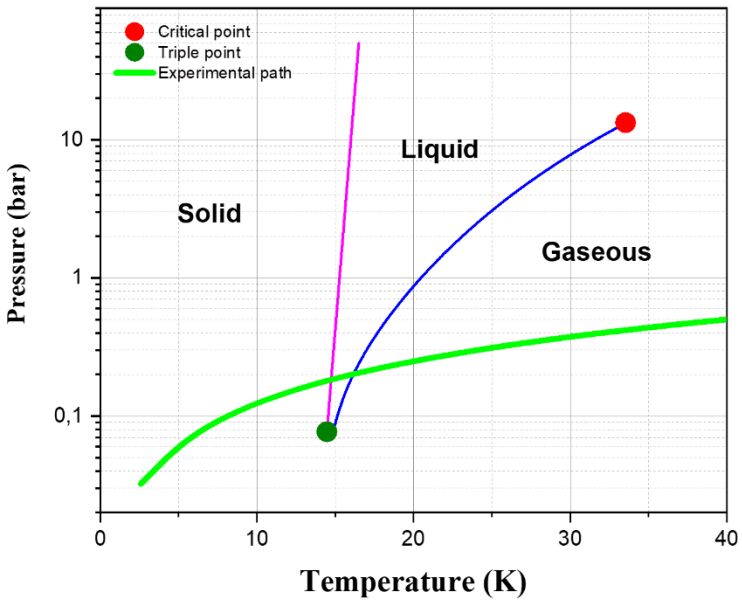

Figure V.10: H_2 phase diagram with the experimental path indicated in green.

In the solid state at 2K, the H_2 dynamical structure factor $S(Q,\omega)$ shows the typical spectral signature of a solid phase: a large intensity in the elastic region with Bragg spots together with a well-structured energy spectrum comprising sharp lines in energy. The most intense inelastic feature is observed at an energy equal to 14.7 meV. It is well known that this peak represents the first rotational excitation ($J = 0, S = 0$) → ($J = 1, S = 1$) of H_2 from the ground state of para-H_2 to the ground state of ortho-H_2 (this feature is therefore called the para-to-ortho transition peak). The intense and relatively sharp band at E ~ 5 meV corresponds to the optical phonon density of state of ortho-H_2. A relatively well-defined feature is observed at a frequency ~20 meV which does not correspond to any expected rotational transition, and appears in a frequency range too low for being of vibrational nature and too high for being a phonon characteristic of a van der Waals lattice. Therefore we assign this feature to a combination of a rotation (J_{01}) and the (optical) phonon modes (roto-phonon excitations), which are expected at E^{01}_{rp} ~ 14.7+5 = 19.7 meV In the anti-Stokes regions (negative energies), the metastability of H_2 -in the absence of local magnetic field variation- is seen by the presence of the ortho-to-para peak reflecting the transition from a quenched ortho ($J = 1, S = 1$) to the ground ($J = 0, S = 0$) state at -14.7 meV. No peak is expected at -5 meV as pure phonons are not populated for this low temperature. The peak at ~ -10 meV is also a roto-phonon transition from ortho-to-para and phonon excitation expected at E^{10}_{rp} ~ -14.7+5 = 9.7 meV. Under melting, the well-defined elastic and phonon features are replaced by a broad signal around the elastic peak, referred to as “quasi-elastic scattering”, which represents the stochastic diffusion of the center of mass of the H_2 molecules. The total scattering, under the assumption that the rotation of the molecules

and their center-of-mass are decoupled, is the convolution of their respective dynamical structure factors. Upon melting then, the sharp, resolution limited lines associated to the rotations are replaced by Lorentzian functions, the width of which being set by the quasielastic scattering, i.e. by the value of the scattering vector Q: at low Q, the quasi-elastic broadening is small, resulting of sharp rotational lines. With increasing values of Q, the signal broadens so much that the lines are lost in a broad continuum scattering, but still visible. In the gaseous state, the intensity of the scattering is much reduced (reduced density), the quasielastic is broader, the rotation lines invisible.

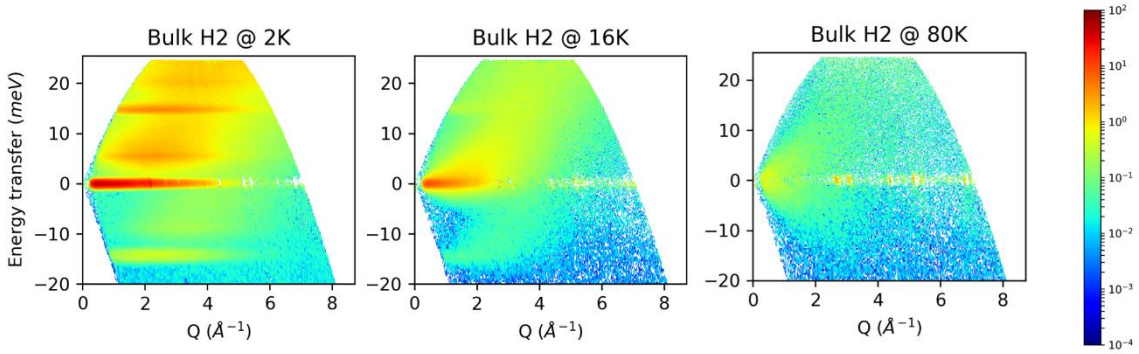

Figure V.11: Dynamical structure factor $\boldsymbol{S(Q,\omega)}$ for bulk H_2, measured using incident energy E_i = 15 *meV* at 2K 16K and 80K.

A more detailed look at the temperature evolution is provided in Figure V.12, through the $S(\omega)$ plot, after integration over Q.

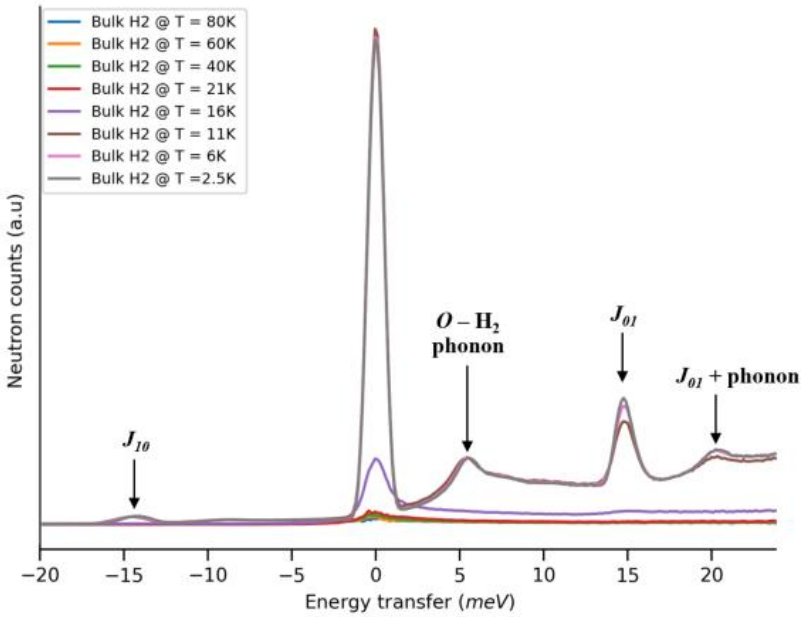

Figure V.12: $\boldsymbol{S(\omega)}$, for bulk H_2, as a function of temperature with E_i = 30 meV.

3.2. H_2 binding sites in Laponite and pre-Laponite

In this subsection, we will use neutron scattering to probe the quantum states of H_2 under the strong confinement of Laponite and (pre)Laponite. We will discuss the INS spectra on the basis of the free rotor picture discussed above for bulk H_2. We will follow the 40K – 1 bar adsorption isotherm by injecting H_2 at low pressure, then gradually increasing the pressure. Under these conditions, bulk H_2 is kept in its gaseous state so that its contribution to the scattering is negligible. Prior to the experiment, 595 mg of powdered pre-Laponite and 565 mg of powdered Laponite were wrapped inside an aluminum foil and outgassed at 150°C for 6 hours under secondary vacuum. The H_2 data presented here are corrected from the scattering of the "dried" (pre-)Laponite sample, by subtracting to all pressure-dependent spectra the spectrum measured at 40K prior to H_2 injection.

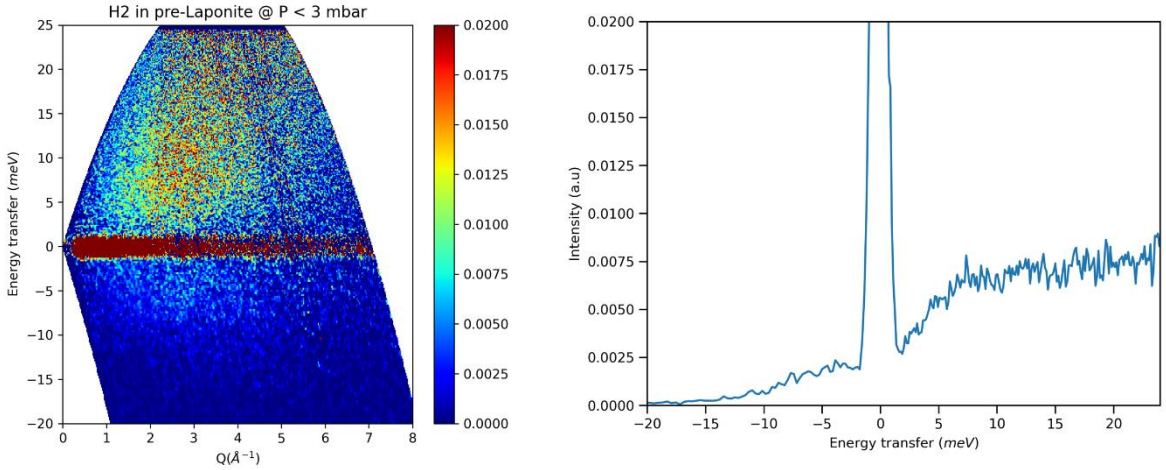

Figure V.13: (a) $\boldsymbol{S(Q,\omega)}$ and (b) $\boldsymbol{S(\omega)}$ of H_2 injected onto pre-Laponite at 40K and pressure below 3 mbar.

Figure V.13 shows the INS data of H_2 injected in pre-Laponite at 40K at a pressure below 3 mbar, i.e. characteristic of the most attractive sites that we tentatively attributed to sites in the interlayer in the preceding chapter. The $S(Q,\omega)$ map does not display any well-defined rotational line. Instead a broad, featureless, band extending from 3 to 20 meV is clearly seen. It has a strong dependence with Q but clearly shows a gap close to the elastic line: no quasi-elastic scattering is seen and a strong elastic line is observed which suggests the absence of liquid-like H_2. H_2 is therefore having a solid-like $S(Q,\omega)$, and the striking absence of clear rotational line signatures suggest that the molecules are strongly confined, in strong interaction with their environment: the spectrum cannot be interpreted on the basis of a perturbed free rotor picture for these low pressures of absorption. In the following, we will refer to "site 0" the local

environment associated to the most attractive sites and for which the H_2 $S(Q,\omega)$ spectrum lacks of clear rotational lines.

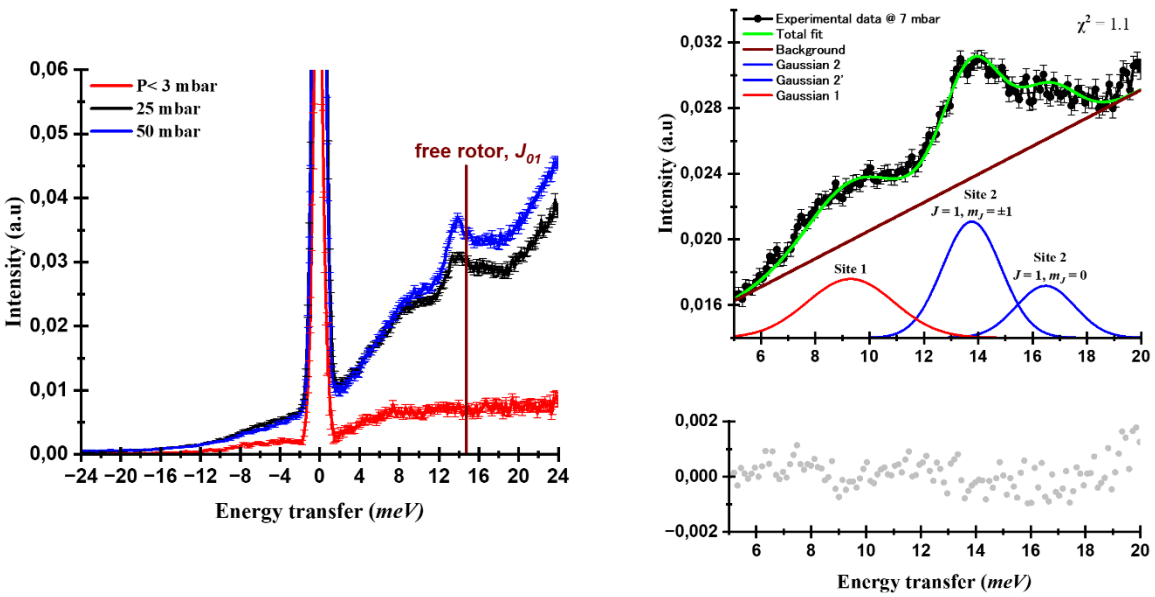

(a) **(b)**

Figure V.14: INS spectra of H_2 injected onto pre-Laponite at 40 K, displayed as a function of pressure with an incident energy E_i = 30 meV. The wine line indicates the position expected for a free rotor. (b) Experimental data at 25 mbar (black) with a total fit (green), composed of three Gaussian functions: Site 1 with a FWHM of 3.7 meV, and Site 2 with two Gaussian components, each having a fixed FWHM of 2.54 meV, and a first-order polynomial background (gray). The individual Gaussian functions (blue and red) are offset vertically for clarity.

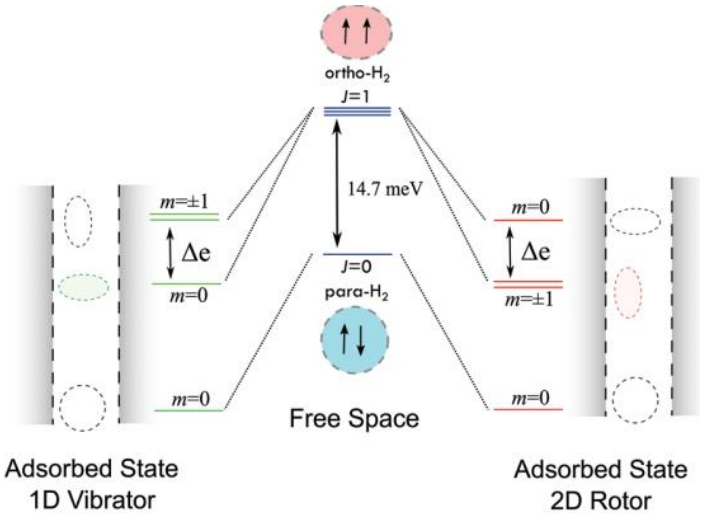

Figure V.15: Quantum rotational levels of H_2 in free space and adsorbed state with a anisotropic potential causing 1D or 2D rotation, adapted from [162].

As shown in Figure V.14(a), upon increase of H_2 pressure, the scattering intensity increases and inelastic features build up in a spectral region close to the para-to-ortho energy: one around 9 meV and two others close to the position of the free rotor (J_{01} = 14.7 meV). In Figure V.14(b), we show the spectrum measured at 25 mbar and the result of its adjustment with a set of three Gaussian functions, lying over a linear background. Let us remind here that the J_{01} rotational line is a triplet which can be split by any anisotropy of the local potential felt by the H_2 molecule (Figure V.15). The extent of the gap between the resulting sublevels directly relates to the energy barrier height for rotation (eq. (I.3) and Figure I.8). The lowest energy peak, which appears at 9.1 ± 0.1 meV, seems to have no counterpart at high energy. As it is found to be very much shifted with regards to the free rotor value, we attributed this feature to the strongest binding sites observed from this spectrum, that we will call "site 1". We assign the doublet at higher energies to another type of site ("site 2"). They are characterized by a much smaller splitting. Their relative intensities show a ratio 2:1, in good agreement with hydrogen molecules behaving as 2D planar rotors, with their long axis preferentially aligned parallel to the surface of adsorption (Figure V.15). According to theory, we assign the low energy peak at 13.76 ± 0.2 meV to J = 1, m_J = ±1, while the component at 16.48 ± 0.2 meV is assigned to J = 1, m_J = 0. Using the Dave software [165], which allows one to calculate the splitting as a function of the potential barrier for an anisotropic rotor (V in equation (I.3)), a good agreement is obtained for a slightly larger rotational constant B than in the free molecule state (B = 7.75 meV to be compared to 7.35 meV) and a value of V ~ - 80K is estimated. The larger B value can be the sign of a slight contraction of the H_2 internuclear distance from 0.74 Å in the bulk phase to 0.72Å under confinement.

If one follows the same line of investigation but for sites 1, two options can be proposed:

1. the peak at 9.1 meV is the doublet (most probable for a 2D planar rotor): in that case the singlet peak is expected to appear in an energy range ~ 50 meV for an energy barrier equal to V ~ - 1300 K.
2. The peak at 9.1 meV is a singlet: in that case the doublet peak is expected to appear at ~ 18.7 meV for an energy barrier equal to V ~ (+) 280 K.

Figure V.16 shows the spectra obtained using a larger incident energy Ei = 60 meV. Some broad and ill resolved contributions are observed in the 20 meV - 40 meV range. At this stage it appears difficult to conclude on their assignment. They could be due to splitting of the para-to-

ortho transition, but could also be reflecting higher transition (J = 1 to J = 2). Further investigations are therefore required to fine tune our understanding of site 1.

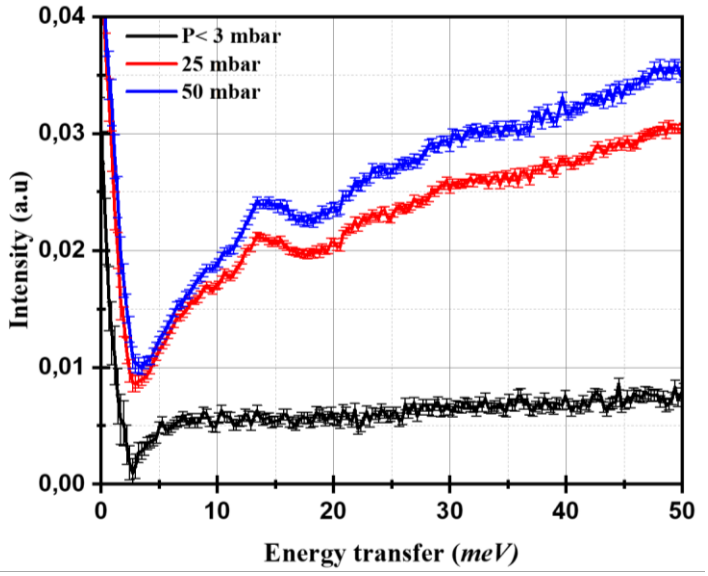

Figure V.16: INS spectra of H_2 injected onto pre-Laponite at 40K, shown as a function of pressure at 40K, with E_i = 60 meV.

Similar to pre-Laponite, INS spectra for Laponite are recorded at different H_2 pressure at 40K.

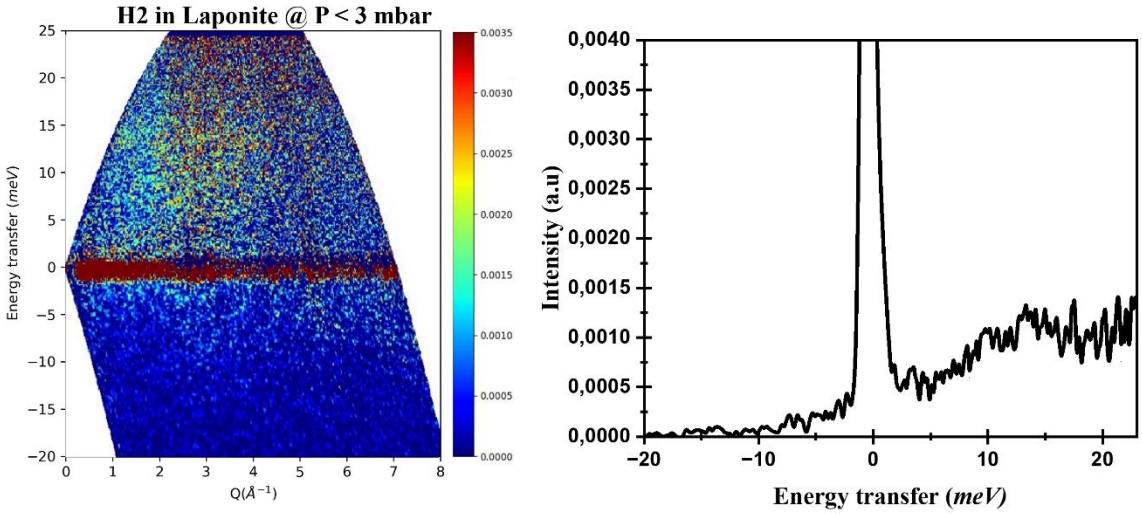

(a) **(b)**

Figure V.17 (a) $\boldsymbol{S(Q,\omega)}$ and (b) $\boldsymbol{S(\omega)}$ of H_2 injected onto Laponite at 40K and pressure below 3 mbar.

Figure V.17(a) shows the $S(Q,\omega)$ spectrum of H_2 adsorbed in the Laponite sample when an equilibrium pressure below 3 mbar is reached. The spectrum has a much-reduced intensity with regards to that of pre-Laponite, which agrees with the isotherm data in this pressure range. Even if the data are noisy, one sees that the spectrum shares similarities with that obtained for pre-

Laponite: a solid-like signature and the same Q dependence. However, one can also observe the presence of a weak "horizontal" component around ~15 meV that one could assign to a ghost-like contribution of a rotational peak. The Q integrated spectrum shown in Figure V.17(b) is clearly more structured in energy than its counterpart measured for pre-Laponite, with weak peaks located around 10 and 14.7 meV, i.e. assigned previously to sites 1 and 2 respectively for pre-Laponite. Clearly, the contribution of site 0 is much lower in the Laponite sample than in pre-Laponite for these pressures. As pressure increases to 7 mbar, the rotational lines corresponding to both site 1 and site 2 appear more clearly, with the definition of the doublet around 14.7 meV building up. The result of the fit of the spectrum at 7 mbar, composed of three gaussian lines, is shown in Figure V.18(b). The peak that we attribute to site 1, i.e. characterizing a large splitting, appears at 9.8 meV, i.e. at a slightly higher energy than its equivalent observed in pre-Laponite. This would indicate the presence of a slightly lower orientational potential barrier for these sites in the Laponite sample. The peaks that we assign to site 2, i.e. corresponding to a smaller splitting, exhibit a doublet $J = 1$, $m_J = \pm 1$ component at 13.8 ± 0.2 meV and a singlet $J = 1$, $m_J = 0$ component at 17.1 ± 0.2 meV. If we use the same approach than the one developed for pre-Laponite, H_2 molecules at site 2 would be preferentially aligned parallel to the surface of adsorption, with a slightly lower internuclear distance (0.71Å) and an orientational potential well depth of approximately - 96K, i.e. slightly larger than in pre-Laponite.

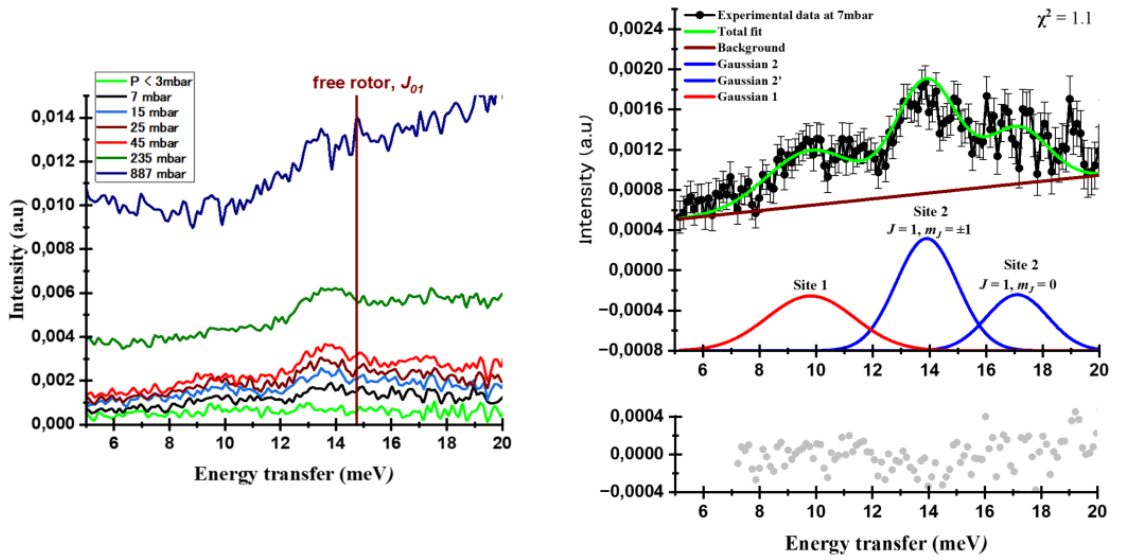

(a) **(b)**

Figure V.18 INS spectra of H_2 injected onto pre-Laponite at 40 K, displayed as a function of pressure with an incident energy E_i = 30 meV. The wine line indicates the position expected for a free rotor. (b) Experimental data at 7 mbar (black) with a total fit (green), composed of three Gaussian functions: Site 1 with a FWHM of 3.63 meV,

and Site 2 with two Gaussian components, each having a fixed FWHM of 2.54 meV, and a first-order polynomial background (gray). The individual Gaussian functions (blue and red) are translated vertically for clarity.

The fitted amplitudes of the Gaussians functions in Laponite and pre-Laponite, corresponding to H_2 molecules adsorbed at sites 1 and 2, are summarized in Table V.2.

Table V.2: Fitted INS parameters for the rotor lines, in Laponite and pre-Laponite at different pressure at 40K. The amplitude normalized to the irradiated pre-Laponite mass.

Pressure (mbar)	**Amplitude** (x 10^{-3})		
	Site 2, $m_J = \pm 1$	Site 2, $m_J = 0$	Site 1
Laponite			
7	2.36 ± 0.04	1.18 ± 0.04	0.55 ± 0.04
15	3.09 ± 0.05	1.55 ± 0.05	0.73 ± 0.04
25	3.22 ± 0.04	1.61 ± 0.04	0.73 ± 0.04
45	3.66 ± 0.04	1.83 ± 0.04	0.73 ± 0.04
235	3.84 ± 0.04	1.92 ± 0.04	0.73 ± 0.04
887	4.36 ± 0.05	2.18 ± 0.05	0.73 ± 0.04
Pre-Laponite			
25	3.6 ± 0.1	1.8 ± 0.1	3.6 ± 0.1
50	4.06 ± 0.1	2.03 ± 0.1	3.6 ± 0.1

To further compare the relative amounts of H_2 adsorbed in Laponite and pre-Laponite at 40K, we systematically evaluated the integrated intensities of the INS spectra as a function of site and pressure. The results are shown in Figure V.19. One has to keep in mind that the integrated intensity of the rotor lines represents only the population of para-H_2 present in the sample. Site 1 and site 2 share similar behavior in both Laponite and pre-Laponite: site 1 appears to follow a Langmuir dependence, with a saturation observed at pressures ≤ 25 mbar for pre-Laponite and ≤ 15 mbar for Laponite. As already discussed in the previous paragraph, the amount of H_2 adsorbed at sites 1 is much larger in pre-Laponite compared to Laponite (by a factor of ~ 5). Similarly, site 2 also follows a Langmuir model, with comparable amounts of H_2 adsorbed at these sites in both Laponite and pre-Laponite.

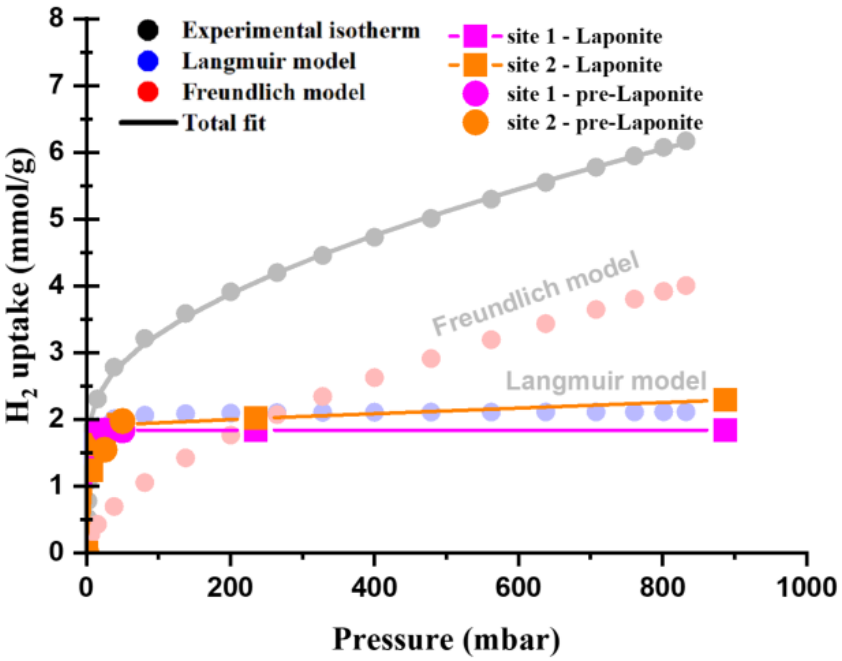

Figure V.19: Integrated intensity under the rotor lines in Laponite (squares) and pre-Laponite (circles) as a function of pressure at 40 K, normalized to the experimental isotherm. Site 1 is shown in purple, and site 2 is shown in orange. The data for sites 1 and 2 in Laponite is fitted with the Langmuir model.

3.3. General discussion

The INS investigations performed on Laponite and pre-Laponite at 40K, for increasing pressure of injected H_2, show the existence of three distinct adsorption sites for H_2. At low pressures, a particularly strong adsorption site (named site 0) is observed, which restricts strongly the rotation of H_2 molecules. As the pressure increases, J_{01} rotational lines appear, corresponding to two additional adsorption sites, termed site 1 and site 2. Site 1 is a stronger adsorption site than site 2, as far as one considers the associated orientational potential. Moreover, it is stronger in pre-Laponite than in Laponite as the rotational line is splitted to a lower energy transfer. This site shows saturation at pressures $\leq$ 15 mbar in Laponite and $\leq$ 25 mbar in pre-Laponite. Furthermore, pre-Laponite displays more amount of adsorbed H_2 at site 0 and 1 compared to Laponite.

Site 2 appears similar in Laponite and pre-Laponite, with associated J_{01} transitions fitted by two gaussian lines with an intensity ratio 2:1. The splitting is in line with 1D hindered rotation i.e. H_2 axis lying preferentially parallel to the adsorption surface and an orientational potential wall equal to ~ 96K in Laponite and ~ 80K in pre-Laponite.

The integrated intensities of the Gaussian peaks corresponding to sites 1 and 2 show a significant increase at low pressures, with intensities approaching saturation as the pressure rises. The integrated intensities of the rotor lines for sites 1 and 2 in Laponite are fitted by the Langmuir model (Figure V.19).

Furthermore, one may underline that the absence of free rotor line indicate that all H_2 are hindered to Laponite and pre-Laponite by adsorption. Additionally, the lack of significant broadening of the elastic peak indicates limited mobility of the adsorbed H_2 at different sites.

Based on our conclusions in **§2.2.1**, we tentatively attribute sites 1 and 2 to the interlayer region.

4. H_2/D_2 structuration: wide angle neutron scattering

At this stage, it is important to localize and understand the structure of adsorbed H_2. For this purpose, in-situ WANS measurements at 40K were performed using the D16 diffractometer. Due to the large incoherent-to-coherent scattering cross section of H_2, we'll discuss D_2 adsorption instead of H_2 adsorption. Prior to the experiment, 100 mg of powdered pre-Laponite and 285 mg of powdered Laponite were wrapped in aluminum foil and outgassed at 150°C for 6 hours under secondary vacuum. To enable a direct comparison to the diffraction diagrams between the two samples, the intensity was normalized to the pre-Laponite sample mass.

The diffraction diagrams of dried samples, corrected from the empty cell, are shown in Figure V.20. The measured data in the Q-range of 1–2.55 $Å^{-1}$ show the *hk* bands along with the *003* peak. The diagram of pre-Laponite is noisy due to the low sample mass in the beam and the increase of intensity in pre-Laponite above 2.45$Å^{-1}$ is attributed to a spurious effect. Taking these points into account, it is found that the diagrams are similar for both samples, as expected, and that pre-Laponite shows a smoother *hk* rising edge, as already evidenced with X-ray scattering measurements in **Chapter IV**.

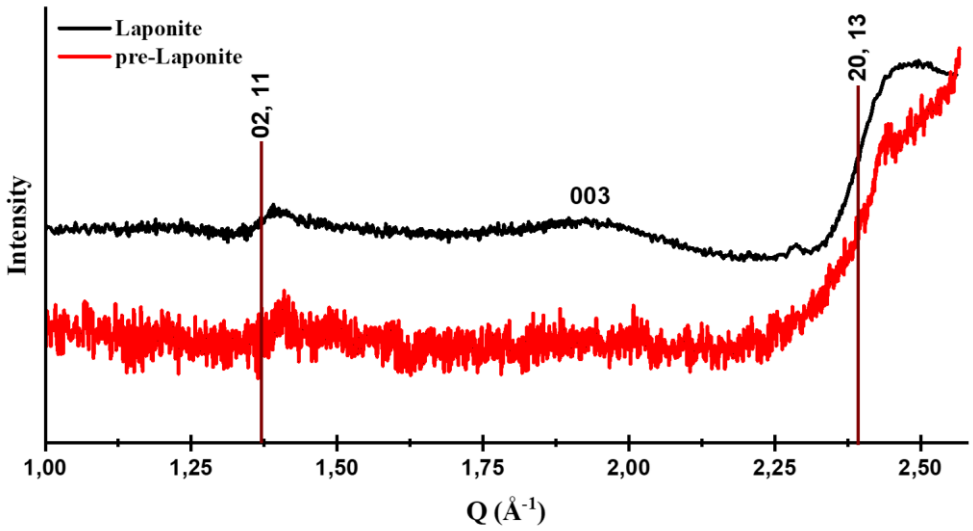

Figure V.20: Diffraction diagrams measured at 40 K for Laponite (black) and pre-Laponite (red). Data are corrected from empty cell. The Laponite diagram is vertically translated for clarity.

Figure V.21 presents the diffraction diagrams of dried Laponite and pre-Laponite, along with those under varying pressures of D_2 at 40 K, corrected from empty cell. The diagrams for Laponite and pre-Laponite show similar trends across the dosing pressures. At the lowest pressure (9 mbar), the first *hk* band is diminished, and there is a noticeable modification in the shape of the second band. Additionally, a broad feature begins to appear in the region of the *003* peak. As pressure increases, the second *hk* band undergoes further modification, while the broad peak in the *003* region completes its build up in both materials. To interpret these observed behaviors, it is essential to highlight that the diagrams across different dosing pressures, three types of correlations could exist: D_2–D_2, D_2–matrix, and matrix–matrix correlations.

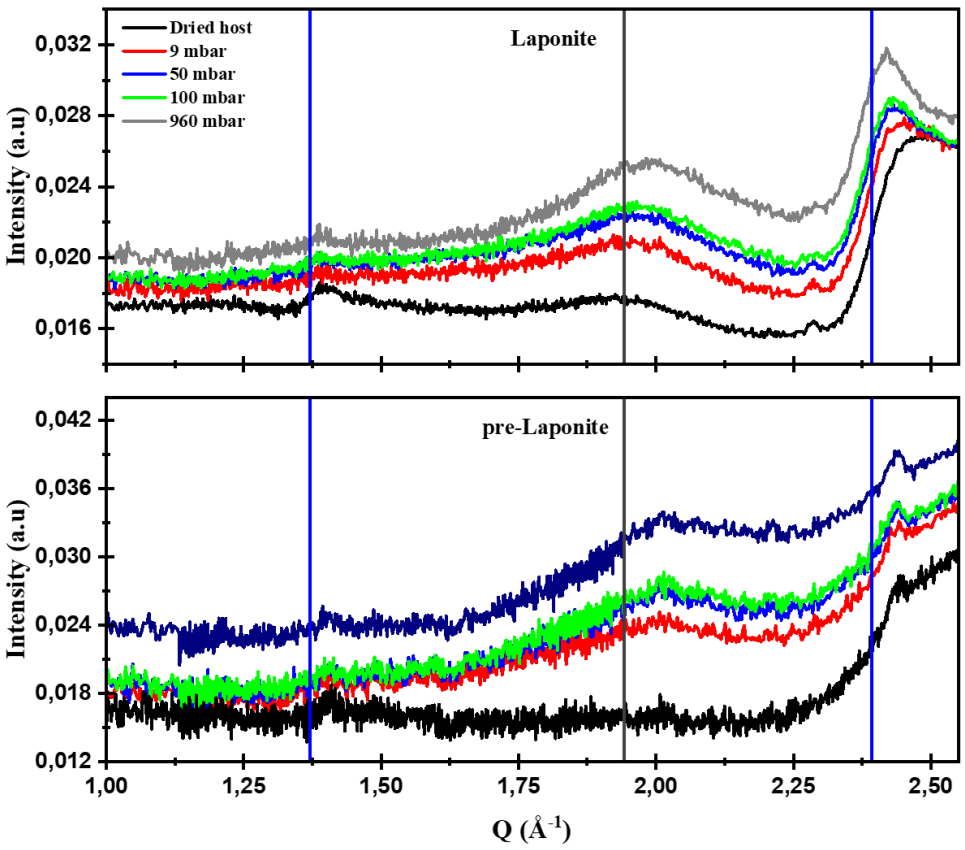

Figure V.21: Diffraction diagrams measured at 40K for Laponite (up) and pre-Laponite (down) for different D_2 pressure values. Data are corrected from empty cell. The solid blue and dark gray lines indicate the positions of the *hk* bands and the *003* peak, respectively.

Therefore, to remove the influence of matrix–matrix correlations, Figure V.22 shows the matrix-subtracted diffraction diagram at different D_2 dosing pressures. In the diffraction diagrams of Laponite and pre-Laponite, a similar broad peak is observed around 2 $Å^{-1}$. Moreover, in Laponite, a peak appears at 1.3 $Å^{-1}$, marked by an asterisk in Figure V.22. This peak is an artifact rather than a true structural feature. It results from a subtraction effect, where the intensity maximum of the *02,11* band in the dried sample (indicated by the arrow) creates a valley region and a peak at slightly smaller Q-values. Additionally, a well-defined feature is observed around 2.4 $Å^{-1}$, likely due to the modification observed in the *20,13* band of Laponite.

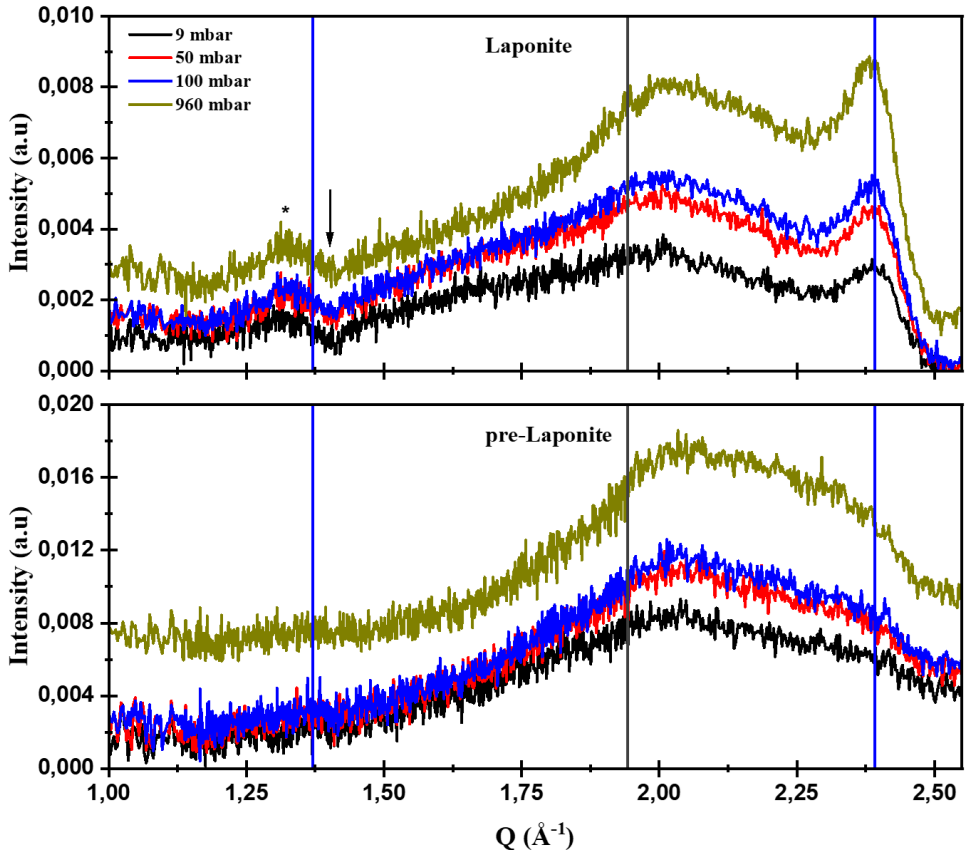

Figure V.22: Diffraction diagrams measured at 40K for Laponite (up) and pre-Laponite (down) for different D_2 pressure values. Data are corrected from dried host and empty cell. The solid blue and dark gray lines indicate the positions of the *hk* bands and the *003* peak, respectively.

Figure V.23 shows the differential diffraction diagrams, that is the diagrams at pressure P minus that at pressure P_0 divided by the difference between the two pressures, for both Laponite and pre-Laponite. The results reveal that at 9 mbar, there is a noticeable increase in intensity, indicating significant D_2 adsorption. As the pressure increases to 50 mbar, the intensity change becomes smaller, suggesting that many adsorption sites to which we are sensitive in this diffraction experiment are already occupied. At higher pressures (100 mbar and 960 mbar), the intensity increments are minimal, indicating that most accessible sites are filled or nearly filled. This pattern suggests an initial rapid adsorption phase, followed by a slower rate of adsorption at higher pressures. Based on the modeling of the adsorption isotherm in Figure V.9, it follows that one mainly observes in the experiment the D_2 molecules in the interlayer.

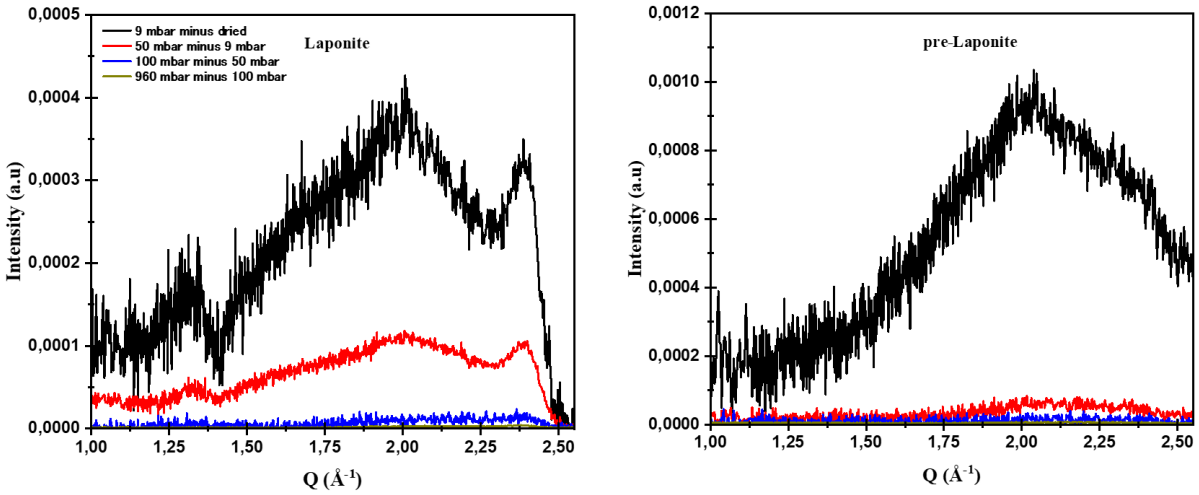

(a) **(b)**

Figure V.23: Differential neutron diffraction diagrams of (a) Laponite and (b) pre-Laponite under different dosing pressure. Each curve represents the difference between consecutive pressures, normalized by the pressure difference. The black curve shows the normalized intensity difference between the dried sample and 9 mbar D_2, the red curve between 9 mbar and 50 mbar, the blue curve between 50 mbar and 100 mbar, and the olive curve between 100 mbar and 994 mbar.

To understand the origin of the observed peaks, we performed calculations of the diffraction diagrams based on atomistic simulations. We used the GCMC configuration at 2 mbar (Figure V.24), as described in **§2.2.2**, where most D_2 molecules are located in the interlayer for d_{001}=12Å. To better match the experimental conditions, the basal spacing in the 2 mbar snapshot configuration was reduced from 12Å to 9.7Å (it corresponds to a translation of the D_2 molecules, there is no distortion of the D_2 structuration), the OH groups in the structure were converted to OD groups, and adsorbed H_2 molecules were replaced with D_2.

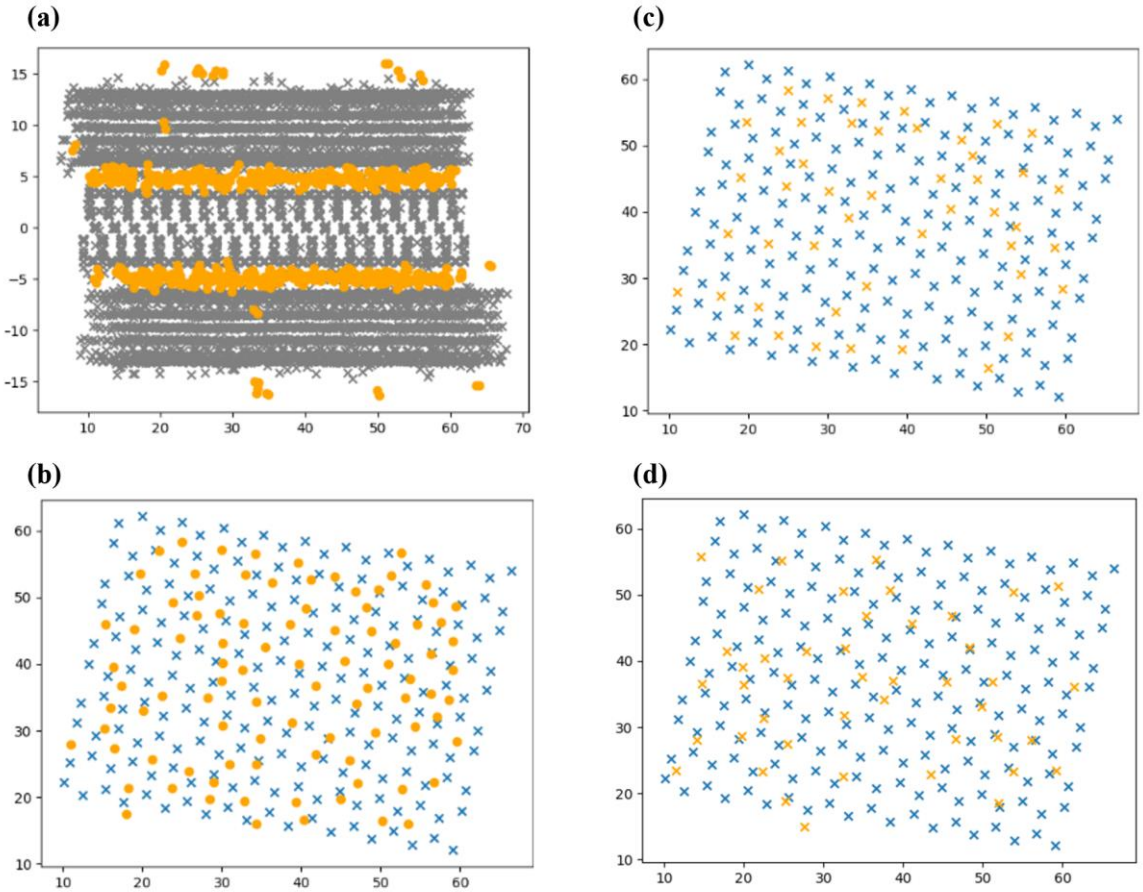

Figure V.24: Configuration of the 2 mbar GCMC snapshot at 40K with n_a= n_b = 1 and n_c=3 with basal spacing adjusted to d_{001} = 9.7 Å. (a) shows the projection of atomic positions in the z-y plane; atoms from Laponite, including Na cations, are represented with grey crosses and D_2 atoms are represented with orange filled circles. (b) shows the positions of Si atoms (blue crosses) that form hexagonal cavities at the top of a layer, in the xy plane, as well as the centers of mass of interlayer D_2 molecules when they are closer to this layer than to the one above (orange filled circles): they are located at a z coordinate smaller than 9.7/2Å from the Mg/Li plane of the Laponite layer, (c) shows the centers of mass of interlayer D_2 molecules which are even more close to this layer than to the ones in (b), with z coordinate smaller than (9.7/2-0.2) Å from the Mg/Li plane (orange crosses). In (d), one shows the positions of the centers of mass of the molecules in the interlayer which are closer to the above layer (their distance in z to the Mg/Li plane of the first layer is greater than (9.7/2+0.2) Å).

By analyzing the positions of interlayer D_2 (or H_2) relative to the Laponite layer at the bottom of the interlayer, we observe that part of the molecules close to this layer are located above the hexagonal cavities (see Figure V.24(b) and (c) where respectively 50% and 80% of the molecules are located above hexagonal cavities). Figure V.24(d) shows that such correspondence is not observed for the molecules closer to the above Laponite layer as Laponite layers present stacking disorder. Figure V.25(a) presents the calculated neutron scattering diagrams for Laponite and for Laponite with the D_2 molecules. The results indicate a modification of the *20,13* band, accompanied by a reduction in the intensity of the *003* peak.

The change in *003* intensity can be easily understood. The intensity of *00l* peaks is proportional to the square of the Fourier transform of the projection of the electronic density along z, so that obviously *00l* peaks are sensitive to the filling of the interlayer with D_2 molecules.

The modification of the intensity of the *20,13* band is attributed to some coherence in x and y positions between the molecules above the Laponite layer and the atoms of the layer itself. If the molecules were randomly positioned in-plane with respect to the Laponite layer, the *20,13*-band intensity should be unchanged. We attribute the change in intensity of the *20,13* band to the existence of molecules close to one layer which are preferentially located above its hexagonal cavities.

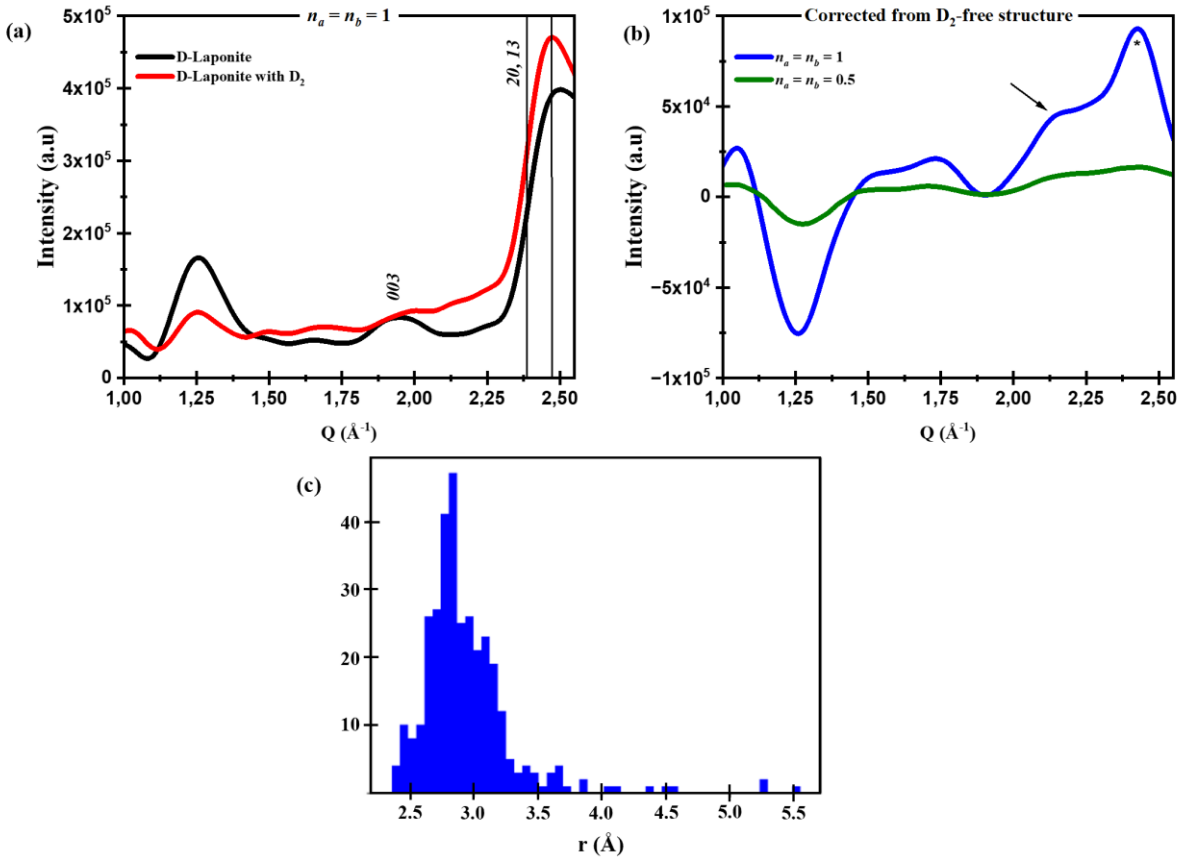

Figure V.25: Calculated neutron scattering diagrams for (a) D_2-free and D_2-adsorbed structures with $n_a = n_b = 1$ and $n_c = 3$, using a reduced basal spacing of $d_{001} = 9.7$Å, highlighting the *003* peak and the second *hk* band – the *20,13* band; (b) Corrected neutron scattering diagrams for $n_a = n_b = 1$ and reduced in-plane coherence length with $n_a = n_b = 0.5$, after subtraction of the scattering by the corresponding D_2-free structures. The broad peak is indicated by an arrow, and the well-defined peak is marked by an asterisk (*). (c) Histogram of nearest-neighbors' distances between the centers of mass of D_2 molecules in the interlayers.

Figure V.25(b) shows diffraction diagrams of D_2-adsorbed structures, corrected from D_2-free structure, which reveal the emergence of a broad peak around 2.15 Å^{-1} (indicated by an arrow) and of a well-defined peak at 2.43 Å^{-1} (marked by asterisks). Calculations with a reduced in-

plane coherence length (n_a = n_b = 0.5) of the TOT sheets demonstrate that the well-defined peak becomes obscured by the broader peak, as it itself becomes broader. The experimental features in Figure V.23, for a pressure of 9 mbar, are thus well rendered, qualitatively, by the calculations in Figure V.25(b), having in mind that in-plane coherence lengths are smaller in pre-Laponite layers than in Laponite ones. To further understand the origin of the broad peak, Figure V.25(c) displays a histogram of the nearest-neighbor distances between the centers of mass of the D_2 molecules. The position of the broad peak in Figure V.25(b) aligns with the mean distance <d> = 2.9Å in the histogram ($Q \approx 2.15\text{Å}^{-1} \approx \frac{2\pi}{\langle d \rangle}$), showing that the broad peak observed in the diffraction diagrams can be associated to $D_2 - D_2$ correlations.

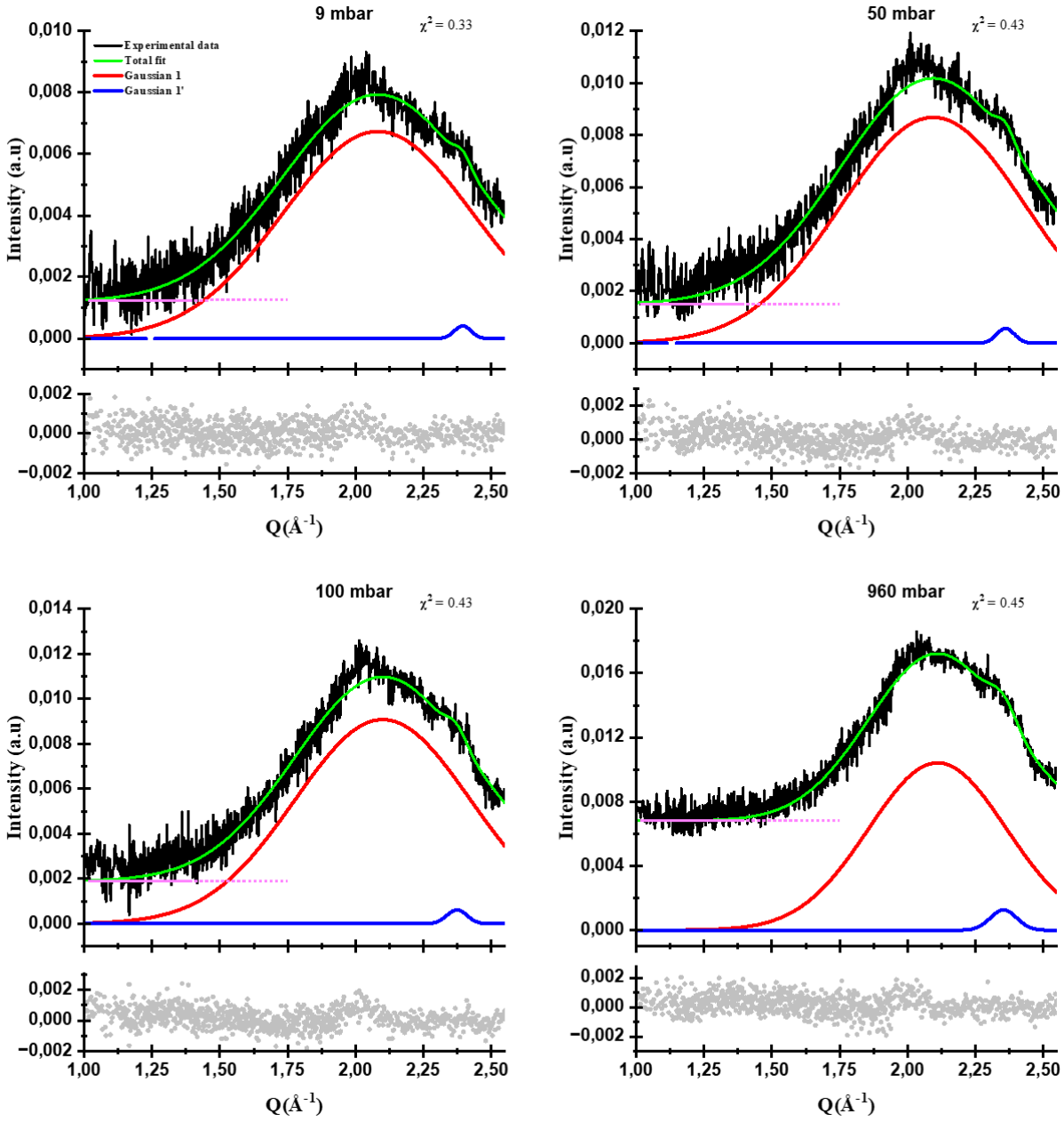

Figure V.26: Experimental data (black) in pre-Laponite, after subtraction of the pre-Laponite diagram, for different D_2 pressures fitted with two Gaussian lines shown in blue and red. The flat background is shown in pink, the total fit in green, and the difference between the fit and the experimental data is represented in gray.

In brief, the broad peak observed in Figure V.23 is associated to D_2-D_2 correlations and gives the mean nearest-neighbor distance between the centers of mass of the molecules. The narrower peak at larger Q value, which is more visible in Laponite than in pre-Laponite due to larger in-plane correlation length for Laponite, is attributed to correlations in x and y positions between D_2 molecules close to a layer and the atoms in the layer. Based on GCMC simulations, it is proposed that D_2 molecules close to a layer are preferentially located above the hexagons defined by the Si atoms.

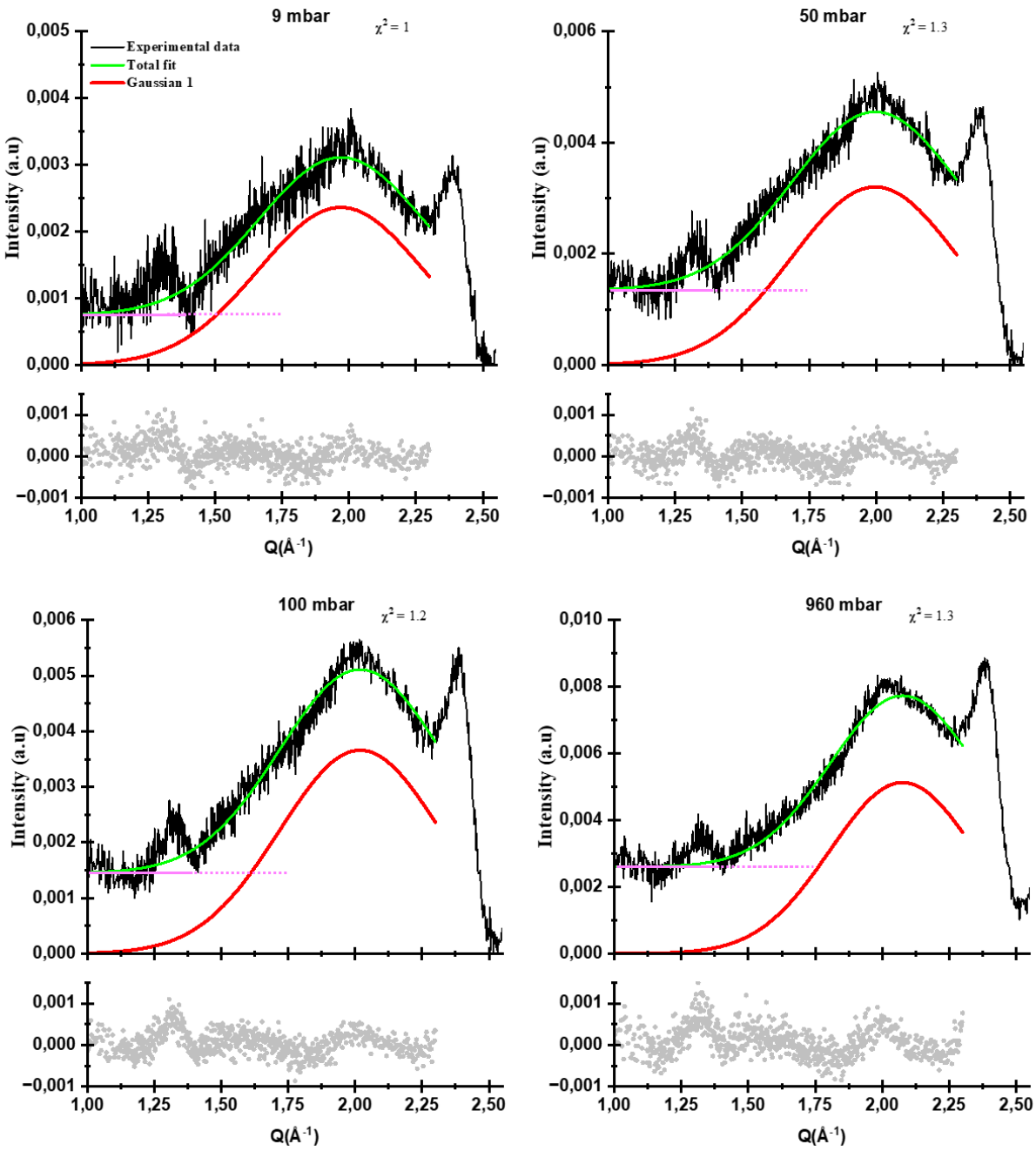

Figure V.27: Experimental data (black) in Laponite, after subtraction of the Lapointe diagram, for different D_2 pressures fitted with a Gaussian line shown in red for its broad component and red. The flat background is shown in pink, the total fit in green, and the difference between the fit and the experimental data is represented in gray.

Fit of experimental data are presented in Figure V.26 and Figure V.27. We defined a flat background, and the data were fitted with two Gaussian lines: one accounting for the broad peak and one for the modified *20,13* band, which is not well detected in pre-Lapointe but necessary for accurate fitting. For Laponite, only a single Gaussian line is required to fit the broad peak, as the second peak is well-defined.

The parameters for the fitted diagrams are summarized in Table V.3. The mean distance for D_2 – D_2 separation at a dosing pressure near 1 bar is found to be approximately 3 Å in both Laponite and pre-Laponite (based on the fitted positions of the broad peak, it would be 3 Å in pre-Laponite and 3.15 Å in Laponite, but this difference may arise from fitting approximations such as the choice of a flat background or of a reduced energy range for the fitting). Strong adsorption is evidenced at low pressure in both samples, with a higher uptake in pre-Laponite compared to Laponite.

Table V.3: Fitted D_2–D_2 correlation peak parameters in Laponite and pre-Laponite at different D_2 dosing pressures at 40K.

Pressure (mbar)	**D_2 – D_2 correlation**		
	Peak center ($Å^{-1}$)	FWHM ($Å^{-1}$)	Amplitude
Laponite			
9	1.97 ± 0.01	0.72 ± 0.01	0.0024
50	2 ± 0.01	0.73 ± 0.01	0.0032
100	2.02 ± 0.01	0.7 ± 0.01	0.0036
960	2.08 ± 0.01	0.64 ± 0.01	0.005
Pre-Laponite			
9	2.08 ± 0.01	0.82 ± 0.01	0.007
50	2.1 ± 0.01	0.8 ± 0.01	0.0087
100	2.1 ± 0.01	0.76 ± 0.01	0.009
960	2.1 ± 0.01	0.6 ± 0.01	0.01

In summary, Laponite and pre-Laponite show similar D_2 adsorption behaviors across various pressures of D_2. In both samples, some adsorbed D_2 molecules align above the hexagonal cavities of the closest layer, leading to a modification of the *20, 13* band intensity.

By plotting the integrated intensity of the D_2-D_2 correlation peak for both Laponite and pre-Laponite versus pressure and normalizing it to the experimental adsorption isotherm, we observe a similar trend in both materials: a sharp increase at low pressure (at 9 mbar), followed by near saturation exhibiting Langmuir-type behavior. Notably, pre-Laponite demonstrates higher D_2 uptake than Laponite at 40K, for the two samples characterized in details in **Chapter**

IV. It follows that the interlayer site is the primary factor driving the enhanced adsorption observed in pre-Laponite

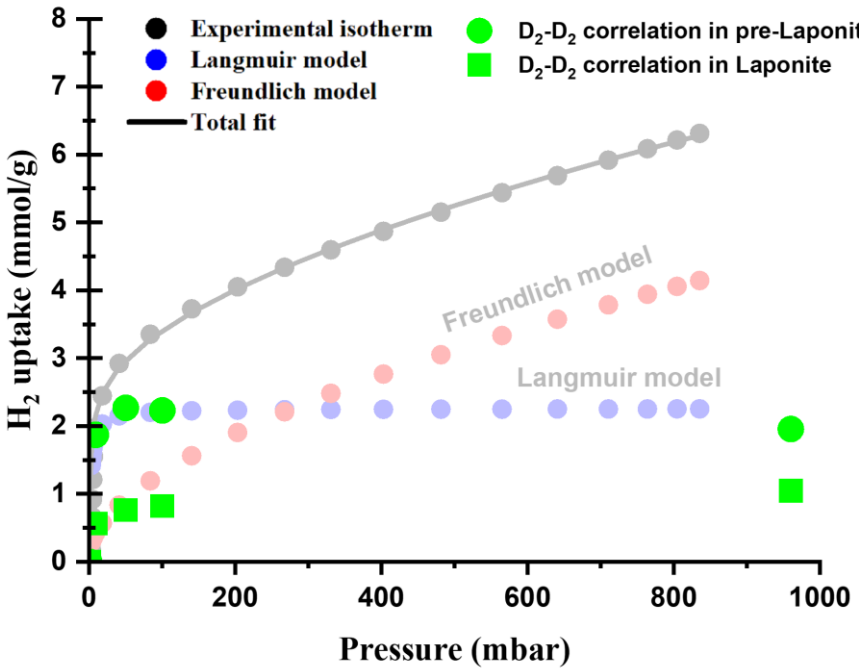

Figure V.28: Integrated intensity under the D_2-D_2 correlation peak in Laponite (squares) and pre-Laponite (circles) as a function of pressure at 40 K, normalized to the experimental adsorption isotherm.

5. H_2/D_2 effect on the *001* peak

The aim of this section is to investigate the impact of H_2 and D_2 adsorption at 40K on the *001* peak using SANS technique. Experiments were performed on D16 at ILL, in the same time as WANS ones, as D16 allows measurement from (relatively) small-Q values to large-Q ones (from 0.06$Å^{-1}$ to 2.6 $Å^{-1}$ in the conditions of our experiment).

5.1. Qualitative analysis

Figure V.30 shows the empty cell corrected SANS diagrams for dried pre-Lapointe for different H_2 and D_2 injected pressures. The intensity of the *001* peak is proportional to the square of the Fourier transform of the electronic density projected along z, the direction perpendicular to the (pre-)Laponite sheets. Moreover, at small A value, for the *001* peak, a homogeneous approximation can be applied so that the impact of H_2 and D_2 on the *001* peak intensity can be understood in terms of the change of the contrast between the interlayer and the TOT sheet. Let us introduce the scattering length densities (SLDs) of both, TOT sheets and the interlayer. For (pre-)Laponite, they are defined by equation (V.1)

$$SLD = \frac{1}{v} \cdot \sum_{i=1}^{n} b_{c_i} \quad \textbf{(V.1)}$$

where b_{c_i} is the coherent scattering length of ith of the n atoms in a (pre-)Laponite layer (excluding Na cations) or of the interlayer, with v the volume of the layer or of the interlayer space. The theoretical SLDs were calculated from the relaxed Laponite model discussed in **§2.1, Chapter III**. The SLD of the TOT sheet found to be 6.5×10^{-6} Å^{-2}, based on sheet thickness of 7.1 Å and a surface area of 24 nm^2, with a composition of 50 units of $Si_8Mg_{4.8}Li_{1.2}O_{20}(OD)_4$. For the interlayer, a thickness of 2.6 Å, and containing 50 units of $Na_{1.2}$, the SLD found to be $\sim 0.3 \times 10^{-6}$ Å^{-2} (Figure V.29).

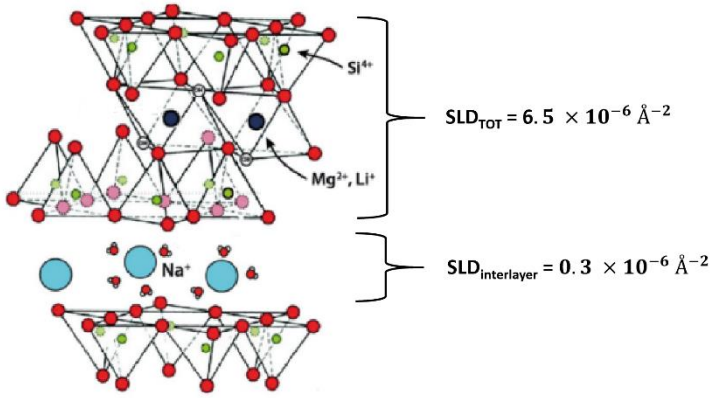

Figure V.29: Schematic representation of the structure of (pre-)Laponite, showing the calculated scattering length densities for the TOT sheet and the interlayer region.

- **Effect of H_2 intercalation:**

H_2 has a negative coherent scattering length ($b_{coh} = -7.4812 \times 10^{-5}$ Å). When H_2 molecules are adsorbed into the pre-Laponite interlayer, the SLD difference between the TOT layer and the interlayer is increased, thereby enhancing contrast. Consequently, this leads to an increase in the intensity of the *001* peak, as seen in the SANS diagram in Figure V.30.

- **Effect of D_2 intercalation:**

In contrast, D_2 has a positive scattering length ($b_{coh} = 13.342 \times 10^{-5}$ Å). When D_2 is adsorbed in the interlayer, the SLD difference between the TOT layer and the interlayer decreases. This increasing in contrast matching between the TOT and interlayer reduces the intensity of the *001* peak. As D_2 pressure increases, the interlayer SLD approaches that of the TOT layer, leading to a completely diminished of *001* peak. To put this in perspective, we calculated the interlayer uptake leading to complete extinction with the simplified, mean structural models proposed for

Laponite and (pre-)Laponite, with $n_a = n_b = 1.5$, n_c=3 for Laponite and $n_a = n_b = 0.5$, $n_c = 2$ for pre-Laponite. They are equal to 2.6 mmol/g in Laponite and 4 mmol/g in pre-Laponite. These values, which can only be considered as order of magnitudes, appear reasonable. Based on Figure V.30, the interlayer uptake in pre-Laponite is of about 3 mmol/g.

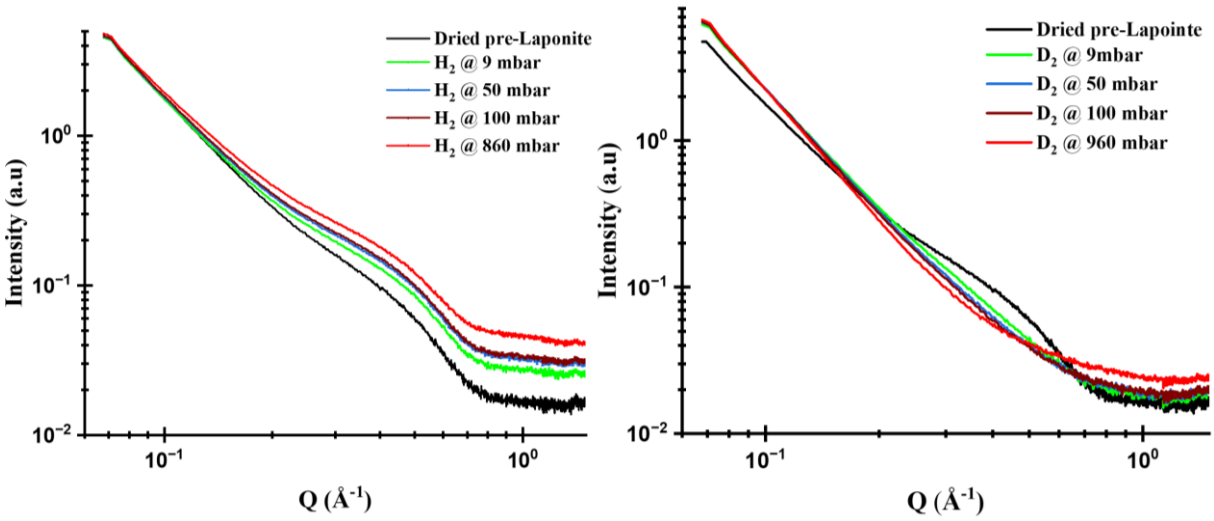

(a) **(b)**

Figure V.30: SANS diagrams measured at 40K for pre-Laponite versus (a) H_2 and (b) D_2 dosing pressures. Data are corrected from empty cell. Both graphs are presented on a log-log scale.

In addition to the coherent scattering observed in the *001* peak, the background in H_2-based spectra is more pronounced compared to D_2-based spectra. This difference results from the significantly higher incoherent scattering length of H_2 (b_{inc} = 50,548 fm) relative to that of D_2 (b_{inc} = 8.08 fm). The SANS diagrams for Laponite in Figure V.31 shows a shift of the *001* peak toward higher Q-values compared to pre-Laponite, resulting in a higher interlayer distance. This observation is consistent with the results from the XRS diagrams shown in **§1.1, Chapter IV**3.1. However, the evolution of the *001* peak with increasing D_2 dosing pressures in Laponite follows a similar trend to that of pre-Laponite.

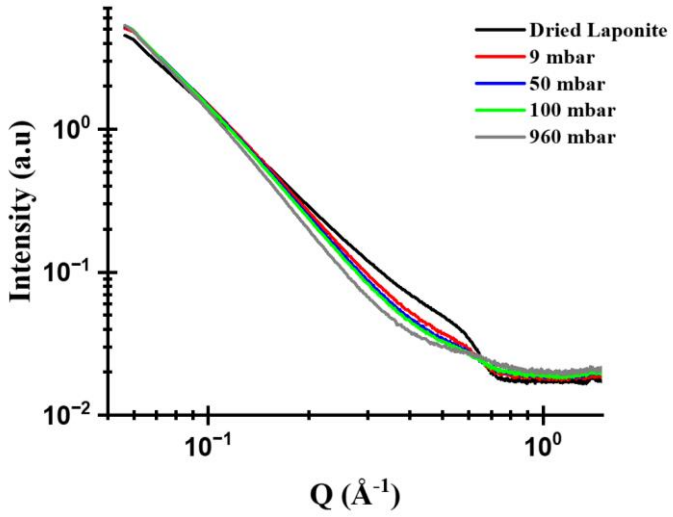

Figure V.31: SANS diagrams measured at 40K for pre-Laponite versus D_2 pressures. Data are corrected from empty cell and presented on a log-log scale.

5.2. An attempt at quantitative analysis

SANS diagrams offer insights into the density of H_2 or D_2 within the interlayer. However, data fitting is challenging due to the complex porous structure and weak stacking of both Laponite and pre-Laponite. This weak stacking allows surface-adsorbed H_2 (or D_2) to impact the *001* signal. However, it is not considered in the first approach developed below.

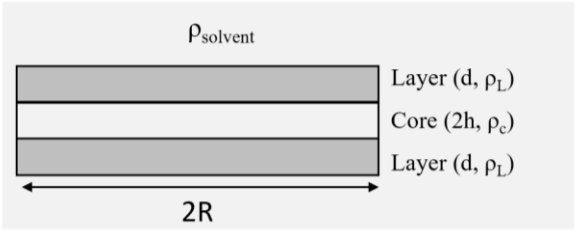

Figure V.32: Schematic representation of the geometry for a single-unit stacked disks model.

Taking these limitations with precautions, the H_2-based SANS diagrams were divided into two parts: the low-Q region, which was fitted using a power law model, and the high-Q region, corresponding to the *001* peak, which was fitted using the stacked disks model, implemented in SASview software within the cylinder category. In this model, stacked disks are dispersed in a solvent.

The geometry of single-unit stacked disks model is shown in Figure V.32 . The scattered intensity *I*(Q) is calculated as:

$$\boldsymbol{I(Q) = scale \cdot N \int_0^{\pi/2} \left[\Delta\rho_t\left(V_t f_t(Q,\alpha) - V_c f_c(Q,\alpha)\right) + \Delta\rho_c V_c f_c(Q,\alpha)\right]^2 S(Q,\alpha)\ \sin\alpha\ d\alpha + background} \quad \textbf{(V.1)}$$

where the background represents the incoherent scattering, N the number of units, V_t and V_c are the total and core volume of a single disk, respectively. The contrast is defined as:

$$\Delta\rho_i = \rho_i - \rho_{solvent} \quad \textbf{(V.2)}$$

where ρ_i represent the SLD for the core (or layer) and $\rho_{solvent}$ is the solvent's SLD. The form factors, $f(Q,\alpha)$, are defined as:

$$f_t(Q,\alpha) = \left(\frac{\sin(Q(d+h)\cos\alpha)}{Q(d+h)\cos\alpha}\right)\left(\frac{2J_1(QR\sin\alpha)}{QR\sin\alpha}\right) \quad \textbf{(V.3)}$$

$$f_c(Q,\alpha) = \left(\frac{\sin(Qh)\cos\alpha)}{Qh\cos\alpha}\right)\left(\frac{2J_1(QR\sin\alpha)}{QR\sin\alpha}\right) \quad \textbf{(V.4)}$$

where h and R are represented in Figure V.32. The structure factor, $S(Q,\alpha)$ writes:

$$S(Q,\alpha) = N + 2\sum_{k=1}^{N-1}(N-k)\cos(kDQ\cos\alpha)\exp[-kQ^2(D\cos\alpha\,\sigma_d)^2/2] \quad \textbf{(V.5)}$$

where $D = 2(d+h)$ (equivalent to d_{001}) is the basal spacing and σ_d represents standard deviation in basal spacings. Here it should be noted that we have checked, making our own program, that formula V.5, derived by us, is the one used in the SASview software as in the SASview's documentation contains an error (it gives $S(Q,\alpha) = 1 + \frac{1}{2}\sum_{k=1}^{N-1}(N-k)\cos(kDQ\cos\alpha)\exp[-kQ^2(D\cos\alpha\,\sigma_d)^2/2)]$)

In SANS diagrams for both Laponite and pre-Laponite, there is no Guinier plateau[13] observed at very low Q. This indicates the presence of large-scale structural domains that are larger than,

[13] *Guinier plateau represents the radius of gyration of the largest particle.*

or of the order of $^{2\pi}/_{Q_{min}} \approx 100$ Å reached in this experiment. The experimental and fitted SANS diagram for pre-Laponite with no H_2 adsorbed molecules is shown in Figure V.33.

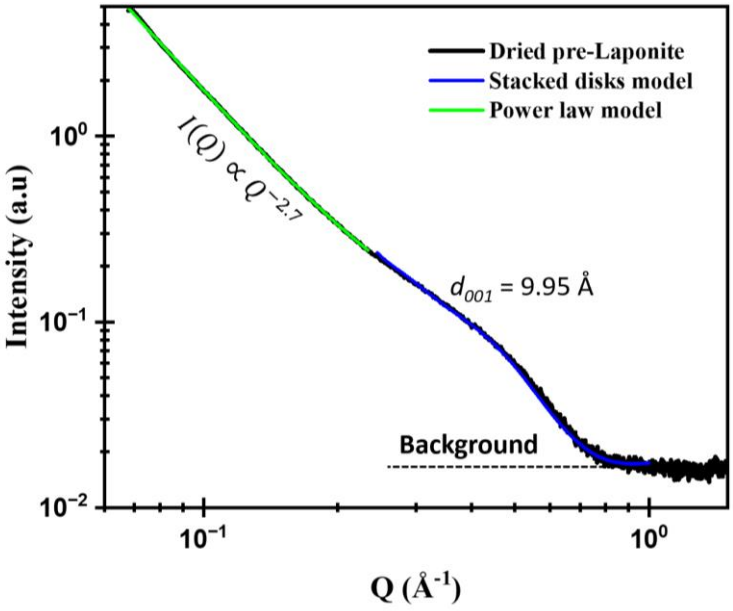

Figure V.33: Experimental SANS data for dried pre-Laponite (black), fitted with a power law model (green) in the low-Q range and a stacked disk model (blue) for the 001 peak. The dashed line represents the incoherent background.

The scattering profile at low-Q follow a power law of $I(Q) \propto Q^{-2.7}$. An exponent of 2.7 suggests a fractal morphology, indicating typically aggregates of structures that persist throughout the system [164].

Table V.4: Calculated parameters for the stacked disk model in dried pre-Lapointe.

Dried pre-Laponite	
Stacked disk, calculated parameters	
Scale	0.2137
Background	0.0168
Thick TOT, 2*h* (Å)	7
Thick interlayer, 2*d* (Å)	2.95
Radius (Å)	40.649
Number of stacking (N)	3
σ_d (Å)	0.45
SLD TOT (10^{-6} / Å^2)	6.7
SLD interlayer (10^{-6} / Å^2)	0.2

The fitted parameters used in the stacked disks model for dried pre-Laponite are summarized in Table V.4. In this analysis, the fitting parameters were chosen to represent the TOT sheet as the core and the interlayer as the layer. We applied a pinhole smearing of dQ/Q = 2.2%, representing the D16 instrumental resolution. Gaussian distributions were assumed for the disc radii and basal spacing, with a polydispersity (PD) [14] ratio of 0.1 for the radii and a standard deviation of 0.45 Å for the basal spacing (see Figure V.34). Moreover, since the analysis was conducted on a powder sample, no SLD solvent is included.

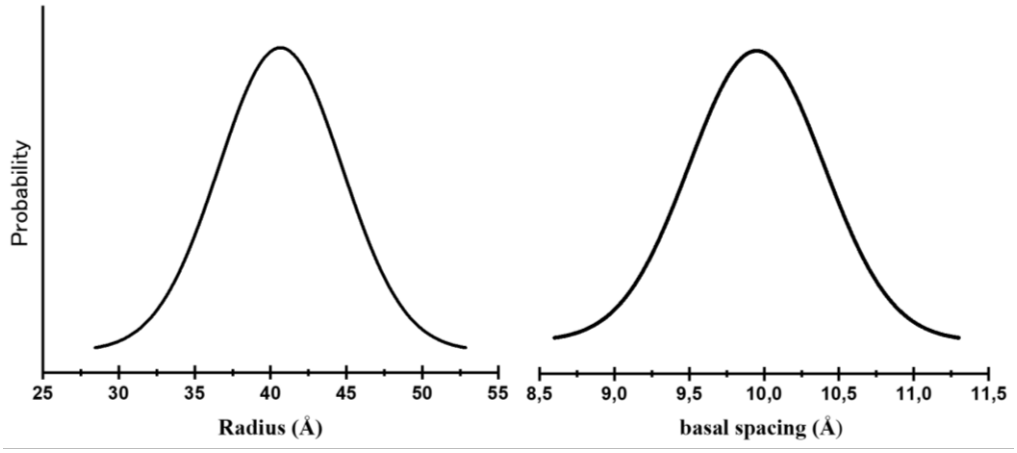

Figure V.34: Gaussian distribution of disc radii and basal-spacing used for pre-Laponite fitting.

The mean value of the fitted basal spacing, closely matched the value derived from the XRS diagrams (d_{001} = 9.7 Å) in **Chapter IV**, **3.1**. Furthermore, SLDs of the TOT sheet and interlayer used to fit pre-Laponite, closely align with the values deduced from the Laponite model deduced from Molecular dynamics discussed previously. Therefore, the fitting presented is a good starting point to further calculate the H_2 interlayer density at different pressures.

We performed calculations with pre-Laponite with and without H_2 molecules on the outer surfaces, from atomistic models, and we found that outer surface-adsorbed H_2 can affect the *001* peak. Indeed, the form factor of this small scattering object is changed with the addition of H_2. However, in our model, we chose to disregard this effect to focus exclusively on the interlayer-adsorbed H_2, to try extract an interlayer H_2 density. The fitted diagrams are presented in Figure V.35, with the varying fitted parameters from dried pre-Laponite provided in Table V.5.

[14] *PD ratio: the ratio of the standard deviation to the mean value.*

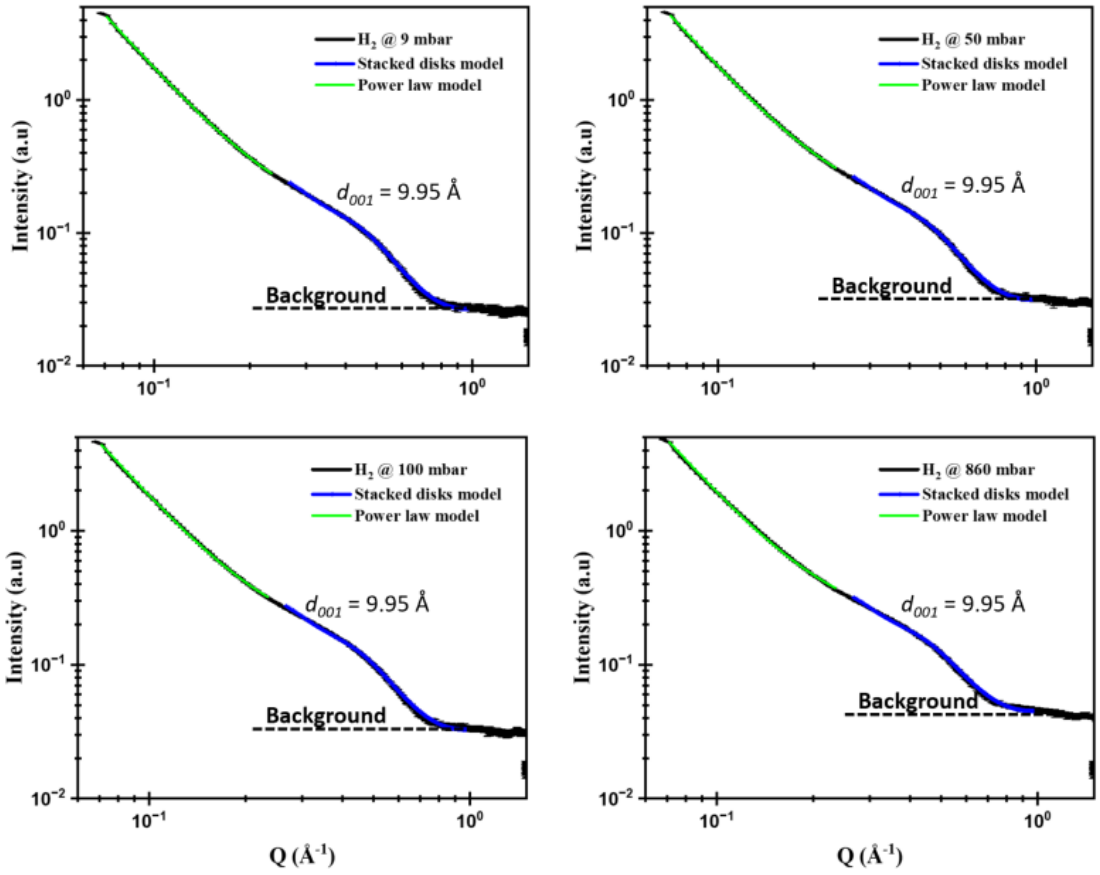

Figure V.35: SANS diagrams at different H_2 pressures at 40K, with experimental data shown in black, the stacked disk model in blue, and the power law model in green. The dashed line represents the incoherent background.

During the fitting process, the scale was expected to remain fixed; however, it was observed to change. We tentatively attribute this variation to the H_2 adsorbed on the outer surface, which is not incorporated into the SLDs. Additionally, the background variation is due to incoherent scattering from H_2 and the most important term is the change of the interlayer SLD, corresponding to the interlayer-adsorbed H_2.

Table V.5: Calculated parameters for the stacked disk model in pre-Laponite at 40K across different H_2 pressures.

	H_2 dosing pressure (mbar)			
Calculated parameters	**9**	**50**	**100**	**860**
Scale	0.274	0.3	0.315	0.36
Background	0.026	0.031	0.032	0.044
SLD interlayer (10^{-6} / Å^2)	-1.142	-1.234	-1.235	-1.3

The interlayer-adsorbed H_2 density, calculated based on interlayer SLD fitted from SANS diagrams at different pressures, taking for the particle radius and number of stacked sheets their mean fitted values, is summarized in Table V.6. The density at low pressures, up to 1 bar, in pre-Laponite at 40K, is found to be comparable to the liquid H_2 density of 71 kg/m³ at 23 K [153]. The density is plotted against H_2 dosing pressure, with data fitted using Langmuir model (Figure V.36). The resulting affinity constant (b = 0.48 ± 0.02 $mbar^{-1}$) of the Langmuir model closely matches the value obtained from fitting the adsorption isotherm measured at 40K discussed in **§2.2.2**.

Table V.6: Calculated interlayer-adsorbed H_2 density at 40K based on SANS diagrams in dried pre-Laponite.

H_2 dosing pressure (mbar)	**Interlayer-H_2 density ($kg.m^{-3}$)**	**Uptake (mmol/g)**
9	60	10.2
50	64.2	10.9
100	65.3	11.1
860	67.1	11.4

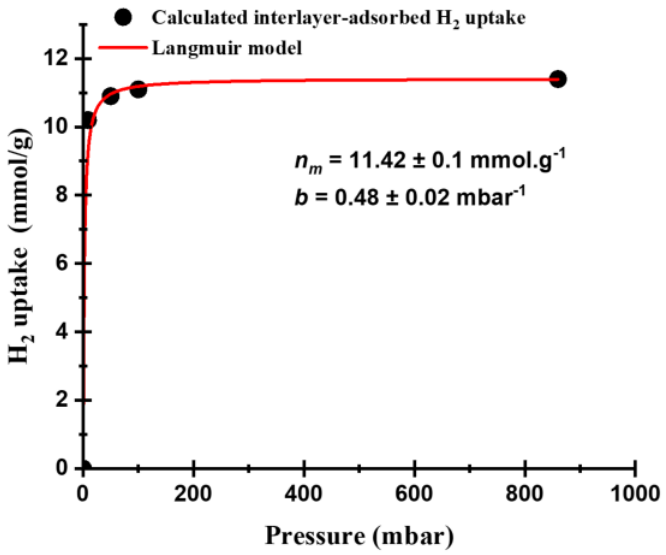

Figure V.36: (a) Calculated interlayer-adsorbed H_2 uptake versus pressure based on SANS data (black), fitted with the Langmuir model (red).

Note that with the model, we have a qualitative agreement but we do not find the values of the isotherm, which may indicate the limit in the small Q modeling proposed. In summary, the stacked disk model used for fitting SANS data is too simple to accurately evaluate H_2 uptake in the pre-Laponite sample, as the values obtained do not align with the experimental isotherm.

5.3. Quantum effect in pre-Laponite interlayer

It is well known that when H_2 molecules are confined in narrow spaces, they can no longer be treated as classical particles, as quantum effects become significant. This concept of quantum sieving was first introduced by *Beenakker et al*. while investigating quantum effects for hard spheres confined in hard cylindrical pores [165]. Additionally, numerous studies [166], [167], [168] have confirmed and expanded on these effects, particularly in the separation of H_2/D_2 isotopes in different nanoporous materials, such as CNTs, zeolites, and MOFs etc...

In all mentioned studies, it has been observed that D_2 diffuses faster than H_2 at temperatures below 100K. This phenomenon occurs because the lighter isotope, H_2, has a larger de Broglie wavelength λ ($\lambda = \frac{h}{mv_r}$, where h is Planck's constant, m is the mass of H_2 or D_2, and v_r is the radial velocity), making the wavelength comparable to the available space for molecular motion. This enhances quantum sieving effects, facilitating isotope separation.

As pre-Laponite is characterized by the presence of a strong adsorption site, the interlayer, with nanoscopic dimensions, it was found that at 40K, a quantum effect is observed in adsorption isotherm between H_2 and D_2 isotopes. The isotherm measured in dried pre-Laponite at 40K is shown in Figure V.37. Prior to adsorption experiments, pre-Laponite is heated at 150°C for 6 hours under secondary vacuum.

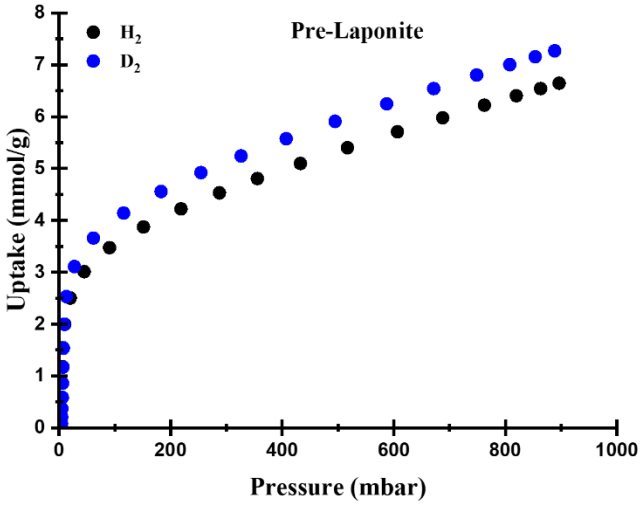

Figure V.37: Adsorption isotherms of H_2 (black) and D_2 (blue) on dried pre-Laponite measured at 40K.

At low pressures, particularly around 10 mbar, the uptake of D_2 is higher than that of H_2, with values of 2.53 mmol/g and 2.16 mmol/g, respectively. As previously mentioned, the interlayer sites dominate adsorption at low pressures. This observation aligns with the principles of

quantum effect, where it become significant due to the nanoscopic interlayer space within the pre-Laponite structure.

Conclusion

In summary, this chapter provides a framework for understanding the H_2 adsorption mechanism in layered clay materials, particularly (pre-)Laponite, by combining adsorption isotherms, neutron spectroscopy and neutron diffraction. The investigation first explored the reasons behind the enhanced H_2 uptake in pre-Laponite compared to Laponite at 77K–1 bar and at room temperature up to 100 bars, and second, the reason behind the deviation of pre-Laponite from the SSA-H_2 uptake correlation line at 77K. To address these questions, it was essential to distinguish between the different adsorption sites.

At 40K, with the help of GCMC simulations, two adsorption regions with different affinities were identified as contributing to the isotherm. At low pressures, interlayer dominates, H_2 forms a monolayer and exhibits a Langmuir-type saturation below 1 bar. In contrast, outer-surface behaves as non-saturating Freundlich-type adsorption surfaces. When comparing pre-Laponite and Laponite adsorption isotherms at 40K, the enhanced uptake in pre-Laponite is primarily attributed to the interlayer sites as it occurs at low pressures. It should be noted that in terms of coherence lengths, the Laponite sample used here is in between pre-Laponite and the Laponite sample presented in Chapter IV and used for neutron scattering, so that adsorption is probably higher in this Laponite sample than in the one studied in more details.

Upon understanding what are the two main adsorption regions, the deviation of pre-Laponite from the SSA-H_2 uptake correlation line can be discussed as follows. Can H_2 access the entire interlayer region in Laponite? And can N_2 do so as well? It is important to note that SSA is calculated based on the N_2 isotherm. In pre-Laponite, H_2 seems to access better the interlayer region than N_2. In Laponite, neither N_2 nor H_2 can access the entire interlayer region, resulting in an SSA estimation that is closer to the actual area available for H_2 adsorption and to lower uptake in the interlayer compared to pre-Laponite. One should remind here that the interlayer spacing was found to be slightly larger in pre-Laponite than in Laponite in **Chapter IV**, which may explain why H_2 fill it better in pre-Laponite.

INS provide valuable insights into the different adsorption sites in the system. By analyzing the inelastic features and in particular the para-to-ortho J_{01} rotational transition, three distinct adsorption sites were identified. At very low pressures (3 mbar), a strong adsorption site –

termed site 0 – is observed. This site restricts H_2 rotation, resulting in a featureless typical spectrum. As the pressure increases, two additional sites – termed site 1 and site 2 –are identified, with H_2 molecules adsorbed on these sites exhibiting distinct rotational lines. The orientational potential of site 1 is stronger than that of site 2, with a higher orientational barrier height, and Site 1 is more prominent in pre-Laponite than in Laponite.

- Site 0 could be associated with H_2 dissociation.
- Sites 1 and 2 are attributed to the interlayer region, where different configurations may be present.
- Site 2, corresponds to H_2 molecules with their axis aligned parallel to the adsorption surface, characterized by an orientational potential well of approximately 96K in Laponite and 80K in pre-Laponite.

Furthermore, atomistic calculations using GCMC configuration at 2 mbar, combined with WANS data, reveal a mean interlayer D_2-D_2 separation of about 3 Å in both Laponite and pre-Laponite, with some D_2 molecules in the interlayer positioned above the hexagonal cavities of the nearest layer. Additionally, Langmuir-type behavior is observed for the D_2-D_2 correlation peak, suggesting that outer-surface adsorbed D_2 does not contribute to the diffraction pattern. Notably, pre-Laponite exhibits higher D_2 uptake compared to Laponite

Take home messages

- **Adsorption isotherms**
  - **H_2 uptake comparison:** Pre-Laponite shows higher H_2 uptake than Laponite at 77K and 1 bar, and at room temperature and 100 bars.
  - **Quantum effect:** At 40K, adsorption of D_2 is higher than adsorption of H_2 in pre-Laponite, which is attributed to a quantum effect, due to the small interlayer spacing.
  - **Interlayer and outer surface sites:** At 40K and 1 bar, the adsorption isotherm was fitted using two models, guided by GCMC simulations using COMPASSIII forcefield. The Langmuir model represents the interlayer site, dominating at low pressures and showing monolayer saturation, while the Freundlich model describes continuous adsorption on the outer surfaces.

- **In-situ INS at 40K:** By focusing on the para-to-ortho, J_{01}, rotational transition, three adsorption sites were identified. At very low pressures (below 3mbar), a strong adsorption site -termed Site 0- is observed, which prohibits H_2 reorientation, producing a broad, featureless, band between 3 and 20 meV. As pressure increases, two additional sites – termed site 1 and site 2 – are identified, H_2 molecules adsorbed on these sites displaying rotational lines. Site 1 is stronger than site 2, that is the orientational barrier height is higher in site 1, and site 0 and 1 are more prominent in pre-Laponite compared to Laponite. Site 0 is attributed to H_2 dissociation. Site 2, where the H_2 axis lies parallel to the adsorption surface, has an orientational potential well of about 96K in Laponite and 80K in pre-Laponite. Furthermore, sites 1 and 2 are attributed to the interlayer region, where different configurations may be present.

- **In-situ WANS/SANS at 40K:** Atomistic simulations using GCMC configuration at 2 mbar, along with WANS data, reveal mean interlayer D_2-D_2 spacing of 3Å layer in both Laponite and pre-Laponite, with some D_2 molecules located above the hexagonal cavities in the closest. Notably, Langmuir-type behavior is observed for the D_2-D_2 correlation peak, indicating that outer-surface adsorbed D_2 does not contribute significantly to the diffraction pattern. Based on WANS analysis, it is found that, pre-Laponite exhibits higher D_2uptake compared to Laponite, confirming that interlayer sites are the primary factor driving the enhanced adsorption observed in pre-Laponite. Additionally, SANS diagrams show D_2 and H_2 adsorption impact on *001* peak. The *001* peak decreases upon D_2 adsorption in the interlayer and it increases upon H_2 adsorption, as expected when considering contrast effects.

This page was intentionally left blank.

General conclusions and perspectives

This thesis presents a new study of the hydrogen adsorption mechanism in a clay material. For that, the present work combines several experimental approaches—including different characterization techniques, X-ray scattering, neutron spectroscopies and neutron diffraction—with GCMC simulations and atomistic calculations, enabling a detailed interpretation of experimental observations.

The thesis work was divided into two main parts. The first part aimed to understand the chemical, structural, and textural differences and similarities between the materials of interest, Laponite and pre-Laponite, using different characterization techniques. The second part focused on providing detailed insights into H_2 adsorption, employing methods like adsorption isotherms, INS, WANS, and SANS.

The synthesis of Laponite follows the Neumann patent. Prior to the final hydrothermal step, we identified a precursor material, termed "pre-Laponite", which interestingly shows enhanced H_2 uptake at 77K – 1bar and 298K – 100 bars. ICP-AES measurements confirm that Laponite and pre-Laponite have similar chemical compositions in line with molecular formula $Si_8Mg_{4.8}Li_{1.2}Na_{1.2}O_{20}(OH)_4$. XRS analysis reveals comparable TOT atomic structures with a basal spacing of about 9.7Å, characteristic of dried Laponite. It is slightly larger in pre-Laponite. Pre-Laponite shows broader *00l* reflections, suggesting weaker stacking or larger distribution of basal spacings compared to Laponite. Additionally, pre-Laponite's smoother *hk* rising edge shows that its lateral correlation lengths are smaller than that of Laponite. It could be related to a smaller lateral sheet dimension or more in-plane defects. Calculated XRS diagrams based on MD-relaxed structure show the best fit with the experimental diffractogram with three stacked TOT sheets and an in-plane coherence surface area of 54 nm^2 for Laponite, while one finds two stacked sheets with a reduced surface area of 6 nm^2, for pre-Laponite. PDF analysis supports these findings, showing similar pair correlation distances but smaller coherent domain sizes in pre-Laponite.

In terms of porosity, N_2 adsorption isotherms reveal significant textural differences. Pre-Laponite exhibits a Type I/II isotherm, with a slightly higher specific surface area (S_{BET} = 472 m^2/g), while Laponite (S_{BET} = 445 m^2/g) shows a Type I/IV isotherm. The hysteresis loops further underscore these differences: pre-Laponite displays an H3 loop, which implies more

open, accessible slit-like pores, whereas Laponite's H4 loop suggests a denser packing of particles with narrower slit-like pores.

Local order of Laponite and pre-Laponite was investigated through IR, ssNMR, and XANES spectroscopy. Identical IR spectra confirm that both materials share similar bonding environments. Moreover, ^{29}Si NMR analysis provides finer details, revealing that while Laponite and pre-Laponite have comparable Si environments, pre-Laponite exhibits a lower Q^3/Q^2 ratio. This difference is attributed to pre-Laponite's smaller layer size, which reduces the surface-to-edge ratio and thus the proportion of Q^3 sites. XANES spectroscopy further clarifies the atomic structure, showing similar Mg K-edge features in both materials. These spectra confirm the trioctahedral nature of both samples. Additionally, Si K-edge measurements support comparable Si environments in both materials, with more defined post-edge features in Laponite suggesting greater homogeneity. The reduced layer size and possible structural defects in pre-Laponite likely contribute to these differences, with Si atoms in pre-Laponite experiencing a higher degree of local variation due to a larger edge-to-bulk ratio or stress effects.

The second part of the thesis focused on H_2 adsorption mechanism. At 40K, guided by GCMC simulations using the COMPASSIII force field, two adsorption sites with different regions were identified in adsorption isotherms. The interlayer exhibits Langmuir behavior, dominating at low pressures and rapidly followed with monolayer saturation, while the outer surface follows non-saturating Freundlich model.

The main focus of the INS experiments measured on PANTHER, was to probe the rotational transition from para-to-ortho (J_{01}) at 40K (above H_2 critical point), from low pressures up to 1 bar. The results show that at low pressures, a strong adsorption site is observed, which significantly hinders the rotation of H_2 molecules, resulting in a broad, featureless, band between 3 and 20 meV. This site is likely associated with H_2 dissociation. As pressure increases, J_{01} rotational lines, corresponding to two additional adsorption sites, Site 1 and Site 2, appear. Site 1, which exhibits a stronger orientational potential than Site 2, is more prominent in pre-Laponite than in Laponite. Site 1 reaches saturation at pressures $\leq$ 25 mbar in Laponite, while in pre-Laponite, saturation is not observed until 50 mbar. Furthermore, pre-Laponite adsorbs more amount of H_2 at this site compared to Laponite. Site 2 behaves similarly in both Laponite and pre-Laponite, where the H_2 axis is preferentially aligned parallel to the adsorption surface, with an associated orientational potential wall of -96K in Laponite and -80K in pre-Laponite.

Both sites, 1 and 2, with Langmuir behavior are attributed to the interlayer regions, where different configurations may exist.

At this stage of the study, it was important to understand the structure of adsorbed H_2. For this, WANS/SANS experiments were performed on D16 beamline using D_2 instead of H_2 due to its better coherent-incoherent signal ratio. WANS results, supported by atomistic simulations based on GCMC configuration, show an interlayer D_2-D_2 separation with a mean value of about 3Å in both Laponite and pre-Laponite, with some D_2 molecules aligning above the hexagonal cavities of the closest layer. Langmuir-type behavior is observed for the D_2-D_2 correlation peak, indicating that outer-surface adsorbed D_2 does not contribute significantly to the diffraction pattern. At 9 mbar, pre-Laponite demonstrates roughly three times higher interlayer D_2 uptake than Laponite at 40 K, confirming that interlayer sites are the primary factor driving the enhanced adsorption observed in pre-Laponite. Furthermore, D_2 and H_2 behaves oppositely in relation to the *001*-peak intensity shown in SANS diagrams, which is due to the inverse sign of their coherent scattering lengths and which confirms their presence in the interlayers.

To further deepen and support our mechanism of H_2 adsorption in (pre-)Laponite materials, and to better differentiate between interlayer and outer surface adsorbed H_2, the following points are recommended:

- Perform GCMC simulations using CLAYFF force field, as the COMPASSIII force field may not be fully suitable for this system.
- Investigate highly stacked smectite materials with much larger particle sizes, allowing one to neglect the outer surface-adsorbed H_2 and enabling a focused study on interlayer sites. It would also allow for larger volumetric adsorption values than in nano-clays if interlayers are accessible in such a compact material. This study could be further extended by pillaring the interlayer to observe its impact on interlayer adsorbed density and H_2/D_2 structuring.

Finally, this study shows that dried (pre-)Laponite, can adsorbed H_2 in its interlayer sites that behaves as most energetically favored site.

References

[1] "Emissions – Global Energy & CO2 Status Report 2019 – Analysis," IEA.

[2] T. Egeland-Eriksen, A. Hajizadeh, and S. Sartori, "Hydrogen-based systems for integration of renewable energy in power systems: Achievements and perspectives," *International Journal of Hydrogen Energy*, vol. 46, no. 63, pp. 31963–31983, Sep. 2021, doi: 10.1016/j.ijhydene.2021.06.218.

[3] A. Z. Arsad *et al.*, "Hydrogen energy storage integrated hybrid renewable energy systems: A review analysis for future research directions," *International Journal of Hydrogen Energy*, vol. 47, no. 39, pp. 17285–17312, May 2022, doi: 10.1016/j.ijhydene.2022.03.208.

[4] M. Yue, H. Lambert, E. Pahon, R. Roche, S. Jemei, and D. Hissel, "Hydrogen energy systems: A critical review of technologies, applications, trends and challenges," *Renewable and Sustainable Energy Reviews*, vol. 146, p. 111180, Aug. 2021, doi: 10.1016/j.rser.2021.111180.

[5] D. Pyza, P. Gołda, and E. Sendek-Matysiak, "Use of hydrogen in public transport systems," *Journal of Cleaner Production*, vol. 335, p. 130247, Feb. 2022, doi: 10.1016/j.jclepro.2021.130247.

[6] Y. Li and F. Taghizadeh-Hesary, "The economic feasibility of green hydrogen and fuel cell electric vehicles for road transport in China," *Energy Policy*, vol. 160, p. 112703, Jan. 2022, doi: 10.1016/j.enpol.2021.112703.

[7] K. Lodders, "Solar System Abundances and Condensation Temperatures of the Elements," *ApJ*, vol. 591, no. 2, p. 1220, Jul. 2003, doi: 10.1086/375492.

[8] L. Truche *et al.*, "A deep reservoir for hydrogen drives intense degassing in the Bulqizë ophiolite," *Science (New York, N.Y.)*, vol. 383, pp. 618–621, Feb. 2024, doi: 10.1126/science.adk9099.

[9] R. K. Ahluwalia, X. Wang, A. Rousseau, and R. Kumar, "Fuel economy of hydrogen fuel cell vehicles," *Journal of Power Sources*, vol. 130, no. 1, pp. 192–201, May 2004, doi: 10.1016/j.jpowsour.2003.12.061.

[10] K. Mazloomi and C. Gomes, “Hydrogen as an energy carrier: Prospects and challenges,” *Renewable and Sustainable Energy Reviews*, vol. 16, pp. 3024–3033, Jun. 2012, doi: 10.1016/j.rser.2012.02.028.

[11] A. Aghmadi and O. Mohammed, “Energy Storage Systems: Technologies and High-Power Applications,” *Batteries*, vol. 10, p. 141, Apr. 2024, doi: 10.3390/batteries10040141.

[12] H. Q. Nguyen and B. Shabani, “Proton exchange membrane fuel cells heat recovery opportunities for combined heating/cooling and power applications,” *Energy Conversion and Management*, vol. 204, p. 112328, Jan. 2020, doi: 10.1016/j.enconman.2019.112328.

[13] J. Lindorfer, D. C. Rosenfeld, and H. Böhm, “23 - Fuel Cells: Energy Conversion Technology,” in *Future Energy (Third Edition)*, T. M. Letcher, Ed., Elsevier, 2020, pp. 495–517. doi: 10.1016/B978-0-08-102886-5.00023-2.

[14] I. F. Silvera, “The solid molecular hydrogens in the condensed phase: Fundamentals and static properties,” *Rev. Mod. Phys.*, vol. 52, no. 2, pp. 393–452, Apr. 1980, doi: 10.1103/RevModPhys.52.393.

[15] A. D. McLean and M. Yoshimine, “Molecular Properties Which Depend on the Square of the Electronic Coordinates; H2 and NNO,” *The Journal of Chemical Physics*, vol. 45, no. 10, pp. 3676–3681, Nov. 1966, doi: 10.1063/1.1727387.

[16] “Jacqueline Edge Thesis.”

[17] B. Ibrahimoglu, Y. Sarikaya, A. Veziroglu, B. Ibrahimoglu, M. Onal, and B. Gokbel, “Supercritical phases of hydrogen,” *International Journal of Hydrogen Energy*, vol. 46, no. 65, pp. 32762–32767, Sep. 2021, doi: 10.1016/j.ijhydene.2021.07.032.

[18] I. F. Silvera, “The solid molecular hydrogens in the condensed phase: Fundamentals and static properties,” *Rev. Mod. Phys.*, vol. 52, no. 2, pp. 393–452, Apr. 1980, doi: 10.1103/RevModPhys.52.393.

[19] P. C. Souers, *Hydrogen Properties for Fusion Energy*. University of California Press, 1986.

[20] J. Leachman, R. Jacobsen, S. Penoncello, and E. Lemmon, "Fundamental Equations of State for Parahydrogen, Normal Hydrogen, and Orthohydrogen," *Journal of Physical and Chemical Reference Data - J PHYS CHEM REF DATA*, vol. 38, Sep. 2009, doi: 10.1063/1.3160306.

[21] J. Y.-C. Chen *et al.*, "Nuclear spin isomers of guest molecules in H2@C60, H2O@C60 and other endofullerenes," *Philosophical Transactions of the Royal Society A: Mathematical, Physical and Engineering Sciences*, vol. 371, no. 1998, p. 20110628, Sep. 2013, doi: 10.1098/rsta.2011.0628.

[22] European Communities, *Hydrogen storage: state-of-the-art and future perspective*. Luxembourg: Publications Office, 2003.

[23] P. C. H. Mitchell, S. F. Parker, T. A. J. Ramirez-cuesta, and J. Tomkinson, *Vibrational Spectroscopy With Neutrons - With Applications In Chemistry, Biology, Materials Science And Catalysis*. World Scientific, 2005.

[24] D. White and E. N. Lassettre, "Theory of Ortho-Para Hydrogen Separation by Adsorption at Low Temperatures, Isotope Separation," *The Journal of Chemical Physics*, vol. 32, no. 1, pp. 72–84, Jan. 1960, doi: 10.1063/1.1700950.

[25] T. B. MacRury and J. R. Sams, "Hindered rotation of adsorbed diatomic molecules," *Molecular Physics*, vol. 20, no. 1, pp. 57–66, Jan. 1971, doi: 10.1080/00268977100100071.

[26] T. Weber *et al.*, "Complete photo-fragmentation of the deuterium molecule," *Nature*, vol. 431, no. 7007, pp. 437–440, Sep. 2004, doi: 10.1038/nature02839.

[27] N. B. Vargaftik, *Tables on the thermophysical properties of liquids and gases : in normal and dissociated states*, 2d ed. in Advances in thermal engineering. Hemisphere Pub. Corp. and distributed by Halsted Press, 1975.

[28] S. Z. A. Ghafri *et al.*, "Hydrogen liquefaction: a review of the fundamental physics, engineering practice and future opportunities," *Energy & Environmental Science*, vol. 15, no. 7, pp. 2690–2731, 2022, doi: 10.1039/D2EE00099G.

[29] M. Simanullang and L. Prost, "Nanomaterials for on-board solid-state hydrogen storage applications," *International Journal of Hydrogen Energy*, vol. 47, no. 69, pp. 29808–29846, Aug. 2022, doi: 10.1016/j.ijhydene.2022.06.301.

[30] A. Züttel, P. Wenger, P. Sudan, P. Mauron, and S. Orimo, "Hydrogen density in nanostructured carbon, metals and complex materials," *Materials Science and Engineering: B*, vol. 108, no. 1, pp. 9–18, Apr. 2004, doi: 10.1016/j.mseb.2003.10.087.

[31] B. Sakintuna, F. Lamaridarkrim, and M. Hirscher, "Metal hydride materials for solid hydrogen storage: A review☆," *International Journal of Hydrogen Energy*, vol. 32, no. 9, pp. 1121–1140, Jun. 2007, doi: 10.1016/j.ijhydene.2006.11.022.

[32] W. Grochala and P. P. Edwards, "Thermal Decomposition of the Non-Interstitial Hydrides for the Storage and Production of Hydrogen," *Chem. Rev.*, vol. 104, no. 3, pp. 1283–1316, Mar. 2004, doi: 10.1021/cr030691s.

[33] M. A. De La Casa-Lillo, F. Lamari-Darkrim, D. Cazorla-Amorós, and A. Linares-Solano, "Hydrogen Storage in Activated Carbons and Activated Carbon Fibers," *J. Phys. Chem. B*, vol. 106, no. 42, pp. 10930–10934, Oct. 2002, doi: 10.1021/jp014543m.

[34] M. Sevilla and R. Mokaya, "Energy storage applications of activated carbons: supercapacitors and hydrogen storage," *Energy & Environmental Science*, vol. 7, no. 4, pp. 1250–1280, 2014, doi: 10.1039/C3EE43525C.

[35] J. Rouquerol, F. Rouquerol, P. Llewellyn, G. Maurin, and K. Sing, *Adsorption by Powders and Porous Solids: Principles, Methodology and Applications*. Academic Press, 2013.

[36] B. Sukhbaatar, W. Qing, J. Seo, S. Yoon, and B. Yoo, "Uniformly dispersed ruthenium nanoparticles on porous carbon from coffee waste outperform platinum for hydrogen evolution reaction in alkaline media," *Sci Rep*, vol. 14, no. 1, p. 5850, Mar. 2024, doi: 10.1038/s41598-024-56510-7.

[37] R. Ströbel *et al.*, "Hydrogen adsorption on carbon materials," *Journal of Power Sources*, vol. 84, pp. 221–224, Dec. 1999, doi: 10.1016/S0378-7753(99)00320-1.

[38] N. Bouaziz, M. Ben Manaa, F. Aouaini, and A. Ben Lamine, "Investigation of hydrogen adsorption on zeolites A, X and Y using statistical physics formalism," *Materials*

Chemistry and Physics, vol. 225, pp. 111–121, Mar. 2019, doi: 10.1016/j.matchemphys.2018.12.024.

[39] H. W. Langmi *et al.*, "Hydrogen storage in ion-exchanged zeolites," *Journal of alloys and compounds*, vol. 404, pp. 637–642, 2005.

[40] J. G. Vitillo, G. Ricchiardi, G. Spoto, and A. Zecchina, "Theoretical maximal storage of hydrogen in zeolitic frameworks," *Physical Chemistry Chemical Physics*, vol. 7, no. 23, pp. 3948–3954, 2005, doi: 10.1039/B510989B.

[41] M. S. B. Reddy, D. Ponnamma, K. Kumar Sadasivuni, B. Kumar, and A. M. Abdullah, "Carbon dioxide adsorption based on porous materials," *RSC Advances*, vol. 11, no. 21, pp. 12658–12681, 2021, doi: 10.1039/D0RA10902A.

[42] D. J. Collins and H.-C. Zhou, "Hydrogen storage in metal–organic frameworks," *J. Mater. Chem.*, vol. 17, no. 30, p. 3154, 2007, doi: 10.1039/b702858j.

[43] J. Ren, H. W. Langmi, B. C. North, and M. Mathe, "Review on processing of metal–organic framework (MOF) materials towards system integration for hydrogen storage," *International Journal of Energy Research*, vol. 39, no. 5, pp. 607–620, 2015, doi: 10.1002/er.3255.

[44] A. Schoedel, "Chapter 2 - Secondary building units of MOFs," in *Metal-Organic Frameworks for Biomedical Applications*, M. Mozafari, Ed., Woodhead Publishing, 2020, pp. 11–44. doi: 10.1016/B978-0-12-816984-1.00003-2.

[45] M. Hirscher, "Hydrogen Storage by Cryoadsorption in Ultrahigh-Porosity Metal–Organic Frameworks," *Angewandte Chemie International Edition*, vol. 50, no. 3, pp. 581–582, 2011, doi: 10.1002/anie.201006913.

[46] N. Rosi *et al.*, "Hydrogen Storage in Microporous Metal-Organic Frameworks," *Science (New York, N.Y.)*, vol. 300, pp. 1127–9, Jun. 2003, doi: 10.1126/science.1083440.

[47] H. Furukawa *et al.*, "Ultrahigh Porosity in Metal-Organic Frameworks," *Science*, vol. 329, no. 5990, pp. 424–428, Jul. 2010, doi: 10.1126/science.1192160.

[48] L. J. Murray, M. Dincă, and J. R. Long, "Hydrogen storage in metal–organic frameworks," *Chemical Society Reviews*, vol. 38, no. 5, pp. 1294–1314, 2009, doi: 10.1039/B802256A.

[49] M. P. Suh, H. J. Park, T. K. Prasad, and D.-W. Lim, "Hydrogen Storage in Metal–Organic Frameworks," *Chem. Rev.*, vol. 112, no. 2, pp. 782–835, Feb. 2012, doi: 10.1021/cr200274s.

[50] E. Garrone, B. Bonelli, and C. Otero Areán, "Enthalpy–entropy correlation for hydrogen adsorption on zeolites," *Chemical Physics Letters*, vol. 456, no. 1, pp. 68–70, Apr. 2008, doi: 10.1016/j.cplett.2008.03.014.

[51] H. Frost, T. Düren, and R. Q. Snurr, "Effects of Surface Area, Free Volume, and Heat of Adsorption on Hydrogen Uptake in Metal−Organic Frameworks," *J. Phys. Chem. B*, vol. 110, no. 19, pp. 9565–9570, May 2006, doi: 10.1021/jp060433+.

[52] F. Bergaya and G. Lagaly, *Handbook of Clay Science*. Newnes, 2013.

[53] H. H. Murray, "Overview — clay mineral applications," *Applied Clay Science*, vol. 5, no. 5, pp. 379–395, Mar. 1991, doi: 10.1016/0169-1317(91)90014-Z.

[54] B. O. Otunola and O. O. Ololade, "A review on the application of clay minerals as heavy metal adsorbents for remediation purposes," *Environmental Technology & Innovation*, vol. 18, p. 100692, May 2020, doi: 10.1016/j.eti.2020.100692.

[55] T. ALLAN MCMASTER, "Sedimentologic and Geochemical Studies of the Bald Eagle - Juniata Color Boundary, Central Pennsylvania - ProQuest."

[56] B. Mysen, "Structure of Chemically Complex Silicate Systems," in *Encyclopedia of Glass Science, Technology, History, and Culture*, John Wiley & Sons, Ltd, 2021, pp. 197–206. doi: 10.1002/9781118801017.ch2.6.

[57] X. Liu, C. Tournassat, S. Grangeon, A. G. Kalinichev, Y. Takahashi, and M. Marques Fernandes, "Molecular-level understanding of metal ion retention in clay-rich materials," *Nat Rev Earth Environ*, vol. 3, no. 7, pp. 461–476, Jul. 2022, doi: 10.1038/s43017-022-00301-z.

[58] A. Negrónk-Mendoza, "Clay," in *Encyclopedia of Astrobiology*, M. Gargaud, W. M. Irvine, R. Amils, H. J. (Jim) Cleaves, D. L. Pinti, J. C. Quintanilla, D. Rouan, T. Spohn, S. Tirard, and M. Viso, Eds., Berlin, Heidelberg: Springer, 2015, pp. 480–483. doi: 10.1007/978-3-662-44185-5_303.

[59] G. M. D. Nascimento, *Clay and Clay Minerals*. BoD – Books on Demand, 2021.

[60] D. M. Moore and J. Hower, "Ordered Interstratification of Dehydrated and Hydrated Na-Smectite," *Clays Clay Miner.*, vol. 34, no. 4, pp. 379–384, Aug. 1986, doi: 10.1346/CCMN.1986.0340404.

[61] C. Tsiantos, V. Gionis, and G. D. Chryssikos, "Smectite in bentonite: Near infrared systematics and estimation of layer charge," *Applied Clay Science*, vol. 160, pp. 81–87, Aug. 2018, doi: 10.1016/j.clay.2018.01.022.

[62] A. Tamayo, J. Kyziol-Komosinska, M. Sánchez, P. Calejas, J. Rubio, and M. Barba, "Characterization and properties of treated smectites," *Journal of the European Ceramic Society*, vol. 32, no. 11, pp. 2831–2841, Aug. 2012, doi: 10.1016/j.jeurceramsoc.2011.12.029.

[63] G. Borchardt, "Smectites," in *Minerals in Soil Environments*, John Wiley & Sons, Ltd, 1989, pp. 675–727. doi: 10.2136/sssabookser1.2ed.c14.

[64] A. El-Ezz, A. Abdou, and M. Temraz, "The Petrography, Mineralogy, and Hydrocarbon Potential of the Shales of the Duwi Formation, Abu Tartur, South Western Desert, Egypt," *Petroleum Science and Technology*, vol. 30, Nov. 2012, doi: 10.1080/10916466.2010.499404.

[65] G. Brown, "Structure, Crystal Chemistry, and Origin of the Phyllosilicate Minerals Common in Soil Clays," in *Soil Colloids and Their Associations in Aggregates*, M. F. De Boodt, M. H. B. Hayes, A. Herbillon, E. B. A. De Strooper, and J. J. Tuck, Eds., Boston, MA: Springer US, 1990, pp. 7–38. doi: 10.1007/978-1-4899-2611-1_1.

[66] I. E. Odom, L. Fowden, R. M. Barrer, and P. B. Tinker, "Smectite clay minerals: properties and uses," *Philosophical Transactions of the Royal Society of London. Series A, Mathematical and Physical Sciences*, vol. 311, no. 1517, pp. 391–409, Jan. 1997, doi: 10.1098/rsta.1984.0036.

[67] J. Zhang, C. H. Zhou, S. Petit, and H. Zhang, "Hectorite: Synthesis, modification, assembly and applications," *Applied Clay Science*, vol. 177, pp. 114–138, Sep. 2019, doi: 10.1016/j.clay.2019.05.001.

[68] B. S. Neumann, "54) PRODUCTION OF MAGNESIUM SILICATES," p. 8.

[69] N. Negrete-Herrera, J.-L. Putaux, and E. Bourgeat-Lami, "Synthesis of polymer/Laponite nanocomposite latex particles via emulsion polymerization using silylated and cation-exchanged Laponite clay platelets," *Progress in Solid State Chemistry*, vol. 34, no. 2–4, pp. 121–137, Jul. 2006, doi: 10.1016/j.progsolidstchem.2005.11.040.

[70] N. P. Ashby and B. P. Binks, "Pickering emulsions stabilised by Laponite clay particles," *Physical Chemistry Chemical Physics*, vol. 2, no. 24, pp. 5640–5646, 2000, doi: 10.1039/B007098J.

[71] B. Ruzicka and E. Zaccarelli, "A fresh look at the Laponite phase diagram," *Soft Matter*, vol. 7, no. 4, p. 1268, 2011, doi: 10.1039/c0sm00590h.

[72] B. Ruzicka and E. Zaccarelli, "A fresh look at the Laponite phase diagram," *Soft Matter*, vol. 7, no. 4, p. 1268, 2011, doi: 10.1039/c0sm00590h.

[73] M. Kosmulski, *Chemical Properties of Material Surfaces*. CRC Press, 2001.

[74] R. Chaudhuri, F. López Arbeloa, and I. López Arbeloa, "Spectroscopic Characterization of the Adsorption of Rhodamine 3B in Hectorite," *Langmuir*, vol. 16, no. 3, pp. 1285–1291, Feb. 2000, doi: 10.1021/la990772c.

[75] D. L. Guerra, R. R. Viana, and C. Airoldi, "Use of raw and chemically modified hectorites as adsorbents for Th(IV), U(VI) and Eu(III) uptake from aqueous solutions," *Desalination*, vol. 260, no. 1, pp. 161–171, Sep. 2010, doi: 10.1016/j.desal.2010.04.045.

[76] A. Gil, R. Trujillano, M. A. Vicente, and S. A. Korili, "Hydrogen adsorption by microporous materials based on alumina-pillared clays," *International Journal of Hydrogen Energy*, vol. 34, no. 20, pp. 8611–8615, Oct. 2009, doi: 10.1016/j.ijhydene.2009.08.057.

[77] P. P. Ziemiański and A. Derkowski, "Structural and textural control of high-pressure hydrogen adsorption on expandable and non-expandable clay minerals in geologic

conditions," *International Journal of Hydrogen Energy*, vol. 47, no. 67, pp. 28794–28805, Aug. 2022, doi: 10.1016/j.ijhydene.2022.06.204.

[78] L. Masci *et al.*, "Hydrogen adsorption on Ni-functionalized saponites and their precursor gel," *International Journal of Hydrogen Energy*, vol. 58, pp. 79–92, Mar. 2024, doi: 10.1016/j.ijhydene.2023.10.314.

[79] A. Spinella and P. Conte, "Nuclear Magnetic Resonance Spectroscopy," in *Spectroscopy for Materials Characterization*, John Wiley & Sons, Ltd, 2021, pp. 281–317. doi: 10.1002/9781119698029.ch10.

[80] A. Pines, M. G. Gibby, and J. S. Waugh, "Proton-enhanced NMR of dilute spins in solids," *The Journal of Chemical Physics*, vol. 59, no. 2, pp. 569–590, Jul. 1973, doi: 10.1063/1.1680061.

[81] J.-R. Li *et al.*, "Carbon dioxide capture-related gas adsorption and separation in metal-organic frameworks," *Coordination Chemistry Reviews*, vol. 255, no. 15, pp. 1791–1823, Aug. 2011, doi: 10.1016/j.ccr.2011.02.012.

[82] K. Hirose, "Hydrogen as a fuel for today and tomorrow: expectations for advanced hydrogen storage materials/systems research," *Faraday Discuss.*, vol. 151, p. 11, 2011, doi: 10.1039/c1fd00099c.

[83] J. U. Keller and R. Staudt, Eds., "Adsorption Isotherms," in *Gas Adsorption Equilibria: Experimental Methods and Adsorptive Isotherms*, Boston, MA: Springer US, 2005, pp. 359–413. doi: 10.1007/0-387-23598-1_8.

[84] B. Alfeeli, R. Hendricks, and L. Taylor, "Chemical Micro Preconcentrators Development for Micro Gas Chromatography Systems".

[85] "'IUPAC Manual of Symbols and Terminology', appendix 2, Part 1, Colloid and Surface Chemistry | CiNii Research."

[86] E. Ferrage, "Investigation of the Interlayer Organization of Water And Ions in Smectite from the Combined Use of Diffraction Experiments and Molecular Simulations. A Review of Methodology, Applications, and Perspectives," *Clays and clay miner.*, vol. 64, no. 4, pp. 348–373, Aug. 2016, doi: 10.1346/CCMN.2016.0640401.

[87] S. Lowell, J. E. Shields, M. A. Thomas, and M. Thommes, *Characterization of Porous Solids and Powders: Surface Area, Pore Size and Density*. Springer Science & Business Media, 2012.

[88] J. Rouquerol, F. Rouquerol, P. Llewellyn, G. Maurin, and K. Sing, *Adsorption by Powders and Porous Solids: Principles, Methodology and Applications*. Academic Press, 2013.

[89] M. Almáši, V. Zeleňák, A. Zukal, J. Kuchár, and J. Čejka, "A novel zinc(II) metal–organic framework with a diamond-like structure: synthesis, study of thermal robustness and gas adsorption properties," *Dalton Trans.*, vol. 45, no. 3, pp. 1233–1242, Jan. 2016, doi: 10.1039/C5DT02437D.

[90] L. Zhou, S. Bai, Y. Zhou, and B. Yang, "Adsorption of Nitrogen on Silica Gel Over a Large Range of Temperatures," *Adsorption*, vol. 8, no. 1, pp. 79–87, Jan. 2002, doi: 10.1023/A:1015274624834.

[91] D. Gallis, I. Ermanoski, J. Greathouse, K. Chapman, and T. Nenoff, "Iodine Gas Adsorption in Nanoporous Materials: A Combined Experiment-Modeling Study," *Industrial & Engineering Chemistry Research*, vol. 56, Jan. 2017, doi: 10.1021/acs.iecr.6b04189.

[92] L. Liu, S. (Johnathan) Tan, T. Horikawa, D. D. Do, D. Nicholson, and J. Liu, "Water adsorption on carbon - A review," *Advances in Colloid and Interface Science*, vol. 250, pp. 64–78, Dec. 2017, doi: 10.1016/j.cis.2017.10.002.

[93] J.-W. Lee, D.-Y. Choi, D.-H. Kwak, H.-J. Jung, W.-G. Shim, and H. Moon, "Adsorption Dynamics of Water Vapor on Activated Carbon," *Adsorption*, vol. 11, no. S1, pp. 437–441, Jul. 2005, doi: 10.1007/s10450-005-5964-x.

[94] M. H. Polley, W. D. Schaeffer, and W. R. Smith, "Development of Stepwise Isotherms on Carbon Black Surfaces," *J. Phys. Chem.*, vol. 57, no. 4, pp. 469–471, Apr. 1953, doi: 10.1021/j150505a019.

[95] E. Greenhalgh and E. Redman, "Stepped isotherms on carbons," *J. Phys. Chem.*, vol. 71, no. 4, pp. 1151–1152, Mar. 1967, doi: 10.1021/j100863a063.

[96] K. S. W. Sing, “Reporting physisorption data for gas/solid systems with special reference to the determination of surface area and porosity (Recommendations 1984),” *Pure and Applied Chemistry*, vol. 57, no. 4, pp. 603–619, Jan. 1985, doi: 10.1351/pac198557040603.

[97] K. Chen, T. Zhang, X. Chen, Y. He, and X. Liang, “Model construction of micro-pores in shale: A case study of Silurian Longmaxi Formation shale in Dianqianbei area, SW China,” *Petroleum Exploration and Development*, vol. 45, no. 3, pp. 412–421, Jun. 2018, doi: 10.1016/S1876-3804(18)30046-6.

[98] M. Dogan, A. U. Dogan, F. I. Yesilyurt, D. Alaygut, I. Buckner, and D. E. Wurster, “Baseline studies of the clay minerals society special clays: Specific surface area by the Brunauer Emmett Teller (BET) method,” *Clays Clay Miner.*, vol. 55, no. 5, pp. 534–541, Oct. 2007, doi: 10.1346/CCMN.2007.0550508.

[99] I. M. K. Ismail, “Adsorption of nitrogen and krypton at 77 K on silicas and graphitized carbons,” *Carbon*, vol. 28, no. 2, pp. 423–434, Jan. 1990, doi: 10.1016/0008-6223(90)90016-R.

[100] J. Rouquerol, P. Llewellyn, and F. Rouquerol, “Is the bet equation applicable to microporous adsorbents?,” in *Studies in Surface Science and Catalysis*, vol. 160, in Characterization of Porous Solids VII, vol. 160. , Elsevier, 2007, pp. 49–56. doi: 10.1016/S0167-2991(07)80008-5.

[101] J. Wang and X. Guo, “Adsorption isotherm models: Classification, physical meaning, application and solving method,” *Chemosphere*, vol. 258, p. 127279, Nov. 2020, doi: 10.1016/j.chemosphere.2020.127279.

[102] C. Scherdel, G. Reichenauer, and M. Wiener, “Relationship between pore volumes and surface areas derived from the evaluation of N2-sorption data by DR-, BET- and t-plot,” *Microporous and Mesoporous Materials*, vol. 132, no. 3, pp. 572–575, Aug. 2010, doi: 10.1016/j.micromeso.2010.03.034.

[103] A. W. C. van den Berg, S. T. Bromley, J. C. Wojdel, and J. C. Jansen, “Molecular hydrogen confined within nanoporous framework materials: Comparison of density functional and classical force-field descriptions,” *Phys. Rev. B*, vol. 72, no. 15, p. 155428, Oct. 2005, doi: 10.1103/PhysRevB.72.155428.

[104] M. J. Sanchez-Martin, M. S. Rodriguez-Cruz, M. S. Andrades, and M. Sanchez-Camazano, "Efficiency of different clay minerals modified with a cationic surfactant in the adsorption of pesticides: Influence of clay type and pesticide hydrophobicity," *Applied Clay Science*, vol. 31, no. 3, pp. 216–228, Mar. 2006, doi: 10.1016/j.clay.2005.07.008.

[105] A. Guinier, *X-ray Diffraction in Crystals, Imperfect Crystals, and Amorphous Bodies*. Courier Corporation, 1994.

[106] E. Ordoñez and H. Mandujano, "Development and Validation of an X-ray Imaging Detector for Digital Radiography at Low Resolution," *Journal of Nuclear Physics, Material Sciences, Radiation and Applications*, vol. 7, Feb. 2020, doi: 10.15415/jnp.2020.72023.

[107] W. D. Coolidge, "Vacuum-tube,".

[108] A. Vamvakeros, "Operando chemical tomography of packed bed and membrane reactors for methane processing," 2017.

[109] "NIST: X-Ray Mass Attenuation Coefficients - Air, Dry."

[110] "SOLEIL in 3 questions | French synchrotron radiation center."

[111] "CRISTAL | French national synchrotron facility."

[112] D. A. Keen, "A comparison of various commonly used correlation functions for describing total scattering," *J Appl Cryst*, vol. 34, no. 2, pp. 172–177, Apr. 2001, doi: 10.1107/S0021889800019993.

[113] Z. Chen *et al.*, "Understanding porous materials with pair distribution functions," *Cell Reports Physical Science*, vol. 4, no. 12, p. 101681, Dec. 2023, doi: 10.1016/j.xcrp.2023.101681.

[114] "Pair Distribution Function (PDF) analysis." https://www.globalsino.com/EM/page3097.html

[115] J. Kowalska and S. DeBeer, "The role of X-ray spectroscopy in understanding the geometric and electronic structure of nitrogenase," *Biochimica et biophysica acta*, vol. 1853, pp. 1406–1415, Jun. 2015, doi: 10.1016/j.bbamcr.2014.11.027.

[116] K. Andersen and C. Carlile, "A Proposal for a Next Generation European Neutron Source," *Journal of Physics: Conference Series*, vol. 746, p. 012030, Sep. 2016, doi: 10.1088/1742-6596/746/1/012030.

[117] "Neutron scattering facilities - E-neutrons wiki."

[118] N. F. Berk, "Outline of Neutron Scattering Formalism," *J Res Natl Inst Stand Technol*, vol. 98, no. 1, pp. 15–30, 1993, doi: 10.6028/jres.098.002.

[119] "Neutron scattering lengths and cross sections." https://www.ncnr.nist.gov/resources/n-lengths/

[120] *Neutron diffraction. 3rd Edition*. Oxford: G. E. Bacon, 1975.

[121] J. Dereziński and R. Früboes, "Fermi Golden Rule and Open Quantum Systems," in *Open Quantum Systems III*, vol. 1882, in Lecture Notes in Mathematics, vol. 1882. , Berlin, Heidelberg: Springer Berlin Heidelberg, 2006, pp. 67–116. doi: 10.1007/3-540-33967-1_2.

[122] A. T. Boothroyd, *Principles of Neutron Scattering from Condensed Matter*. Oxford University Press, 2020.

[123] T. Brückel and Forschungszentrum Jülich, Eds., *Neutron scattering: lectures of the JCNS laboratory course held at Forschungszentrum Jülich and the research reactor FRM II of TU Munich*. in Schriften des Forschungszentrums Jülich Reihe Schlüsseltechnologien, no. 15. Jülich: Forschungszentrum Jülich, 2010.

[124] O. Arnold *et al.*, "Mantid—Data analysis and visualization package for neutron scattering and μSR experiments," *Nuclear Instruments and Methods in Physics Research Section A: Accelerators, Spectrometers, Detectors and Associated Equipment*, vol. 764, pp. 156–166, Nov. 2014, doi: 10.1016/j.nima.2014.07.029.

[125] F. Björn, R. Stéphane, M. Giuliana, and M. Olivier, "Panther — the new thermal neutron time-of-flight spectrometer at the ILL," *EPJ Web of Conferences*, 2022.

[126] T. E. Karakasidis and C. A. Charitidis, "Multiscale modeling in nanomaterials science," *Materials Science and Engineering: C*, vol. 27, no. 5, pp. 1082–1089, Sep. 2007, doi: 10.1016/j.msec.2006.06.029.

[127] D. Frenkel and B. Smit, *Understanding Molecular Simulation: From Algorithms to Applications*. Elsevier, 2023.

[128] G. E. Norman and V. S. Filinov, "Investigations of phase transitions by a Monte-Carlo method," *High Temperature*, vol. 7, no. 2, p. 216, 1969.

[129] D. Dubbeldam, A. Torres-Knoop, and K. S. Walton, "On the inner workings of Monte Carlo codes," *Molecular Simulation*, vol. 39, no. 14–15, pp. 1253–1292, Dec. 2013, doi: 10.1080/08927022.2013.819102.

[130] L. Zhu *et al.*, "Investigation of methane adsorption in kaolinite–methanol intercalation complex interlayer by Monte Carlo simulations," *Energy Exploration & Exploitation*, vol. 42, no. 1, pp. 220–230, Jan. 2024, doi: 10.1177/01445987231196167.

[131] V. S. Neverov, "XaNSoNS: GPU-accelerated simulator of diffraction patterns of nanoparticles," *SoftwareX*, vol. 6, pp. 63–68, Jan. 2017, doi: 10.1016/j.softx.2017.01.004.

[132] L. J. Michot, I. Bihannic, M. Pelletier, E. Rinnert, and J.-L. Robert, "Hydration and swelling of synthetic Na-saponites: Influence of layer charge," *American Mineralogist*, vol. 90, no. 1, pp. 166–172, Jan. 2005, doi: 10.2138/am.2005.1600.

[133] A. Derkowski and A. Kuligiewicz, "Thermal Analysis and Thermal Reactions of Smectites: a Review of Methodology, Mechanisms, and Kinetics," *Clays Clay Miner.*, vol. 70, no. 6, pp. 946–972, Dec. 2022, doi: 10.1007/s42860-023-00222-y.

[134] G. E. Christidis *et al.*, "The Nature of Laponite: Pure Hectorite or a Mixture of Different Trioctahedral Phases?," *Minerals*, vol. 8, no. 8, Art. no. 8, Aug. 2018, doi: 10.3390/min8080314.

[135] G. Lagaly, "Chapter 5 Colloid Clay Science," in *Developments in Clay Science*, vol. 1, Elsevier, 2006, pp. 141–245. doi: 10.1016/S1572-4352(05)01005-6.

[136] R. C. Jones, "X-ray diffraction by randomly oriented line gratings," *Acta Crystallographica*, vol. 2, no. 4, pp. 252–257, 1949, doi: 10.1107/S0365110X49000643.

[137] C. Bousige *et al.*, "Progressive melting in confined one-dimensional C 60 chains," *Phys. Rev. B*, vol. 86, no. 4, p. 045446, Jul. 2012, doi: 10.1103/PhysRevB.86.045446.

[138] O. Goncharuk *et al.*, "Thermoresponsive hydrogels physically crosslinked with magnetically modified LAPONITE® nanoparticles," *Soft Matter*, vol. 16, no. 24, pp. 5689–5701, 2020, doi: 10.1039/D0SM00929F.

[139] J. T. Kloprogge, "Chapter 8 - Application of Vibrational Spectroscopy in Clay Minerals Synthesis," in *Developments in Clay Science*, vol. 8, in Infrared and Raman Spectroscopies of Clay Minerals, vol. 8. , Elsevier, 2017, pp. 222–287. doi: 10.1016/B978-0-08-100355-8.00008-4.

[140] T. Ebata, A. Iwasaki, and N. Mikami, "Vibrational Relaxation of OH and OD Stretching Vibrations of Phenol and Its Clusters Studied by IR−UV Pump−Probe Spectroscopy," *J. Phys. Chem. A*, vol. 104, no. 34, pp. 7974–7979, Aug. 2000, doi: 10.1021/jp0015022.

[141] T. Seki *et al.*, "The Bending Mode of Water: A Powerful Probe for Hydrogen Bond Structure of Aqueous Systems," *J Phys Chem Lett*, vol. 11, no. 19, pp. 8459–8469, Oct. 2020, doi: 10.1021/acs.jpclett.0c01259.

[142] H. Pálková, J. Madejová, M. Zimowska, and E. M. Serwicka, "Laponite-derived porous clay heterostructures: II. FTIR study of the structure evolution," *Microporous and Mesoporous Materials*, vol. 127, no. 3, pp. 237–244, Feb. 2010, doi: 10.1016/j.micromeso.2009.07.012.

[143] A. Z. Khalifa *et al.*, "Advances in alkali-activation of clay minerals," *Cement and Concrete Research*, vol. 132, p. 106050, Jun. 2020, doi: 10.1016/j.cemconres.2020.106050.

[144] P. A. Wheeler, J. Wang, J. Baker, and L. J. Mathias, "Synthesis and Characterization of Covalently Functionalized Laponite Clay," *Chem. Mater.*, vol. 17, no. 11, pp. 3012–3018, May 2005, doi: 10.1021/cm050306a.

[145] N. N. Herrera, J.-M. Letoffe, J.-P. Reymond, and E. Bourgeat-Lami, "Silylation of laponite clay particles with monofunctional and trifunctional vinyl alkoxysilanes," *J. Mater. Chem.*, vol. 15, no. 8, p. 863, 2005, doi: 10.1039/b415618h.

[146] Negrete, J.-M. Letoffe, J.-L. Putaux, L. David, and E. Bourgeat-Lami, "Aqueous Dispersions of Silane-Functionalized Laponite Clay Platelets. A First Step toward the

Elaboration of Water-Based Polymer/Clay Nanocomposites," *Langmuir*, vol. 20, no. 5, pp. 1564–1571, Mar. 2004, doi: 10.1021/la0349267.

[147] H. Pálková *et al.*, "Laponite-derived porous clay heterostructures: I. Synthesis and physicochemical characterization," *Microporous and Mesoporous Materials*, vol. 127, no. 3, pp. 228–236, Feb. 2010, doi: 10.1016/j.micromeso.2009.07.019.

[148] R. A. Kinsey, R. J. Kirkpatrick, J. Hower, K. A. Smith, and E. Oldfield, "High resolution aluminum-27 and silicon-29 nuclear magnetic resonance spectroscopic study of layer silicates, including clay minerals," *American Mineralogist*, vol. 70, no. 5–6, pp. 537–548, Jun. 1985.

[149] M. Vespa, R. Dähn, T. Huthwelker, and E. Wieland, "Soft X-ray absorption near-edge investigations of Mg-containing mineral phases relevant for cementitious materials," *Physics and Chemistry of the Earth, Parts A/B/C*, vol. 99, pp. 168–174, Jun. 2017, doi: 10.1016/j.pce.2017.03.006.

[150] K. Inoue *et al.*, "Systematic comparison of Mg K-edge XANES spectra of magnesium-bearing clay minerals and magnesium silicate hydrates: A promising tool for identifying magnesium silicate hydrate in natural samples," *Applied Clay Science*, vol. 245, p. 107152, Dec. 2023, doi: 10.1016/j.clay.2023.107152.

[151] B. Jabłońska, M. Busch, A. V. Kityk, and P. Huber, "Natural and Chemically Modified Post-Mining Clays—Structural and Surface Properties and Preliminary Tests on Copper Sorption," *Minerals*, vol. 9, no. 11, Art. no. 11, Nov. 2019, doi: 10.3390/min9110704.

[152] H. Rennhofer, D. Loidl, S. Puchegger, and H. Peterlik, "Structural development of PAN-based carbon fibers studied by in situ X-ray scattering at high temperatures under load," *Carbon*, vol. 48, no. 4, pp. 964–971, Apr. 2010, doi: 10.1016/j.carbon.2009.11.012.

[153] J. S. Edge *et al.*, "Structure and Dynamics of Molecular Hydrogen in the Interlayer Pores of a Swelling 2:1 Clay by Neutron Scattering," *J. Phys. Chem. C*, vol. 118, no. 44, pp. 25740–25747, Nov. 2014, doi: 10.1021/jp5082356.

[154] M. Didier, L. Leone, J.-M. Greneche, E. Giffaut, and L. Charlet, "Adsorption of Hydrogen Gas and Redox Processes in Clays," *Environ. Sci. Technol.*, vol. 46, no. 6, pp. 3574–3579, Mar. 2012, doi: 10.1021/es204583h.

[155] C. Mondelli *et al.*, "Hydrogen adsorption and diffusion in synthetic Na-montmorillonites at high pressures and temperature," *International Journal of Hydrogen Energy*, vol. 40, no. 6, pp. 2698–2709, Feb. 2015, doi: 10.1016/j.ijhydene.2014.12.038.

[156] K. M. Thomas, "Adsorption and desorption of hydrogen on metal–organic framework materials for storage applications: comparison with other nanoporous materials," *Dalton Trans.*, no. 9, p. 1487, 2009, doi: 10.1039/b815583f.

[157] "Hydrogen Storage in Metal–Organic Frameworks | Chemical Reviews."

[158] B. Panella, M. Hirscher, and S. Roth, "Hydrogen adsorption in different carbon nanostructures," *Carbon*, vol. 43, no. 10, pp. 2209–2214, Aug. 2005, doi: 10.1016/j.carbon.2005.03.037.

[159] R. Sips, "On the Structure of a Catalyst Surface," *The Journal of Chemical Physics*, vol. 16, no. 5, pp. 490–495, May 1948, doi: 10.1063/1.1746922.

[160] S. Ma *et al.*, "Further Investigation of the Effect of Framework Catenation on Hydrogen Uptake in Metal−Organic Frameworks," *J. Am. Chem. Soc.*, vol. 130, no. 47, pp. 15896–15902, Nov. 2008, doi: 10.1021/ja803492q.

[161] H. Furukawa, M. A. Miller, and O. M. Yaghi, "Independent verification of the saturation hydrogen uptake in MOF-177 and establishment of a benchmark for hydrogen adsorption in metal–organic frameworks," *J. Mater. Chem.*, vol. 17, no. 30, p. 3197, 2007, doi: 10.1039/b703608f.

[162] L. R. Terry, S. Rols, M. Tian, I. Da Silva, S. J. Bending, and V. P. Ting, "Manipulation of the crystalline phase diagram of hydrogen through nanoscale confinement effects in porous carbons," *Nanoscale*, vol. 14, no. 19, pp. 7250–7261, 2022, doi: 10.1039/D2NR00587E.

[163] R. T. Azuah *et al.*, "DAVE: A Comprehensive Software Suite for the Reduction, Visualization, and Analysis of Low Energy Neutron Spectroscopic Data," *Journal of Research of the National Institute of Standards and Technology*, vol. 114, no. 6, p. 341, Dec. 2009, doi: 10.6028/jres.114.025.

[164] D. McDowall, D. J. Adams, and A. M. Seddon, "Using small angle scattering to understand low molecular weight gels," *Soft Matter*, vol. 18, no. 8, pp. 1577–1590, 2022, doi: 10.1039/D1SM01707A.

[165] J. J. M. Beenakker, V. D. Borman, and S. Yu. Krylov, "Molecular transport in subnanometer pores: zero-point energy, reduced dimensionality and quantum sieving," *Chemical Physics Letters*, vol. 232, no. 4, pp. 379–382, Jan. 1995, doi: 10.1016/0009-2614(94)01372-3.

[166] H. Tanaka, H. Kanoh, M. Yudasaka, S. Iijima, and K. Kaneko, "Quantum Effects on Hydrogen Isotope Adsorption on Single-Wall Carbon Nanohorns," *J. Am. Chem. Soc.*, vol. 127, no. 20, pp. 7511–7516, May 2005, doi: 10.1021/ja0502573.

[167] A. V. A. Kumar, H. Jobic, and S. K. Bhatia, "Quantum Effects on Adsorption and Diffusion of Hydrogen and Deuterium in Microporous Materials," *J. Phys. Chem. B*, vol. 110, no. 33, pp. 16666–16671, Aug. 2006, doi: 10.1021/jp063034n.

[168] Y. Wang and S. K. Bhatia, "Quantum Effect-Mediated Hydrogen Isotope Mixture Separation in Slit Pore Nanoporous Materials," *J. Phys. Chem. C*, vol. 113, no. 33, pp. 14953–14962, Aug. 2009, doi: 10.1021/jp9044397.